Comprehensive Multi-Disciplinary Design of an Electric Vertical Take-off and Landing Aircraft

Lim Kin Yip, Shawn

School of Mechanical & Aerospace Engineering

A thesis submitted to the Nanyang Technological University

in partial fulfilment of the requirements for the degree of

Doctor of Philosophy

2024

Statement of Originality

I hereby certify that the work embodied in this thesis is the result of original research, is free of plagiarised materials, and has not been submitted for a higher degree to any other University or Institution.

5 December 2024

Date

Lim Kin Yip, Shawn

Supervisor Declaration Statement

I have reviewed the content and presentation style of this thesis and declare it is free of plagiarism and of sufficient grammatical clarity to be examined. To the best of my knowledge, the research and writing are those of the candidate except as acknowledged in the Author Attribution Statement.
I confirm that the investigations were conducted in accord with the ethics policies and integrity standards of Nanyang Technological University and that the research data are presented honestly and without prejudice.

5 December 2024
.....
Date

james wang
.....
Professor James Wang

Authorship Attribution Statement

This thesis contains material from five papers published in the following peer-reviewed journals / from papers accepted at conferences in which I am listed as an author.

Chapter 4 is published as: Lim Kin Yip, Shawn, Andy Koh Jun Hoong & James Wang, "Simplified Model for Evaluating eVTOL Conceptual Designs and with Example Results for Three Types of eVTOL Aircraft Configurations," Paper 132. *48th European Rotorcraft Forum (ERF)*, Winterthur, Switzerland, September 2022.

The contributions of the co-authors are as follows:

- I proposed the initial idea and conceptualization.
- Professor James Wang provided the supervision and revised the manuscript.
- I prepared the manuscript and presented the presentation.
- I designed the overall methodology for its formulation and implementation.
- Andy Koh Jun Hoong assisted in the implementation and set up of the algorithm.
- All authors were involved in the investigation and discussions.

Chapter 5 is published as: Lim Kin Yip, Shawn, Boon Zhi Yuan & James Wang, "Trajectory Modelling of Transition Regime Using Blade Element Method for Different eVTOL Configuration," Paper 175. *49th European Rotorcraft Forum (ERF)*, Bückeburg, Germany, September 2023.

The contributions of the co-authors are as follows:

- I proposed the initial idea and conceptualization.
- Professor James Wang provided the supervision and revised the manuscript.
- I prepared the manuscript and presented the presentation.
- I designed the overall methodology for its formulation and implementation.
- Boon Zhi Yuan assisted in the implementation and set up of the algorithm.
- All authors were involved in the investigation and discussions.

Chapter 6 is published as:

1. Abhijnan Dikshit, Lim Kin Yip, Shawn. & James Wang, "Parametric Study on Wing Design Variables for Tandem Wing Configuration eVTOL Aircraft," Paper 133. *48th European Rotorcraft Forum (ERF)*, Winterthur, Switzerland, September 2022.

   The contributions of the co-authors are as follows:

   - Professor James Wang provided the supervision and revised the manuscript.
   - I co-designed the study and prepared the manuscript with the co-authors.
   - I prepared the manuscript drafts with the co-authors.
   - I presented the presentation and its contents.
   - Abhijnan Dikshit prepared the results and assisted with the iterative task.
   - All authors were involved in the investigation and discussions.

2. Abhijnan Dikshit, Tom Caton Arnaud Stokkermans, Lim Kin Yip, Shawn. & James Wang, "Effect of Lifting Surface and Tail Configuration on the Aerodynamics and Flight Mechanics of VTOL Aircraft," Paper 1237, *Vertical Flight Society (VFS) Forum 78*, Fort Worth, Texas, May 2022.

   The contributions of the co-authors are as follows:

   - Professor James Wang provided the initial project direction and revised the manuscript.
   - I co-designed the study and prepared the manuscript with the co-authors.
   - I prepared the manuscript drafts with the co-authors.
   - I presented the presentation for (1) and (2) and its contents.
   - Abhijnan Dikshit conducted the AVL analysis and prepared the results.
   - Tom Caton Arnaud Stokkermans integrated the optimizer and conducted the CFD simulations.
   - All authors were involved in the investigation and discussions.

Chapter 7 is published as: Lim Kin Yip, Shawn, Philemon Koh Jun Kai, Satish Suppiah, Eden Lee Yao Rong & James Wang, "Experimental and Analytical Approach Towards Determining an Optimal Wing Arrangement for eVTOL Aircraft based on Aerodynamic Performance and Handling Qualities," Paper 1251. *Vertical Flight Society (VFS) Forum 80*, Montréal, Canada, May 2024.

The contributions of the co-authors are as follows:

- Professor James Wang provided the supervision and revised the manuscript.
- I designed the overall methodology and its implementation.
- I prepared the manuscript and presented the presentation.
- Philemon Koh Jun Kai assisted in the writing of the manuscript.
- Satish Suppiah piloted the subscale models.
- Eden Lee Yao Rong assisted in the construction of the subscale models.
- All authors were involved in the investigation and discussions.

5 December 2024
.....
Date

.....
Lim Kin Yip, Shawn

Acknowledgement

First and foremost, I extend my deepest gratitude to Professor James Wang for his unwavering support, exceptional guidance, boundless wisdom, and tremendous inspiration. His exemplary mentorship has been pivotal throughout my research journey, setting a high standard of excellence that will inspire me throughout my career. I am profoundly thankful for the opportunity to work under his supervision.

I would also like to express my heartfelt thanks to Assistant Professor Ng Bing Feng and Assistant Professor Chan Wai Lee for their constant guidance and treasured encouragement, which have been invaluable since my undergraduate studies and throughout the Ph.D. program. Additionally, I extend my thankful appreciation to Associate Professor Christopher Ho Tin Lee for his insightful feedback and support during my program.

My sincere thanks go to the fellow members of the *eVTOL Research and Innovation Centre*, including both researchers and students. Their steadfast support and invaluable assistance have been instrumental in the successful completion of this research. A special mention goes to Philemon Koh and Eden Lee, who have been great colleagues and friends. Their support with technical and administrative matters, even under tight deadlines and spontaneous tasks, has been greatly appreciated.

Lastly, and most importantly, I dedicate my profound love and fathomless appreciation to my mom Annie, my dad Jason, my brother Kenny and my late beloved grandmother. Their unwavering encouragement, continuous understanding, and unconditional support have been a constant source of strength and motivation throughout my Ph.D. journey.

"*If I have seen further it is by standing upon the shoulders of Giants.*"

– Isaac Newton

Abstract

The advent of electric Vertical Take-Off and Landing (eVTOL) aircraft represents a significant shift in aerospace design, driven by the promise of cleaner, quieter, and more efficient urban air mobility solutions. This research addresses the critical need to understand and optimize eVTOL aircraft design and performance through a comprehensive, multidisciplinary approach. The current body of knowledge on eVTOL aircraft design is expanding, yet significant gaps and limitations persist. Traditional non-electric VTOL aircraft and commercial aviation designs do not adequately address the unique complexities introduced by electric propulsion such as energy efficiency, power-to-weight trade-offs, and integrated aerodynamic and propulsion systems. This research aims to bridge these gaps by conducting a detailed comparative study on the advancements in eVTOL aircraft design and configurations, providing critical insights into design trade-offs and innovations enabled by electric propulsion.

The objectives of this research are fourfold: First, to conduct a detailed comparative study on the advancement of eVTOL aircraft design and configurations. This study identifies and compares evolving attributes and configuration types that influence aircraft sizing and performance, highlighting how electric propulsion technology diverges from traditional non-electric VTOL and commercial aviation design paths. Second, the research involves designing and developing a comprehensive multidisciplinary eVTOL aircraft model to assess and evaluate aircraft performance across various flight regimes. This model uses a generalized framework to account for different eVTOL components from initial to detailed design phases, integrating theoretical formulations and empirical data to provide a full performance analysis of all flight segments during an aircraft mission. Third, the study characterizes eVTOL aircraft transition performance during the conversion between vertical and horizontal flight phases. Utilizing a trimming approach and flight trajectory model with Blade-Element Momentum Theory, this research offers improved modeling and characterization of the critical transition phase for different eVTOL configurations. Fourth, the research quantifies the benefits and designs of lifting surfaces for eVTOL aircraft in terms of aerodynamics, stability, and handling qualities. It develops and validates both analytical and experimental models to optimize wing configurations, with subscale flight testing providing empirical validation of the performance and characteristics of different wing designs.

Methodologies employed in this research include aircraft parametric design and performance analysis, developing a comprehensive model to analyze and compare the performance of various eVTOL configurations, considering aerodynamics, propulsion, and flight performance. Additionally, flight trajectory-based transition analysis is formulated through detailed transition models based on transitional trajectories to characterize the transition phase for different eVTOL configurations. Wing configuration design and optimization is also conducted through a parametric study and subscale experimental testing to validate wing configurations, focusing on aerodynamics, flight performance, stability, and handling qualities.

This research provides a detailed framework for evaluating eVTOL aircraft design and performance, offering specific insights into key design trade-offs such as wing and rotor configurations, energy efficiency, aerodynamic stability, and transition flight dynamics enabled by electric propulsion. The findings introduce methodologies for optimizing aircraft configurations to balance efficiency, stability, and power requirements, directly addressing challenges such as minimizing drag, enhancing lift, and achieving smooth transition phases. These contributions deliver practical tools for aerospace engineers, eVTOL manufacturers, urban air mobility planners, and regulatory bodies, supporting the development of sustainable and efficient urban air mobility solutions.

This thesis presents a comprehensive exploration into the design, performance, and optimization of winged eVTOL aircraft such as Lift+Cruise, Tiltrotors and Lift+Tiltrotor configurations. This research achieves its objectives by conducting a detailed comparative study, developing a robust performance model, characterizing critical transition phases, and optimizing wing configurations for eVTOL aircraft. These advancements provide a significant contribution to the field by delivering valuable insights and practical tools for future eVTOL design and development. The study underscores the dynamic and multidisciplinary nature of eVTOL innovation, emphasizing the necessity of rigorous validation through both analytical and experimental methodologies. As eVTOL technology progresses, the findings of this research will play a pivotal role in shaping the next generation of aerial transportation, ensuring improved efficiency, enhanced safety, and suitability for the expanding demands of urban and regional air mobility.

Table of Contents

List of Figures

List of Tables

Nomenclature

Abbreviations

AC	–	Aerodynamic center
AAM	–	Advanced air mobility
AGL	–	Above ground level
AOB	–	Angle of bank
AVL	–	Athena vortex lattice
BEMT	–	Blade element momentum theory
CG	–	Center of gravity
CAD	–	Computer aided design
CFD	–	Computational fluid dynamics
CHR	–	Cooper Harper rating
CNR	–	Canard aircraft configuration
CNV	–	Conventional aircraft configuration
CANA	–	Canard wing
CONV	–	Conventional wing
COBYLA	–	Constrained optimization by linear approximation
DEP	–	Distributed electric propulsion
EASA	–	European union aviation safety agency
eVTOL	–	Electric vertical takeoff and landing
FM	–	Figure of merit
FAA	–	Federal aviation administration
FWG	–	Flying wing configuration
FLOPS	–	Flight optimization system
HAR	–	High aspect ratio
ISA	–	International standard atmosphere
L/D	–	Lift-to-drag ratio / aerodynamic efficiency
LAR	–	Low aspect ratio
MH	–	Martin Hepperle
MAC	–	Mean aerodynamic chord
MLT	–	Medium level turn
MTE	–	Mission task element
MTGW	–	Maximum takeoff gross weight
MATLAB	–	Matrix laboratory
NP	–	Neutral point
NACA	–	National advisory committee for aeronautics
NASA	–	National aeronautics and space administration
NDARC	–	NASA design and analysis of rotorcraft
openMDAO	–	Open-source multidisciplinary aircraft optimization
RPC	–	Rotor power correction
SM	–	Static margin
S&L	–	Straight and level
STOL	–	Short takeoff and landing
S/VTOL	–	Short/vertical take-off and landing
TWG	–	Tandem wing configuration
UAM	–	Urban air mobility
UAV	–	Unmanned aerial vehicle
VLM	–	Vortex lattice method
VTOL	–	Vertical takeoff and landing
XFLR5	–	XFOIL low Reynolds number 5

Alphabetical Symbols

a	–	Speed of sound	m/s
$\vec{a}$	–	Acceleration vector	m/s^2
A	–	Planform area	m^2
AR	–	Aspect ratio	-
b	–	Wingspan dimension	m
c	–	Chord length dimension	m
C_d	–	Component drag coefficient	-
C_D	–	Total drag coefficient	-
C_{D_i}	–	Induced drag coefficient	-
C_{D_o}	–	Parasite / zero-lift drag coefficient	-
C_f	–	Skin friction drag coefficient	-
C_l	–	Component lift coefficient	-
C_{l_β}	–	Rolling moment derivative with sideslip / dihedral effect	-
C_L	–	Total lift coefficient	-
C_{L_α}	–	Lift curve slope	-
C_m	–	Pitching moment coefficient	-
C_{m_α}	–	Pitching moment curve slope / pitch stiffness	-
C_{m_q}	–	Pitching moment derivative with pitch rate / pitch damping	-
C_{n_β}	–	Yawing moment derivative with sideslip / yaw stiffness	-
C_P	–	Power coefficient	-
C_T	–	Thrust coefficient	-
d	–	Diameter dimension	m
D	–	Drag force variable	N
e	–	Battery specific energy	Wh/kg
e	–	Oswald efficiency factor	-
E	–	Energy variable	kWh
f	–	Function / factor	-
F	–	Force variable	N
$\vec{F}$	–	Force vector	N
F_P	–	Parasite drag area	m^2
FM	–	Figure of merit	-
g	–	Gravitational acceleration	m/s^2
h	–	Height dimension	m
k	–	Induced drag factor	-
l	–	Length dimension	-
L	–	Lift force variable	N
L/D	–	Lift-to-drag ratio	-
m	–	Mass variable	Kg
M	–	Moment / torque variable	Nm
MAC	–	Mean aerodynamic chord dimension	m
MTGW	–	Maximum takeoff gross weight	kg
N	–	Number of units	-
P	–	Power variable	W
q	–	Dynamic pressure	Pa
Q_{wing}	–	Volume of wing	m^3
r	–	Radius dimension	m
R	–	Range variable	m
Re	–	Reynolds number	-
RPC	–	Rotor power correction	-

s	–	Displacement variable	m
S	–	Wing planform area	m^2
SE	–	Pack level specific energy	kWh/kg
SM	–	Static margin	-
t	–	Time taken variable	s
		Thickness dimension	-
T	–	Thrust force variable	N
T_2	–	Time to double amplitude	s
$\vec{v}$	–	Induced velocity vector	m/s
V	–	Velocity variable	m/s
$\vec{V}$	–	Velocity vector	m/s
w	–	Width dimension	m
W	–	Weight variable	N
x	–	Longitudinal x – coordinate distance	m
y	–	Lateral y – coordinate distance	m
z	–	Vertical z – coordinate distance	m

Greek Symbols

α	–	Angle of attack	degree (^{o})
β	–	Sideslip angle	degree (^{o})
γ	–	Induced climb/descent angle	degree (^{o})
Γ	–	Dihedral angle	degree (^{o})
ζ	–	Damping ratio	-
η	–	Efficiency parameter	-
θ	–	Pitch angle	degree (^{o})
κ	–	Rotor loss factor	-
λ	–	Taper ratio	-
		Inflow ratio	-
Λ	–	Sweep angle	degree (^{o})
μ	–	Dynamic viscosity	kg/ms
		Advance ratio	-
ν	–	Induced velocity	m/s
ρ	–	Density parameter	kg/m^3
σ	–	Solidity ratio	-
τ	–	Tiltrotor angle	degree (^{o})
τ	–	Time constant	1/s
Φ_f	–	Form factor	-
χ	–	Vortex ring state ratio	-
ω_n	–	Natural frequency	rad/s
Ω	–	Rotor tip speed	m/s

Subscript Symbols

b	–	Battery
br	–	Best range
c	–	Component
cg	–	Center of gravity
cyl	–	Cylinder
dr	–	Dutch roll mode
eff	–	Effective
eqv	–	Equivalent
f	–	Friction
fw	–	Front wing
front	–	Frontal area
hemi	–	Hemispherical
i	–	Index i^{th} component
le	–	Leading edge
mac	–	Mean aerodynamic chord
max	–	Maximum
min	–	Minimum
np	–	Neutral point
p	–	Profile / parasite
P	–	Power
ph	–	Phugoid mode
rw	–	Rear wing
ref	–	Reference condition
req	–	Required
spo	–	Short period oscillation
T	–	Thrust
tot	–	Total
x	–	X – axis coordinate
y	–	Y – axis coordinate
z	–	Z – axis coordinate
o	–	Zero value
¼	–	Quarter value
∞	–	Freestream condition

Chapter 1: Introduction

The advent of electric Vertical Take-Off and Landing (eVTOL) aircraft heralds a transformative shift in aerospace engineering, offering cleaner, quieter, and more efficient solutions for urban air mobility. However, the eVTOL aircraft introduces unique challenges and opportunities, including performance-to-weight trade-offs, complexities of transitioning between vertical and horizontal flight, and the integration of electric propulsion. This research addresses these challenges through a comprehensive, multidisciplinary approach, targeting the critical gaps in the current eVTOL design and analysis methodologies.

Urban traffic congestion is a growing global issue, resulting in wasted time, environmental pollution, and significant economic costs of trillions of dollars [1]. eVTOL aircraft is a key component of the Urban Air Mobility (UAM) concept, offer a promising solution to alleviate traffic congestion by introducing shared aerial transportation networks operating in three-dimensional space [2, 3]. These aircraft are designed for on-demand passenger, medical, and cargo transport, leverage electric propulsion to reduce operational costs and noise while enhancing sustainability. Furthermore, studies have shown that coupling electric power with vertical flight technology can provide substantial performance and noise benefits, reducing operating costs by up to 26% compared to conventional gas-powered aircraft [4–7].

Despite their potential, the adoption of eVTOL technology is hindered by several factors, including air traffic management, infrastructure challenges, community acceptance, and the limited performance of current designs [8, 9]. Specifically, the range of eVTOL aircraft is constrained by energy storage limitations and the additional weight and complexity of vertical flight systems. These challenges are closely tied to the design and sizing of eVTOL aircraft, which significantly impact vehicle performance, emissions, operations, and certification for UAM. Overcoming these challenges could lead to a significant reduction in flight costs, potentially lowering costs by 78% to 87% compared to traditional private helicopter services [10–12].

The eVTOL market is projected to reach a total addressable market of $1 trillion by 2040, with over 600 startups and companies developing various eVTOL designs [13, 14]. Recent eVTOL developments explore diverse design concepts, incorporating

technologies such as distributed electric propulsion, multi-copters/rotors, ducted fans, vectored propulsion, and fixed-wings in various configurations [15–22].

Electric propulsion presents new design challenges, particularly in terms of energy management, efficiency and system integration and certification requirements, existing non-electric VTOL and commercial aviation design frameworks are inadequate to fully address these complexities, which are often too complex for early-stage design or fail to account for multidisciplinary performance considerations. There is a need for new or modified analytical tools capable of comprehensively evaluating unconventional eVTOL configurations across a wide range of operating conditions, supporting the various stages of the aircraft design process.

While single-disciplinary methods have traditionally been used for aircraft design, they fall short in capturing the interdependent nature of aerodynamics, stability, and energy consumption, which are critical for eVTOL performance. For instance, existing aerodynamic frameworks often focus solely on lift and drag characteristics without accounting for their impact on energy efficiency or stability during critical phases such as transition between vertical and horizontal flight. Similarly, propulsion models typically optimize power systems in isolation, neglecting their aerodynamic interactions and the resulting impact on overall performance. Stability assessments are also frequently treated independently, ignoring the influence of energy consumption and aerodynamic trade-offs.

This research overcomes these limitations by introducing a multidisciplinary framework that integrates aerodynamics, stability, and propulsion into a cohesive model. For example, the framework evaluates the aerodynamic effects of lifting surfaces and rotors in tandem with energy consumption metrics, ensuring that improvements in one area do not detract from performance in another. Additionally, the transition-phase characterization combines trajectory optimization with aerodynamic stability analysis, providing a holistic view of system behavior during this critical flight phase. By addressing these interdependencies, the proposed framework offers a more robust and comprehensive solution, leading to designs that are not only more efficient and stable but also better suited to the unique demands of eVTOL operations.

This research identifies and addresses five key technical and methodological areas:

1. **Incorporating Unique eVTOL Design Factors**: Current frameworks often overlook the distinctive features of eVTOL aircraft, including the diverse combinations of tilting and fixed configurations, as well as the specific operational requirements of urban environments. These factors have critical implications for aerodynamic performance, energy usage, and mission viability, yet they are not adequately considered in existing methodologies.
2. **Simplifying Early-Stage Design Analysis**: Advanced tools and programs, while highly capable, are often too complex and require numerous well-defined input variables that may not be available during the conceptual design phase. This complexity creates a barrier to their application for early-stage design exploration, where rapid iteration and flexibility are essential.
3. **Developing Comprehensive Multidisciplinary Frameworks**: There is a lack of versatile design frameworks that integrate key performance considerations across disciplines, such as aerodynamics, propulsion, stability, and flight mechanics. Existing methods often focus on isolated aspects, neglecting the holistic approach needed to capture the interdependencies critical to eVTOL aircraft performance.
4. **Characterizing Transition Phases**: Insufficient attention has been given to accurately modeling and understanding the transition phase between vertical and horizontal flight such as the peak power management and coordination of wing lift and rotor thrust. This phase is crucial for eVTOL efficiency and stability but remains poorly characterized in current studies.
5. **Optimizing eVTOL Wing and Rotor Configurations**: Limited methodologies exist for systematically optimizing configurations, such as wing placements, rotor designs, and their interactions. These elements are vital for maximizing aerodynamic efficiency and minimizing energy consumption, yet the optimization processes remain underexplored.

This study bridges critical gaps by developing a versatile multidisciplinary framework that integrates early-stage design tools with detailed aerodynamic and transition-phase analyses, enabling comprehensive performance assessment across all flight regimes. By optimizing lifting surfaces and rotor configurations, the research enhances

aerodynamics, stability, handling qualities, and energy efficiency while reducing weight.

While the transition phase between vertical and horizontal flight presents critical challenges for eVTOL aircraft, including managing peak power demands, coordinating lift transfer from rotors to wings, and addressing the complex dynamics of tilt-rotor systems. These challenges are unsatisfactorily characterized in existing research, which lacks comprehensive models for handling the aerodynamic, propulsion, and control issues during this phase. This study addresses these gaps by developing a transition-phase modeling framework that integrates trimming techniques and trajectory-based analyses to capture dynamic interactions. It identifies optimized power management strategies to meet peak energy demands while maintaining efficiency and investigates different eVTOL aircraft configurations to determine optimal transition parameters. Additionally, existing aerodynamic models are used to ensure smooth lift transfer and stable flight across varying configurations. These contributions enhance the safety, efficiency, and robustness of eVTOL aircraft during one of the most complex stages of flight. The research also develops and validates analytical and experimental models to optimize wing designs tailored to eVTOL applications.

The outcomes of this research provide targeted benefits to key stakeholders in the aerospace industry. For aerospace engineers and eVTOL manufacturers, the detailed comparative studies and performance analysis tools offer practical frameworks for optimizing design parameters such as wing configurations, rotor placements, and energy efficiency. These tools enable the development of lighter, more aerodynamic, and operationally viable aircraft. Urban air mobility planners can apply the transition performance models to refine route planning, airspace integration, and operational safety strategies, ensuring reliable and efficient urban transportation networks. Regulatory authorities can use the developed performance and trajectory models to establish precise metrics and benchmarks for safety, stability, and energy efficiency, informing certification requirements tailored to eVTOL aircraft. By addressing critical challenges such as energy management, transition dynamics, and design trade-offs, this research contributes actionable insights and methodologies that support the evolution of sustainable and efficient urban air mobility systems.

1.1 Background and Motivations

Global connectivity and transportation networks are essential for the growth and sustainability of countries, particularly for a resource-limited nation like Singapore, which is one of the world's most connected countries [23]. In recent years, transportation networks within many major cities have become heavily congested due to rising population numbers, placing immense strain on existing infrastructure such as urban roads and railways.

Singapore's public transport system accommodates over 5.5 million train and bus rides daily, while its overland border crossings handle more than 450,000 travelers each day, making it one of the busiest hubs in the region. In July 2015, a major disruption involving two of Singapore's main train networks left over 410,000 commuters stranded, significantly impacting local businesses and services [24, 25]. Despite Singapore's relatively compact size, it is recognized as one of the most pivotal aviation hubs in the region, transport links to neighboring countries are vital for tourism and both intercity and regional connectivity such as Malaysia, Indonesia and Thailand. To address increasing transportation demands, Singapore expanded its main airport with a fourth terminal in 2022, and a fifth terminal is slated to open in 2025 to accommodate 140 million passenger per year. Additionally, in 2019, German start-up Volocopter established operations in Singapore, aiming to introduce air taxi services to support regional transport and alleviate pressure on existing infrastructure.

Similarly, cities worldwide, such as Bogotá, Jakarta, New York, and Bangkok, face severe road congestion. In Boston, Massachusetts, for example, drivers lose an average of 164 hours annually in traffic, costing up to $2,291 per driver [26]. A promising solution to alleviate such congestion lies in implementing a three-dimensional urban transportation network. By incorporating eVTOL aircraft, this multimodal approach can significantly reduce the burden on ground transportation systems while enhancing connectivity and efficiency.

Since the introduction of the first eVTOL aircraft, the AgustaWestland Project Zero, in 2013, there has been significant interest in developing analytical models to investigate the feasibility of electric-based aerial vehicles in urban environments [15, 27]. However, most studies focus on eVTOL aircraft design from a single perspective, such as energy-

based performance analysis or aerodynamic efficiency for a truncated mission [16–22]. This narrow focus results in a discrete design approach, where propulsors and wing structures for vertical and horizontal flight operate independently, leading to sub-optimal performance across various flight regimes, such as high-power requirements, weight limitations, and unfavorable aerodynamics. Consequently, existing eVTOL designs may lack complete integration, restricting potential performance advancements.

This motivates the development of a new methodology to analyze and integrate various eVTOL aircraft architectures, aiming to achieve greater performance and efficiency through a multidisciplinary design approach.
This research addresses imperative questions in the:

→ Aircraft Parametric Design and Performance Analysis: What are the critical design parameters and interactions that influence the aerodynamic performance, energy efficiency, and operational effectiveness of eVTOL aircraft, and how can these parameters be incorporated into a comprehensive multidisciplinary modeling framework?

→ Flight Trajectory-Based Transition Analysis: What methodologies can be developed to accurately model and analyze the transition phase between vertical, translational, and horizontal flight modes, ensuring sufficient fidelity to capture the transition parameters, power requirements and dynamics challenges across various eVTOL configurations?

→ Wing Configuration Design and Optimization: How do variations in wing and rotor configurations impact the aerodynamic performance, energy consumption, and handling qualities of eVTOL aircraft, and what optimization strategies can be employed to achieve an optimal balance of these factors for practical applications?

This work aims to develop comprehensive modeling methods for eVTOL aircraft to identify an optimal design that enhances performance and efficiency.

1.2 Objectives and Contributions

The objective of this dissertation is to develop and validate multidisciplinary methods to optimize the design and performance of eVTOL aircraft with aerodynamic lifting surfaces. Through a combination of analytical and experimental investigations, this research addresses the critical challenges of aerodynamics, stability, propulsion, and performance optimization for diverse eVTOL configurations. The ultimate goal is to enhance operational efficiency and commercial viability, advancing the technology for passenger-carrying eVTOL aircraft.

The existing body of eVTOL research lacks robust methodologies that comprehensively integrate the critical aspects of design and performance across multiple disciplines. This dissertation bridges these gaps by addressing key challenges within the three primary elements outlined in Figure 1.1.

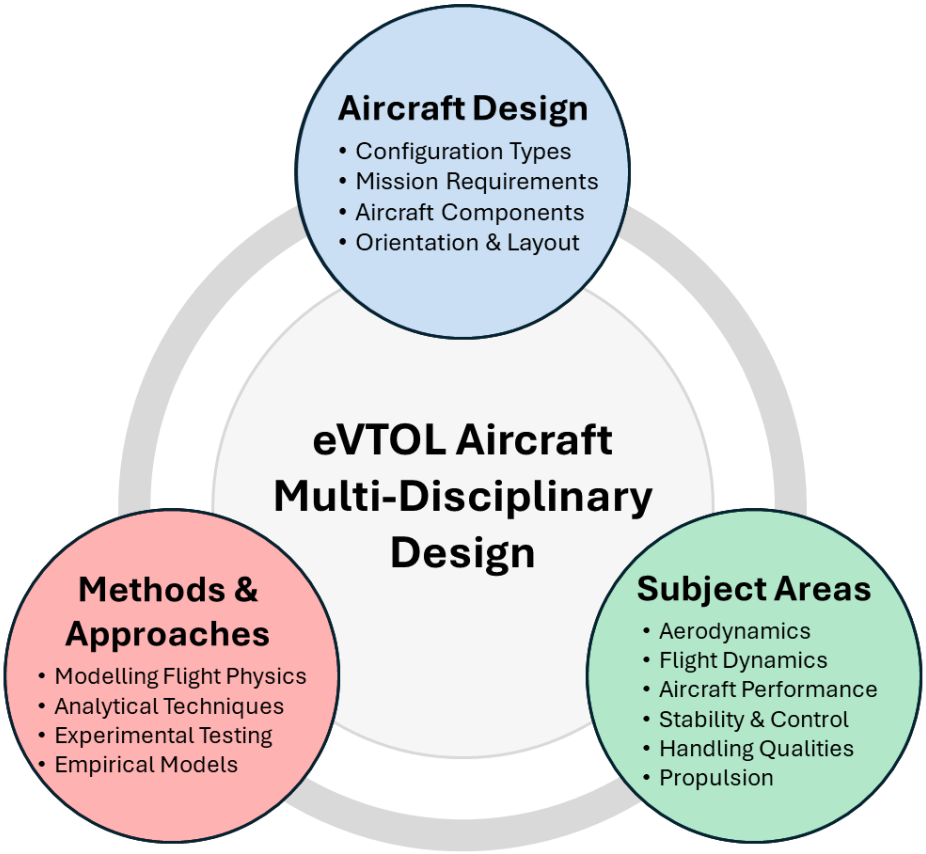

Figure 1.1: Research gaps and area of contribution.

This research directly addresses these gaps through three specific objectives and their contributions:

→ **Aircraft Design Limitations**

- Gaps: Existing frameworks fail to adequately account for diverse configuration types such as tilting rotors, fixed wings, mission-specific requirements, and the integration of propulsion systems with various aerodynamic components. This leads to incomplete or overly narrow design evaluations.
- Contribution: This research develops a flexible Aircraft Parametric Design and Performance Analysis framework, developed in MATLAB. The model enables detailed comparisons of eVTOL aircraft configurations and provides performance assessments across a wide range of missions and operating conditions. Additionally, it offers the versatility to extend its analysis to studies on cost efficiency and operational feasibility.

→ **Insufficient Methods & Approaches**

- Gaps: Traditional design tools lack versatility and fail to integrate multidisciplinary considerations, such as flight physics, stability, and propulsion. Moreover, existing tools are often overly complex, making them unsuitable for early-stage design phases where rapid iteration is critical.
- Contribution: This work introduces a Flight Trajectory-Based Transition Analysis method for winged eVTOL aircraft. This approach couples trajectory modeling with established low-fidelity aerodynamic theories, providing a detailed characterization of the transition phase—critical for stability, energy efficiency, and operational safety.

→ **Underexplored Subject Areas**

- Gaps: There is a lack of optimization techniques that systematically address the interplay between aerodynamics, stability, and propulsion, particularly for wing and rotor configurations. Existing studies often overlook experimental validation, reducing the practical applicability of their findings.
- Contribution: A Wing Configuration Design and Optimization framework was developed to optimize lifting surfaces and rotor placements. Subscale experimental testing validated the model, providing actionable insights into aerodynamic efficiency, stability, and energy consumption.

1.3 Scope and Organization

With the alignment to the proposed objectives, the scope of the work has covered:

1. **Conduct and present a detailed comparative study** on the advancement of eVTOL aircraft designs and configurations. This aims to identify and compare evolving attributes and configuration types that influence aircraft sizing and performance. The introduction of electric propulsion technology has enabled new concepts and approaches towards aircraft design, differing from the design path of non-electric VTOL aircraft and commercial aviation.
2. **Design and develop a comprehensive multidisciplinary eVTOL aircraft model** to assess and evaluate aircraft performance in various flight regimes. The approach uses a generalized framework to account for different eVTOL components from the initial design to the detailed design phase developed in MATLAB. The developed framework integrates theoretical formulations using analytical models with empirical models, generating comprehensive modeling for both vertical and horizontal flight components. This approach offers a full performance analysis of all flight segments during an aircraft mission and is generalized to be applicable for various types of eVTOL aircraft configurations.
3. **Characterize the eVTOL aircraft transition performance and its effects** based on a projected trajectory for different eVTOL configurations during the conversion between vertical and horizontal flight phases. The proposed approach uses a trimming method, and a flight trajectory model combined with Blade-Element Momentum Theory (BEMT) to improve the characterization and modeling of the transition phase. While BEMT simplifies complex aerodynamics by dividing the rotor into segments, it is sufficiently accurate for the transition phase, providing a practical balance between computational efficiency and the required fidelity for preliminary design assessments and performance optimization.
4. **Quantify the benefits and design of lifting surfaces for eVTOL aircraft** in terms of aerodynamics, stability, and handling qualities. The theoretical model uses Vortex Lattice Methods and Ansys Fluent to assess the full spectrum of wing designs. Subscale experimental flight testing is then conducted to validate these findings and provide insights into the real-world behavior. While subscale testing captures critical trends, it may not fully represent effects like full-scale turbulence and dynamics. Therefore, this approach integrates both experimental and computational methods for a comprehensive assessment and optimization of eVTOL wing designs.

The context and scope of this dissertation are illustrated in Figure 1.2.

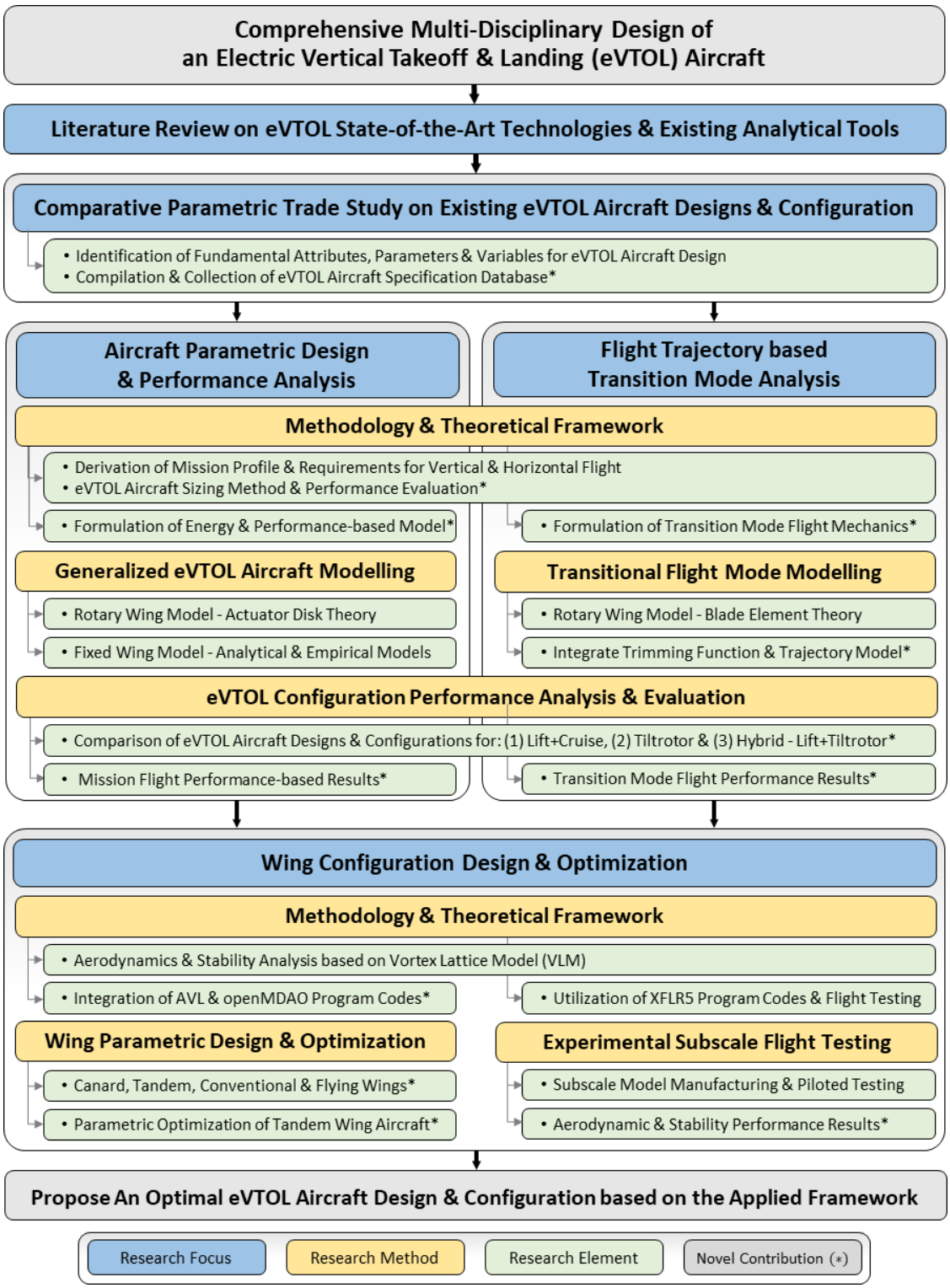

Figure 1.2: Research scope and organization.

The organization of the chapters is as follows:

Chapter 1: provides a brief background on electric vertical flight and its relevance for future applications, outlining the motivation for this research.

Chapter 2: reviews the state-of-the-art in eVTOL aircraft technologies and methods, offering an in-depth literature review on previous research in eVTOL aircraft design.

Chapter 3: compares various types and configurations of eVTOL aircraft to generate a database and parameters for defining an eVTOL aircraft. It includes a survey of current eVTOL designs and a trade study summarizing typical sizes and parameter values used in eVTOL design.

Chapter 4: details the development of an eVTOL performance tool for analyzing and comparing eVTOL aircraft. This chapter covers the integration of rotary wing and fixed-wing effects to determine mission performance and includes validation and comparison with actual eVTOL aircraft data.

Chapter 5: introduces a transition mode model for transition climb and descent, incorporating aircraft trim conditions, a trajectory model, and blade-element momentum theory to enhance the characterization of transition mode. It also includes a detailed investigation and comparison with actual eVTOL aircraft.

Chapter 6: presents aerodynamic and stability analysis to quantify the benefits of wing surfaces for eVTOL aircraft. This chapter develops a framework to compare different wing configurations, study parametric effects of tandem wings, and demonstrate an optimization method for eVTOL wing design.

Chapter 7: describes the experimental approach to validate and determine an optimal wing design for eVTOL aircraft. It includes methodologies using qualitative and quantitative approaches to assess aerodynamics, performance, and stability on a subscale aircraft across various wing designs. A ranking system based on design criteria is demonstrated to determine the appropriate wing configuration.

Chapter 8: concludes the dissertation and recommends future work, highlighting challenges encountered during the research.

Appendix: A contains the relevant equations and formulations for the estimation of aerodynamic drag for various aircraft components, based on both existing analytical and empirical methods.

Chapter 2: Literature Review

This chapter reviews previous eVTOL research relevant to this thesis. Section 2.1 highlights the state-of-the-art technologies and developments for eVTOL aircraft, including its applications, classification, and challenges of electric propulsion and VTOL technology, particularly Distributed Electric Propulsion (DEP). Section 2.2 covers existing methods for disciplinary-specific and multidisciplinary tools based on both existing and advanced models used for aircraft design, performance analysis, and evaluation.

2.1 eVTOL Aircraft Design and Applications

eVTOL technologies represent a significant leap in aviation, promising to revolutionize urban and regional transportation. These aircraft leverage electric propulsion to achieve vertical take-off and landing capabilities, offering a versatile solution for congested urban environments, reducing the need for extensive runway infrastructure. This section explores the applications of eVTOL aircraft, highlighting landmark research and developments alongside evolving technologies, challenges, and solutions in eVTOL aircraft design and performance advancements.

2.1.1 Advanced Air Mobility

Urban traffic congestion is a significant issue in many major cities, affecting economies, environments, and public health [28]. With the global population at 7.9 billion and projected to reach 8.5 billion by 2030, traffic congestion will likely become a pressing issue in developing countries [29]. To address this, eVTOL aircraft are being developed to serve as shared air taxi services, expanding transportation networks into three-dimensional space with highly autonomous and regulated aerial vehicles. They hold potential for transforming emergency medical services by enabling rapid transportation of patients and medical supplies. Additionally, eVTOL aircraft can enhance logistics by facilitating quick and efficient parcel delivery, particularly in hard-to-reach areas.

Advanced Air Mobility (AAM), a multidisciplinary concept, is known by several terms including Urban Air Mobility (UAM), On-Demand Mobility (ODM) and Regional Air Mobility (RAM). Various studies have highlighted the importance and challenges of future air mobility.

For instance, Straubinger et al. provided a comprehensive overview of the current state of UAM research, identifying various fields critical for its development, including vehicle concepts, infrastructure, regulations, and public acceptance. The paper emphasizes the technological advancements that have enabled UAM, such as distributed electric propulsion, but also highlights significant challenges, including noise mitigation, airspace integration, and infrastructure demands like vertiports. It discusses operational concepts, market structures, and the integration of UAM into existing transportation systems, while also identifying gaps in public perception studies and modeling approaches [3].

Furthermore, Cokorilo critically examines the safety challenges in UAM, emphasizing the need for robust risk management frameworks to address human error, certification of new electric and vertical flight technologies, and the integration of air traffic management systems into urban environments [8]. Similarly, Sirirojvisuth et al. conducted a feasibility analysis using a multidisciplinary economic framework for the AAM market [12], while Haddad et al. identified key factors influencing UAM adoption and its potential applications [30], highlighting the diverse approaches required to address the complexities of UAM development.

Joby Aviation is advancing UAM with a six-propeller, eVTOL aircraft designed to prioritize low noise and safety for urban operations. Extensive studies identified the tilt-propeller configuration as optimal for achieving high speed, long range, and low noise. Full-scale flight tests showcased impressive capabilities, including a 249 km flight, speeds exceeding 322 km/h, and noise levels of 45 dB(A) at 500 m flyover and under 65 dB(A) at 100 m hover [31]. A refined propeller design, incorporating increased solidity, reduced tip speed, and swept anhedral blade tips, achieved a 3 dBA noise reduction in hover and was successfully flight-tested using multi-fidelity aerodynamic and acoustic tools [32–34]. Additionally, a calibrated transition aerodynamics model integrating surrogate CFD and semi-empirical approaches defined the “conversion corridor” for shaft tilt and airspeed combinations. A novel automated flight control system further enhanced performance during transitions by optimizing angle-of-attack and shaft angle adjustments [35]. These advancements underline Joby’s commitment to delivering efficient, quiet, and innovative eVTOL solutions for urban environments.

Volocopter has contributed rigorous aerodynamic and acoustic research on its multi-rotor eVTOL aircraft, the Volocopter 2X. High-fidelity CFD simulations have been conducted to analyze key performance aspects, including installation effects, ground proximity impacts, and cruise flight aerodynamics. In hover, studies on installation effects revealed that the airframe influences rotor wake, thrust, and acoustic pressure fluctuations, increasing overall noise levels by 1.5 dB and locally by 3–4 dB in certain configurations, with rotor-rotor interactions dominating aerodynamic and acoustic performance [36]. Ground effect studies showed reduced power requirements at lower altitudes due to diminished airframe download, alongside complex vortex interactions between the rotors and the ground [37]. For cruise flight, a comparison between full and half-model simulations demonstrated that the half-model approach effectively reduces computational demand without significant deviation in overall rotor speeds or pitch attitude, though localized rotor-airframe interactions remain prominent [38]. These findings, validated against experimental data, underscore Volocopter's commitment to optimizing multi-rotor performance and acoustic characteristics for urban environments.

Archer Aviation, in collaboration with Politecnico di Milano and DLR, conducted wind tunnel tests to investigate aerodynamic interactions between wing sections and propellers mounted on a boom in a representative eVTOL configuration. Using Infrared Thermography, the study quantified laminar flow on the baseline and propeller-affected wing sections under different thrust conditions. The results offer valuable insights into wing-propeller integration, contributing to the optimization of aerodynamic performance and stability for eVTOL aircraft in cruise flight [39].

Significant research in academia on UAM application, concept, and ecosystem has since been published. For example, Silva and Johnson presented several concept vehicles for UAM technology development [16], Johnson developed a quiet single main rotor helicopter for UAM applications based on NASA's Design and Analysis of Rotorcraft (NDARC) [40], Antcliff et al. studied the adoption of on-demand mobility in Silicon Valley [41].

Despite the ground research on the operational requirements, Uber outlines 10 major unsolved challenges for making eVTOL aircraft commercially viable [2]:

- → Certification Process
- → Battery Technology
- → Vehicle Efficiency
- → Air Traffic Control
- → Cost And Affordability
- → Safety
- → Aircraft Noise
- → Emissions
- → Vertiport Infrastructure in Cities
- → Pilot Training

The rising demand for numerous eVTOL aircraft to support UAM has led to many startups, existing aircraft Original Equipment Manufacturers (OEMs), and automotive companies such as Boeing, Airbus, Mercedes, Audi, Toyota, and Hyundai, as well as research teams at NASA and DLR, to develop eVTOL technologies and solutions [42]. Early prototypes and flight tests have demonstrated the feasibility of electric propulsion systems and advanced aerodynamics, setting the stage for further innovation. Companies like Joby Aviation and Archer Aviation have made substantial progress, showcasing the potential of eVTOL aircraft through successful test flights and robust design iterations. In Singapore, Volocopter begun flight testing their 2X model, with support from the Civil Aviation Authority of Singapore (CAAS), Ministry of Transport (MOT), and Economic Development Board (EDB), towards developing air taxi capabilities in the near future [43].

eVTOL aircraft research has rapidly developed in both academia and industry, employing diverse approaches and design methodologies, many of which are adapted from conventional aircraft design practices or tailored to specific operational requirements. However, traditional design methods often focus on isolated aspects, such as aerodynamics or propulsion, without fully capturing the multidisciplinary interactions critical to eVTOL performance. This thesis builds upon these existing methods by identifying their limitations and proposing an integrated, multidisciplinary framework for eVTOL design. The developed methodology offers an alternative to traditional design approaches by emphasizing the simultaneous optimization of aerodynamics, propulsion, and flight mechanics across all flight phases, addressing key challenges such as transition performance, energy efficiency, and configuration-specific trade-offs. This holistic approach aims to meet the growing demand for aerial mobility more effectively than existing methods.

2.1.2 Development and Challenges of VTOL Aircraft

The underlying technology enabling UAM operations is based on vertical flight capabilities, particularly vertical take-off and landing (VTOL), allowing aircraft to operate in urban environments. Initially developed for military applications in the 1950s, VTOL technology provided the capability to take off and land from any terrain, eliminating the need for runways and enabling a broader range of flight capabilities for various missions [44]. Since then, VTOL architectures have evolved into Personal Aerial Vehicles (PAV), with historical developments illustrated in Figure 2.1 [45].

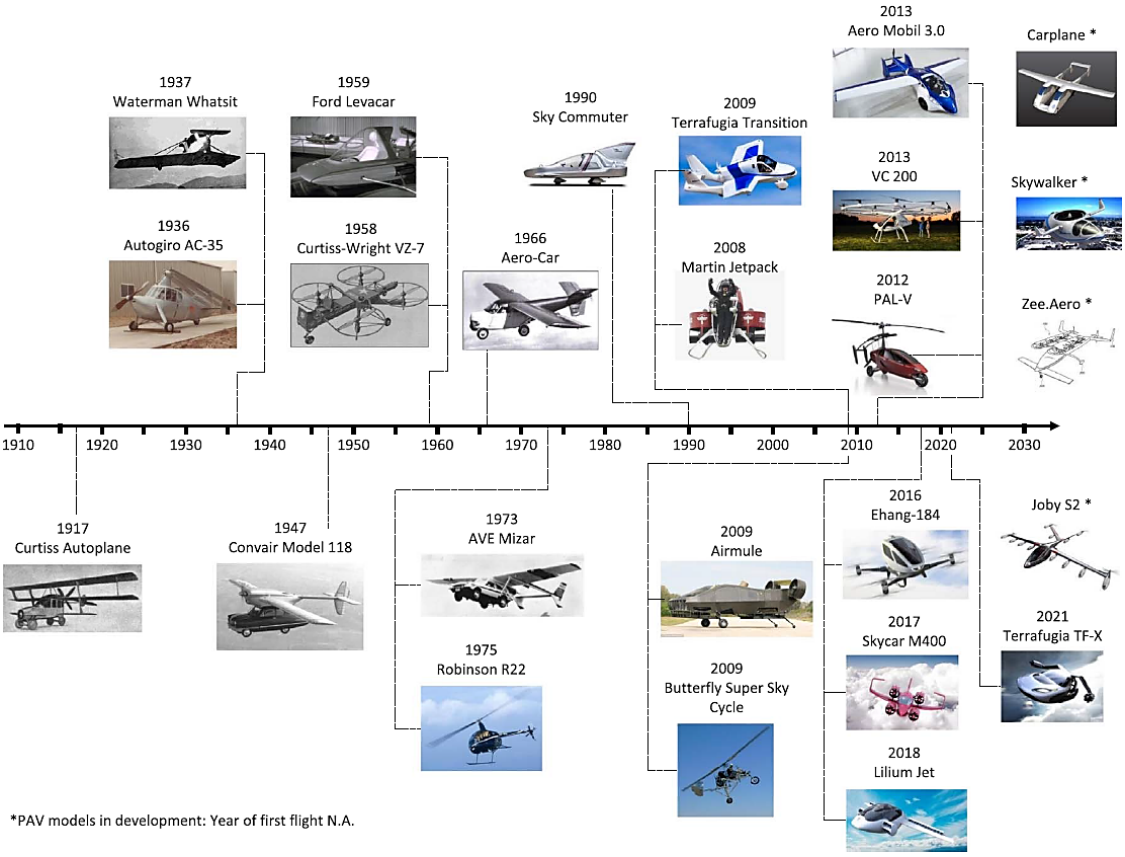

Figure 2.1: Historical personal aerial vehicles developments in US and Europe [45].

VTOL technology roots stem from helicopter developments, with aerodynamic and flight performance requirements based on the combination of helicopter and airplane mechanics and theory for both the vertical and horizontal flight segments. Notable VTOL aircraft include the Canadair CL-84 Dynavert, Bell X-22A, Ryan XV-5 Vertifan, Bell Boeing V-22 Osprey, AgustaWestland AW609, McDonnell Douglas AV-8B Harrier II, and Lockheed Martin F-35 Lightning II, shown in Figure 2.2 [46–52]. These early VTOL aircraft have complex systems and transition maneuvers, leading to increased aircraft weight, high operational requirements, increased risk of failure, and maintenance costs. Consequently, having most VTOL technology being designed for military and research applications, with limited research towards integrating VTOL capabilities for commercial passenger applications.

Figure 2.2: Gas powered VTOL aircraft with various configurations [46–52].

In the last decade, the demand for autonomous electric cars has driven the development of high-capacity electrical energy storage devices, more powerful and efficient electric motors, artificial intelligence and robust control algorithms, Microelectromechanical Systems (MEMS), semiconductors, and lightweight structures. These advancements, combined with VTOL technologies, have revived interest in this niche aviation area with all electric and advanced autonomous flight control systems. Figure 2.3 shows the relatively short history of electric aircraft and recent eVTOL developments [53].

One of the main advantages of eVTOL aircraft is the mechanical simplification of components and systems compared to conventional gas-powered propulsors. Direct electric drive systems eliminate the need for gearboxes and transmissions, benefiting the

entire spectrum of aircraft processes, including design, supply chain, manufacturing, assembly, operation, inspection, maintenance, repair, and decommissioning. While pitch-change rotor systems provide performance benefits over a wider range of flight conditions and maneuvers, eVTOL aircraft primarily rely on their vertical lift mechanism for short periods during hover and transition phases. This limited use reduces the necessity for complex variable-pitch blades, allowing for simpler designs that increase flexibility in the number and placement of rotors, enhance safety, and support a wide range of configurations.

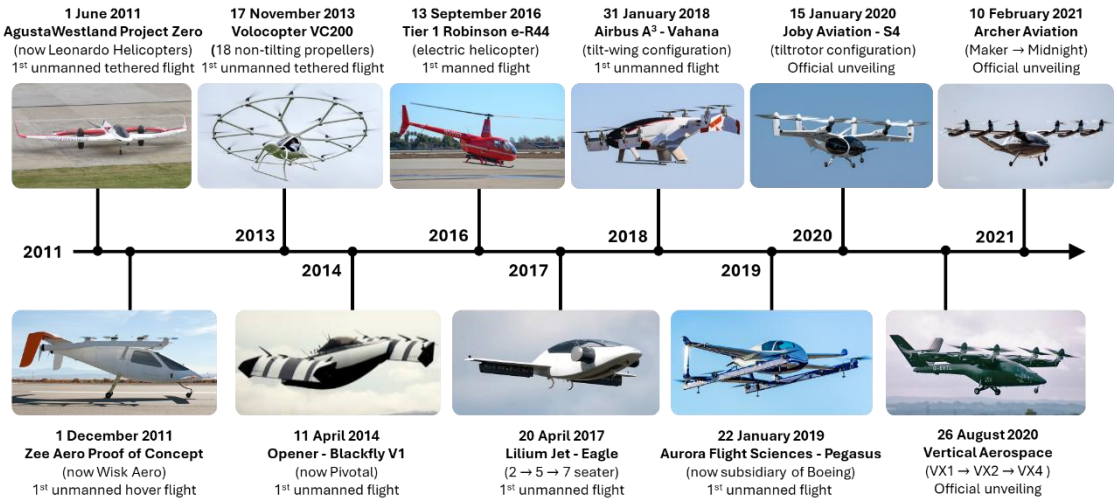

Figure 2.3: eVTOL development timeline [53].

Stoll stated that:

> "*The relatively scale-free nature of electric motors (referring to thrust and power) which allows the use of a relatively large number of smaller motors placed in strategic locations around the aircraft without the great increase in complexity and weight that would accompany the use of a similar number of independent combustion engines and/or gearboxes and driveshafts*" [27].

However, eVTOL aircraft are limited by the energy capacities and efficiency of current energy storage devices. State-of-the-art lithium-ion batteries from Tesla have a specific energy density of 260 Wh/kg or 0.936 MJ/kg, compared to typical aviation fuel at 43 MJ/kg, representing just over 2% of aviation fuel's energy density [54]. This results in a large portion of eVTOL aircraft weight and volume being allocated to energy storage devices, limiting achievable range and scalability of eVTOL designs.

Additionally, the pricing and availability of energy storage devices are critical factors for the adoption of electric aviation. Interest in the electrification of land-based vehicles

has driven the development of lithium-ion batteries, increasing energy capacity and lowering prices by 80% from 2010 to 2020, as shown in Figure 2.4 [55].

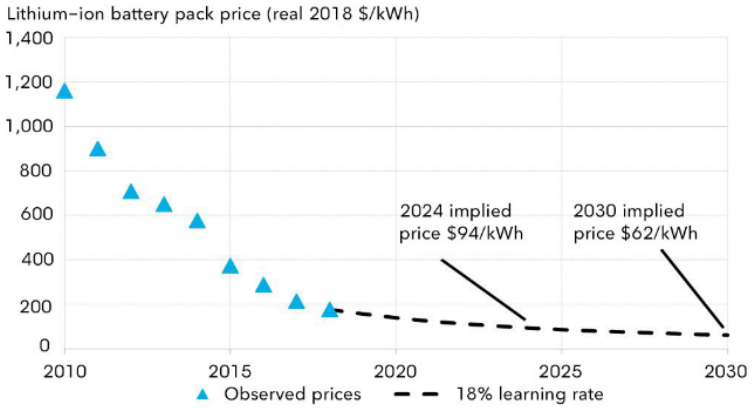

Figure 2.4: Forecast of Lithium-ion battery price from 2010 to 2030 [55].

This trend paints an optimistic picture for sustainable eVTOL integration. Other critical specifications for eVTOL aircraft energy storage devices include the charging/ discharging rate and cycle life, due to the high-power consumption during take-off and landing phases and the high frequency of flights. Extensive research is being conducted on various energy storage developments, such as lithium-sulfur, lithium-air, Li-ion, solid-state, and fuel cells, for electrification of aircraft [56–59].

Another hurdle for eVTOL aircraft is the regulatory framework and certification process due to their unique operational characteristics. The aviation industry has stringent certification requirements to ensure the safety of aircraft and passengers. The Federal Aviation Administration (FAA) and European Union Aviation Safety Agency (EASA) are leading efforts to develop a regulatory framework for certifying this new class of aircraft. The FAA adopts a dynamic approach, working with eVTOL industry leaders to identify necessary certification standards based on existing Code of Federal Regulations (CFR) for airplanes and rotorcraft. In contrast, EASA employs a more conservative, standardized framework, with clear guidelines published by industry experts in documents such as the Means of Compliance (MOC) and Special Condition Electric/Hybrid Propulsion System [60–62]. These requirements guide the development of eVTOL aircraft with a Maximum Gross Take-off Weight (MGTW) of 3175 kg and a maximum passenger capacity of nine. More complex eVTOL designs will require rigorous testing and validation to achieve certification levels mandated by either agency.

Distributed Electric Propulsion Architecture

The introduction of electric propulsion has enabled new aircraft designs characterized by increased simplicity, efficiency, robustness, and safety. A novel design architecture emerging from these advancements is Distributed Electric Propulsion (DEP), which features multiple propellers and motors to offer benefits such as active controls, reduced noise, and flight redundancy. Generally, distributed propulsion refers to any aircraft with more than one propulsor. Examples of early distributed propulsion are illustrated in Figure 2.5. However, according to Kim, DEP specifically involves the spanwise distribution of the propulsive thrust stream such that overall vehicle benefits in terms of aerodynamic, propulsive, structural, and/or efficiencies are mutually maximized to enhance the vehicle mission [63].

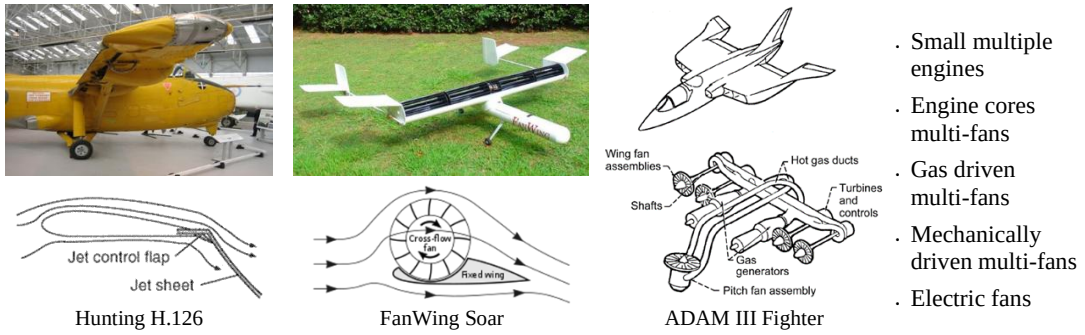

Hunting H.126 — FanWing Soar — ADAM III Fighter

Blown/Jet Flaps — Cross-Flow Fan — Multiple Discrete Propulsors

Figure 2.5: Early examples of distributed propulsion system and designs [63].

DEP allows for engine failures to result in reduced performance rather than catastrophic events, owing to robust control of the remaining propulsors. DEP aircraft typically utilize smaller propulsors, which generate less noise compared to helicopters. In addition to noise and efficiency improvements, DEP facilitates VTOL designs by minimizing rotor download interaction on lifting surfaces and integrating recovery systems like ballistic parachutes for added safety during critical flight segments such as takeoff and landing. Hence, DEP can result in increased reliability, lower maintenance, and operating costs. Since 2014, NASA has been actively researching and testing DEP aircraft for commercial aviation, publishing several technical papers and developing multiple prototype demonstrators to study and assess the DEP architecture, as shown in Figure 2.6 [64–66].

Studies have demonstrated that DEP reduces energy consumption through both drag reduction and boundary layer ingestion (BLI), reduces aircraft propulsion installation weight by synergistic inlet/nozzle/wing structure integration, enables differential and vectoring thrust control to eliminate the need for conventional aircraft control surfaces, enhances noise reduction through airframe shielding with the integration of the propulsion and airframe systems, and facilitates high production rates and direct replacement of compact and modular propulsors [65].

NASA GL-10, 2014
Greased Lightning

NASA X-57, 2017
Maxwell

NASA LA-8, 2020
Langley Aerodrome

Figure 2.6: NASA Distributed Electric Propulsion prototype demonstrator aircraft [64–66].

The increased aerodynamic, control, and structural performance enabled by DEP allows for smaller wing designs, reducing overall aircraft weight and enhancing capabilities for short or vertical takeoff. This also leads to substantial reductions in vehicle noise. The relatively scale-free nature of electric motors allows for the flexibility of placing multiple rotors strategically to optimize aircraft performance. Consequently, various eVTOL aircraft types, designs, and configurations based on the DEP architecture have emerged, offering varying capabilities and performance in terms of range, power requirements, and safety.

Several notable publications have contributed to the advancement of DEP technologies. Gohardani et al. presented a historical review and development of distributed propulsion technology and the challenges of all-electric aircraft [6]. Gallani et al. studied the effects of DEP on the performance of a general aviation aircraft, evaluating the lift augmentation system and its effects on thrust and aerodynamic efficiency [20]. Stoll et al. conducted computational fluid dynamics (CFD) simulations for drag reduction through DEP and performed design studies for thin-haul commuter aircraft with DEP based on aerodynamic, weight, powertrain, and cost models [22, 67]. NASA designed and evaluated the performance of their Scalable Convergent Electric Propulsion Technology Operations Research (SCEPTOR) project utilizing DEP [68]. Khajehzadeh

analyzed an over-the-wing distributed propulsion system to evaluate the inviscid flow effects of wing-propeller interactions [69]. Shi et al. modeled the kinematics and dynamics equations for a general VTOL aircraft and developed a unified framework for designing controllers for the non-linear control of a DEP winged aircraft [70]. Ma et al. conducted a sizing method and sensitivity analysis for a DEP aircraft based on analytical models to investigate the impact of VTOL and STOL requirements [71].

2.1.3 Gaps of eVTOL-Specific Design Considerations

The literature on the existing eVTOL aircraft design and applications reveals gaps in addressing specific challenges unique to eVTOL design:

- **Aerodynamic and Propulsion Interactions:** Existing models inadequately account for the aerodynamic effects of distributed propulsion systems, rotor-wing interactions, and their impact on energy efficiency and stability.
- **Flight Mechanics and Dynamics:** Comprehensive models for eVTOL flight characteristics, particularly during transition phases, are scarce, hindering accurate assessments of performance across flight regimes.
- **Validation Through Experimental Testing:** Few studies integrate analytical modelling with subscale experimental validation, particularly for novel eVTOL configurations and transition-phase dynamics. This limits the confidence in the applicability of proposed design methodologies.

This review illustrates the potential and ongoing development of technologies in advancing eVTOL aircraft design and performance. DEP architecture fundamentally transforms eVTOL design by enabling new aircraft configurations that were previously impractical or impossible with traditional propulsion systems, allowing for unprecedented flexibility in design. DEP has catalyzed the proliferation of novel eVTOL aircraft designs, each tailored to specific use cases and operational requirements. However, this diversity also presents new challenges. Traditional methods of evaluating aircraft performance, developed for conventional fixed-wing and rotorcraft designs, are often inadequate for the unique characteristics of the new eVTOL configurations. This necessitates the development of new evaluation methodologies, forming the basis of this thesis.

2.2 eVTOL Performance Modelling Tools

Since the inception of aviation, numerous experiments and studies have aimed to enhance flight performance and efficiency across various aircraft configurations. However, much theoretical work relies on complex, time consuming and specifically formulated models that are challenging to apply to new technologies like eVTOL aircraft, requiring expertise across multiple domains and appropriate tools. Furthermore, eVTOL aircraft, with their multiple components and structures, necessitate a comprehensive understanding of each component to assess overall performance. Key aerodynamic interactions relevant to eVTOL aircraft include wing-to-tail, propeller-to-wing, propeller-to-propeller (adjacent, fore, and rearward), and rotor-to-boom interactions. Each interaction presents unique challenges and insights essential for constructing accurate models and simulations, as illustrated in Figure 2.7 [72–80].

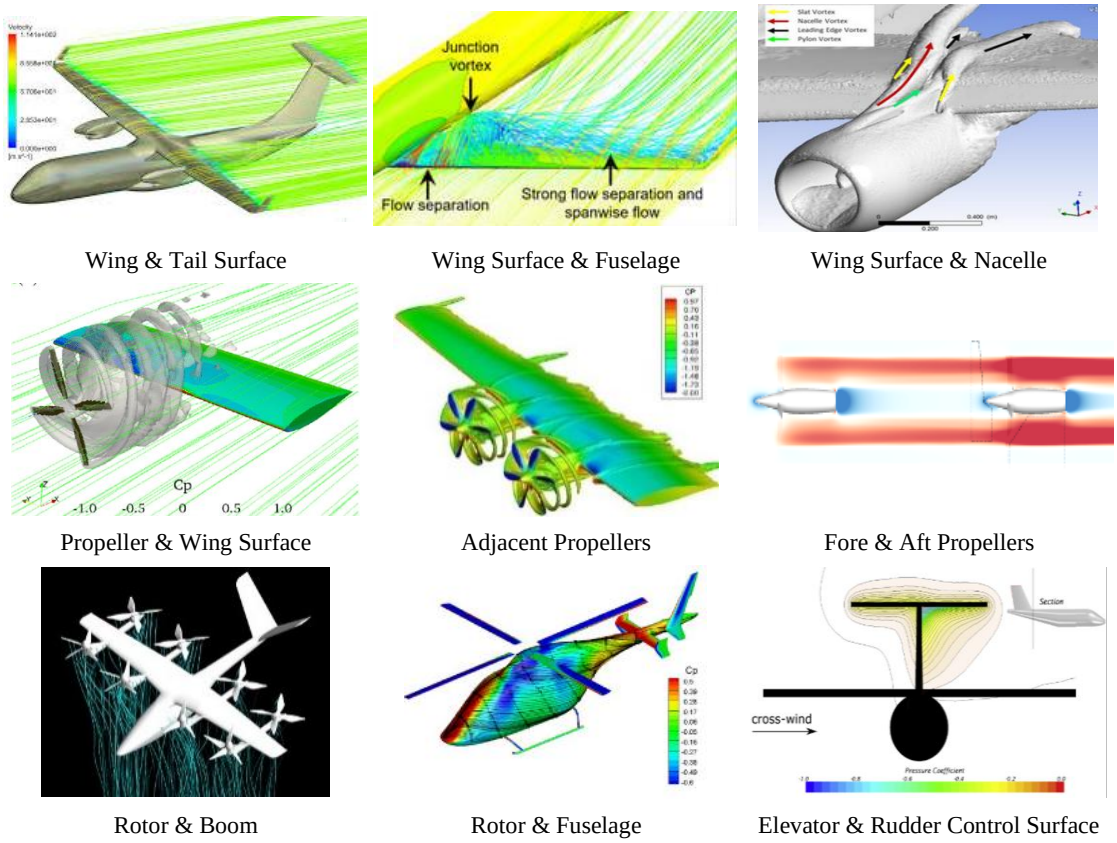

Wing & Tail Surface | Wing Surface & Fuselage | Wing Surface & Nacelle

Propeller & Wing Surface | Adjacent Propellers | Fore & Aft Propellers

Rotor & Boom | Rotor & Fuselage | Elevator & Rudder Control Surface

Figure 2.7: Different component types and their aerodynamic interactions [72–80].

Comprehensive analytical modeling techniques for eVTOL aircraft involve both subject-oriented analysis and multidisciplinary optimization. Several studies have investigated various elements using these techniques. Brown and Harris conducted a

trade study using geometric conceptual design programming tool to analyze the performance, noise profiles, and costs of different eVTOL configurations like Lift + Cruise, compound helicopter, tiltwing, and tiltrotor [15]. They found that tiltrotor eVTOL aircraft had the lowest battery mass and overall weight, though several assumptions and simplifications might reduce the study's applicability.

Johnson and Silva employed sophisticated tools like NDARC and CAMRAD II to compare eVTOL concepts such as quadrotors, side-by-side helicopters, tiltwing, and Lift + Cruise configurations [81]. Their results highlighted critical research areas for eVTOL development, including propulsive efficiency, aerodynamic interactions, aircraft performance, design, operational effectiveness, and cost.

Bacchini and Cestino compared wingless multicopters, winged Lift + Cruise, and winged vectored thrust (tiltrotor and tiltwing) configurations [82]. Using a systematic yet simplistic method with analytical equations, they estimated hover and aerodynamic performance, concluding that multicopters excel in hover but have limited range compared to Lift + Cruise and vectored thrust eVTOL aircraft.

Several other notable works have evaluated eVTOL aircraft: Duffy et al. compared the cost of vertical flight between helicopters and eVTOLs, contrasting electric propulsion with fuel-powered vehicles [7]. Melo et al. modeled an integrated life cycle engineering analysis framework to study the environmental effects of eVTOL vehicles [10]. Khavarian et al. analyzed eVTOL implementation costs through a life-cycle analysis based on energy, material, and infrastructure [11]. Nathan et al. assessed the performance and range of a Ducted Vectored Thrust Concept (DVTC) for the Lilium Jet eVTOL aircraft for urban and regional air mobility markets [21]. Finger et al. studied the impact of electric propulsion on VTOL performance, focusing on electric lift systems, rotor disk loading, and flight time [4, 83]. Bolam et al. reviewed electrically powered aircraft propulsion mechanisms, electrical power generation, and storage [84]. Zhou et al. reviewed the historical developments of VTOL technologies and programs for unmanned and manned aerial vehicles [85].

These studies highlight the importance of early-stage preliminary analysis and assessment for evaluating and optimizing new eVTOL designs. However, most rely on simplified models and lack actual data from the latest eVTOL aircraft. This research

aims to develop an analysis framework for eVTOL design, studying the impact of various configurations on performance.

2.2.1 Existing Modelling Methodologies and Tools

This section provides a list of well-known subject-oriented tools for aircraft design, crucial from the preliminary to detailed design phases. Table 2.1 lists programs used for: fixed wing aerodynamic design, propulsion and blade design, and flight controls and simulators.

Table 2.1: List of subject oriented tools and programs.

Developed Program	Component	Discipline / Analysis	Developed by	
Aircraft Synthesis (ACSYNT)	Aircraft	CAD	NASA	1997
ASWING	Wing	Aerodynamics, Aeroelasticity	MIT	2000s
AEROS2S	Wing	Aerodynamics	NASA	1980s
Aircraft Noise Prediction Program (ANOPP)	Aircraft	Aeroacoustics	NASA	1980s
Athena Vortex Lattice (AVL)	Wing	Aerodynamics, Stability	MIT	1990s
Ducted Fan Design Code (DFDC)	Ducted Fan	Propulsion	MIT	1990s
Easy Aeroelasticity (EZASE)	Aircraft	Aeroservoelasticity	NASA	2010s
FlightGear	Aircraft	Flight Dynamics	FlightGear Project	1997
FLOW5	Wing	Aerodynamics	Cère-Aéro	2016
FUN3D	Aircraft	Aerodynamics, CFD	NASA	1980s
Generalized Advanced Propeller Analysis System (GAPAS)	Propeller	Propulsion	NASA	1983
Gazebo	Aircraft	Flight Simulation Environment	Open Robotics	2004
GT-Hybrid	Rotor	Aerodynamics, CFD	GeorgiaTech	2010s
GTM_DesignSim	Aircraft	Flight Dynamics	NASA	2015
JBLADE	Rotor / Propeller	Propulsion	José Morgado Proença	2013
JSBSim	Aircraft	Flight Dynamics	Jon S. Berndt	1996
Microsoft Flight Simulator	Aircraft	Flight Dynamics	Microsoft	1982
MSES	Airfoil	Aerodynamics	MIT	1995
NASA Structural Analysis System (NASTRAN)	Aircraft	Structure FEA	NASA	1960s
OpenCOPTER	Rotor	Aerodynamics, Aeroaacocoustics	Penn State	
Open Vehicle Sketch Pad (OpenVSP)	Aircraft	CAD, Aerodynamics	NASA	2012
Optimal Trajectories by Implicit Simulation (OTIS)	Aircraft	Flight Trajectory	NASA	1985
PANAIR	Wing	Aerodynamics	NASA	1980
PROP_DESIGN	Propeller	Propulsion	Anthony Falzone	2000s
PSU-WOPWOP	Rotor	Aerodynamics, Aeroacoustics	Penn State	2000s
QPROP / QMIL	Rotor / Propeller	Propulsion	MIT	2000s
Rotorcraft Optimization Tools (RCOTOOLS)	Rotorcraft	Optimization	NASA	2018
RealFlight	Aircraft	Flight Dynamics	Knife Edge Software	1998
Tornado	Wing	Aerodynamics	KTH	2001
Trajectory-Based Route Analysis and Control (TRAC)	Aircraft	Flight Trajectory	NASA	2009
Wing Design and Analysis Code (WDES)	Wing	Aerodynamics	NASA	1983
X-PLANE	Aircraft	Aerodynamics, Flight Dynamics	Laminar Research	1995
XFOIL	Airfoil	Aerodynamics	MIT	1986
XFLR5	Airfoil, Wing	Aerodynamics, Stability	André Deperrois	2004
XROTOR	Rotor / Propeller	Propulsion	MIT	1980s

The selection of Athena Vortex Lattice (AVL) and XFLR5 among the various subject-oriented tools for this research is guided by their suitability for the specific objectives and scope of the study, focusing on eVTOL wing design and subsonic aerodynamics. Both tools are open source, readily available, and well-documented, making them accessible for a wide range of users, including researchers and practitioners. AVL is chosen for its robustness in analyzing the aerodynamic and flight dynamic behavior of wing and tail configurations using a Vortex Lattice Method (VLM). This approach is computationally efficient and well-suited for early-stage design and optimization of thin lifting surfaces. Among other VLM-based tools, such as Tornado or PANAIR, AVL's integration of flight dynamics capabilities and eigenmode analysis makes it particularly advantageous for assessing stability and handling qualities, which are critical aspects of this research.

Similarly, XFLR5 is selected for its specialized capability to model low Reynolds number aerodynamics and its ease of use in simulating the aerodynamic performance of wing-fuselage configurations. These tools are also widely used in the research community and industry for wing design and analysis, which reinforces their credibility and relevance. While higher-fidelity computational tools like CFD solvers, such as Ansys Fluent or OpenFOAM, can provide detailed viscous flow solutions, these methods are computationally expensive and less practical for parametric studies or iterative design processes in this research. Thus, AVL and XFLR5 offer a balanced approach, combining computational efficiency, sufficient fidelity, accessibility, and extensive documentation to meet the aerodynamic and design analysis requirements of this study.

Athena Vortex Lattice

Athena Vortex Lattice, developed by Mark Drela and Harold Youngren, is a Vortex Lattice Method (VLM) program for aerodynamic and flight dynamics analysis of arbitrary wing and tail aircraft configurations [86]. The VLM is an inviscid approach well-suited for calculating the lift and induced drag of wing or tail surfaces [87]. However, it does not account for viscous or turbulence effects and does not resolve the boundary layer, making it best suited for thin lifting surfaces at small angles of attack and sideslip. AVL employs a simplified flight dynamics model assuming unsteady flight variables consist of a steady-state and control terms with a time-dependent perturbation. By using the linearized equations of motion, AVL performs eigenmode analysis to evaluate damping ratios and natural frequencies of stability modes, aiding in the assessment of handling qualities of aircraft configurations. It has been widely used in the design of various aerial vehicles, making it a valuable tool for aircraft configuration design studies [88, 89].

XFoil Low Reynolds number 5

XFoil Low Reynolds number 5 (XFLR5), developed by André Deperrois, utilizes the VLM to analyze wing design while using panel methods to model the aircraft fuselage at low Reynolds numbers [90]. XFLR5 enables simulation of designed aircraft under various flight conditions, such as different airspeeds or sideslip angles, to predict performance. The simulation results provide essential aerodynamic coefficients and non-dimensional derivatives, such as trim conditions, mass inertia, aerodynamic derivatives, control derivatives, and performance curves. XFLR5 is useful for studying how aerodynamic parameters and characteristics change with different design and operational parameters.

2.2.2 Existing Multi-Disciplinary Modelling Techniques

This section reviews several well-known multidisciplinary tools used for aircraft design that consider multiple disciplines in the evaluation of an aircraft design. A challenge faced by aircraft designers is the coupled nature of design variables such as aerodynamics, propulsion, stability, and flight performance, complicating the optimization of the entire aircraft design. Multidisciplinary optimization frameworks address this by simultaneously evaluating and optimizing multiple variables. Table 2.2 lists programs developed for multidisciplinary analysis and optimization, critical from preliminary to detailed design phases [91].

Table 2.2: List of multidisciplinary codes and tools.

Developed Program	Component	Discipline / Analysis	Developed by	
Advanced Aircraft Analysis	Aircraft	Aerodynamics, Flight Performance, Stability & Control	DAR Corporation	1995
Comprehensive Analytical Model of Rotorcraft Aerodynamics and Dynamics (CAMRAD II)	Rotorcraft	Multibody, Aerodynamics, Structural Dynamics, Control, Flight Performance	Johnson Aeronautics	1980s
Comprehensive Hierarchical Aeromechanics Rotorcraft Model (CHARM)	Rotorcraft	Aerodynamics, Structural & Flight Dynamics, Aeroacoustics	Continuum Dynamics	1990s
Convex Engineering	Aircraft	Aerodynamics, Structure	MIT	2010s
Coupled Rotor Fuselage Model (CRFM)	Rotorcraft	Aerodynamics, Flight & Structural Dynamics	Westland	1997
Comprehensive Program for Theoretical Evaluation of Rotorcraft (COPTER)	Rotorcraft	Aerodynamics, Structural Dynamics	Bell	1980s
Concepts of Rotorcraft Enhanced Assessment Through Integrated Optimization Network (C.R.E.A.T.I.O.N)	Rotorcraft	Aerodynamics, Structure, Flight Performance, Aeroacoustics	ONERA	2011
DYMORE	Rotorcraft	Multibody, Aerodynamics, Structural Dynamics	GeorgiaTech	1990s
FLIGHTLAB	Rotorcraft	Aerodynamics, Flight Dynamics	ART	1990
Flight Optimization System (FLOPS)	Aircraft	Aerodynamics, Flight Performance, Propulsion	NASA Langley	1980s
Future Aircraft Sizing Tool (FAST)	Aircraft	Aerodynamics, Propulsion, Flight Performance	UMich	2024
Helicopter Simulation Tool (HOST)	Rotorcraft	Aerodynamics, Flight Dynamics & Performance	Eurocopter	2000
Helicopter Sizing and Performance Computer (HESCOMP)	Rotorcraft	Aerodynamics, Flight Performance	Boeing	1979
Hybrid Design and Rotorcraft Analysis (HYDRA)	Rotorcraft	Aerodynamics, Structure	GeorgiaTech	2010s
MATLAB / SIMULINK – Aerospace Toolbox	Aircraft	Aerodynamics, Flight Dynamics	MathWorks	1984
Multi-Body Dynamics (MBDyn)	Rotorcraft	Multibody, Structure	Politecnico di Milano	1999
NASA Design and Analysis of Rotorcraft (NDARC)	Rotorcraft	Aerodynamics, Flight Performance	NASA	2007
OpenMDAO / OpenAeroStruct	Aircraft	Aerodynamics, Structure, Optimization	UMich	2010s
Second Generation Comprehensive Helicopter Analysis System (2GCHAS)	Rotorcraft	Aerodynamics, Structural Dynamics Flight Performance, Stability & Control	U.S. Army	1990
Stanford University Aerospace Vehicle Environment (SUAVE)	Aircraft	Aerodynamics, Flight Performance, Optimization	Stanford	2010s
Rotorcraft Comprehensive Analysis System (RCAS)	Rotorcraft	Aerodynamics, Structural Dynamics	U.S. Army	1990s
Rotorcraft Conceptual Design and Analysis (RCDA)	Rotorcraft	Aerodynamics, Flight Performance Cost	Boeing	2008
University of Maryland Advanced Rotorcraft Code (UMARC)	Rotorcraft	Aerodynamics, CFD, Structure, Flight Dynamics	UMD	1990
Unconventional Aircraft Design and MDAO [92]	Aircraft	Aerodynamics, Structure, Aeroelasticity, Optimization	UC3M	2010s
V/STOL Aircraft Sizing and Performance (VASCOMP)	Aircraft	Aerodynamics, Flight Performance	Boeing	1980

The listed multidisciplinary tools each offer unique strengths and limitations depending on their theoretical foundations, fidelity, inclusion of disciplines, and applicability to different aircraft configurations. Relevant multidisciplinary tools for eVTOL aircraft such as NDARC and SUAVE provide comprehensive frameworks for analyzing rotorcraft and fixed-wing aircraft, with NDARC focusing on quasi-steady trimmed conditions and SUAVE excelling in physics-based modeling of unconventional configurations. OpenMDAO stands out for its robust optimization capabilities, enabling detailed multidisciplinary analyses across aerodynamics, structures, and propulsion. However, these tools vary significantly in computational demands, with OpenMDAO and SUAVE being more resource-intensive due to their higher-fidelity modeling capabilities, while others like NDARC balance fidelity with efficiency for conceptual design phases.

The choice of tools also depends on the research gaps they address. For instance, NDARC's calibrated surrogate models are less suited for holistic integration of flight phases, which is critical for eVTOL applications. Conversely, SUAVE's modularity allows for adding higher fidelity or unconventional configuration analyses, making it more adaptable for emerging aircraft designs. OpenMDAO’s flexibility in multidisciplinary design optimization is unmatched, but its usability requires extensive customization, posing challenges for rapid prototyping in preliminary studies. Additionally, open-source tools like OpenMDAO and SUAVE provide the advantage of accessibility and adaptability, while proprietary tools such as NDARC and CAMRAD II may offer better validation but come with licensing constraints. The tools also differ in their handling of the transition phase, with many rotorcraft-centric models offering simplistic or empirical approaches that are insufficient for detailed eVTOL performance evaluations.

Ultimately, the selection of tools must align with the specific research objectives and constraints. While listed tools like NDARC and SUAVE are not directly used in this study, they serve as important references that inform the development of the custom eVTOL aircraft analysis framework. Key elements derived from these tools include the consideration of mission profiles, the integration of diverse components and parameters to model critical input variables, and the structured setup and formulation of the analytical framework. Additionally, insights from these tools guide the connection and

handling of various modules and models within the study, ensuring a cohesive and adaptable framework tailored to eVTOL-specific requirements. This approach balances computational efficiency with the need for sufficient fidelity, enabling a targeted and holistic analysis of eVTOL designs while addressing identified research gaps.

NASA Design and Analysis of Rotorcraft

NASA Design and Analysis of Rotorcraft (NDARC) is an aircraft system analysis tool developed by NASA for conceptual design and technology impact assessments of helicopters and rotorcraft with the NDARC's tasks and outputs is shown in Figure 2.8 [93]. For its rotor model, NDARC uses surrogates for profile, parasite, and induced power calibrated to CAMRAD II results, with wing aerodynamics based on finite wing theory and hover-cruise conversion dynamics in quasi-steady trimmed conditions [94]. NDARC has an empirical database for various components weight, such as wings, tails, fuselage, rotors, motors, and landing gear, based on existing established fixed-wing, rotary-wing, and tiltrotor aircraft. NDARC's main tasks include designing and sizing rotor systems and flight missions, as well as performance analysis of rotorcraft based on specified requirements and conditions.

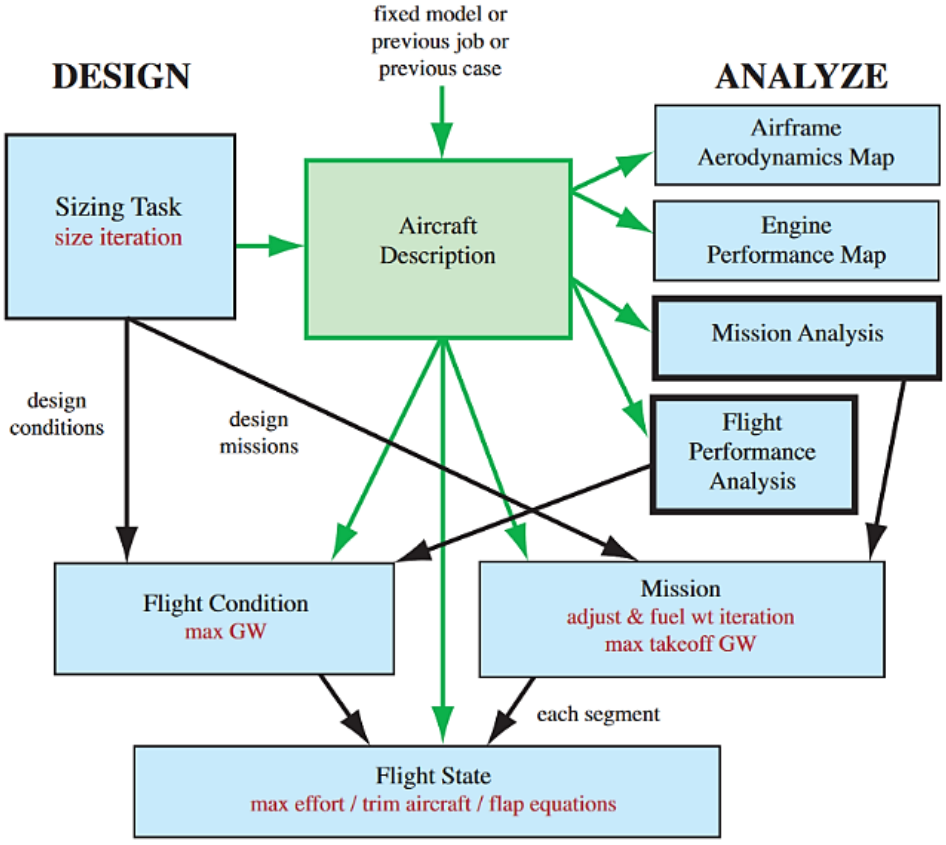

Figure 2.8: Framework and architecture for NDARC tasks [93].

Stanford University Aerospace Vehicle Environment

Stanford University Aerospace Vehicle Environment (SUAVE) is an open-source aircraft design environment based in Python, as illustrated in Figure 2.9 [95]. It consists of a modular set of analysis tools allowing for additional capabilities to be incorporated. For its rotor model, SUAVE uses a blade element model with empirical hover correction, with wing aerodynamics based on the Weissinger's VLM and hover-cruise conversion dynamics using collocation point-based dynamic simulation. Its physics-based approach allows higher fidelity conceptual design analyses of both conventional and non-conventional aircraft configurations [96].

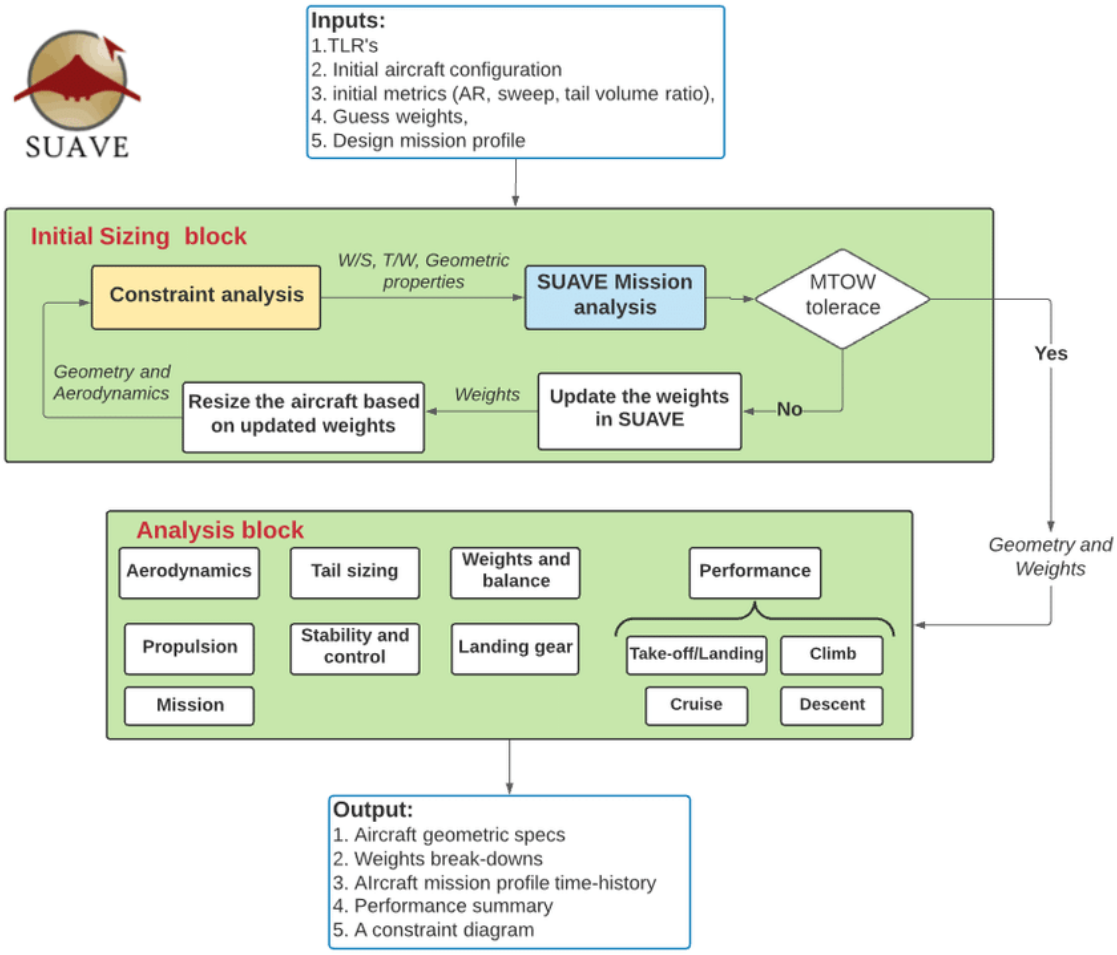

Figure 2.9: Sizing framework for SUAVE analysis [95].

Open-source Multidisciplinary Design, Analysis, and Optimization

Open-source Multidisciplinary Design, Analysis, and Optimization (OpenMDAO) is a Python-based open-source multidisciplinary optimization framework used for optimizing combinations of aerodynamics, structures, and propulsion. Figure 2.10 shows OpenMDAO's class structure [97]. With its robust optimization framework, OpenMDAO has been used in multidisciplinary aerospace optimization problems, such as optimizing aerodynamics, structures, and propulsion on fixed-wing aircraft [98, 99].

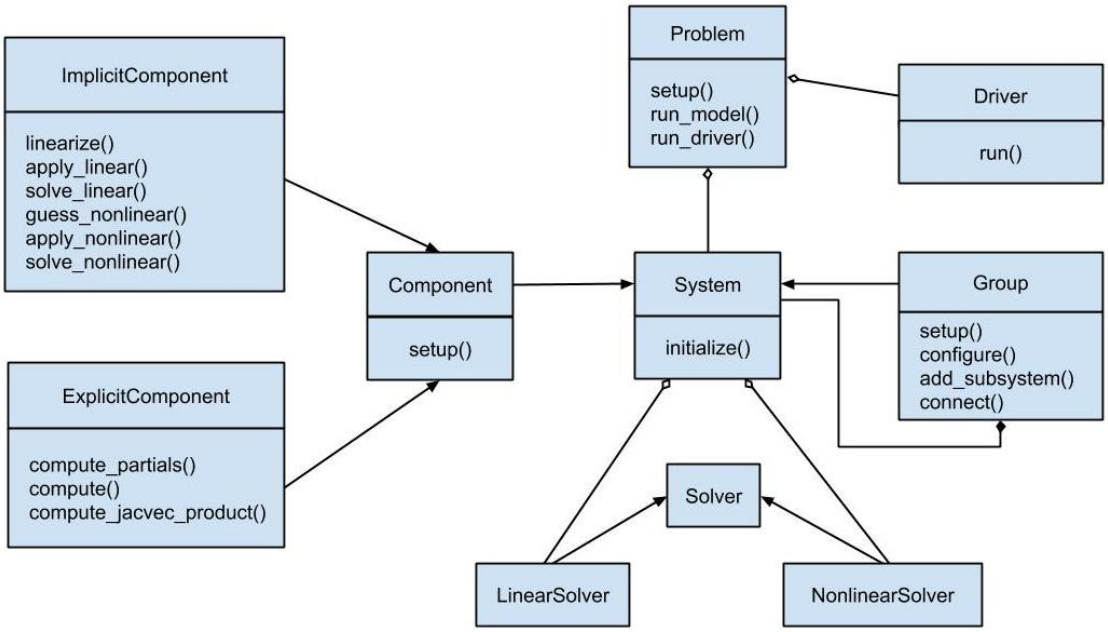

Figure 2.10: OpenMDAO class structure [97].

2.2.3 Gaps of Existing Frameworks

Existing multidisciplinary frameworks for aircraft design face several key challenges when applied to eVTOL configurations:

- **Lack of Holistic Integration**: Many frameworks focus on single aspects, such as aerodynamics or propulsion, without adequately addressing the interdependencies among aerodynamic loads, propulsion system performance, and vehicle stability. This segmented approach often leads to suboptimal designs that fail to leverage multidisciplinary synergies.
- **Limited Applicability to eVTOL Configurations**: Traditional frameworks are tailored to conventional fixed-wing or rotorcraft designs and cannot accommodate the diverse range of eVTOL configurations, including tiltrotor systems, distributed electric propulsion, and hybrid lift-and-cruise designs. As a result, these methods often yield incomplete or inaccurate performance predictions for eVTOL aircraft.
- **Simplistic Transition-Phase Modelling**: The transition between vertical and horizontal flight, a critical phase for eVTOL operations, is inadequately represented in existing methods. Current models often oversimplify aerodynamic interactions, power management, and control dynamics during this phase, limiting their ability to capture the complexities of real-world flight scenarios.
- **High Computational and Data Demands**: Advanced multidisciplinary tools require extensive input data and computational resources, making them impractical for early-stage design exploration, where rapid prototyping and iterative evaluations are essential.

This section provides a comprehensive overview of the tools and methodologies crucial for advancing eVTOL aircraft design, focusing on the complexity and multidisciplinary nature of eVTOL configurations. Low-fidelity models, such as AVL and XFLR5 for aerodynamic analysis, and NDARC, SUAVE, and OpenMDAO for multidisciplinary optimization, are emphasized due to their ability to provide rapid insights during early-stage design exploration. While these tools excel in computational efficiency and sensitivity analysis, they have limitations, such as reduced accuracy in capturing detailed aerodynamic interactions or transition-phase dynamics, which may require validation through higher-fidelity models or experimental testing. Nevertheless, it provides foundational understanding on eVTOL aircraft emerging from synthesizing insights gained through iterative simulations, comparative studies, and validation processes, translating raw data into actionable knowledge. These methodologies collectively enable the evaluation of eVTOL concepts, optimization of design parameters, and assessment of performance metrics, forming the basis for advancing efficiency, aerodynamics, and operational capabilities in next-generation aerial vehicles.

Chapter 3: eVTOL Aircraft Configurational Comparative Trade Study

This chapter provides a comprehensive comparative study of various eVTOL aircraft types and configurations, by collating a set of data and parameters essential for defining an eVTOL aircraft. It includes a detailed survey of current eVTOL aircraft design configurations and their classifications, as well as considerations for wing surfaces in eVTOL aircraft. The chapter culminates in a trade study that summarizes typical sizes and parameter values used in eVTOL design, offering valuable insights for future development in this field.

3.1 VTOL Designs and Rotor Configurations

Vertical flight configurations play a critical role in determining how an aircraft will perform, operate, and behave in flight. Depending on these configurations, performance parameters such as lifting capacity, flight speed, range, endurance, safety, operational complexity, weight, energy consumption, noise emissions, certification, and reliability can vary significantly.

Avera notes that:

> "*Vehicle configuration and propulsion system architecture are two key drivers for vehicle performance attributes. The two are interconnected in the sense that the chosen vehicle configuration imposes constraints on the design space of the propulsion architecture and vice versa*." [100].

Yazici further emphasizes that:

> "*The airframe shape or form becomes single fundamental element that will affect all; regulatory, environmental or public concerns*." [101].

One way to understand how eVTOL aircraft configurations affect power requirements is by examining disk loading for various configurations. For any VTOL aircraft, the highest power consumption occurs during the vertical hover and high-speed segments. High disk loading indicates an increase in power required and powerplant sizes, thus increasing the aircraft's weight. Figure 3.1 illustrates that the most efficient configuration, with the lowest disk loading, is the helicopter, while the least efficient is the direct lift aircraft [102].

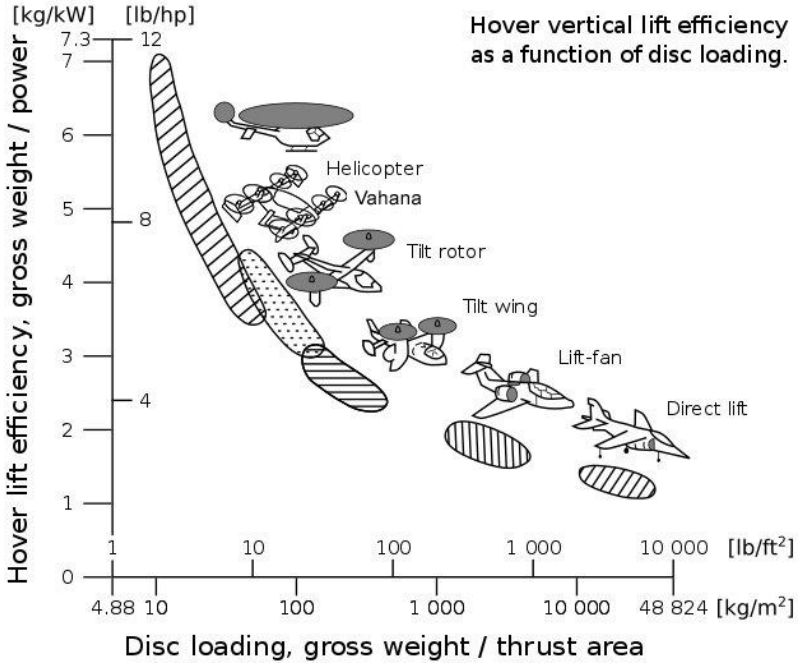

Figure 3.1: Hover efficiency and disk loading for various aircraft configurations [102].

However, when considering eVTOL aircraft for UAM applications, other factors such as cost, reliability, noise, and control aspects must be considered to determine the most optimal configuration for any particular flight mission. Investigating and understanding the different configurations of eVTOL aircraft and models is crucial. Finger et al. summarize various current configurations and unconventional platforms with different types of propulsors, including propeller-driven designs, lift fans, ducted fans, jet lift, and hybrid systems [103] as shown in Table 3.1, Table 3.2 and Table 3.3.

3.1.1 Aircraft Configurations and Classification

The simplest VTOL configuration is the wingless model, commonly known as multi-rotors or copters. Table 3.1 lists various types of wingless configurations, with a single rotor referred to as a helicopter. These wingless models use fixed downward-facing rotors for various phases of flight, providing exceptional maneuverability and agility at low speeds and enhancing redundancy in case of rotor failures, particularly in models with more than six rotors. However, these models have limited flight speeds and inefficiencies in forward flight compared to winged models, as lifting force is solely generated by the rotors without the benefit of wing lift, resulting in asymmetrical longitudinal lift effects at increased flight speeds.

Table 3.1: Examples of wing-less and multi-rotor configurations [103].

Wing-less/Multi-rotor Configurations		
	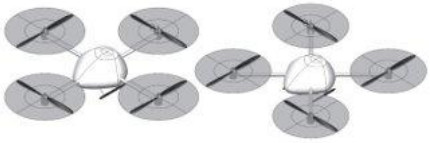	
Tri-copter	Quad-copter (+ / ×)	Penta-copter (Planar / Symmetrical)
	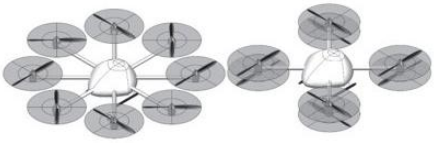	
Hexa-copter (Planar / Coaxial)	Octo-copter (Planar / Coaxial)	

The other VTOL configuration is based on winged models, classified according to the orientation of the propulsors as shown in Table 3.2. Lift elements refer to the vertical force or motion for hover and climb flight, while cruise elements refer to the forward force or motion for horizontal flight.

Table 3.2: List of VTOL classification based on propulsors [103].

Lift + Cruise	Lift = Cruise	Lift + Lift/Cruise
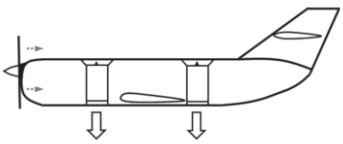	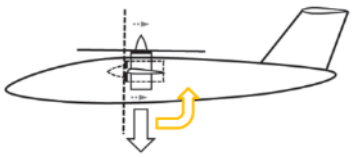	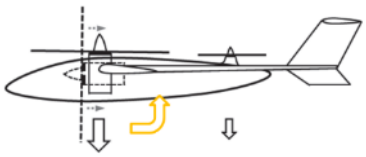
Lift Plus Cruise (Independent) Separate lift & cruise propulsors	Lift Equal Cruise (Vectored Thrust) Same lift & cruise propulsors	Combination of the two (Hybrid) Cruise propulsor support lift propulsors

Winged models follow several architectures where propulsors can be fixed or rotated to provide lift during hover and thrust during forward flight. Table 3.3 provides various examples of each configuration. The main benefit of winged models is the lift generated by the wings, resulting in improved Lift-to-Drag ratios (L/D). In horizontal flight, this allows the propulsors to provide only the forward force to compensate for drag, which is relatively lower than the lift force in hover. Consequently, winged models have greater range, endurance, and cruise efficiency. However, the main drawback is the substantial weight increase due to the wing structures and increased power requirements due to interference with rotor downwash during hover.

Table 3.3: Lift + Cruise, Lift = Cruise and Lift + Lift/Cruise configurations [103].

Lift + Cruise Configurations	
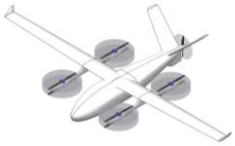	
Octocopter / Conventional Pusher	Jet Powered Lift + Cruise

Lift = Cruise Configurations		
		
Distributed Propulsion Tiltwing	Tiltrotor	Tandem-wing Tiltrotor/Tiltduct
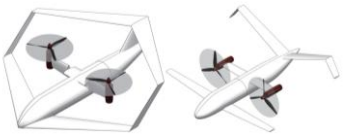		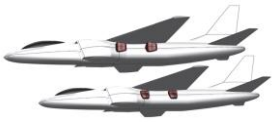
Box-wing/ Three-Surface Tiltrotor	Tiltrotor/Tiltwing (Hybrid)	Fan-core - Nozzle Thrust Vectoring

Lift + Lift/Cruise Configurations		
		
Front Tilt Tri-copter	Aft Tilt Tri-copter	Jet Vectoring

The aforementioned VTOL classifications allow any VTOL aircraft to be categorized into four configurations: wingless, Lift + Cruise, Lift = Cruise and Lift + Lift/Cruise configurations based on the propulsor's orientation. However, the commonly used aircraft classifications in the eVTOL industry for various eVTOL aircraft follows:

- Helicopters and Gyrodyne – single rotor rotorcraft.
- Multirotors – multiple fixed powered vertical propulsors.
- Lift + Cruise – combination of multirotor with fixed wing structures.
- Vectored Thrust – includes tiltrotor, tiltduct, tiltwing, hybrid configurations.

Several top eVTOL models are classified according to their configuration, as shown in Figure 3.2 [104–121].

Airbus *CityAirbus*, France
Multirotor

Ehang *216*, China
Multirotor

Volocopter *VoloCity*, Germany
Multirotor

Wisk *Cora*, USA
Lift + Cruise

Hyundai / Supernal *S-A1*, Korea
Vectored Thrust (Tiltrotor)

Beta Technologies *Alia*, USA
Lift + Cruise

Joby Aviation *S4*, USA
Vectored Thrust (Tiltrotor)

Kitty Hawk *Heaviside*, USA
Vectored Thrust (Tiltrotor)

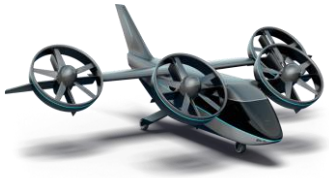

Bell *Nexus 4EX*, USA
Vectored Thrust (Tiltduct)

Airbus *Vahana*, France
Vectored Thrust (Tiltwing)

Archer *Maker*, USA
Vectored Thrust (Tiltrotor)

Vertical Aerospace *VA-X4*, UK
Vectored Thrust (Tiltrotor)

Lilium *Jet* , Germany
Vectored Thrust (Tiltduct)

Jaunt Air Mobility *Journey*, USA
Gyrodyne

Volocopter *VoloRegion*, Germany
Lift + Cruise

Dufour Aerospace *aEro3*, Switzerland
Vectored Thrust (Tiltwing)

Ehang *VT-30*, China
Lift + Cruise

EmbraerX *Eve*, USA
Lift + Cruise

Figure 3.2: Example of latest eVTOL aircraft prototypes and its configurations [104–121].

Numerous papers have been published on various VTOL configurations and prototypes. Bustamante et al. developed and flight tested a UAV VTOL in ducted-fan and tilt-rotor configurations using analytical tools such as XFLR5 and Ansys Fluent [19]. Seth conducted a historical overview of V/STOL aircraft technology, highlighting performance and handling qualities of multiple VTOL aircraft [44]. Muraoka et al. developed a proof-of-concept prototype for the quad tandem tiltwing configuration, evaluated through wind tunnel and flight testing [122]. Hoffmann et al. studied the effect of forward velocity, airframe drag, and blade flapping on quadcopter trajectory control at high speeds [123]. Saeed et al. evaluated past V/STOL aircraft with jet and non-jet propulsion systems, concluding that optimal aircraft must be lightweight with low wing loading [124]. Collectively, these studies underscore the diverse approaches and design considerations in VTOL development, emphasizing the importance of configuration-specific analysis to optimize performance, handling, and efficiency.

NASA has also highlighted the techniques and advances required to develop the GL-10 tiltwing aircraft, including propeller testing, wind tunnel testing, multi-body modeling, aerodynamic simulations, VTOL control optimization, and flight testing [125]. Subsequently, NASA designed and fabricated the tandem tiltwing DEP VTOL LA-8 aircraft, performing wind tunnel measurements and verification of acoustic and flight dynamics to conclude optimal conditions for transitioning between vertical and horizontal flight [66, 126]. Rotaru et al. presented a summary of fundamental helicopter flight physics for various flight phases, helicopter configurations, and systems, including autorotation and ground effects [127]. Muchowski et al. presented a preliminary aerodynamic concept of a UAV in the gyrodyne configuration compared to a helicopter and tiltrotor based on power requirements for a mission [128]. ICAO compiled and recognized various concepts, prototypes, and new technologies for the future of aviation from many industries and applications [129]. These studies highlight the importance of multidisciplinary approaches and rigorous testing in advancing VTOL and eVTOL technologies. Key takeaways include the critical role of transition optimization for tiltwing and tiltrotor designs, the need for comprehensive flight dynamics and acoustic verification, and the value of benchmarking new configurations against established designs to identify performance advantages and mission suitability.

3.1.2 eVTOL Design and Mission Evaluation

The major limitation in eVTOL aircraft lies in their highly complex design. These aircraft rely on multiple key performance parameters from numerous disciplines and are affected by mission profiles, aerodynamics, control systems, and propulsion mechanisms during each phase of flight, encompassing horizontal, vertical, and transitional segments. Depending on the eVTOL design and configuration, the generated forces and power requirements define a unique trajectory for the aircraft, as illustrated in Figure 3.3 for the takeoff phase, and similarly applicable to the critical landing phase [60].

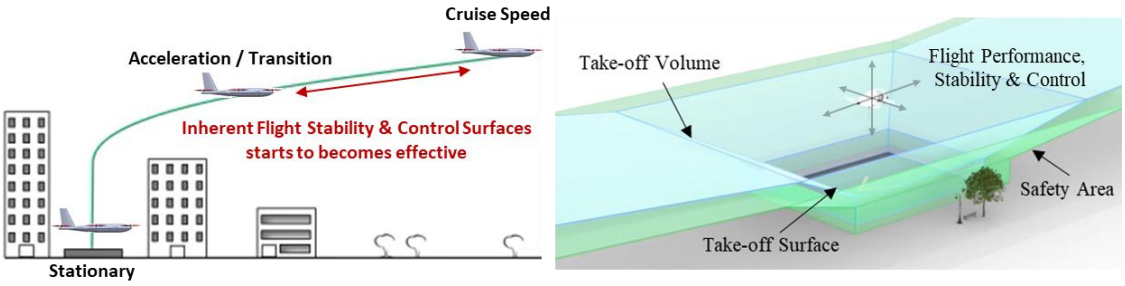

Figure 3.3: Flight phases for an eVTOL aircraft and restricted operating trajectory [60].

Most existing performance calculations for eVTOL aircraft focus primarily on two main segments: hover and cruise. For the cruise segment, where flight velocity remains mostly constant, analytical models typically use airplane theory with steady-level assumptions. For the hover segment, where the aircraft translates vertically, models typically use helicopter theory for each flight condition. Combining both models directly neglects the transition segment, during which the eVTOL aircraft experiences transient and dynamic behavior.

One notable study by Lovering and Bower analyzed the performance of a tiltwing eVTOL aircraft modeled after the Airbus Vahana [130–132]. This study focused on evaluating the direct operating cost based on the performance and operational requirements of a tiltwing eVTOL aircraft. An array of models was implemented to consider different aspects such as cost, structure, and mass. However, it lacked the modeling of the transition phase, considering only the hover and cruise segments, thereby limiting comparisons with other eVTOL configurations.

Subsequently, another study by Johnson et al. compared different eVTOL configurations, such as a quadrotor, tiltwing, and side-by-side helicopter. Their analysis, using NASA's Design and Analysis of Rotorcraft (NDARC), focused on evaluating the performance of hybrid and electric propulsion systems [81]. Johnson et al. highlighted that future work should further investigate and refine the mission profile for the aircraft. While these papers presented detailed comparisons of the characterization of each configuration, they did not carefully consider the transition phase for each aircraft.

Shamsheer suggested a method to model the full flight regime of a tiltwing eVTOL configuration [133]. In this study, the transition regime was modeled for each individual time step. Additionally, the study covered stall modeling for the tiltwing aircraft, highlighting that the aircraft would operate past the stall region during the transition phase, prompting the use of high angle of attack airfoils. However, the scope was limited to a tiltwing configuration, neglecting other possible configurations and trajectories. Nevertheless, their model was able to determine the power requirements for a given trajectory for a tiltwing aircraft.

Alternatively, Senkans et al. offered a different approach to model the transition segment [134]. In their paper, they broke down the transition modeling into different segments, with specific requirements for each segment. This allowed for a more realistic and controlled trajectory for a typical transition flight, comprising different individual segments with varying flight conditions. However, their trajectory model lacked flexibility as it was restricted to using constant acceleration, with power calculations derived using momentum theory. This approach might not fully represent the dynamic transition regime with non-uniform inflows, thereby neglecting other power losses incurred during vertical flight.

Existing approaches to modeling eVTOL aircraft often adopt simplified or truncated methodologies to determine the overall mission performance, neglecting certain features and characteristics, such as the intricacies of the transition regime and specific eVTOL components and structures. Therefore, this work aims to enhance the modeling fidelity of eVTOL aircraft analysis by utilizing a multidisciplinary approach that incorporates various component parameters and transitional characteristics, as highlighted in Section 1.2.

3.2 Wing and Wingless eVTOL Aircraft Designs

Research on the effects of wing arrangement for vertical lift aircraft often questions the benefits and impacts of fixed wing surfaces on rotorcraft. While numerous studies have examined the incorporation of fixed wings to enhance aircraft performance, there is limited research comparing different wing arrangements or configurations for rotorcraft across various disciplines such as flight performance, aerodynamics, stability, and handling qualities.

Aerodynamic and Flight Performance

Escobar and Yeo performed analytical studies using the Rotorcraft Comprehensive Analysis System (RCAS) alongside wind tunnel experiments to evaluate a hingeless rotor with and without a single wing on the retreating side for lift compounding [135]. Their findings demonstrate the potential of adding wing surfaces to enhance rotorcraft performance. Specifically, at an advance ratio of 0.5, the wing contributed a significant portion of the lift and rolling moment, enabling the rotor to sustain its own roll moment. This resulted in a 31.3% increase in lift from the wing and a 24% improvement through lift offset. Additionally, structural loads were significantly reduced, with normal and chord bending moments decreased by 16.1% and 90.6%, respectively. These results emphasize the aerodynamic and structural benefits of incorporating wing surfaces, particularly in improving flight efficiency and alleviating blade loading, making it a viable consideration for enhanced rotorcraft design despite potential weight and design complexity trade-offs.

Similarly, a recent study by Su et al. conducted flight test experiments with a quadcopter, with and without a wing surface, to assess flight performance characteristics [136]. Their study showed that equipping a lifting surface onto a quadcopter allowed for lower required power and increased range with minimal effects on stability and controllability. Their results concluded that the lift-augmented wing generated up to 66.56% of the lift required for the modified quadcopter and improved endurance by 18.97% and range by 6.9% compared to the quadcopter without the wing surface. This demonstrated the tangible benefits of equipping vertical lift aircraft with wing surfaces to provide augmented lift and increased performance.

Stability and Handling Qualities

Another crucial aspect of rotorcraft equipped with wing surfaces is their flying and handling qualities, and flight stability. This is vital for eVTOL aircraft operating in restricted and congested urban areas, requiring high precision in control and responsiveness, especially during critical flight phases such as take-offs, transitions, and landings. One common approach to assess stability and handling qualities is based on pilot evaluation, utilizing the Cooper Harper Handling Quality Rating (CHR), widely used for fixed-wing aircraft since its introduction [137, 138].

Previous developments have modified and expanded the applicability of CHR to various specific performance criteria and task elements for unmanned vehicles [139, 140]. For instance, Garcia et al. utilized a flight simulation-based approach with various mission task elements to assess several vertical flight maneuvers of an eVTOL aircraft [141]. Furthermore, current research by Klyde et al. is directed towards developing an applicable handling qualities matrix to aid the progressing eVTOL certification process, focusing on a mission-oriented approach [142, 143]. Therefore, assessing the stability and handling qualities of any given aircraft design and configuration is essential.

These studies highlighted the importance and advantages of implementing wing and lifting surfaces on vertical flight aircraft to grant better aerodynamic and stability performance. Similarly, equipping an eVTOL aircraft with a lifting surface enhances performance by reducing power required for cruise, thereby increasing the attainable range. However, there is a vital need for evaluation and validation of the effects of wing surfaces for eVTOL aircraft to ensure the success of the designs, especially with the vast number of possible wing arrangements currently being adopted for eVTOL aircraft. Validation through experimental flight testing of different aircraft designs can be both resource-intensive and time-consuming. Hence, this work expands on the previous works to highlight the elements to achieve an optimal wing arrangement for an eVTOL aircraft, as highlighted in Section 1.2.

3.2.1 Conventional and Canard Wing Configurations

At a more conservative level, the success of any eVTOL aircraft depends on its general wing configuration like the relative placement of the wing and tail surfaces. The four basic configurations are shown in Figure 3.4 [144–147]. While rotor configurations and rotor-wing configurations impact eVTOL performance, designing a wing configuration that offers the best performance is critical.

Horten HX-2	Rutan Long-EZ	Cessna Skyhawk 172	Rutan Quickie
Flying Wing / Tail-less	Canard Wing	Conventional Wing	Tandem Wing

Figure 3.4: Types of aircraft wing configurations [144–147].

Despite extensive research on various eVTOL aircraft configurations, the most optimal wing configuration has yet to be determined. This research gap motivates the search for an optimal wing arrangement for eVTOL aircraft that provides excellent aerodynamic efficiency, good inherent stability, and pleasant handling qualities.

Numerous past research by Staszek [148, 149] and other researchers [150, 151] compared the differences in fundamental aerodynamic properties and characterization between canard and conventional aircraft designs. Studies on aircraft design optimization have shown that aircraft wing design is influenced by multiple variables and disciplines, such as aerodynamics, structural weight, and propulsion mechanisms [98, 99]. Building on this, Selberg et al. conducted optimizations and aerodynamic-structural studies on dual and multiple wing systems with canard and conventional configurations for a six-passenger aircraft [152, 153].

Reviewing the studies mentioned above reveals a gap in eVTOL aircraft configuration design. There is a need for a more exhaustive comparison of wing configurations for eVTOL aircraft, focusing on wing designs to leverage the latest technologies for developing effective eVTOL aircraft. Past studies have primarily focused on aerodynamics, but a more exhaustive comparison is required to provide a comprehensive comparison of the aerodynamics, stability, and handling qualities.

3.2.2 Tandem Wing Configurations

In recent years, tandem wing configurations have gained popularity, especially in the design of eVTOL aircraft as shown in Figure 3.5 [113, 118, 154–160], as they permit easier placement of many lift rotors for hover. Tandem wing can be considered as the middle point between the spectrum of canard and conventional wing, with differing front and rear wing parameters. Prominent eVTOL aircraft such as the Airbus A^3 - Vahana and Volocopter - VoloRegion have incorporated the tandem wing configuration. An important aspect of the tandem wing eVTOL design is the independent wing parameters for both forward and aft wing surfaces, which directly influence aerodynamic efficiency and flight stability. These performance aspects are vital for an eVTOL aircraft to achieve operational and commercial success. Aerodynamic efficiency directly affects achievable flight range, while flight stability affects the ease of piloting and passenger comfort.

Figure 3.5: Examples of tandem wing eVTOL aircraft designs [113, 118, 154–160].

Since the start of the 21st century, numerous studies on tandem wing designs have provided insights solely into their aerodynamic properties and characteristics [161, 162]. For example, computational and experimental studies on tandem wing aircraft have focused on how wing spacing and Reynolds number affect wing interactions and aerodynamic properties [163, 164].

In the past, a few prominent studies have focused on the analytical comparison of aircraft configurations. One of the earliest studies was conducted by McGeer and Kroo, comparing conventional and canard aircraft configurations based on maximum coefficient of lift, drag, and structural weight [150]. They concluded that a tandem wing configuration could be a good middle ground between the conventional and canard configurations in terms of aerodynamics. However, they found that the conventional configuration is more structurally efficient than the tandem wing configuration. They also noted that a reference wing configuration, resembling a flying wing, offers the best possible aerodynamic performance.

Similar analytical studies by Schoser et al. [159], Andrews and Perez [165], and Boling and Zha [166] demonstrated the effect of wing geometrical parameters and Center of Gravity (CG) location on the aerodynamics, stability, and controllability of a tandem wing aircraft. They identified a conflict between aerodynamics and stability, noting that a specific CG position provides the best aerodynamic efficiency but renders the aircraft unstable. Andrews and Perez concluded that a smaller front wing area could improve longitudinal stability. Both Schoser and Boling and Zha concluded that a smaller aspect ratio on the front wing enhances stability. These studies indicate that wing size and aspect ratio play crucial roles in tandem wing aircraft design.

Recent advanced research to develop commercial tandem wing aircraft has adopted a multidisciplinary approach based on aerodynamics, stability, and control [167, 168]. These studies have highlighted the benefits of the tandem wing configuration, which provides increased lift at high angles of attack due to the slotted wing effect, while showcasing adequate stability characteristics in flight with and without a flight controller. Through these detailed studies, insights were gathered regarding the possible benefits of wing surfaces for use in vertical flight aircraft.

These studies provide initial insights into the role of wing design on the aerodynamics and stability of tandem wing aircraft. However, past studies have investigated only a limited list of wing design variables and have not provided an exhaustive consideration of the effects of various wing design variables on performance and handling qualities.

3.3 eVTOL Aircraft Trade Study

Determining the performance and characteristics of an eVTOL aircraft involves identifying the fundamental design attributes that define and affect the aircraft. Optimizing an eVTOL aircraft design necessitates understanding the typical values and ranges of the latest technology and designs. These design attributes are compiled for various eVTOL aircraft in Table 3.4, which are used in the trade study. The eVTOL aircraft selection is based on the performance specifications, technology progression, funding, certifiability and companies' reputability. Trade studies are decision-making activities that identify the most acceptable technical solutions among a set of proposed options. Conducting these trade studies underscores the applicability of this research towards assessing and developing eVTOL aircraft.

Table 3.4: Various eVTOL aircraft data used for trade study.

Aircraft Specifications	Joby Aviation JAS4-1	Wisk Aero Cora Gen 5	Lilium Jet (7-Seater)	Lilium Jet (5-Seater)	Supernal / Hyundai S-A1	Bell Nexus 4EX	Airbus A^3 Vahana	Kitty Hawk Heaviside	Beta Technologies Alia-250c	Archer Aviation Maker	Vertical Aerospace VA-X4	Volocopter VoloCity	Airbus Helicopter CityAirbus	EHang 216
Max. Gross Take -off Weight (kg)	2177	1224	3175	3175	3125	3175	815	374	2722	1508	3175	900	2200	620
Number of Seats	5	2	7	5	5	5	1	1	5	2	5	2	4	2
Maximum Speed (km/h)	332	160	300	300	290	241	220	289	300	241	321	110	120	100
Hover Rotor Diameter (m)	2.90	1.36	0.30	0.23	2.50	2.44	1.60	0.69	3.50	1.55	3.00	2.30	2.80	1.87
Cruise Propeller Diameter (m)	3.11	2.00			2.50				2.33	1.55				
Wingspan (m)	11.6	11.0	13.9	11.0	15.0	6.8	6.3	6.0	15.2	12.4	15.0	9.3	8.0	5.6
Wing Chord (m)	1.74	0.86	1.70	0.95	1.50	1.20	0.90	0.86	1.63	1.28	1.42	-	-	-
Aspect Ratio	8.8	12.8	8.2	11.5	10.0	5.7	6.9	7.0	9.3	9.7	10.6	-	-	-
Wing Area (m^2)	14.4	9.4	18.4	10.4	22.5	16.9	9.5	5.1	22.5	15.4	20.8	-	-	-
Fuselage Height (m)	1.60	1.44	1.50	1.58	1.98	2.18	1.26	0.89	1.73	1.97	1.60	1.40	1.80	1.70
Fuselage Length (m)	6.4	3.3	8.0	5.0	11.0	12.0	5.7	5.0	8.6	6.0	6.0	3.8	8.0	2.6
Fuselage Width (m)	1.52	1.45	1.70	1.46	1.70	1.41	0.93	1.00	1.52	1.60	1.67	1.45	1.50	1.40
Aircraft Length (m)	6.4	6.4	8.0	5.0	11.5	12.2	5.7	5.0	12.1	8.9	13.0	3.8	8.0	1.8
Range (km)	241	40	261	300	97	97	100	160	400	97	193	35	97	35
Disk Loading (lb/ft^2)	15.34	23.50	243.53	357.72	16.56	34.81	20.37	68.01	14.48	13.64	10.76	4.93	13.20	14.97
Wing Loading (lb/ft^2)	45.06	26.57	25.68	39.34	28.90	38.41	24.53	39.83	24.73	20.03	30.63	-	-	-
Hover Power (kW)	401.0	228.0	2570.0	2866.1	547.2	812.6	113.9	107.0	588.7	327.0	592.0	61.3	288.6	45.8
Cruise Power (kW)	217.8	91.8	224.0	187.7	186.5	237.8	69.5	74.0	116.0	59.5	143.5	179.9	329.6	181.7

Figure 3.6 presents the aircraft specifications, encompassing several dimensional and sizing variables that influence eVTOL aircraft design. The plotted values compare the aircraft wing and rotor characteristics as well as their targeted operating requirements. Specifically, Figure 3.6 (a) and (b) show the main parameters influencing horizontal and vertical flight performance, where rotor diameters are dictated by the number of hover rotors, and the maximum wingspan is restricted by landing requirements to below 15 meters. Figure 3.6 (c) and (d) illustrate the fuselage dimensions, indicating the size and payload capacity of an eVTOL aircraft. Additionally, Figure 3.6 (e) and (f) display the passenger count and maximum cruise speeds, highlighting the scale of the aircraft based on their payload and operating requirements.

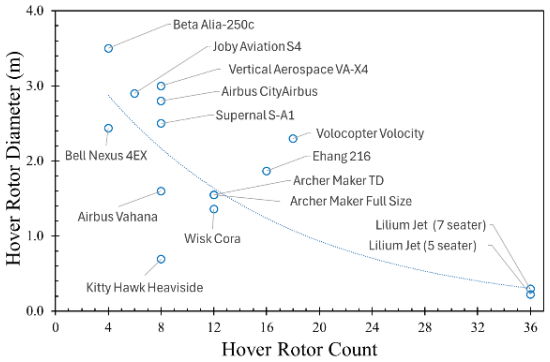

(a) Hover rotor diameter & quantity.

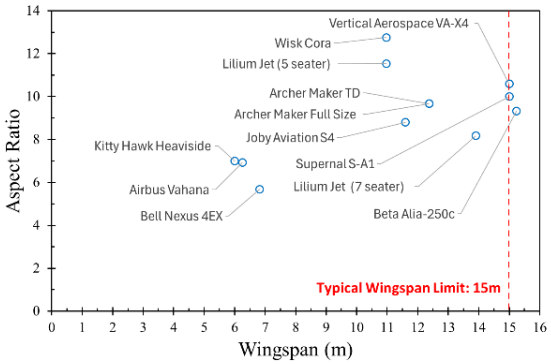

(b) Aspect ratio vs wingspan.

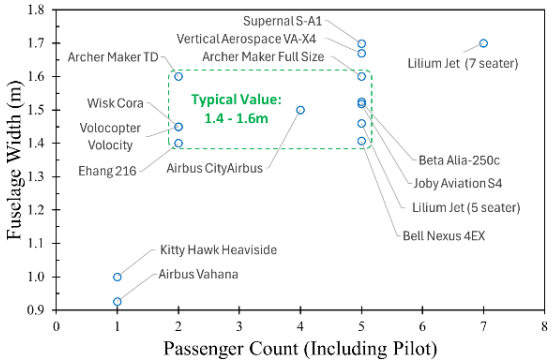

(c) Fuselage width & passenger count.

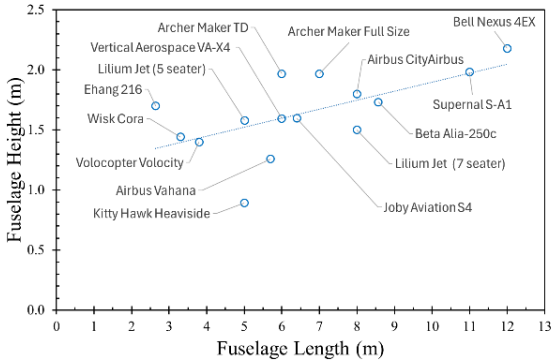

(d) Fuselage height & length.

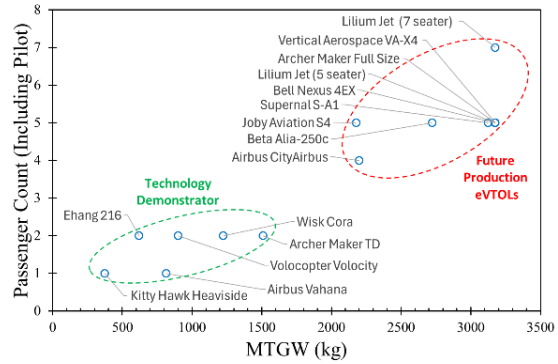

(e) Passenger count & MTGW.

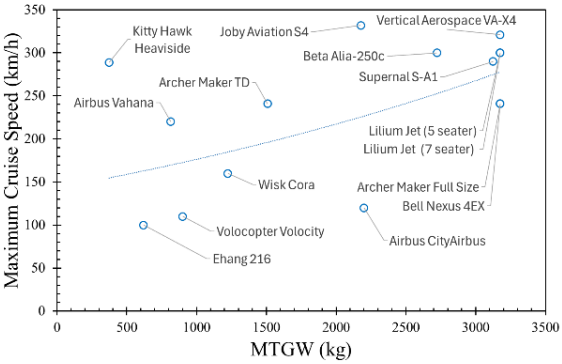

(f) Maximum cruise speed & MTGW.

Figure 3.6: Trade study comparison of aircraft specifications.

Similarly, Figure 3.7 illustrates the aircraft performance parameters, consisting of several performance variables that influence eVTOL aircraft design. The calculated values, based on publicly available data, determine the disk loading, wing loading, hover power, and cruise power. Figure 3.7 (a) and (b) depict the disk and wing loading bands and recommended limits for an eVTOL aircraft. Figure 3.7 (c) and (d) show the required hover and cruise powers against the maximum takeoff gross weight, indicating the effect of weight on power requirements. Figure 3.7 (f) presents the published ranges for each eVTOL aircraft, highlighting the benefits of wings in improving achievable flight range.

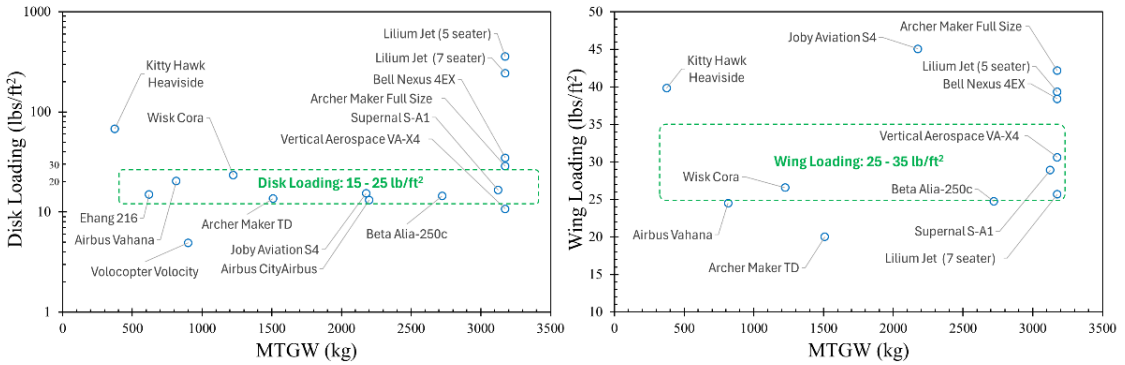

(a) Disk loading & MTGW.

(b) Wing loading & MTGW.

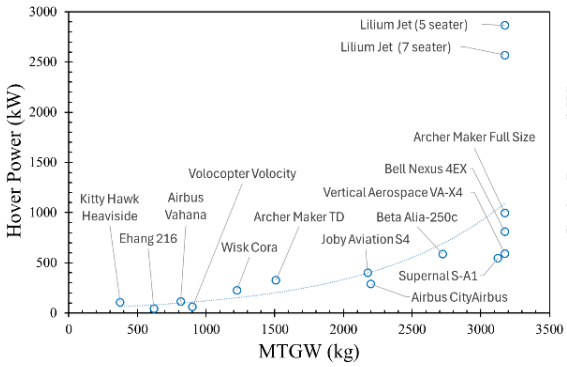

(c) Estimated hover power & MTGW.

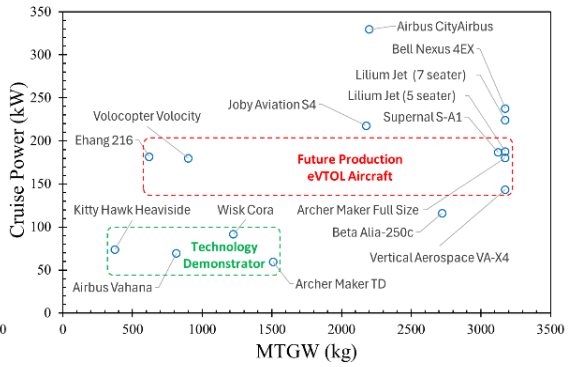

(d) Estimated cruise power & MTGW.

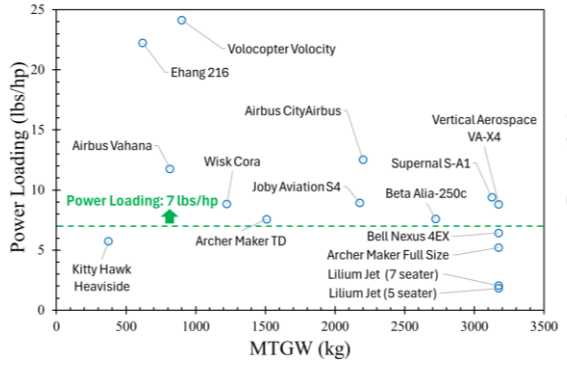

(e) Power Loading & MTGW.

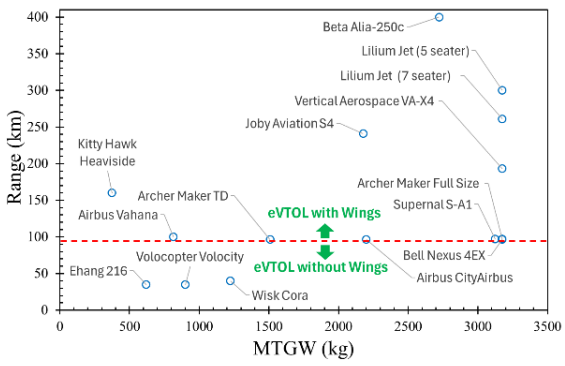

(f) Range & MTGW.

Figure 3.7: Trade study comparison of aircraft performance parameters.

Table 3.5 summarizes the aircraft parameters based on their lower and upper bound values. The trade study concludes with typical value ranges and corresponding remarks for each aircraft parameter used by eVTOL aircraft designers. These parameters highlight the trends and design elements among the latest eVTOL aircraft.

Table 3.5: Summary of eVTOL aircraft parameters.

	Parameters	Lower Bound	Upper Bound	Typical Range	Remarks
Aircraft Specific	Weight (kg)	620	3175	2000 – 3175	MTGW by EASA /FAA.
	Passenger Count	2	7	5 – 7	Passenger count affect operating cost.
	Range (km)	40	400	60 – 250	Improves with battery technology.
	Fuselage Width (m)	0.93	1.7	1.4 – 1.6	Affect structure and aerodynamics.
	Fuselage Height (m)	0.98	2.18	1.5 – 2.0	Affect structure and aerodynamics.
Vertical Flight	Rotor Diameter (m)	0.23	3.50	2.0 – 3.5	Dependent on number of rotors.
	Number of Rotors	4	36	4 – 12	Indication of safety and redundancy.
	Disk Loading* (lb/ft^2)	4.93	357.72	15 – 25	Affect hover flight performance.
	Power Loading* (lb/hp)	1.82	24.14	7 >	Higher values are preferred.
	Hover Power* (kW)	45.8	2866.1	< 1000	Lower values are preferred.
Horizontal Flight	Wingspan (m)	6	15.2	11 – 15	Restricted by infrastructure/helipad.
	Aspect Ratio	5.7	12.8	8 – 12	Improve cruise performance.
	Wing Loading* (lb/ft^2)	24.53	45.06	25 – 35	Affect cruise flight performance.
	Lift-to-Drag Ratio*	9.5	18.3	10 >	Higher values are preferred.
	Max. Speed (km/h)	100	332	200 – 300	Aircraft operates in subsonic regime.
	Cruise Power* (kW)	69.5	329.6	< 250	Lower values are preferred.

*Estimated values using compiled data.

This trade study highlights the critical role of early-stage comparative analysis in evaluating and optimizing eVTOL designs. In addition to the parameters already discussed, several other eVTOL-specific factors should be considered to ensure comprehensive performance assessment. For rotor blade design, key parameters include solidity, tip speed, pitch angles, and blade profile. Similarly, for wing design, crucial factors encompass geometrical parameters such as sweep, taper, dihedral, aspect ratios, and airfoil profiles, all of which directly impact aerodynamic efficiency and stability. Beyond aerodynamic components, mission-specific parameters—such as flight duration for each segment (hover, cruise, and transition)—must be carefully defined. Electrical system parameters, including battery capacity, energy density, motor power, and thermal management systems, are also essential as they govern power availability and efficiency. By systematically identifying and analyzing these fundamental design attributes across diverse configurations, this study offers valuable insights into the key trends and technological advancements shaping eVTOL development.

Chapter 4: eVTOL Aircraft Design and Performance Analysis

This chapter details the development of an eVTOL performance tool designed for analyzing and comparing eVTOL aircraft, following the flow diagram in Figure 4.1. It encompasses the integration of rotary wing and fixed-wing effects to accurately determine mission performance, alongside validation and comparison with actual eVTOL aircraft data.

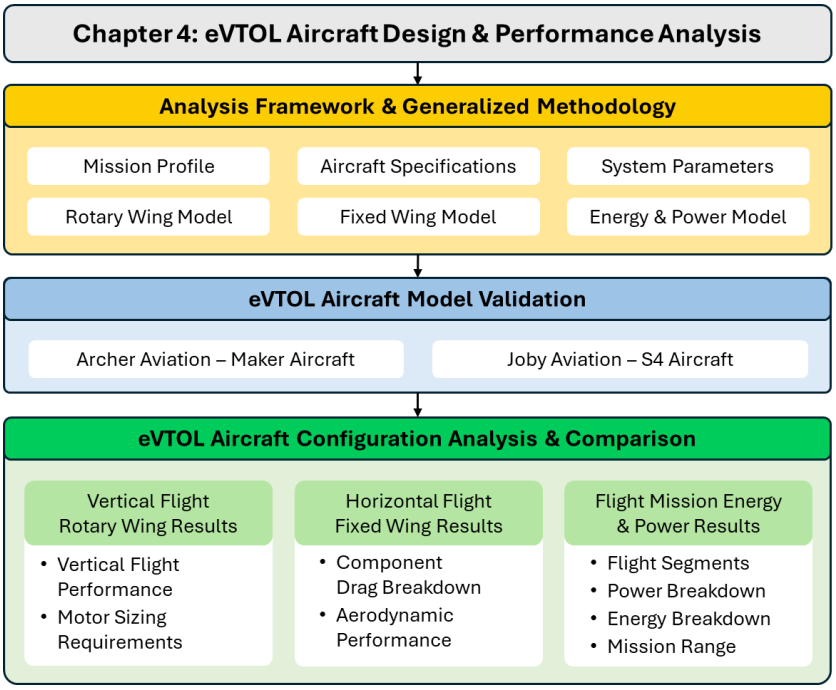

Figure 4.1: Chapter 4 - outline and flow diagram.

4.1 Analysis Framework and Methodology

The eVTOL Performance Analysis tool, developed in MATLAB, is designed to evaluate the performance of various conceptual fixed-wing eVTOL configurations. An overview is provided in Figure 4.2. The tool consists of three main modules: (1) a rotary wing model for hover flight, (2) a drag model for steady-state cruise, and (3) an energy model for estimating the achievable range of the eVTOL design. It is particularly suitable for preliminary design phases, requiring only four main sets of input variables: detailed design dimensions, estimated efficiency factors, defined battery parameters, and the desired mission profile.

The framework is structured into modular sections to provide eVTOL designers with flexibility to perform rapid trade studies of different design parameters and configurations, enabling a comprehensive performance evaluation across all flight segments. The following sections document and explain the inputs required and the methodology behind each model in detail.

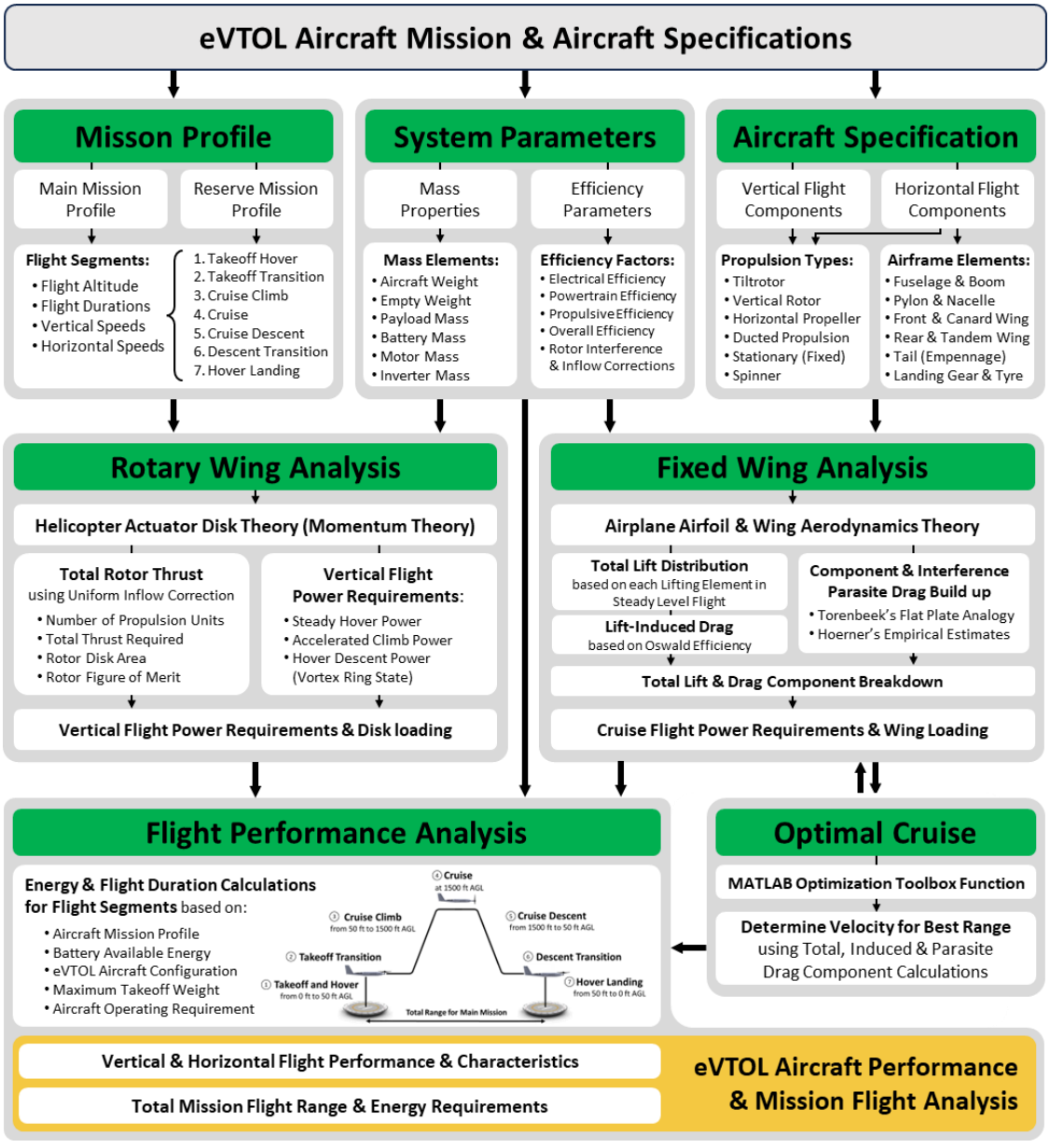

Figure 4.2: Structure of developed framework.

4.1.1 Main and Reserve Mission Profile

For an eVTOL aircraft, Uber Elevate has defined standard mission requirements [169]. These requirements have been adapted to create various flight segments for an eVTOL mission profile. A general main mission profile for an eVTOL aircraft consists of seven segments, as illustrated in Figure 4.3 (a): (1) takeoff hover from the aerodrome, (2) takeoff transition from stationary hover to cruise flight, (3) cruise climb to cruising altitude, (4) cruise flight for the main mission, (5) cruise descent from cruising altitude, (6) descent transition from cruise to stationary hover, and (7) hover landing at the destination. Similar to conventional aircraft, such as transport aircraft and helicopters, an eVTOL aircraft must be able to perform a reserve mission in the event of unforeseen circumstances. The flight phases of a reserve mission profile are similar to the main mission but are flown at a lower altitude, as shown in Figure 4.3 (b).

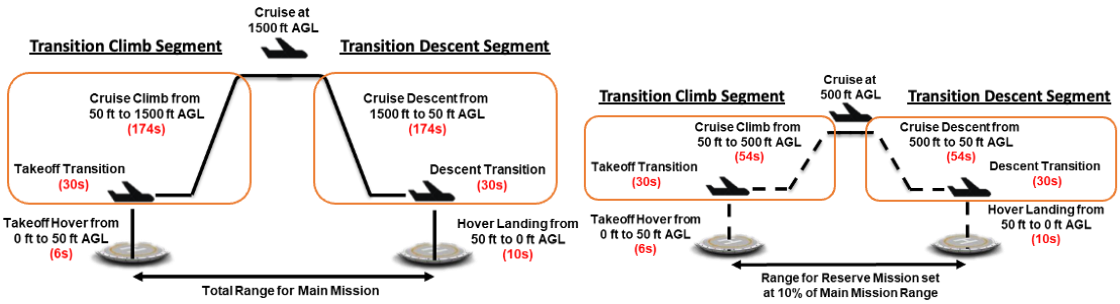

(a). Main mission profile for an eVTOL aircraft consisting of the various flight segments from start to finish.

(b). Reserve mission profile for an eVTOL aircraft for emergency situations and in the event of failure.

Figure 4.3: Mission profiles with transition segments highlighted in orange.

The main and reserve missions consist of different flight phases, each governed by specific bounding conditions summarized in Table 4.1, including Above-Ground-Level (AGL) altitudes, vertical speeds, and horizontal velocities for each flight segment. The main mission cruise altitude is set at 1,500 ft, consistent with regulatory guidelines for eVTOL operations [169], while the reserve mission operates at a reduced altitude of 500 ft. This lower altitude facilitates quicker landing or recovery in emergency scenarios and minimizes disruption to higher-priority airspace. Vertical climb and descent speeds are set at 500 ft/min and 300 ft/min, respectively, based on standard practices for conventional helicopters. For segments other than cruise, all eVTOL configurations are assumed to take the same amount of time, enabling a consistent and representative

comparison of performance across designs. The assumptions made in deriving these parameters aim to balance operational realism with the need for standardized evaluation.

Table 4.1: Main and reserve mission bounding condition for each flight segment. Main and reserve missions have similar hover and landing parameters while cruise altitude and duration are reduced during the reserve mission.

Flight Segments	Vertical Speed (m/s)	Horizontal Speed (m/s)	Main Mission		Reserve Mission	
			Altitude (m)	Time taken (s)	Altitude (m)	Time taken (s)
Takeoff Hover	+2.54	0	15.24	6	15.24	6
Takeoff Transition	0	0 to $\vec{V}_{\text{br}}$	15.24	30	15.24	30
Cruise Climb	+2.54		457.2	174	152.4	54
Cruise	0	$\vec{V}_{\text{br}}$	457.2	TBD	152.4	TBD
Cruise Descent	-2.54		15.24	174	15.24	54
Descent Transition	0	$\vec{V}_{\text{br}}$ to 0	15.24	30	15.24	30
Hover Descent	-1.52	0	0	10	0	10

TBD: To be determined from the analysis

The cruise duration is determined by each eVTOL's available residual energy after the vertical flight segments, based on the power required for cruise and its velocity at the best range $\vec{V}_{\text{br}}$. The ambient conditions during cruise, shown in Table 4.2, are interpolated based on the International Standard Atmosphere (ISA) model at an altitude of 1500 ft or 457.2 m [170].

Table 4.2: Ambient conditions based on ISA at 1500 ft.

Parameter	Value	Reference
Gravitational Acceleration g (m/s^2)	9.81	According to ISA standard
Density ρ (kg/m^3)	1.17	According to ISA standard
Dynamic Viscosity μ (kg/(ms))	1.18	According to ISA standard
Speed of Sound a (m/s)	338.55	According to ISA standard

The takeoff and descent transition segments, which model the eVTOL's shift between hover and forward flight configurations, are assumed to take 30 seconds each. This assumption is based on observations from an official video showcasing the complete flight profile of the Joby S4 eVTOL aircraft [171]. The 30-second duration aligns with typical operational goals for minimizing transition time due to its critical nature. The transition phase involves high peak power and energy consumption, primarily driven by the simultaneous demands of vertical lift and forward acceleration. Extended transitions would lead to prolonged periods of high energy draw, potentially impacting the overall mission efficiency and reducing available energy reserves for cruise and landing phases. Additionally, prolonged exposure to transitional aerodynamics and control dynamics increases the risk of instability, as the aircraft shifts from rotor-dominated lift and thrust to wing-dominated aerodynamics. A shorter transition time also enhances passenger

comfort by reducing the period of heightened maneuvering and potential turbulence, ensuring smoother flight dynamics. From a regulatory and safety perspective, limiting the duration of this phase minimizes the time spent in a less stable configuration, reducing exposure to control and stability challenges associated with dynamic aerodynamic and propulsion changes. Thus, the chosen 30-second transition duration reflects a balance between operational efficiency, safety, and passenger experience, supported by observed real-world eVTOL performance.

During transition, the vertical speed is assumed to be negligible, and the average horizontal speed is taken to be the velocity for minimum cruise power $\vec{V}_{\text{min power}}$, which can be approximated with transition factor, $f_{\text{transition}}$ to be 0.76 [172]:

$$\vec{V}_{\text{min power}} = f_{\text{transition}} \times \vec{V}_{\text{br}} \tag{4.1}$$

In the reserve mission profile, the cruise altitude is lowered from 1500 ft (457.2 m) AGL to 500 ft (152.4 m) AGL, and the reserve mission range is set as an additional 10% of the main mission range as f_{reserve} equal to 0.1. This adjustment reduces the amount of time spent during cruise climb and cruise descent. Other flight segments and parameters remain the same, as shown in Figure 4.3 (b) and Table 4.1.

4.1.2 Efficiency and System Parameters

Five efficiency factors are specified for performance estimation during hover and cruise phases. These factors are standardized across different eVTOL aircraft to allow for fair comparison of their respective design configurations. A description of each factor is provided below, along with their suggested values, as shown in Table 4.3.

Table 4.3: Values applied for eVTOL aircraft efficiencies.

Specified Factors	Symbol	Parameter Value
Rotor Power Correction	RPC	0.80
Oswald Efficiency	e	0.75
Electrical Efficiency	$\eta_{\text{electrical}}$	0.90
Propulsive Efficiency	$\eta_{\text{propulsive}}$	0.85
Overall Efficiency	η_{overall}	0.765

Electrical Efficiency

The electrical efficiency of the eVTOL system is estimated at 90%, reflecting typical power losses in motors, inverters, controllers, wiring, and auxiliary systems, consistent with the benchmark identified by Brown and Harris for electric aircraft across cruise and hover phases [15]. The 10% efficiency loss primarily arises from motor inefficiencies (internal resistance, heat, and magnetic hysteresis), inverter and controller losses (DC to AC conversion and power modulation), wiring and connector resistance, and power consumption by auxiliary systems such as cooling, avionics, and sensors.

Rotor Power Correction in Vertical Flight

The Rotor Power Correction (RPC) factor accounts for the additional power losses experienced by an installed rotor in actual hover flight compared to an isolated open rotor measured in wind tunnel experiments. As a preliminary estimate, this correction factor is set at 20%. The aerodynamic interference loss, estimated at 10%, accounts for the effects of rotor wake interaction with the eVTOL's body, which results in additional drag and power consumption. This loss is primarily due to the downwash and the altered airflow caused by and between the rotors, which affects the efficiency of both the rotors and the surrounding airframe. The loss is configuration-dependent, as the extent of interference varies based on rotor placement, airframe shape, and other design factors. This preliminary estimate assumes typical interference effects but should be refined as more specific data for the eVTOL configuration becomes available. Combined with the 10% electric powertrain loss, the total correction factor of 20% provides a conservative estimate for the system's performance losses.

Oswald Efficiency Factor

The Oswald efficiency factor *e* relates the induced drag of a wing to that of an ideal elliptical wing with the same aspect ratio and lift coefficient. An empirical estimate of *e* for eVTOL aircraft is derived from data on 10 general aviation and 6 propeller aircraft [173]. Based on these 16 aircraft, the median value is 0.75, and the mean value is 0.76. A baseline value of 0.75 is selected for the comparison of eVTOL aircraft using the performance code.

Propulsive Efficiency in Steady State Cruise

For an eVTOL aircraft, propulsive efficiency is defined as the ratio of useful thrust produced by the propellers to the supplied energy, reflecting how effectively the propellers convert power into thrust. McDonald and German suggest using a value of 85% for steady-state cruise [174]. Sensitivity studies on propulsive efficiency would typically explore the impact of variations in parameters such as propeller or rotor design (blade shape, diameter, and pitch), motor efficiency, and airspeed on the overall performance. For instance, changes in the propeller blade pitch or rotor speed could result in significant variations in the thrust-to-power ratio, affecting the efficiency. However, due to the complexity and variety of eVTOL designs, the efficiency may also be sensitive to factors such as rotor-stator interference and aerodynamic losses that are configuration-dependent. Future studies could refine the propulsive efficiency value by incorporating these sensitivities, especially as more detailed experimental or computational data becomes available. This would provide a more accurate model for specific eVTOL aircraft and mission profiles.

Overall Efficiency in Steady State Cruise

The overall efficiency of the eVTOL is calculated by taking the product of its electrical efficiency and its propulsive efficiency during steady-state cruise flight.

$$\eta_{\text{overall}} = \eta_{\text{electrical}} \times \eta_{\text{propulsive}} \tag{4.2}$$

While η_{overall} is load-dependent and typically varies nonlinearly with operating conditions, a fixed efficiency value was assumed in this analysis to simplify performance assessment and ensure standardized comparisons across different eVTOL configurations, preserving the relative performance trends. This approach aligns with typical efficiency ranges reported for electric propulsion systems under steady-state

conditions, maintaining the validity of the analysis for preliminary design evaluations. By standardizing these parameters, the eVTOL Performance Analysis tool provides consistent and comparative insights into various design configurations.

Battery Parameters

The pack-level specific energy SE, and mass of the battery m_{battery}, are crucial inputs to define the battery system. The total available battery energy E_{total} is estimated using these parameters.

$$E_{\text{total}} = SE \times m_{\text{battery}} \tag{4.3}$$

Table 4.4 lists the suggested battery input parameters for five leading fixed-wing cruise eVTOL aircraft currently in development: Archer Aviation - Maker, Beta Technologies - ALIA 250, Joby Aviation - S4, Kitty Hawk - Heaviside 2, and Vertical Aerospace - VX4. The values presented exhibit a broad spectrum due to the varying data made publicly available by eVTOL companies. It is important to note that the data compiled here is based on the information released by these companies at the time of the study, as specifications for battery systems are often not disclosed or are provided in limited detail. This variability reflects the evolving nature of the industry and the differences in design approaches among eVTOL manufacturers.

Table 4.4: Battery input parameters for eVTOL aircraft.

Aircraft	SE (Wh/kg)	E_{total} (kWh)	m_{battery} (kg)	MTGW (kg)	$\frac{m_{\text{battery}}}{\text{MTGW}}$ (%)
Archer Aviation - Maker	152.5	61	400	1508	26.5
Beta Technologies - Alia 250	180	230	1278	3175	40.3
Joby Aviation - S4	200	160	800	2177	36.7
Kitty Hawk - Heaviside 2	180	22	122	408	30.0
Vertical Aerospace - VX4	180	230	1278	3175	40.3

For commercially available lithium-ion batteries, the current limit for specific energy at the pack level is 180 Wh/kg. eVTOL manufacturers are also developing new battery pack designs and better integration of battery management systems to improve the pack-level specific energy [175, 176]. However, it is theoretically possible to achieve up to 220 Wh/kg with ideal integration of the best battery cell technology [177].

4.1.3 eVTOL Aircraft Specification

The analysis requires various geometrical inputs and dimensions for its rotary wing and drag model calculations, as shown in Table 4.5.

Table 4.5: Required input dimensions for eVTOL aircraft performance analysis.

Component	Input Dimensions
Fuselage	Length (m), Width (m) & Height (m)
Boom and Pylons	Quantity Length (m) & Diameter (m)
Front Wing	Wingspan (m) & Wing Reference Area (m^2) Wing Aspect Ratio
Rear Wing*	Wing Taper Ratio and Wing Root Chord (m) Wing Thickness to Chord Ratio Lift Fractions of Front and Rear Wings*
Empennage	Horizontal and Vertical Areas (m^2)
Canard	Canard Span (m) Canard Root and Tip Chords (m)
Wheeled Landing Gear	Total Tire Frontal Area (m^2) Estimated Drag Coefficient based on Frontal Area
Stationary Propellers Hover Propellers Horizontal Propellers	Quantity Spinner Type, Radius (m) and Height (m) Number of Blades per Propeller Average Blade Chord (m) Propeller Diameter (m) Thrust Percentage Figure of Merit (FM)

* Only applicable for tandem wing configurations

Front Wing

The wing reference area refers to the planform area of the wing through the fuselage, excluding nacelle widths and areas when nacelles are mounted at the wingtips, as shown in Figure 4.4 (a) based on the Joby Aviation S4 aircraft [178]. The input values used for the calculations are derived from publicly available images and documentation of various eVTOL aircraft, with careful consideration of standardized measurements where possible. While these values are based on visual estimation, they are reasonably accurate for the purpose of preliminary design analysis. However, it is important to acknowledge that inaccuracies can arise from the limitations of image-based measurements, which could lead to small discrepancies in the calculated geometry and dimensions. The aspect ratio of the wing is determined by dividing the square of the wingspan by the wing reference area. This method provides a reliable approximation, but any uncertainty in the wing area or wingspan can contribute to slight variations in the aspect ratio.

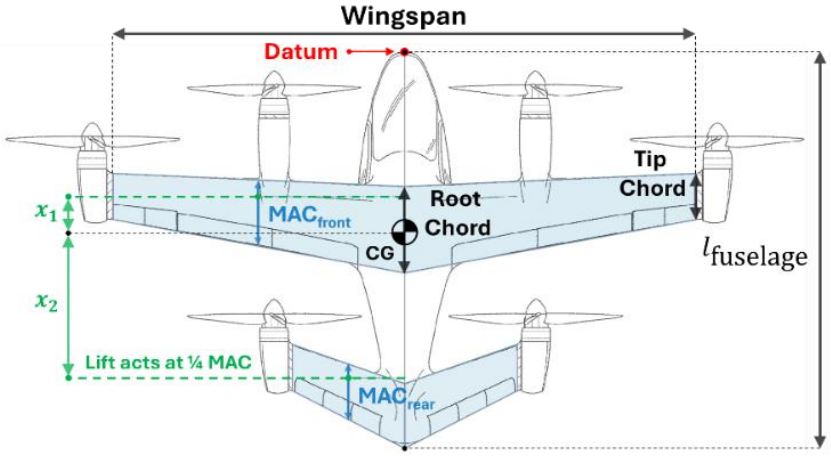

(a) Top view of Joby Aviation – S4 in forward flight.

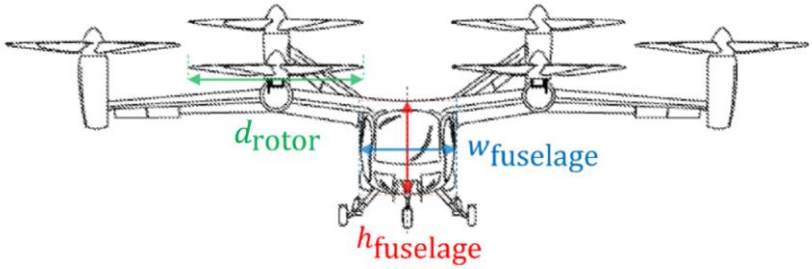

(b) Front view of Joby Aviation – S4 in hover flight.

Figure 4.4: Illustration with input parameters for wing surfaces and fuselage [178].

The wing taper ratio λ is calculated by dividing the tip chord by the root chord of the wing. For a linearly tapered wing, the Mean Aerodynamic Chord (MAC) is derived from its root chord and taper ratio. To provide sufficient space for the battery system, a thickness-to-chord ratio of 0.13 is suggested. This value is based on the need to accommodate standard cylindrical lithium-ion batteries, such as 18650 and 21700 cells, commonly used in eVTOL aircraft. Additionally, extra height is required for battery packaging and structural components. The height limitation affects the wing's thickness-to-chord ratio, which must be considered during design to ensure adequate space for both the batteries and the necessary structural elements.

$$\mathrm{MAC}_{\mathrm{wing}} = \frac{2}{3} \times c_{\mathrm{wing,\,root}} \times \frac{1 + \lambda + \lambda^2}{1 + \lambda^2} \tag{4.4}$$

Rear Wing and Wing Lift Fractions

For tandem wing eVTOLs, the same inputs are required for both the front and rear wings. The total wing reference area is the sum of the front and rear wing reference areas. Additionally, the front and rear lift fractions L_{fw} and L_{rw} are needed to compute the induced drag coefficients. These can either be set directly or determined using a first-

order estimate based on the lift forces from each wing in steady level flight, assuming zero resultant moment about the CG and zero pitching moment coefficients. It should be noted, however, that this assumption may not hold in all cases, as pitching moments and moments about the CG can influence the overall aerodynamic behavior. The use of this simplified method, however, was deliberately chosen to facilitate easy calculations during the early design phase, where overly complex formulations or computations are often avoided. This approach offers flexibility for the user to adjust the method or perform sensitivity studies as needed. The necessary parameters include the CG location and the leading-edge locations of the MACs of the front and rear wings defined as x_1 and x_2 respectively, measured from the datum, set at the fuselage nose, as shown in Figure 4.4 (a).

By taking moments about the CG:

$$L_{\text{fw}} \cdot W_{\text{eVTOL}} \cdot x_1 = L_{\text{rw}} \cdot W_{\text{eVTOL}} \cdot x_2$$
$$L_{\text{fw}} = \frac{x_2}{x_1} \cdot L_{\text{rw}} \tag{4.5}$$

Since $L_{\text{fw}} + L_{\text{rw}} = 1$, the lift fractions of each wing can be determined to be:

$$L_{\text{rw}} = \frac{1}{\frac{x_2}{x_1} + 1} \quad \text{and} \quad L_{\text{fw}} = 1 - L_{\text{rw}} \tag{4.6}$$

Empennage and Canard

The empennage typically consists of a horizontal and vertical stabilizer, which determines the total wetted surface area. In the case of a V-tail configuration, the wetted area is split equally between the horizontal and vertical surfaces. For canard configurations, the span and chord inputs are treated separately from the tandem wing, following the same convention used for the front wing. It is important to note that the calculations for canard or conventional aircraft configurations differ from those used for tandem wing designs, as they are based on distinct aerodynamic principles and user-defined inputs. In all cases, both the empennage and canard are assumed to contribute negligible lift compared to the main wing. These variations are accounted for in the model, with flexibility for the user to define the specific configuration based on the desired design parameters.

Fuselage Section

The fuselage length l_{fuselage}, is measured from the vertex of the nose to the endpoint. For non-circular fuselage, the diameter is half the input fuselage width and height or the square root of the product of the fuselage width and height [172], as shown in Figure 4.4 (a) and (b).

$$d_{\text{fuselage}} = \frac{1}{2}\left(h_{\text{fuselage}} + w_{\text{fuselage}}\right) \approx \sqrt{h_{\text{fuselage}} \cdot w_{\text{fuselage}}} \tag{4.7}$$

Booms and Pylons

Booms and pylons are rigid structures mounted on the eVTOL's wing, carrying stationary or a combination of stationary and horizontal propellers, as shown in Figure 4.5 [108]. Pylons are shorter versions of booms, used when the eVTOL has booms of different lengths or diameters, such as the Supernal S-A1 eVTOL.

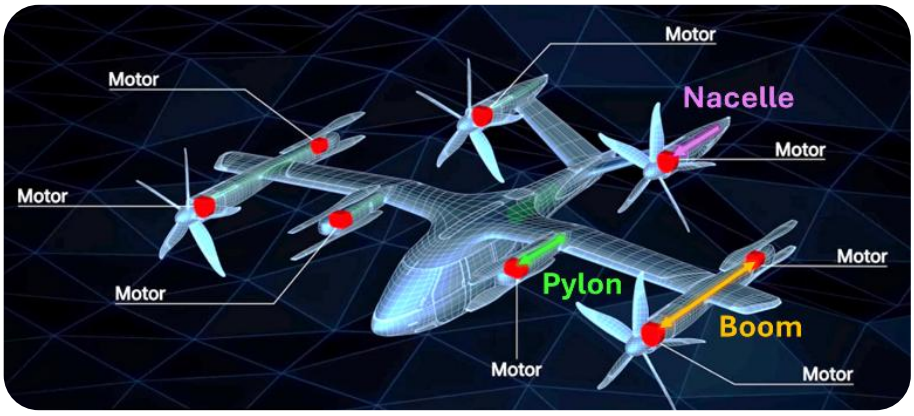

Figure 4.5: Booms, pylons and nacelles structures on the Supernal S-A1 aircraft [108].

Stationary, Hover and Horizontal Propellers

The analysis models four propeller configurations used in current eVTOL designs, with naming conventions and definition as:

- Stationary: Propellers used only for hover and are exposed during cruise.
- Hover: Propellers used only for hovering and are hidden during cruise.
- Horizontal Fixed: Propellers that face forwards or back during cruise flight.
- Horizontal Tiltrotor: Propellers that can be used in both hover and cruise flights.

Two types of spinners, cylindrical and hemispherical, are accounted for, as shown in Figure 4.6 [114]. The frontal area of the cylindrical and hemispherical spinners can be taken as a rectangle or semi-circle respectively. The propeller diameter is twice the sum

of the blade length and the spinner radius. Thrust for hover flight is assumed to be equally distributed among the rotors, with each rotor having a figure of merit (FM) of 0.78 based on experimental findings [179].

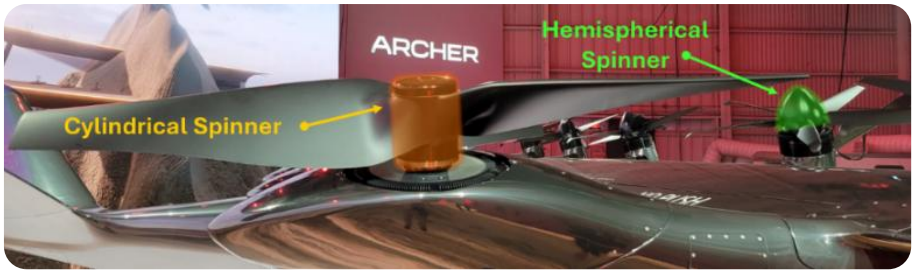

Figure 4.6: Spinner types on the Archer Maker eVTOL aircraft [114].

Landing Gear

The analysis includes retractable or fixed (non-retractable) wheeled landing gears. Retractable landing gears do not contribute to drag in steady cruise. For fixed landing gears, suggested drag coefficients are provided in Appendix: A. If the frontal area of each tire is unknown, a value of 0.065 m² is suggested for eVTOLs with tricycle landing gears and MTGWs between 2000 kg and 3175 kg.

eVTOL Empty Mass

Each passenger is assumed to contribute 100 kg of payload, including baggage. The eVTOL empty mass is estimated by subtracting 100 kg for each passenger from its claimed mass. Table 4.6 contains estimated empty masses for different eVTOLs based on their claimed MTGW.

Table 4.6: Estimated empty masses of eVTOLs based on published MTGW.

Aircraft	No. of Passengers	MTGW (kg)	Empty Mass (kg)
Archer Aviation - Maker	2	1508	1308
Beta Technologies - Alia 250	6	3175	2575
Joby Aviation - S4	5	2177	1677
Kitty Hawk - Heaviside 2	1	408	308
Vertical Aerospace - VX4	5	3175	2675

4.1.4 Rotary Wing Model

The rotary wing model utilizes helicopter momentum theory to perform calculations during hover, vertical climb, and vertical descent. The hover thrust required during each phase is equal to the eVTOL's weight, assuming constant vertical climb and descent velocities throughout each phase. Ideal results are adjusted with correction factors to account for rotor Figure of Merit (FM) and additional electrical and interference losses. This methodology is applied to stationary, hover, and horizontal propellers. The relevant equations for the rotary wing model are based on Figure 4.7, with detailed derivations for (4.8) to (4.17) available in [180, 181].

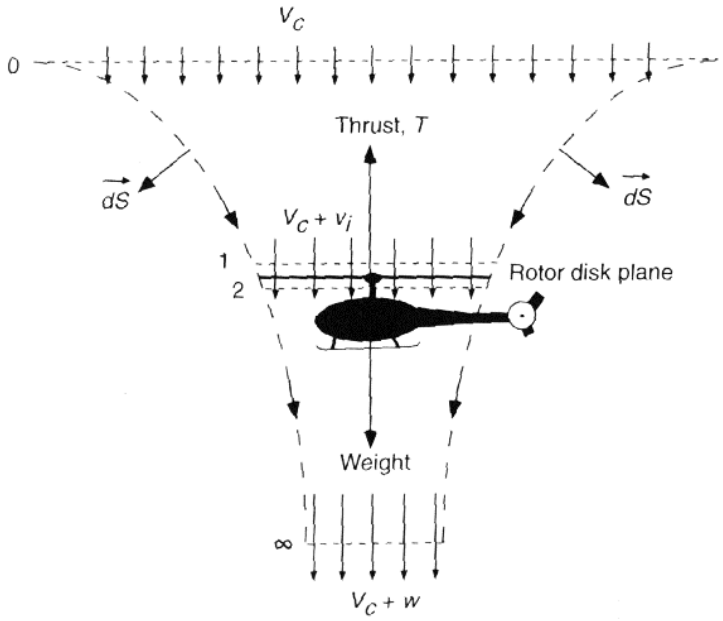

Figure 4.7: Momentum theory flow model for vertical flight [180].

Power to Hover

In hover, the hover thrust T provided by the rotors is given by:

$$T = (\rho\, A\, \vec{v}_{\text{hover}}) \times 2\, \vec{v}_{\text{hover}} \tag{4.8}$$

$$\text{where } A = N_{\text{rotors}} \times \frac{\pi}{4} d_{\text{rotor}}^2 \tag{4.9}$$

Rearranging (4.8), the inflow or induced hover velocity $\vec{v}_{\text{hover}}$, is be expressed as:

$$\vec{v}_{\text{hover}} = \sqrt{\frac{T}{2\rho A}} = \sqrt{\frac{\text{Disk Loading}}{2\rho}} \tag{4.10}$$

$$\text{where Disk Loading} = \frac{T}{A} \tag{4.11}$$

The ideal induced power needed for hover can be calculated using:

$$P_{\text{hover, ideal}} = T \times \vec{v}_{\text{hover}} = \sqrt{\frac{T^3}{2\rho A}} \tag{4.12}$$

To correct for losses, the ideal induced power is adjusted by the rotor FM = 0.78 and RPC = 0.8 factor to obtain the actual power needed for hover.

$$P_{\text{hover, actual}} = \frac{P_{\text{hover, ideal}}}{\text{FM} \times \text{RPC}} \tag{4.13}$$

Power to Vertical Climb

The ratio between ideal hover and vertical climb power is given in (4.14), where $\vec{V}_{\text{climb}}$ is the vertical speed in vertical climb.

$$\frac{P_{\text{vertical climb, ideal}}}{P_{\text{hover, ideal}}} = \frac{1}{2}\frac{\vec{V}_{\text{climb}}}{\vec{v}_{\text{hover}}} + \sqrt{\frac{1}{4}\left(\frac{\vec{V}_{\text{climb}}}{\vec{v}_{\text{hover}}}\right)^2 + 1}, \quad \text{valid for } \frac{\vec{V}_{\text{climb}}}{\vec{v}_{\text{hover}}} \geq 0 \tag{4.14}$$

The actual power needed for vertical climb is:

$$P_{\text{vertical climb, actual}} = \frac{P_{\text{vertical climb, ideal}}}{\text{FM} \times \text{RPC}} \tag{4.15}$$

Power to Vertical Descent

The ratio χ is defined as the ratio between specified vertical speed in vertical descent and induced velocity in hover:

$$\chi = -\vec{V}_{\text{descent}}/\vec{v}_{\text{hover}} \tag{4.16}$$

In vertical descent, when $-2 \leq \chi \leq 0$, the eVTOL is assumed to be in the vortex ring state. The flow involved is unsteady and turbulent, having both upward and downward velocities [127]. Therefore, momentum theory cannot be directly applied. An empirical approximation of the power needed for vertical descent is:

$$\frac{P_{\text{vertical descent, ideal}}}{P_{\text{hover, ideal}}} = \chi + 0.974 - 1.125\,\chi - 1.372\chi^2 - 1.718\chi^3 - 0.655\chi^4 \tag{4.17}$$

The actual power needed for vertical descent is:

$$P_{\text{vertical descent, actual}} = \frac{P_{\text{vertical descent, ideal}}}{\text{FM} \times \text{RPC}} \tag{4.18}$$

Motor Sizing

Among the three hover phases, the vertical climb phase requires the highest amount of power. For safety requirements [182], motors are sized to provide sufficient power during vertical climb during one motor inoperative conditions with N_{failure} equal to 1. The minimum power each motor must provide can be calculated as:

$$P_{\text{motor}} = \frac{P_{\text{vertical climb, actual}}}{N_{\text{rotors}} - N_{\text{failure}}} \tag{4.19}$$

4.1.5 Fixed Wing Aerodynamic Model

The aerodynamic efficiency of the eVTOL aircraft is evaluated within the steady-state subsonic cruise regime. The lift required is equal to the aircraft's weight, while the total drag acting on the aircraft comprises parasite drag and induced drag. The component build-up method by Torenbeek [183] is used to model the parasite drag of major structural components using the flat plate analogy, whereas empirical estimates from Hoerner [184] are employed for the remaining components listed in Table 4.7.

Table 4.7: Drag modelling methods for different eVTOL components.

Component	Component Drag Modelling Method
Wing Surface Fuselage Booms and Pylons Empennage Canard Surface Blades of Stationary Propellers	Torenbeek's Flat Plate Analogy
Spinner of Stationary Propellers Landing Gear Nacelles of Horizontal Propellers Interference Drag between Wing and Fuselage	Hoerner's Empirical Estimates (based on Component Frontal Area)

The total parasite drag coefficient is calculated using (4.20), where $C_{f,c}$ is component skin friction coefficient, $\Phi_{f,c}$ is component form factor, $S_{\text{wetted},c}$ is the component wetted area, $C_{d,c}$ is the component empirical drag coefficient based on frontal area and $S_{\text{front},c}$ is the component frontal area. The empirical estimates used for the drag estimation is covered in the Appendix: A.

$$\left(C_{D_{\text{parasite}}}\right)_{\text{total}} = \frac{\sum(C_{f,c} \cdot \Phi_{f,c} \cdot S_{\text{wetted},c}) + \sum\left(C_{d,c} \cdot S_{\text{front},c}\right)}{S_{\text{wing, ref}}} \tag{4.20}$$

The induced drag is calculated using the Oswald span efficiency [172]. As parasite drag increases and induced drag decreases with flight velocity, there exists an optimal cruise velocity where the L/D is highest. This optimal cruise velocity, known as the cruise velocity for best range $\vec{V}_{br}$ is determined using the MATLAB Optimization Toolbox [185].

4.1.6 Energy and Power Model

The energy model combines outputs from the rotary wing and drag models with battery input parameters to calculate energy and power requirements for each flight phase, estimating the total range based on mission profiles. The cumulative average energy and power approach was used for simplicity and computational efficiency in early-stage design assessments, providing a quick estimate of energy consumption, especially during transition phases and where detailed modeling of power profiles may not yet be feasible due to limited data or the complexity of the system. While it is useful for making initial comparisons, it does not account for transient power spikes, potentially underestimating powertrain sizing needs. In contrast, the nonlinear power profile more accurately captures dynamic changes in power over time, especially during transitions, but introduces greater computational complexity and requires detailed flight dynamic modeling, making it more suitable for later stages of design. In Chapter 5, a detailed analysis with a nonlinear power profile is conducted to refine the power and energy predictions. Ultimately, the cumulative average energy and power approach balances simplicity with the need for initial estimates, while more complex models provide better precision for later design phases.

Takeoff Hover Phase

The power required for the takeoff hover phase is the actual power to climb, which is derived from the rotary wing model:

$$P_{\text{takeoff hover}} = P_{\text{climb, actual}} \tag{4.21}$$

The energy required for this phase is calculated using (4.22). The time taken to execute the takeoff hover is determined based on the AGL ending altitude and the vertical speed set for the takeoff hover for this phase.

$$E_{\text{takeoff hover}} = P_{\text{takeoff hover}} \times t_{\text{takeoff hover}} \tag{4.22}$$

Transition Phase

For the transition phase, the power required is approximated as the actual power to hover, which is also derived from the rotary wing model:

$$P_{\text{transition}} = P_{\text{hover, actual}} \tag{4.23}$$

This approximation follows the transition power model presented by Fredericks and Shripad [186], where the initial power requirement is assumed to be equal to $P_{\text{actual, hover}}$ without any wind gust. However, as the aircraft transitions forward, the total upward force decreases, as the wings begin to generate lift, and the propulsion system provides forward thrust. During this time, the power required peaks and fluctuates as the aircraft balances weight and lift. Initially, more power is required to counteract the reduction in vertical thrust until the wings generate sufficient lift. As the aircraft reaches the end of the transition and the wing lift contribution increases, the power demand decreases and stabilizes. Given this fluctuation, using $P_{\text{actual, hover}}$ as an average value is a reasonable simplification for the overall transition, providing a conservative estimate. This assumption is consistent with the methodology used in previous studies, while acknowledging that a more detailed model could refine the power variation during transition, as addressed in Chapter 5: Transition Flight Mode Analysis.

The energy required for takeoff transition is:

$$E_{\text{takeoff transition}} = P_{\text{hover, actual}} \times t_{\text{takeoff transition}} \tag{4.24}$$

Since takeoff transition and landing transition are assumed to be equivalent, the total energy needed for both transitions is:

$$E_{\text{transition}} = 2 \times P_{\text{hover, actual}} \times t_{\text{takeoff transition}} \tag{4.25}$$

Cruise Climb Phase

Cruise climb calculations are divided into horizontal and vertical components. The energy required for the vertical portion of the cruise climb is the gain in gravitational potential energy, corrected by the overall efficiency in (4.26). $h_{\text{cruise climb}}$ is the difference in altitudes between cruise climb and takeoff transition.

$$E_{\text{cruise climb, vertical}} = \frac{m_{\text{eVTOL}} \times g \times h_{\text{cruise climb}}}{\eta_{\text{overall}}} \tag{4.26}$$

The power for the vertical and horizontal portions of the cruise climb are:

$$P_{\text{cruise climb, vertical}} = \frac{E_{\text{cruise climb, vertical}}}{t_{\text{cruise climb}}} \tag{4.27}$$

$$P_{\text{cruise climb, horizontal}} = P_{\text{cruise}} \tag{4.28}$$

The total power required for the cruise climb is the sum of the power required for the vertical and horizontal components:

$$P_{\text{cruise climb}} = P_{\text{cruise climb, vertical}} + P_{\text{cruise climb, horizontal}} \tag{4.29}$$

Cruise Flight Phase

The energy required to cruise is the work done to overcome drag for the range achieved, corrected by the overall efficiency. The aerodynamic efficiency L/D, is obtained from the drag model as:

$$E_{\text{cruise}} = \frac{\text{Range} \times D}{\eta_{\text{overall}}} = \left(\frac{W_{\text{eVTOL}} \times \text{Range}}{L/D}\right) / \eta_{\text{overall}} \tag{4.30}$$

The power to cruise is calculated by dividing the energy required by the time taken for the cruise phase:

$$P_{\text{cruise}} = \frac{E_{\text{cruise}}}{t_{\text{cruise}}} = \frac{E_{\text{cruise}}}{\text{Range} / \vec{V}_{\text{cruise}}} = \left(\frac{W_{\text{eVTOL}} \times \vec{V}_{\text{cruise}}}{L/D}\right) / \eta_{\text{overall}} \tag{4.31}$$

Cruise Descent Phase

For the cruise descent phase, the calculations are split into horizontal and vertical components. The power required for the vertical component is assumed to be negligible, and only the horizontal component is accounted for under cruise calculations.

Hover Landing Phase

The power required for hover landing is the actual power to descend from the rotary wing model:

$$P_{\text{hover landing}} = P_{\text{descent, actual}} \tag{4.32}$$

The energy required for hover landing is calculated by:

$$E_{\text{hover landing}} = P_{\text{descent, actual}} \times t_{\text{hover landing}} \tag{4.33}$$

Total Achievable Mission Range

The total energy for all phases excluding cruise in the main and reserve missions is:

$$\begin{gathered}\text{Total used energy, } E_{\text{used}} = \\ E_{\text{takeoff hover, main}} + E_{\text{transition, main}} + E_{\text{cruise climb, main}} + E_{\text{hover landing, main}} \\ + E_{\text{takeoff hover, reserve}} + E_{\text{transition, reserve}} + E_{\text{cruise climb, reserve}} + E_{\text{hover landing, reserve}}\end{gathered} \tag{4.34}$$

The remaining energy for cruise is:

$$E_{\text{remain}} = E_{\text{total}} - E_{\text{used}} \tag{4.35}$$

For one kilometer cruise range, the total energy required for the main and reserve missions is:

$$\begin{aligned} E_{\text{cruise, total, 1km}} &= E_{\text{cruise, main, 1km}} + E_{\text{cruise, reserve, 1km}} \\ &= \left\{\left(\frac{W_{\text{eVTOL}}}{L/D}\right) / \eta_{\text{overall}}\right\} \times (1 + f_{\text{reserve}}) \end{aligned} \tag{4.36}$$

The reserve mission factor is used in (4.36) to accounts for the reserve mission cruise range being 10% of the main mission cruise range.

The total achievable cruise range for both missions is:

$$R_{\text{cruise, total}} = \frac{E_{\text{remain}}}{E_{\text{cruise, total, 1km}}} \tag{4.37}$$

The achievable cruise ranges for the main and reserve missions are:

$$R_{\text{cruise, main}} = \frac{R_{\text{cruise, total}}}{1 + f_{\text{reserve}}} \tag{4.38}$$

$$R_{\text{cruise, reserve}} = R_{\text{cruise, main}} \times f_{\text{reserve}} \tag{4.39}$$

The total achievable range, including transition phases, is:

$$R_{\text{total}} = R_{\text{cruise, total}} + \vec{V}_{\text{min power}} \times (t_{\text{transition, main}} + t_{\text{transition, reserve}}) \tag{4.40}$$

4.2 Model Validation of Framework

The analysis was applied to predict the performance of the Archer Aviation - Maker and Joby Aviation - S4 aircraft for the mission profiles specified in Section 4.1.1. Two models, eVTOL (ARCH) and eVTOL (JOBY), representing both aircraft respectively, were generated based on publicly available dimensions and media. Input parameters for these models are detailed in Table 4.8.

Table 4.8: Input parameters for eVTOL (ARCH) and eVTOL (JOBY).
Bold text highlights the main input parameters.

Input Parameter		eVTOL (ARCH)	eVTOL (JOBY)
Aircraft	**Configuration Type**	**Lift + Tiltrotor**	**Tiltrotor**
	Max. Takeoff Gross Weight (kg)	**1508**	**2177**
	Empty Mass (kg)	1308	1677
	Number of Passengers	2	5
Battery	Specific Energy (Wh/kg)	152.5	200
	Available Energy (kWh)	61	160
Fuselage	Length (m)	8.288	6.4
	Width (m)	1.6	1.65
	Height (m)	1.792	1.6
Boom	Number	6	0
	Diameter (m)	0.4	0
	Length (m)	3.696	0
Wing Surface	**Wingspan (m)**	**12.2**	**10.48**
	Wing Area (m^2)	**13.57**	**11.58**
	Taper Ratio	0.635	0.53
	Root Chord (m)	1.36	1.44
	Aspect Ratio	10.97	9.19
	Thickness-to-chord ratio	0.13	0.13
Empennage	Vertical Area	6.844	3.11
	Horizontal Area	6.844	3.11
Landing Gear	Number of Tyres	3	3
	Frontal Area of Tyre (m^2)	0.056	0.054
	Estimated Drag Coefficient	0.25	0.25
Stationary Propellers	**Lift Rotor Quantity**	**6**	**0**
	Lift Rotor Diameter (m)	**1.664**	**0**
	Number of Blades	2	0
	Average Blade Chord (m)	0.15	0
	Thrust Percentage	50	0
	Figure of Merit	0.78	0.78
	Spinner Type	Cylinder	Cylinder
	Spinner Radius (m)	0.064	0
	Spinner Height (m)	0.23	0.23
Horizontal Propeller	**Cruise Propeller Quantity**	**6**	**6**
	Cruise Propeller Diameter (m)	**1.6**	**3.1**
	Propeller Type	Tiltable	Tiltable
	Number of Blades	5	5
	Thrust Percentage	50	100
	Figure of Merit	0.78	0.78
	Hub Diameter (m)	0.288	0.44
	Nacelle Drag Coefficient	0.092	0.092

Results were compared against the projected performance specifications of the Archer Aviation - Maker and the actual flight performance of the Joby Aviation - S4. The comparisons demonstrated good agreement, confirming the analysis's capability to produce reasonable performance predictions.

4.2.1 Archer Aviation - Maker Aircraft

Table 4.9 provides a detailed comparison of the key input and output parameters for the eVTOL (ARCH), representing the Archer Maker aircraft, against the published performance specifications from Archer Aviation.

The analysis reveals a high degree of similarity between Archer's claims and the results generated for both aerodynamic performance and energy breakdown. Minor deviations in values are expected due to inaccuracies in geometrical modeling between the eVTOL (ARCH) model and the actual Maker aircraft, as well as potential slight differences in the mission profile used.

Table 4.9: Comparison of Archer - Maker's data and eVTOL (ARCH) results.

Parameter	Published Archer Maker Values	eVTOL (ARCH) Calculated Outputs
Max. Takeoff Gross Weight (kg)	1508	1508
Battery Mass (kg)	400	400
Available Energy (kWh)	61	61
Overall Efficiency η_{overall}	-	0.765
Flight Speed for $\vec{V}_{\text{br}}$ (km/h)	-	155.7
Max. Cruise Range (km)	97.0	91.2
Lift-to-Drag Ratio L/D at $\vec{V}_{\text{br}}$	12.0	12.5
Energy for Vertical Flight (kWh)	9.0	10.3
Cruise Energy at $\vec{V}_{\text{br}}$ (kWh)	37.0	38.3
Reserve Energy (kWh)	15.0	12.4
Hover Power (kW)	325	376

Overall, the comparison indicates that the analysis method used can provide a reasonable estimation of performance and energy modeling for the different phases of flight in eVTOL aircraft. This similarity validates the approach taken for modeling and simulating the Archer Aviation - Maker's performance.

4.2.2 Joby Aviation - S4 Aircraft

The Joby Aviation - S4 prototype's weight and the amount of battery reserves for its 250 km flight test were not specified. However, it is reasonable to assume that its actual weight falls between its assumed empty weight and its Maximum Takeoff Gross Weight (MTGW). For the modeling of eVTOL (JOBY), representing the Joby Aviation - S4, its MTGW was set to vary from 1677 kg to 2177 kg to account for zero to full payload scenarios.

The performance of eVTOL (JOBY) was evaluated by comparing the predicted range and cruise velocity against actual data from the Joby Aviation S4 prototype. This analysis involved an aircraft weight sweep, following the mission profile outlined in Section 4.1.1. The vertical flight energy requirements were computed using the rotary wing model outlined in Section 4.1.4, which provided the residual energy available for cruise flight. This remaining energy was then applied to the fixed-wing aerodynamic model detailed in Section 4.1.5 to estimate the mission range and cruise velocity.

Figure 4.8 presents the mission range plotted against cruise velocity for various MTGWs. The optimal cruise velocities, identified as the peaks of each plot, fall within the projected range of 200 to 240 km/h. Furthermore, a 250 km mission range was achieved for MTGWs between 1877 and 1977 kg, aligning with the expected weight variation for eVTOL (JOBY). This demonstrates a consistent application of the models and equations to generate and validate the results shown.

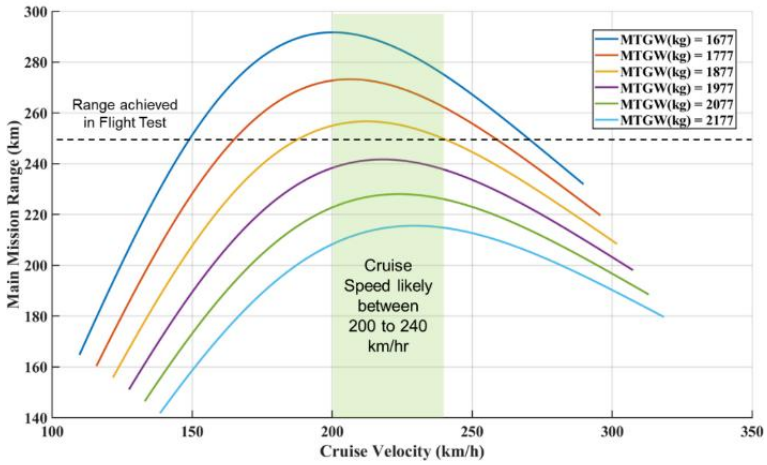

Figure 4.8: Main mission range for eVTOL (JOBY) at various MTGW.

However, this analysis is based on estimated MTGW values and may not account for all real-world variables, such as environmental conditions, battery degradation, or operational factors that could affect performance. Furthermore, discrepancies between the model and actual flight test data may arise due to simplifications in the model, particularly in terms of aerodynamic effects and energy consumption during transitions.

The comparison demonstrates a good match between the cruise range and cruise velocity of the theoretical results for eVTOL (JOBY) and the actual flight data of the Joby Aviation - S4 prototype. Coupled with the comparisons presented for the Archer Aviation - Maker and eVTOL (ARCH), this demonstrates the capability of the analysis in generating representative performance results for an eVTOL aircraft, further validating the accuracy and reliability of the simulation model used in this study.

4.3 Analysis of eVTOL Aircraft Configurations

The analysis aimed to evaluate three different eVTOL aircraft configurations: Lift + Cruise, Tiltrotor, and Lift + Tiltrotor, as summarized in Table 4.10. Three separate models, eVTOL (A), eVTOL (B), and eVTOL (C), were created to represent each configuration respectively. The full list of input parameters for these models is detailed in Table 4.11.

Table 4.10: Lift + Cruise, Tiltrotor and Lift + Tiltrotor eVTOL configurations.
Reference eVTOL aircraft used in modelling: Beta Technologies - Alia 250 (left), Joby Aviation - S4 (center) and Vertical Aerospace - VX4 (right)

		
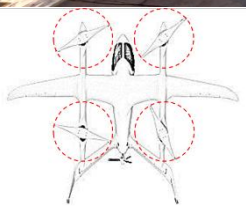	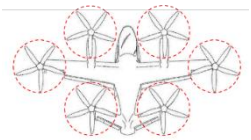	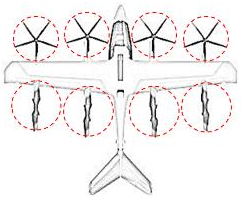
eVTOL (A): Lift + Cruise E.g., Beta Technologies, *BETA ALIA-250* [187]	eVTOL (B): Tiltrotor E.g., Joby Aviation, *JA S4-1* [188]	eVTOL (C): Lift + Tiltrotor E.g., Vertical Aerospace, *VA-X4* [189]

Table 4.11: Input parameters for the various eVTOL aircraft configurations.
Bold text highlights the main input parameters.

Input Parameter		eVTOL (A)	eVTOL (B)	eVTOL (C)
Aircraft	**Configuration Type**	**Lift + Cruise**	**Tiltrotor**	**Lift + Tiltrotor**
	Max. Takeoff Gross Weight (kg)	**3175**	**2177**	**3175**
	Empty Mass (kg)	2575	1677	2675
	Number of Passengers	6	5	5
Battery	Specific Energy (Wh/kg)	180	200	180
	Available Energy (kWh)	230	160	230
Fuselage	Length (m)	7.81	6.4	10.45
	Width (m)	1.5	1.65	1.65
	Height (m)	1.83	1.6	1.9
Boom	Number	2	0	4
	Diameter (m)	0.43	0	0.45
	Length (m)	9.1	0	6.1
Wing Surface	**Wingspan (m)**	**15.24**	**10.48**	**15**
	Wing Area (m^2)	**19.82**	**11.58**	**26.76**
	Taper Ratio	0.207	0.53	0.394
	Root Chord (m)	2.13	1.44	2.77
	Aspect Ratio	11.72	9.19	8.41
	Thickness-to-chord ratio	0.13	0.13	0.13
Empennage	Vertical Area	6.231	3.11	6.5835
	Horizontal Area	2.42	3.11	6.5835
Landing Gear	Number of Wheels	4	3	0
	Frontal Area of Wheel (m^2)	0.0697	0.054	0
	Estimated Drag Coefficient	0.21	0.25	0
Stationary Propellers	**Lift Rotor Quantity**	**4**	**0**	**4**
	Lift Rotor Diameter (m)	**3.91**	**0**	**3.3**
	Number of Blades	2	0	4
	Average Blade Chord (m)	0.36	0	0.44
	Thrust Percentage	100	0	50
	Figure of Merit	0.78	0.78	0.78
	Spinner Type	Cylinder	Cylinder	Cylinder
	Spinner Radius (m)	0.32	0	0.225
	Spinner Height (m)	0.23	0.23	0.23
Horizontal Propeller	**Cruise Propeller Quantity**	**1**	**6**	**4**
	Cruise Propeller Diameter (m)	**2.15**	**3.1**	**3.05**
	Propeller Type	Fixed	Tiltable	Tiltable
	Number of Blades	3	5	5
	Thrust Percentage	0	100	50
	Figure of Merit	0.78	0.78	0.78
	Hub Diameter (m)	0.05	0.44	0.45
	Nacelle Drag Coefficient	0.092	0.092	0.092

4.3.1 Vertical Flight Rotary Wing Results

Vertical Flight Performance

The rotary wing model was employed to predict the power required for each eVTOL during hover, vertical climb, and vertical descent phases at different Maximum Takeoff Gross Weight (MTGW). This analysis uses the formulations of the rotary wing model in Section 4.1.4, the rotor disk area and disk loading follows (4.9) and (4.11). The primary variables in the rotary wing model using inputs from Table 4.11 are listed in Table 4.12.

Table 4.12: Rotor disk area and disk loading values at MTGW.

Aircraft	MTGW (kg)	Rotor Disk Area (m^2)	Rotor Disk Loading (N/m^2)
eVTOL (A)	3175	48.03	648.5
eVTOL (B)	2177	45.29	471.6
eVTOL (C)	3175	63.44	491.0

The hover performance results for each eVTOL aircraft at various MTGWs are depicted in Figure 4.9, using equations (4.13), (4.15) and (4.18), with each data point representing a 100 kg increment on the x-axis. This variation in MTGW simulates the payload change carried by each eVTOL from zero to six passengers. Across all three models, the power requirement is highest during the vertical climb phase, followed by hover, and lowest during the vertical descent phase.

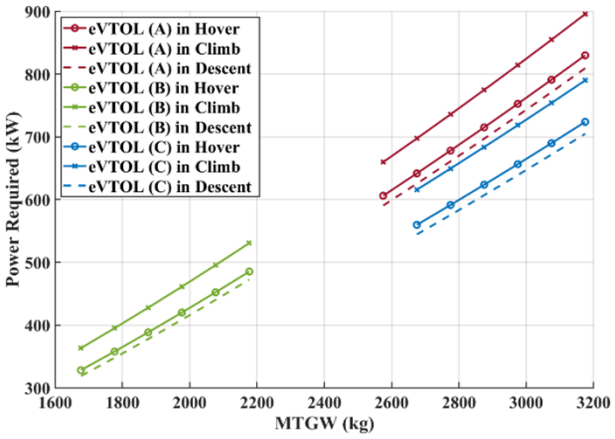

Figure 4.9: Comparison of power required in vertical flight phases and MTGW.

Among the configurations, eVTOL (B) requires the least power for hover flight, followed by eVTOL (C), with eVTOL (A) requiring the most power. This is attributed to the significantly lighter MTGW range defined for eVTOL (B). In hover, the square of the power required is proportional to the cube of the aircraft weight, as expressed in

(4.12). Despite eVTOL (B) and (C) having similar rotor disk loading values, eVTOL (B) requires much lower power for hover flight due to its lower weight. Therefore, minimizing aircraft weight is crucial for optimal hover performance, as any decrease in weight results in a more than proportional decrease in the power required for hover.

Between eVTOL (A) and (C), which share the same specified MTGW of 3175 kg, rotor disk loading becomes the determining factor for hover performance. eVTOL (C) requires less power for all hover phases due to its lower rotor disk loading compared to eVTOL (A). A lower rotor disk loading can be achieved by increasing the rotor disk area. However, a higher rotor disk area is only desirable if it does not significantly increase the aircraft's weight. According to (4.12), the power required for hover is inversely proportional to the square root of the rotor disk area, indicating that any increase in rotor disk area will lead to a less than proportional decrease in the power required for hover. Hence, aircraft weight remains the primary factor influencing the hover performance of an eVTOL.

Motor Sizing Requirements

The analysis also estimated the motor power requirements for each eVTOL configuration. Motor sizing was determined based on two critical factors: the peak power demand during vertical climb phases, calculated using (4.15), and the power needed to compensate for rotor failure, where operational motors supplement the thrust as per (4.19). Table 4.13 compares the estimated minimum power required for each motor across the three eVTOL configurations, highlighting differences in power demands under these operational conditions.

Table 4.13: Motor vertical climb power sizing with one motor inoperative condition.

Parameter	eVTOL (A)	eVTOL (B)	eVTOL (C)
MTGW (kg)	3175	2177	3175
Number of Hover Rotor	4	6	8
Vertical Climb Power (kW)	895.6	530.6	298.5
Minimum Motor Power (kW)	298.5	106.1	112.8

eVTOL (B) and (C) were observed to require similar motor power sizes of 106.1 kW and 112.8 kW, respectively, whereas eVTOL (A) required approximately three times as much power at about 300 kW. Based on these power sizes, the total weight of the motors and inverters for each configuration was estimated. The motor and inverter specific powers were set at 5 kW/kg and 7 kW/kg, respectively, values were estimated based on

eVTOL literature and supported by existing motor and inverter technologies [190]. Assuming each rotor is powered by one motor and two inverters for redundancy, the estimated total mass for each configuration is shown in Table 4.14. The results suggest that configurations with more rotors distribute power demands more effectively, leading to lower overall weight for motors and inverters. This highlights the importance of rotor count in optimizing the design and efficiency of eVTOL aircraft.

Table 4.14: Estimated total mass of motors and inverters.

Parameter	eVTOL (A)	eVTOL (B)	eVTOL (C)
Number of Motors	4	6	8
Motor Mass per Unit (kg)	59.7	21.2	22.6
Number of Inverters	8	12	16
Inverter Mass per Unit (kg)	42.6	15.2	16.1
Total Mass (kg)	580.0	309.3	438.5
Percentage of MTGW (%)	18.3	14.2	13.8

4.3.2 Horizontal Flight Fixed Wing Results

Component Drag Breakdown

The analysis generated individual component drag breakdowns for each eVTOL according to Section 4.1.5 with their inputs from Table 4.11, based on the total parasite drag coefficient is calculated using (4.20) following the order in Appendix: A, to investigate the contributions of specific components to the total drag during steady cruise. For eVTOL (A) and (C), the components include booms, as well as the blades and spinners of stationary propellers. For eVTOL (B), the components include the nacelles of its horizontal tiltrotors. The drag breakdowns for each eVTOL at their MTGW and cruise velocity $\vec{V}_{\text{br}}$ are shown in Table 4.15.

Table 4.15: Drag breakdown of each component at MTGW.
Values are expressed as a percentage of total drag.

Drag (%)	Components	eVTOL (A)	eVTOL (B)	eVTOL (C)
General Components	Fuselage	6.9	10.4	8.6
	Wing Parasite	12.6	13.6	14.4
	Wing Induced	48.3	48.4	47.9
	Wing Interference	0.2	0.3	0.4
	Empennage	6.5	8.9	8.4
	Landing Gear	4.6	6.0	-
eVTOL Specific	Booms	4.7	-	6.8
	Stationary Propellers	16.2	-	13.5
	Nacelles of Tiltrotors	-	12.4	-

Across all three aircraft, induced drag contributes the largest portion of total drag, while wing interference drag contributes the smallest portion. The induced drag values obtained show similarity across different configurations, which can be attributed to the

combined effects of the induced drag coefficient and flight speed. Specifically, eVTOL (B) operates at a higher flight speed but has a lower induced drag coefficient compared to eVTOL (A) and (C), as illustrated in Table 4.16. The drag distribution among general aircraft components remains relatively consistent, with empty cells reflecting the absence of certain components or the use of retractable landing gear. Notably, eVTOL-specific components exhibit relatively high drag contributions, with eVTOL (B) at 12% of total drag and eVTOL (A) and (C) approximately 20%. This highlights a significant trade-off in cruise performance to accommodate VTOL capabilities.

Aerodynamic Performance

The drag model results were also used to compare the best aerodynamic performance of each eVTOL in cruise flight. The key parameters compared include the optimal cruise velocity for best range $\vec{V}_{\text{br}}$, the peak L/D, and the required power to cruise P_{cruise}. These parameters for each eVTOL model at MTGW are summarized in Table 4.16.

Table 4.16: Comparison of aerodynamic performance in steady-state cruise.

Parameter	eVTOL (A)	eVTOL (B)	eVTOL (C)
MTGW (kg)	3175	2177	3175
Wing Area (m^2)	19.82	11.58	26.76
Wing Loading (N/m^2)	1573	1841	1162
Flight Velocity for Best Range (m/s)	53.7	63.5	52.9
Lift-to-Drag Ratio for Best Range	14.4	13.4	13.4
Cruise Power for Best Range (kW)	152.3	132.0	161.1

In contrast, eVTOL (B) has the highest $\vec{V}_{\text{br}}$ due to its highest wing loading. $\vec{V}_{\text{br}}$ is directly proportional to the square root of wing loading, as shown in (4.41), assuming that the induced drag factor *k* and zero-lift drag coefficient C_{D_0} do not vary with velocity, which is reasonable at subsonic speeds.

$$\vec{V}_{\text{br}} = \vec{V}_{D_{\min}} \approx \sqrt{\frac{2}{\rho} \cdot \frac{W}{S} \cdot \left(\frac{k}{C_{D_0}}\right)^{1/2}} \tag{4.41}$$

Figure 4.10 (a) and (b) illustrate the variation of L/D and power to cruise at different velocities for the three aircraft. The power to cruise is the most indicative parameter for cruise performance as it accounts for the MTGW, aerodynamic efficiency, and velocity of each aircraft. Despite being less aerodynamically efficient, eVTOL (B) requires the lowest power to cruise at $\vec{V}_{\text{br}}$ due to its low weight. This highlights the importance of having a low aircraft weight in achieving better cruise performance.

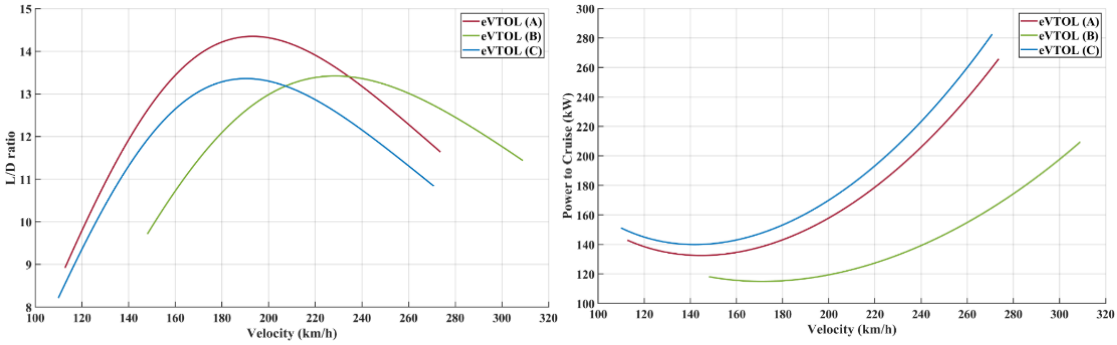

(a) L/D ratio against velocity. (b) Power to cruise against velocity.

Figure 4.10: L/D and cruise power against velocity at their respective MTGW.

The induced and zero-lift drag coefficients at MTGW and $\vec{V}_{\text{br}}$ for each aircraft are shown in Table 4.17. These coefficients are normalized with respect to their wing areas, and the results indicate similar values for each aircraft. This is expected since zero-lift drag increases with velocity while induced drag decreases with velocity.

Table 4.17: Induced and zero-lift drag coefficients at their MTGW and $\vec{V}_{\text{br}}$.

Parameter	eVTOL (A)	eVTOL (B)	eVTOL (C)
Wing Area (m^2)	19.82	11.58	26.76
Induced Drag Coefficient C_{D_i} @ $\vec{V}_{\text{br}}$	0.03062	0.02916	0.02412
Parasite Drag Coefficient C_{D_0} @ $\vec{V}_{\text{br}}$	0.03269	0.03107	0.02627

Figure 4.11 plots the variation of drag against velocity for eVTOL (C) at MTGW. The minimum drag point is slightly to the right of the intersection between calculated induced and zero-lift drag, where their rates of change sum to zero.

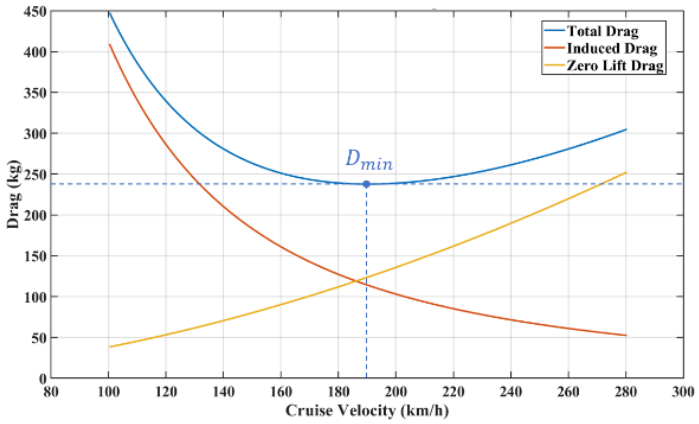

Figure 4.11: Types of drag components against velocity for eVTOL (C) at 3175kg.

Aerodynamic Performance at Different MTGW

Figure 4.12 (a) and (b) compares the variation in peak L/D ratios and $\vec{V}_{br}$ for each aircraft at different MTGW. The peak L/D ratios remain relatively constant, indicating that total drag increases almost linearly with weight. $\vec{V}_{br}$ increases with total weight, with eVTOL (B) showing the steepest increase due to its smallest wing area. This results in a higher increase in best cruise velocity with the same weight increase.

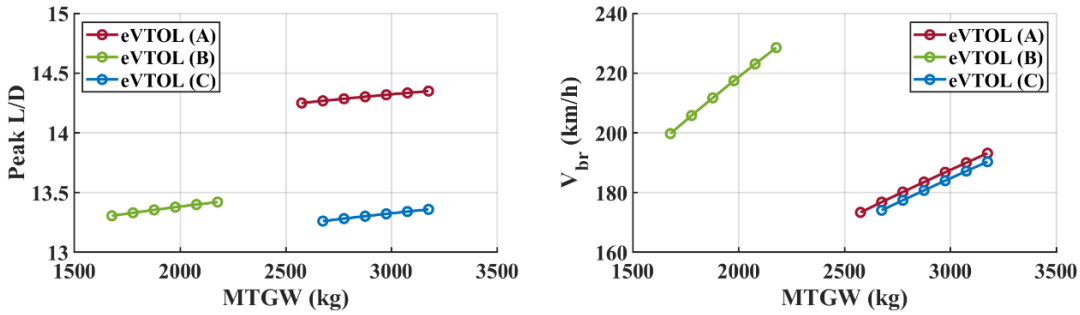

(a) Peak lift-to-drag against MTGW. (b) Velocity at best range against MTGW.

Figure 4.12: Peak L/D ratios and corresponding $\vec{V}_{br}$ against MTGW.

To verify the combined impact of both mass and velocity changes on aerodynamic performance, this section focuses on the results obtained for model eVTOL (B), as eVTOL (A) and (C) exhibit similar trends. Figure 4.13 (a) and (b) presents the variation of L/D ratio and lift coefficient against velocity at different MTGW for eVTOL (B). The L/D plots shift to the right and slightly upwards as MTGW increases. The lift coefficient plot for different MTGWs also decreases and coalesces as velocity increases.

Figure 4.13 (c) and (d) presents the induced and zero-lift drag results obtained at different MTGW for eVTOL (B). At the same velocity, a higher MTGW results in higher induced drag due to the increase in lift coefficient needed to support the aircraft's weight in cruise. Zero-lift drag remains independent of takeoff weight at the same velocity, assuming no changes in the dimensions.

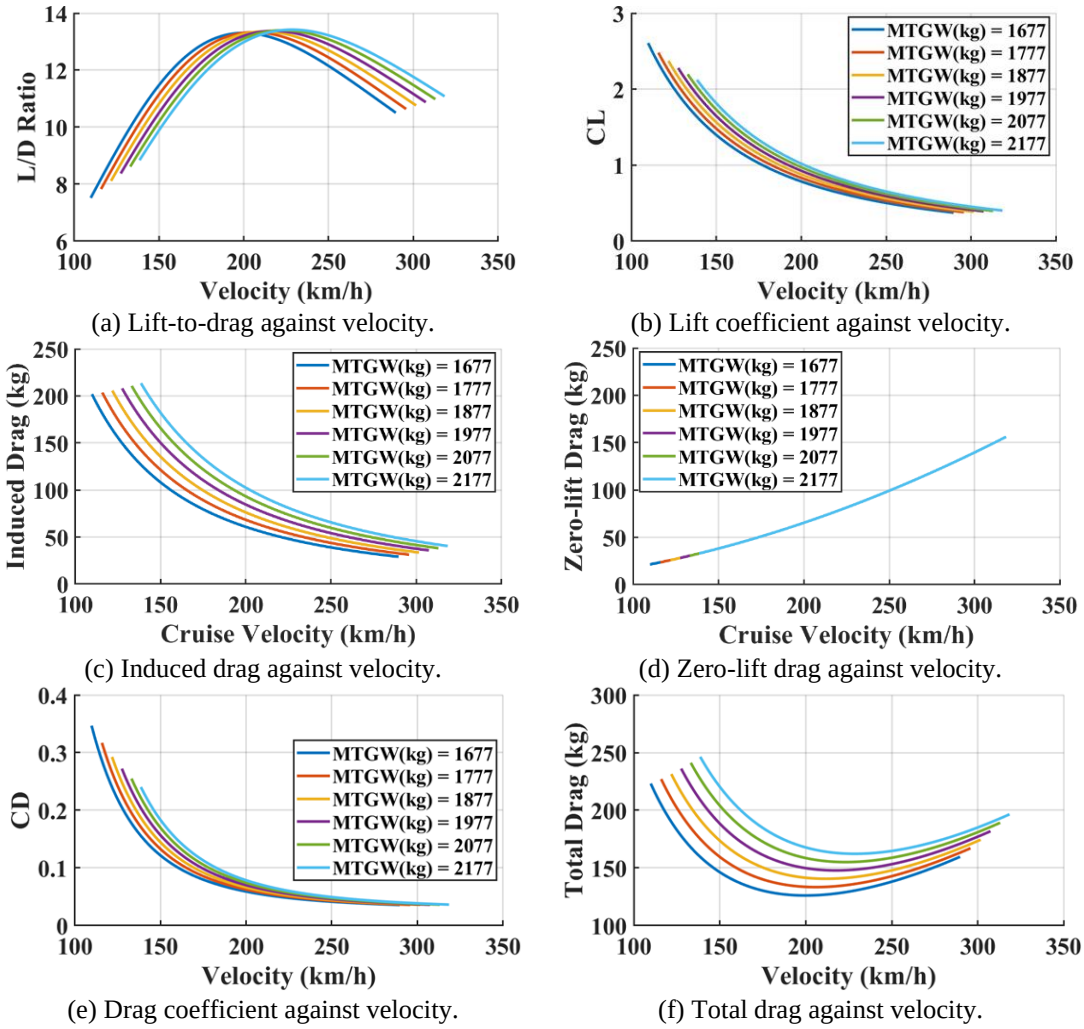

(a) Lift-to-drag against velocity.

(b) Lift coefficient against velocity.

(c) Induced drag against velocity.

(d) Zero-lift drag against velocity.

(e) Drag coefficient against velocity.

(f) Total drag against velocity.

Figure 4.13: Aerodynamic lift and drag plot for eVTOL (B) at different MTGW.

Figure 4.13 (e) and (f) illustrates the variation in drag coefficient and total drag against velocity at different MTGW for eVTOL (B). As velocity increases, the curves for both C_D and total drag converge, aligning with the theoretical understanding of drag behavior. Specifically, the left side of the drag curve, dominated by induced drag, is highly sensitive to weight changes, while the right side, dominated by parasite drag, exhibits minimal sensitivity to weight. This theory underpins the observed behavior, where the induced drag diminishes at higher velocities, making parasite drag the primary contributor. Additionally, the observed increase in $\vec{V}_{\text{br}}$ with higher MTGW further supports the influence of weight on optimal cruise performance, consistent with theoretical predictions.

4.3.3 Flight Mission Energy and Power Results

Power Breakdown for each Flight Segment

The energy model compares the power requirements for different mission flight segments for each eVTOL at their MTGW. Figure 4.14 summarizes the power breakdown for each eVTOL. Hover flight segments require the most power, followed by cruise climb, with cruise requiring the least. For the eVTOLs with an MTGW of 3175 kg, vertical climb power requirements are five to six times greater than those for cruise. Thus, to maximize range performance, a typical eVTOL mission profile aims to maximize time spent in cruise and minimize time in hover flight phases.

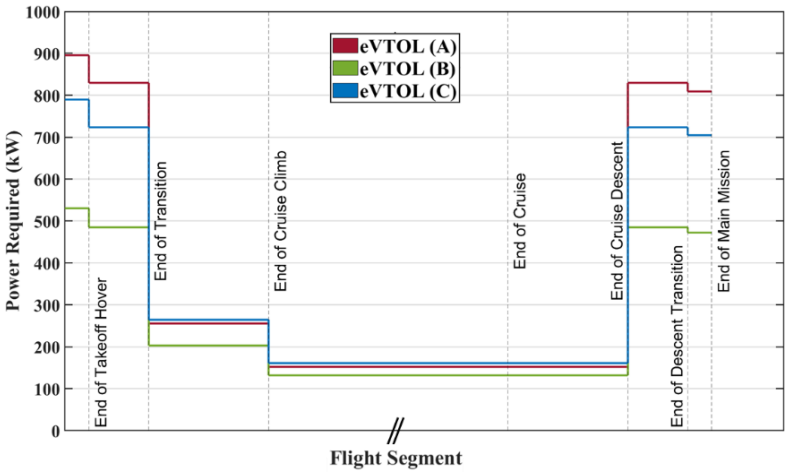

Figure 4.14: Main mission power breakdown for each flight segment at MTGW.
Note that the cruise segment has been truncated to better reflect the mission power required results.

Comparing the three aircraft, eVTOL (B), with the lowest MTGW, has the lowest power requirements in all flight segments, highlighting the importance of weight reduction in achieving power savings. Among models with the same MTGW, eVTOL (A) performs better in cruise, whereas eVTOL (C) excels in hover, consistent with results from the rotary wing and drag models.

Energy Breakdown for each Flight Segment

The energy breakdown for each aircraft at MTGW, to achieve maximum range, depends on the power required and the duration of each flight segment. Table 4.18 compares the duration and proportion of energy used in the main and reserve missions for each eVTOL until its battery is fully depleted. On average, 85% of the mission time is spent in the main and reserve mission cruise phases for all three eVTOLs. However, eVTOL (B) demonstrates a 3% increase in cruise energy usage during the main mission

compared to eVTOL (A) and a 0.4% increase compared to eVTOL (C). Additionally, eVTOL (B) uses 1.2% less energy in vertical flight main mission segment than eVTOL (A) and 0.2% less than eVTOL (C). These improvements highlight the efficiency of eVTOL (B) in terms of energy allocation between vertical and cruise phases, while eVTOL (A) shows the highest energy consumption in the vertical flight segments. Such comparisons highlight the performance variations across different configuration and help in understanding the operational efficiency of each eVTOL model.

Table 4.18: Duration and segment percentage in vertical and cruise flight segments.

Parameter	eVTOL (A)	eVTOL (B)	eVTOL (C)
MTGW (kg)	3175	2177	3175
Total Energy (kWh)	230	230	230
Vertical Flight - Main Duration (s)	424	424	424
Vertical Flight - Main Energy (%)	9.8	8.6	8.8
Cruise - Main Duration (s)	3708	3003	3575
Cruise - Main Energy (%)	74.6	76.8	76.3
Vertical Flight - Reserve Duration (s)	184	184	184
Vertical Flight – Reserve Energy (%)	8.2	6.9	7.2
Cruise - Reserve Duration (s)	371	300	358
Cruise - Reserve Energy (%)	7.5	7.7	7.6

Figure 4.15 presents a comparison of the energy expended in different vertical flight phases. The transition phase consumes the most energy, followed by the vertical portion of cruise climb and hover landing. Takeoff hover, despite having the highest power requirement, uses the least energy due to its short duration. Among the three aircraft, eVTOL (B), with the highest hover efficiency, expends the least energy in vertical flight.

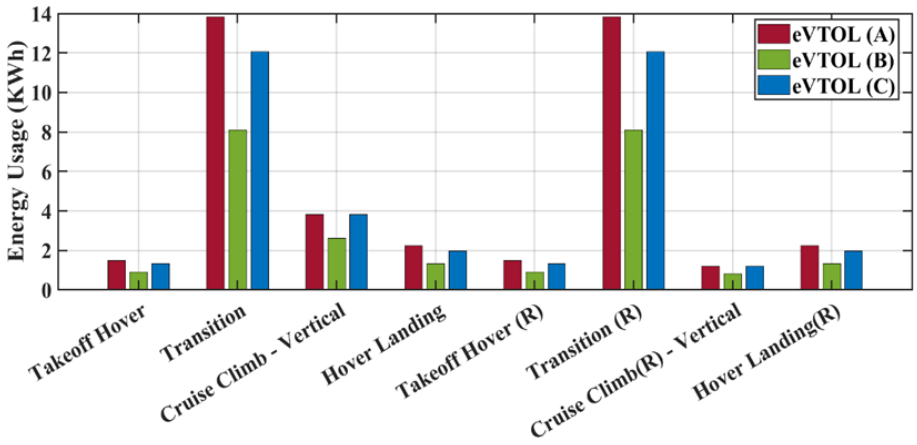

Figure 4.15: Breakdown of energy usage for vertical flight phases, excluding cruise.

Achievable Mission Range Comparison

The energy model estimates the achievable main mission range for each eVTOL at different MTGW. Excluding the cruise segment, the time spent in each flight segment is assumed to be the same for all eVTOLs. Cruise time is determined based on the rotary wing and drag models' results and user-defined battery capacity.

Figure 4.16 compares the main mission range results for each eVTOL at different MTGWs, based on passenger occupancy with each person weighing 100 kg. The main mission range depends on aerodynamic efficiency, battery energy, and eVTOL mass. At their baseline MTGW, all three aircraft have similar ranges of averaging at 219.2 km, with ranges of 230.1 km, 216.5 km and 210.9 km for eVTOL (A), (B) and (C) respectively. A 100 kg decrease in mass increases attainable range by approximately 10 to 15 km.

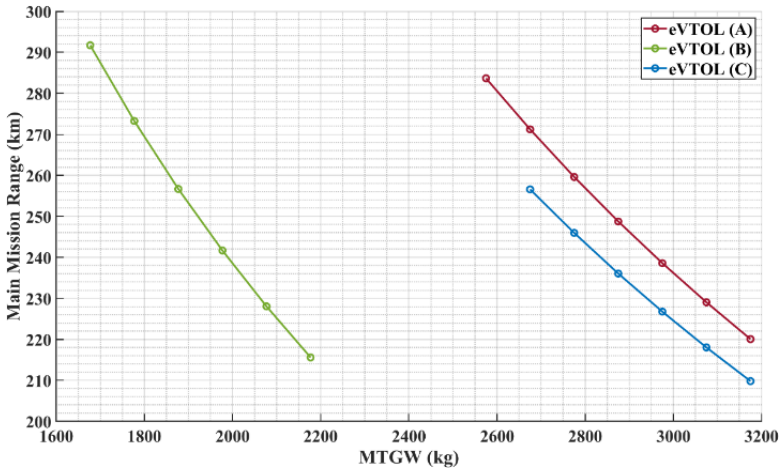

Figure 4.16: Main mission range against MTGW using energy model.
Available battery energy used are 160kWh for eVTOL (B), and 230 kWh for eVTOL (A) and (C).

Figure 4.17 projects the total battery energy needed for each eVTOL at MTGW to travel the specified main mission range with sufficient reserves. At a range of zero kilometers, the battery energy required reflects the hover efficiency of each eVTOL. The total battery energy needed is similar between eVTOL (A) and (C) for both intracity and intercity ranges. eVTOL (B), with the lowest MTGW, requires the least battery energy.

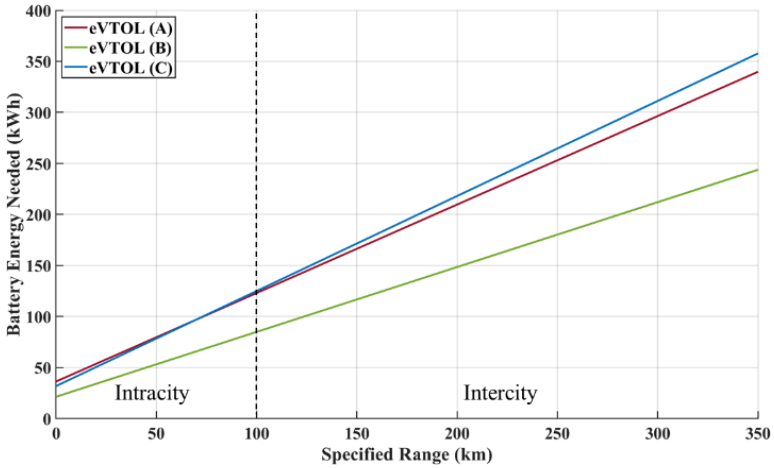

Figure 4.17: Projected battery energy needed against range.

4.4 Summary

This chapter has outlined a comprehensive analysis methodology comprising three primary modules: the rotary wing module, the drag module, and the energy module. These modules, developed using a blend of empirical and theoretical equations, form a robust performance analysis tool tailored for eVTOL aircraft. The tool's validity was reinforced through comparative modeling of eVTOL aircraft data published by leading industry players, including Archer Aviation's Maker and Joby Aviation's S4. By simulating these aircraft based on publicly available specifications and estimated dimensions, the tool produced results closely aligned with the performance figures reported by the manufacturers. This alignment demonstrates the tool's reliability and accuracy in evaluating eVTOL configurations, despite inherent uncertainties in input parameters.

The analysis of hover performance revealed that eVTOL (B), with the lowest MTGW of 2177 kg, exhibited superior hover performance, requiring 40.8% and 33.6% less power as compared to eVTOL (A) and (C) across hover, vertical climb, and vertical descent phases. This underscores the critical importance of minimizing aircraft weight to enhance hover efficiency. In contrast, eVTOL (A), despite sharing a similar MTGW with eVTOL (C), required the most power in hover due to its higher rotor disk loading, emphasizing the impact of rotor disk loading on hover performance.

In terms of cruise performance, eVTOL (A) demonstrated the highest L/D ratio of 14.4, indicating superior aerodynamic efficiency in cruise flight. Despite being less

aerodynamically efficient, eVTOL (B) required 13.3% and 18.1% less power to cruise as compared to eVTOL (A) and (C) at the fastest optimal velocity of 63.5 m/s due to its lower weight, highlighting the importance of weight reduction in cruise performance. The energy utilization analysis identified hover flight segments as the most power-intensive, whereas cruise segments were the most energy-efficient. eVTOL (B) had the lowest energy requirements across all flight segments due to its lighter weight, reinforcing the role of weight reduction in enhancing energy efficiency.

The achievable mission range for all three eVTOLs at their baseline MTGW averages at 219.2 km, with eVTOL (A) having 5.9% and 8.3 % more range than eVTOL (B) and (C). A reduction in weight was shown to significantly increase the range, with every 100 kg decrease in mass resulting in a 10 to 15 km increase. For both intracity and intercity ranges, eVTOL (B) required the least battery energy, reflecting its overall efficiency due to lower weight. The battery energy needed for eVTOL (A) and eVTOL (C) was similar, aligning with their comparable MTGW and energy consumption profiles.

The study concluded that the tiltrotor configuration outperformed the Lift + Cruise and Lift + Tiltrotor configurations, primarily due to its lower weight. This finding underscores the paramount importance of weight reduction in achieving superior performance in eVTOL aircraft. The results provide valuable insights for the design and optimization of future eVTOL aircraft, highlighting that while aerodynamic efficiency is crucial, weight reduction plays a more significant role in improving hover and cruise performance, energy efficiency, and mission range.

Chapter 5: Transition Flight Mode Analysis

This chapter introduces a transition mode model for transition climb and descent, incorporating aircraft trim conditions, a trajectory model, and blade-element momentum theory to enhance the characterization of transition mode. It also includes a detailed investigation and comparison with actual eVTOL aircraft. The chapter follows the flow diagram in Figure 5.1.

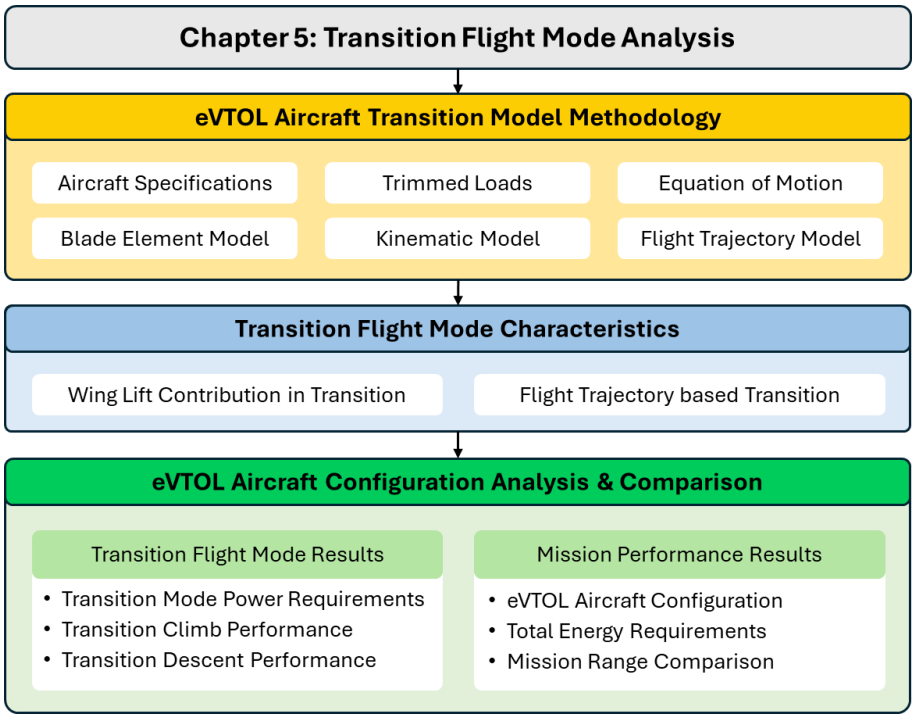

Figure 5.1: Chapter 5 - outline and flow diagram.

Challenges in Transition Flight

During the transition segment of eVTOL flight, there are two main types of transition trajectories: unlevelled and levelled, as illustrated in Figure 5.2 (a) and (b). In the unlevelled transition, the aircraft pitches its nose downward to gain forward speed before tilting its front rotors forward, similar to helicopters and multicopters, In the levelled transition, the aircraft maintains a level fuselage while tilting the front rotors forward to accelerate.

Each eVTOL aircraft has a specific transition corridor for converting from hover to forward flight, influenced by its design and power requirements. Throughout the transition, kinematic properties and aerodynamic forces change continuously. Due to variations in eVTOL designs, such as tiltrotors or different rotor/propeller configurations, the optimal transition trajectory from hover to cruise is unique for each aircraft. The two main parameters in the transition regime are power requirements and desired trajectory. Investigating the transition behavior for different eVTOL configurations is essential to determine the optimal transition trajectory and to optimize motor and energy system sizing based on the required power.

(a) Unlevelled transition trajectory.

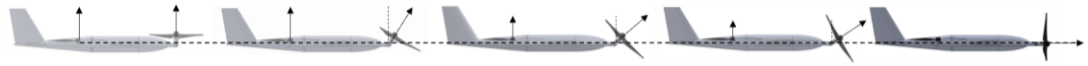

(b) Levelled transition trajectory.

Figure 5.2: Different types of eVTOL transition trajectories.
(a) Aircraft loses altitude during transition phase due to unbalanced forces in the vertical axis, from the saturation of motor power or the rapid rotation of tiltrotors. (b) Aircraft maintains current altitude during the transition phase with forces balanced in the vertical axis. This involves balancing of vertical forces with the horizontal acceleration.

Hence, eVTOL aircraft trajectories are essential for certification, impacting urban operations and vertiport requirements by regulating take-off and landing flexibility and influencing power and energy needs during missions. In 2023, EASA outlined technical requirements in the Special Condition VTOL document [60–62], setting performance objectives for basic and enhanced categories, including various take-off profiles shown in Figure 5.3. Trajectory analysis is necessary to determine operating trajectories for controlled emergency landings (CEL) and continued safe flight and landing (CSFL), as well as to define the funnel-shaped take-off volume and safety area to prevent collisions with obstacles. Furthermore, trajectory studies can address interferences such as obstacles and emergency landing scenarios, ensuring safety and operational efficiency.

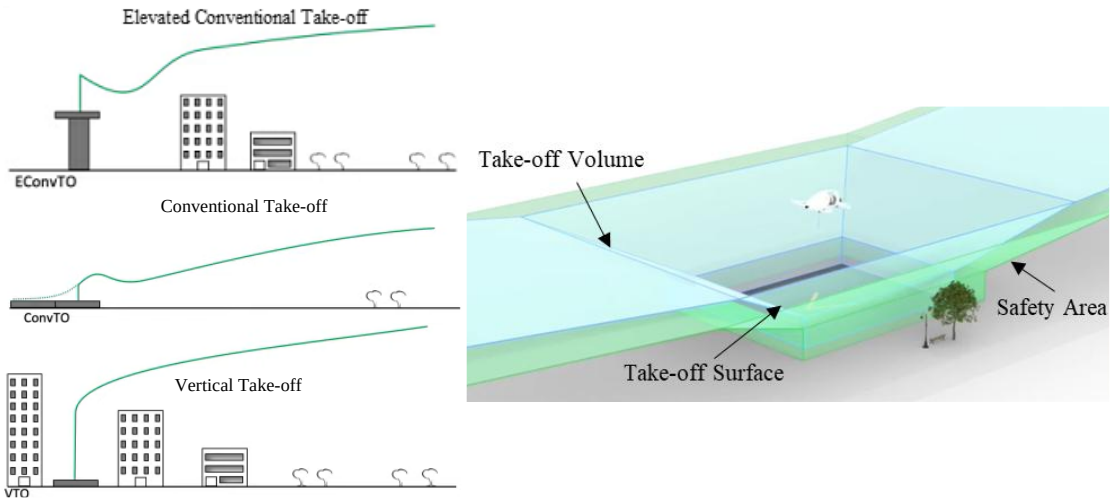

Figure 5.3: eVTOL certification requirements for take-off profiles and trajectory.
eVTOLs can execute several take-off profiles such as an elevated conventional take-off, conventional take-off and vertical takeoff with each profile following requirements for a dedicated take-off volume to ensure operational safety and clearance between obstacles in accordance with EASA [60–62].

5.1 Transition Model Methodology

The transition model consists of several modules designed to capture the different aspects of the transition flight phase of an eVTOL aircraft, are shown in Figure 5.4. These modules are developed in MATLAB as modular units, ensuring their applicability to various eVTOL aircraft types.

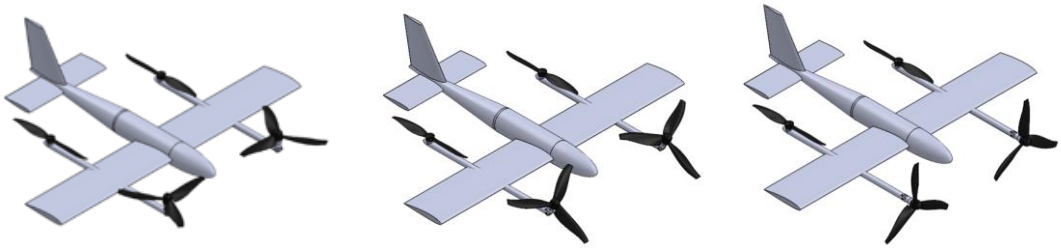

(a) Hover (τ_{90°) (b) Transition ($0° < \tau < 90°$) (c) Cruise (τ_{0°)

Figure 5.4: Aircraft in different stages of transition, where τ is the tilt shaft angle.
Generic Lift + Tiltrotor eVTOL aircraft with dual front tilting rotors and dual rear fixed rotors. At τ_{90°, aircraft is in hover flight using the vertical lift rotors. When τ is between 0° and 90°, aircraft transition between hover to cruise flight where the aircraft accelerates. At τ_{0°, cruise flight is achieved.

The analysis employs quasi-steady-state method to approximate unsteady aerodynamic effects by calculating the aerodynamic forces and moments at each instantaneous motion through incremental time segments during the mission's trajectory. For each time step, the changing angle of attack, velocities, and accelerations are used to determine the corresponding aerodynamic loads. This approach simplifies the analysis by assuming that aerodynamic forces and moments can be treated as steady within each

small-time increment, reducing computational complexity while still capturing the time-varying nature of the transition.

However, this quasi-steady-state assumption does not fully account for unsteady aerodynamic phenomena inherent in the transition maneuver, such as dynamic load variations, rotor wake interference, and transient flow separations induced by rotor tilt and acceleration. These complex interactions could underestimate transient power and load fluctuations during the transition phase that would introduce additional aerodynamic forces and moments that are not captured in this study. Despite these limitations, the method provides a practical and efficient framework for early-stage design evaluations, offering valuable insights into the overall transition performance with manageable computational demands.

In modelling the transition phase, the mission profile consolidates typical takeoff transition and cruise climb into a single transition climb phase, while merging cruise descent and descent transition into a transition descent phase, as illustrated in Figure 4.3. The aerodynamic modelling adheres to the steady-state formulation outlined in Section 4.1.5.

Figure 5.5 presents an outline of the modeling framework and the interconnections between its modules. The required input data includes the eVTOL aircraft mission parameters and specifications, such as aircraft geometry, dimensions, and airfoil properties. Additionally, the framework defines the trajectory model and system parameters, incorporating the trajectory function along with inertia and efficiency parameters. The computational modules encompass the kinematic model, rotor aerodynamics, wing aerodynamics, and trim module, collectively used to determine the aircraft's motion and forces. The outputs are then processed through the transition mode performance model, enabling the visualization of key parameters, including aerodynamic characteristics, power and energy requirements, thrust values, and the overall trajectory.

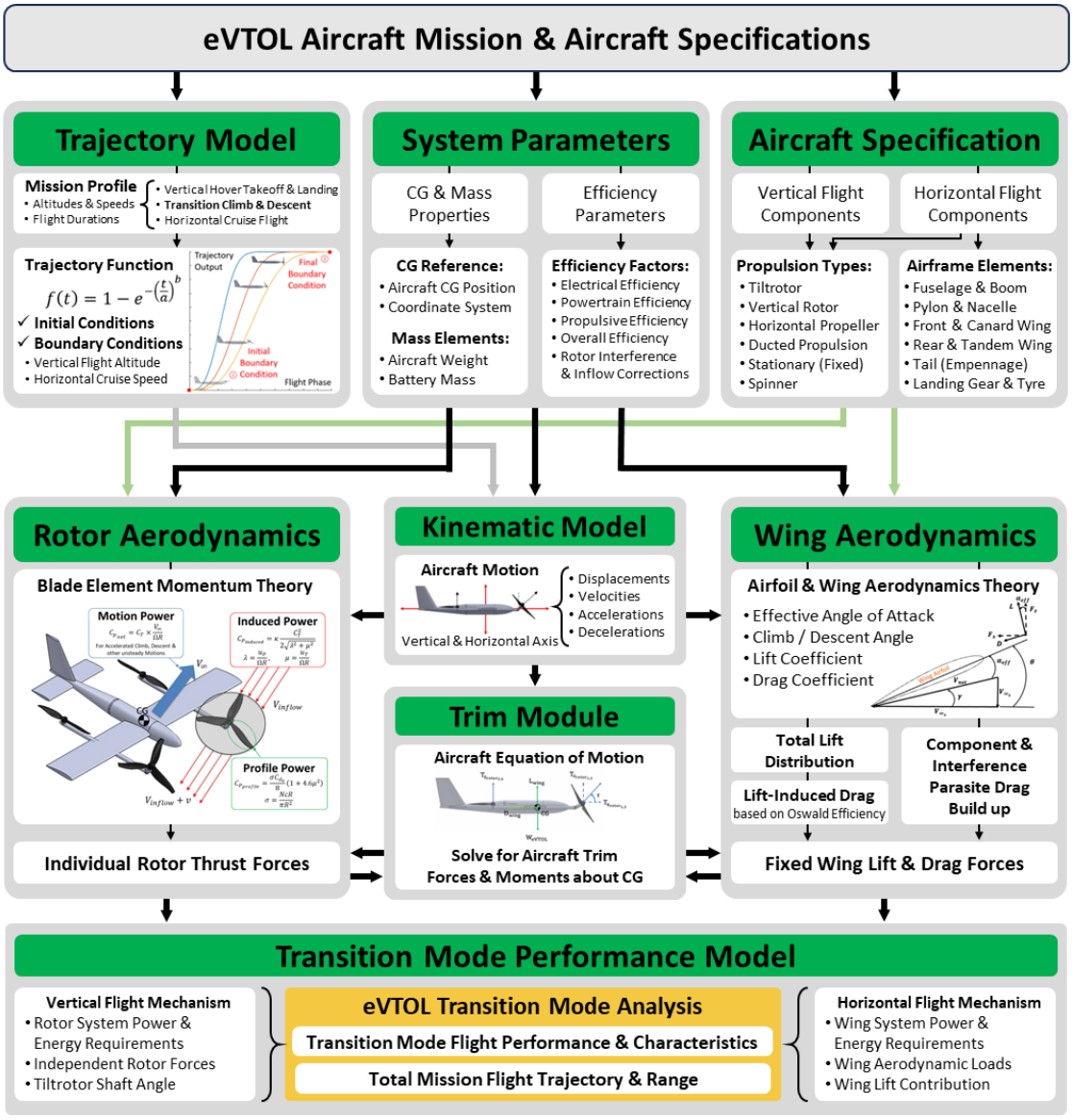

Figure 5.5: eVTOL aircraft transition mode analysis framework.

5.1.1 Power Required Model

The power required model in this study is based on the well-established Blade Element Momentum Theory (BEMT) from Helicopter Theory [180]. BEMT combines the Blade Element Method, which accounts for rotor blade properties such as the number of blades, rotor tip speed, and blade drag coefficient, with Momentum Theory, or Actuator Disk method, which estimates the inflow through the rotor disk. This provides an efficient means of calculating induced and profile power for each blade element across the rotor span. Additionally, the BEMT framework used in this analysis includes adjustments for motion power to account for maneuvers during the transition flight

phase, providing a reasonable approximation of the power required for various operating conditions. This analysis does not include a rotor wake model, which would capture detailed wake interactions and rotor-airframe interference effects. The exclusion of a rotor wake model limits the ability to accurately simulate wake dynamics and their impact on power consumption and performance during transition. Despite this limitation, BEMT offers a robust and computationally efficient approach for early-stage design and comparative studies of eVTOL configurations.

The assumed values used in the BEMT model are derived from existing aircraft and rotorcraft data, as shown in Table 5.1. The rotor tip speed, set at 600 ft/s (Mach 0.53), balances considerations of noise, drag, and stall effects. Other parameters and correction factors are based on typical values for fixed- and rotary-wing aircraft, as covered in Section 4.1.2. While these values provide a reasonable basis for early-stage analysis, their sensitivity to variations can impact the accuracy of the performance predictions. For example, changes in rotor tip speed or loss factors can alter the power requirements and aerodynamic efficiency. Therefore, the use of constant or simplified assumptions introduces uncertainties. To mitigate this, sensitivity studies could be conducted to assess the robustness of the results and to quantify the potential range of outcomes based on variations in these key parameters.

Table 5.1: Input analysis parameters and applied assumptions.

Parameter	Value	Condition
Rotor Tip Speed Ω (m/s)	183	Constant speed
Rotor Blade Drag Coefficient C_{blade,d_o}	0.012	Constant value
Non-uniform Inflow Losses Factor κ_{inflow} (%)	9.0	Correction factor
Tip Losses Factor κ_{tip} (%)	3.0	Correction factor
Swirl Losses Factor κ_{swirl} (%)	3.0	Correction factor
Oswald Efficiency e	0.75	Constant value
Electrical Efficiency $\eta_{\text{electrical}}$	0.90	Constant value
Propulsive Efficiency $\eta_{\text{propulsive}}$	0.85	Constant value

Due to the diverse eVTOL configurations, rotor blade designs and properties vary significantly. To generalize the applicability of BEMT for different eVTOL aircraft, this model assumes a uniform untwisted rectangular blade in the blade element calculations. Despite this assumption, BEMT provides a more accurate power requirement estimation compared to momentum theory. BEMT allows for better accountability of the power requirements for eVTOL aircraft rotor systems, which may have rotors of different dimensions, numbers of blades, or blade profiles, thereby increasing the fidelity of the power calculations. In this study, BEMT is used to calculate the power requirements for

both vertical and horizontal propulsors. For rotor components, vertical thrust is determined by the distributed weight of the aircraft; for propeller components, horizontal thrust is determined by the drag generated by the eVTOL aircraft.

The total power required can also be expressed as a normalized value as shown in (5.1) and (5.2), where P_{req} represents the total power required, P_{induced} is the total induced power, P_{profile} is the total profile power, and P_{net} is the total motion power. It should be noted that parasite power is not explicitly accounted for in the power required module. In conventional helicopter theory, parasite power represents the power required to overcome the drag of non-lifting components such as the fuselage. However, in this study, the aerodynamic model already incorporates the parasite drag contributions for various aircraft components, including the fuselage, nacelles, and landing gear, through a cumulative drag coefficient obtained via the component build-up method, as detailed in (5.15). To ensure consistency and prevent double-counting, the parasite drag term from BEMT, which introduces its own simplified fuselage drag term, is omitted in the power calculation. This approach allows for a more accurate and comprehensive accounting of drag forces, leveraging the higher fidelity aerodynamic model to provide a detailed breakdown of drag contributions across all components. By integrating the parasite drag directly into the aerodynamic model, the study ensures that all drag effects are appropriately considered without redundancy, which enhances the accuracy of the power and performance predictions.

$$P_{\text{req}} = P_{\text{induced}} + P_{\text{profile}} + P_{\text{net}} \tag{5.1}$$

The normalized power required, denoted as C_P, comprises of the area of the rotor disk πR^2, the density ρ, and the rotor tip speed Ωr, as shown in (5.2).

$$C_P = C_{P_{\text{induced}}} + C_{P_{\text{profile}}} + C_{P_{\text{net}}} \text{ where } C_P = \frac{P_{\text{req}}}{\pi r^2 \rho (\Omega \text{r})^3} \tag{5.2}$$

The normalized induced power in (5.4) accounts for non-uniform inflow distribution and tip losses using an empirical correction factor κ. A value of 1.15 is set for the correction factor κ, with the breakdown shown in Table 5.1. As normalized values are used for the velocity component, such as the inflow ratio λ and the advance ratio μ, the induced power and thrust generated are also normalized. The normalized thrust is denoted as C_T in (5.4).

$$C_{P_{\text{induced}}} = \kappa \frac{C_T^2}{2\sqrt{\lambda^2 + \mu^2}} \tag{5.3}$$

$$C_T = \frac{T}{\pi r^2 \rho (\Omega \text{r})^2} \tag{5.4}$$

The normalized profile power, denoted as $C_{P_{\text{profile}}}$ in (5.5), is modified to account for radial flow and reversed flow effects. To account for the normalized profile power, rotor solidity σ and blade airfoil drag coefficient C_{d_0} are considered. Rotor solidity σ, is the ratio of the area of the rotor blades to the area of the rotor disk. To account for rotor solidity, the number of rotors N, the chord length of the rotor blade c, and the radius of the rotor r are considered, as shown in (5.6).

$$C_{P_{\text{profile}}} = \frac{\sigma C_{d_0}}{8}(1 + 4.6\mu^2) \tag{5.5}$$

$$\sigma = \frac{Ncr}{\pi r^2} \tag{5.6}$$

The normalized net power, denoted as $C_{P_{\text{net}}}$ in (5.7), for the unsteady motions of the aircraft is formulated similarly to the induced power, where V_{net} is the velocity in the motion axis. These motions include accelerated climb, descent, and other unsteady behavior during the aircraft flight phase.

$$C_{P_{\text{net}}} = \frac{T}{\pi r^2 \rho (\Omega R)^2} \times \frac{V_{\text{net}}}{\Omega \text{r}} = C_T \lambda_{\text{net}} \tag{5.7}$$

5.1.2 Trimmed Force and Moment Model

Aircraft Reference Coordinate System

One of the main elements required for power calculation, as seen in Figure 5.5, is the thrust force generated by each individual rotor or propeller. During the transition segment, the thrust force constantly changes depending on the flight condition of the aircraft at any given time. Moreover, different eVTOL configurations have varied rotor layouts and positions, affecting how thrust and moment loads are distributed across the entire rotor system.

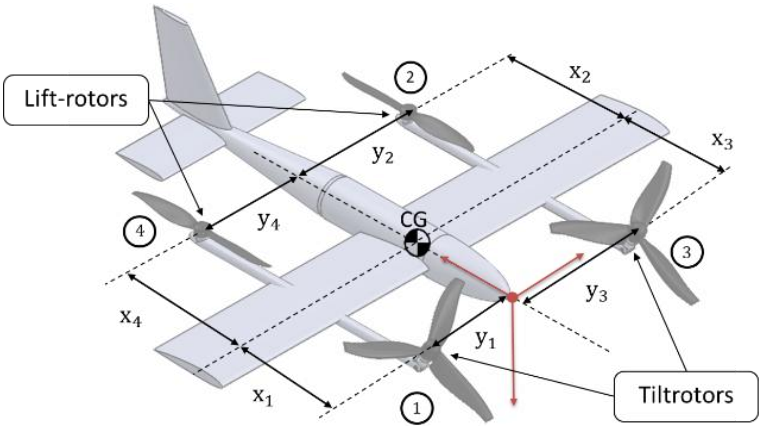

Figure 5.6: Aircraft coordinate system and rotor location from CG.
Individual rotors are placed and positioned based on their x and y distances from the CG.

To generalize the rotor configuration, a defined coordinate system with the specified CG of the eVTOL aircraft is used. This allows for the study of different rotor numbers and layouts. The general coordinate system is derived with respect to the nose of the aircraft, as shown in Figure 5.6. The sign convention for this coordinate system is indicated, which helps determine the direction of loads during the calculation of trimmed forces and moments.

Generalized eVTOL Aircraft Equation of Motion

Using the general coordinate system for rotor locations and the CG, the thrust and moment generated by each rotor relative to the CG can be calculated, as illustrated in Figure 5.7. Under the quasi-steady-state assumption, the forces and moments are formulated in equilibrium. The individual force balance equations for each axis are given in (5.8), where F_x, F_y and F_z are the forces in the x, y, and z axes. The thrust tilt angle τ is either a variable for tiltrotors or equals to zero for fixed / stationary rotors.

$$F_x = \sum T_{x_{\text{rotor}_i}} \cos\tau \ , \qquad F_y = \sum T_{y_{\text{rotor}_i}} \sin\tau \ , \qquad F_z = \sum T_{z_{\text{rotor}_i}} \tag{5.8}$$

where $T_{\text{axis rotor}_i}$ is the thrust in each axis and i is the index of each rotor.

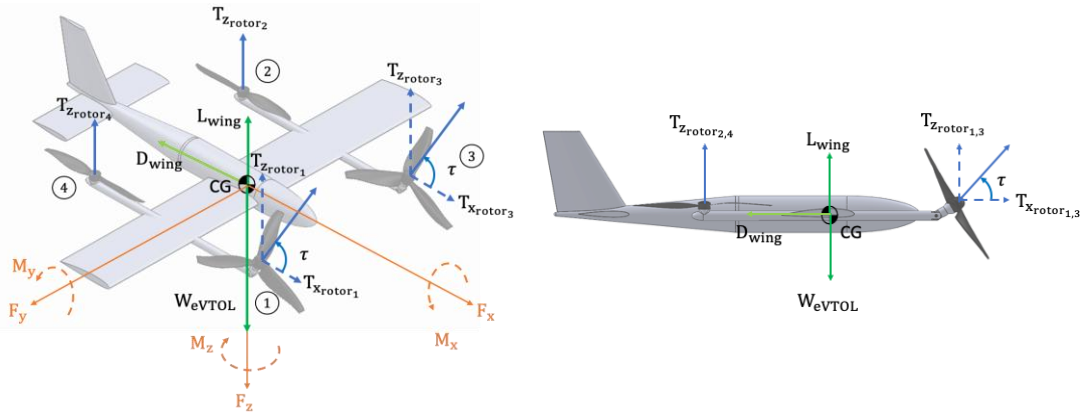

Figure 5.7: Modelling and free body diagram for the generic eVTOL aircraft.
Forces and moments are determined from the equilibrium of the vertical and horizontal forces, and pitching moments generated by the individual rotor and wing aerodynamic forces.

The moment balance about the CG is calculated using the matrix in (5.9), where M_{x_i}, M_{y_i} and M_{z_i} are the moments about the x, y, and z axes and i is the index of each rotor. In this study, symmetry is applied along the X-Z plane, with no unbalanced forces acting along the y-axis, thus $F_y = \sum T_{y_{\text{rotor}}} = 0$.

$$\begin{bmatrix} M_{x_i} \\ M_{y_i} \\ M_{z_i} \end{bmatrix} = \begin{bmatrix} T_{x_{\text{rotor}_i}} \\ T_{y_{\text{rotor}_i}} \\ T_{z_{\text{rotor}_i}} \end{bmatrix} \times \begin{bmatrix} X_{\text{cg}} - X_{\text{rotor}_i} \\ Y_{\text{cg}} - Y_{\text{rotor}_i} \\ Z_{\text{cg}} - Z_{\text{rotor}_i} \end{bmatrix} \tag{5.9}$$

Aerodynamic Forces and Moments

In addition to rotor forces and moments, aerodynamic forces and moments acting on wing surfaces are accounted for using two-dimensional airfoil theory with airfoil elements along the wingspan. The velocity components and respective angles are shown in Figure 5.8 to determine the aerodynamic forces acting on the airfoil. The airfoil pitch angle θ is measured from the inertial frame axis to the body frame axis of the airfoil. As the aircraft translates horizontally and vertically, additional velocity components act on the airfoil from horizontal and vertical velocity components V_{∞_x} and V_{∞_z}, respectively.

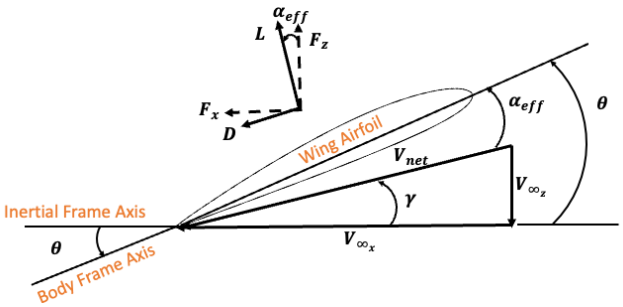

Figure 5.8: Velocity components and aerodynamic forces on the wing airfoil. Referenced in both the inertial and body frame.

This results in a resultant velocity V_{net} with an induced angle γ, known as the aircraft climb angle, calculated using (5.10). The airfoil is thus at an effective angle of attack, α_{eff}, which is the difference between pitch angle θ and climb angle γ calculated using (5.11). Here, V_{∞_x} and V_{∞_z} are the freestream velocities in the x and z axes. The effective angle of attack α_{eff} is used to determine the lift and drag forces.

$$\gamma = \tan^{-1}\frac{V_{\infty_z}}{V_{\infty_x}} \tag{5.10}$$

$$\alpha_{\text{eff}} = \theta - \gamma \tag{5.11}$$

$$\text{V}_{\text{net}} = \sqrt{V_z^2 + V_x^2} \tag{5.12}$$

Lift and drag forces are calculated according to (5.13) and (5.14), respectively. These forces are functions of the resultant velocity V_{net}, air density ρ, wing area S, and the lift and drag coefficients C_L and C_D. As the effective angle of attack α_{eff} changes with pitch angle θ and climb angle γ, it affects the lift coefficient C_L and drag coefficient C_D, which are functions of α_{eff}. The drag coefficient C_D comprises two components: the parasite drag coefficient C_{D_0} and the induced drag coefficient C_{D_i}, as shown in (5.15).

$$L_{\text{wing}} = \frac{1}{2}\,\rho\, V_{\text{net}}^2\, S\, C_{L_\alpha}\, \alpha_{\text{eff}} \tag{5.13}$$

$$D_{\text{wing}} = \frac{1}{2}\,\rho\, V_{\text{net}}^2\, S\, (C_{D_\alpha}\, \alpha_{\text{eff}} + C_{D_{\text{fuselage}}}) \tag{5.14}$$

The induced drag coefficient C_{D_i} is a function of the aspect ratio AR and Oswald efficiency, e taken to be 0.75 as defined in Section 4.1.2. Experimental data from Delft is used to account for the wide range of angles of attack for lift and drag coefficients [191]. Figure 5.9 shows the lift coefficient C_L and drag coefficient C_D for angles of attack α between 0° and 360°. For this study, extrapolated C_L and C_D values are used for the range of angles of attack α between −90° and +90°.

$$\sum C_{D_\alpha} = C_{D_0} + C_{D_i} = C_{D_0} + k\left(C_{L_\alpha}\alpha_{\text{eff}}\right)^2 \text{ where } k = \frac{1}{\pi\, e\, AR} \tag{5.15}$$

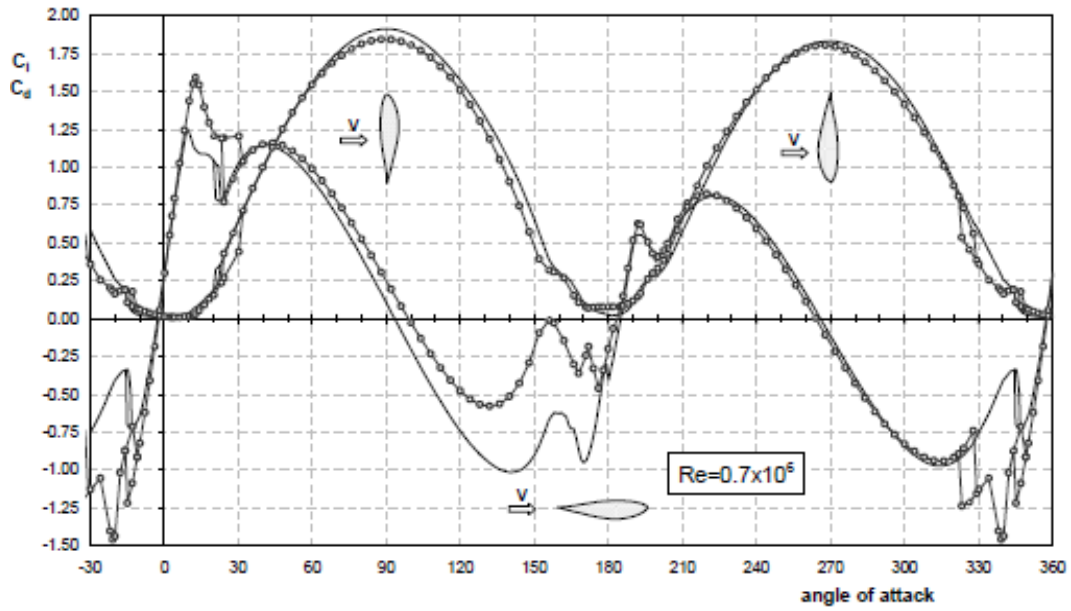

Figure 5.9: DU 96-W-180 airfoil lift and drag coefficients between α = 0° to 360°. Upper smooth line represents the airfoil drag coefficient and the lower uneven line with the stall region represents the airfoil lift coefficient [191].

5.1.3 Kinematic and Trajectory Model

General Kinematic Equations for Modelling

The transition segment of an eVTOL aircraft is dynamic and transient, unlike the cruise and hover segments that are typically evaluated under steady conditions. During the transition, velocities and accelerations change continuously. Therefore, the equation of motion derived from the trim matrix alone is insufficient without a kinematic model to

define the aircraft's trajectory. Using Newton's second law, as shown in (5.16), the force is a function of acceleration for a given mass along each axis, whereby $\sum\overrightarrow{F_i}$ and $\overrightarrow{a_i}$ are the resultant force and acceleration in each axis. Thus, the acceleration component is necessary to determine the instantaneous forces and moments required to balance the eVTOL aircraft.

$$\sum\overrightarrow{F_i} = m_{\text{eVTOL}}\overrightarrow{a_i} \tag{5.16}$$

In the vertical axis, the aircraft starts at a vertical displacement s_z for the given trajectory, representing the flight altitude. The vertical velocity V_z and vertical acceleration a_z are determined using:

$$V_z = \frac{ds_z}{dt}, \qquad a_z = \frac{dV_z}{dt} \tag{5.17}$$

Similarly, in the horizontal axis, the aircraft starts with a horizontal velocity V_x for a given trajectory, representing the flight velocity. The horizontal acceleration a_x and horizontal displacement s_z are determined using:

$$a_x = \frac{dV_x}{dt}, \qquad s_x = \int V_x\, dt \tag{5.18}$$

Trajectory Parabolic Function

The applicability of the trajectory parabolic function stems from its simplicity and effectiveness in modeling smooth, continuous transitions between two states, such as vertical climb to the desired altitude and horizontal acceleration to cruise speed during the transition phase, as shown in Figure 5.3. This function models key operational parameters and captures the gradual change in both altitude and velocity, offering a practical approach to simulating the transition dynamics and estimating power and energy consumption while ensuring compliance with regulatory guidelines for smooth and controlled transitions, minimizing abrupt changes in flight dynamics.

Furthermore, the function considers physical aircraft constraints, ensuring that the flight trajectory avoids urban obstacles and adheres to restricted airspace requirements, where straight level transitions or direct vertical climbs may not be feasible due to limited space or height restrictions. By modeling gradual climb and acceleration, the trajectory facilitates safe and compliant navigation through urban environments, meeting

operational safety standards and minimizing risks in crowded airspaces. Thus, this approach offers both a practical power/energy analysis and a viable trajectory for integrating eVTOLs into urban air mobility systems.

The parabolic function $f(t)$ in (5.19) represents the vertical translation s_z or horizontal velocity V_x as a function of time t. This approach ensures a smooth trajectory that reflects the gradual acceleration to cruise speed and climb to the desired altitude, as illustrated in Figure 5.10. The coefficients a and b are critical in shaping the curve to match the desired transition profile. In this study, coefficient a is varied to explore its impact on transition dynamics, particularly on the gradient of the trajectory curve, while coefficient b is held constant at 3 for consistency.

$$f(t) = 1 - e^{-\left(\frac{t}{a}\right)^b} \tag{5.19}$$

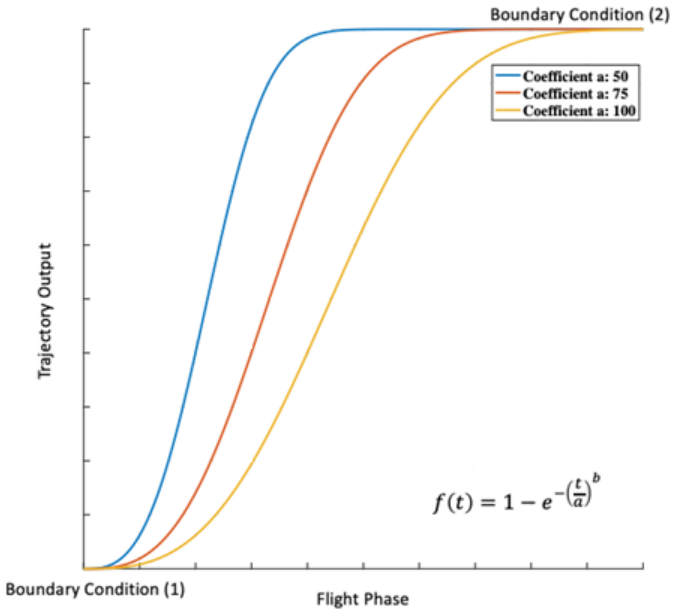

Figure 5.10: Trajectory function for vertical translation and horizontal velocity.
Steep trajectory is represented by blue line with a = 50, moderate trajectory is represented by red line with a = 75, and gradual trajectory is represented by yellow line with a = 100.

A moderate transition trajectory is used, with specific inputs for altitude and velocity given by (5.19) and detailed in Table 5.2. A cruising velocity of 70 m/s is selected, which falls within the typical range for an eVTOL aircraft between 69 to 91 m/s, based on published data [192, 193].

Table 5.2: Trajectory function coefficients for both transition takeoff and descent.
A standard linear glide trajectory is used for the non-vertical landing transition descent.

Flight Phase	Parameters	C_1	a	b
Transition Climb	Altitude	460	100	3
	Velocity	70	100	3
Transition Descent (Vertical Landing)	Altitude	460	110	3
	Velocity	70	143	3
Transition Descent (Non-vertical Landing)	Altitude	460	-	-
	Velocity	70	-	-

Two studies were conducted using the presented modeling modules on a generic full-size passenger carrying eVTOL aircraft with front tilting rotors and the inputs for the analysis are shown in Table 5.3. The aircraft model employed is the generic Lift + Tiltrotor model, as shown in Figure 5.4. The first study examined the ratio of lift contribution by the wing for various tilt angles of a tiltrotor, representing different types of eVTOL aircraft configurations. The second study investigated transition climb and descent based on the eVTOL aircraft trajectory. The purpose of these studies was to evaluate the performance of eVTOL aircraft under different conditions and trajectories.

Table 5.3: Input parameters for the generic eVTOL aircraft model.
Generic eVTOL has a dual tiltrotor with dual fixed rotor with various specifications and parameters.

Parameter	Generic Lift + Tiltrotor eVTOL Aircraft Model
Aircraft Mass m_{eVTOL} (kg)	3175
Wing Area (m^2)	26.76
Wing Aspect Ratio	8.41
Oswald Efficiency	0.75
Rotor Diameter (m)	3.91
Disk Solidity	0.115
Rotor Blade Drag Coefficient C_{d_0}	0.012
Rotor Tip Speed (m/s)	183
Fuselage Drag Coefficient $C_{d_{\text{fuselage}}}$	0.02
Max Rotor Thrust (N)	20000

5.2 Tilt Angle on Wing Lift Contribution

This section examines the influence of tilt shaft angle and flight velocity on the lift contribution ratio and power requirements of a generic eVTOL aircraft equipped with tilting front rotors in a straight and level transition between the vertical and horizontal flight phases. Understanding these factors is essential for analyzing the transitional flight characteristics of such eVTOL configurations.

The analysis assumes steady level horizontal flight without any climb or altitude change, thus vertical velocity and acceleration are not considered. Prop-wash and rotor-wing interference effects, which refer to the aerodynamic interaction between rotor outwash and downstream components, are assumed secondary and omitted due to the absence of

a rotor wake model. This simplification allows for a more streamlined aerodynamic analysis without introducing uncertainties from complex unsteady flow phenomena. Component interferences are addressed using the methods outlined in Section 4.1.5. Furthermore, the tail lift contribution is assumed negligible because the large tail moment arm enables the main wing to generate the majority of lift.

The test cases, as shown in Table 5.4, model different shaft angles for the front tilting rotors: (1) τ_{90° resembling a helicopter or multicopter, (2) τ_{60° and (3) τ_{30° resembling a tiltrotor aircraft, and (4) τ_{0° resembling a conventional airplane. The impact of tilt angle on wing lift contribution is discussed for each case. The lift contribution ratio is defined by (5.20), where L_{wing} is the lift generated by the wing and W_{eVTOL} is the aircraft weight:

$$\text{Wing lift contribution ratio} = \frac{L_{\text{wing}}}{W_{\text{eVTOL}}} \tag{5.20}$$

Table 5.4: Aircraft model with different tilt shaft angle for front tiltrotors.

Case	Shaft Angle τ	Illustration of Tiltrotor Shaft Angle Position	Configuration / Mode Type
1	τ_{90°	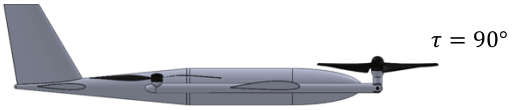	Multicopter (Vertical Flight)
2	τ_{60°	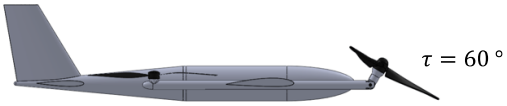	Tiltrotor (Transition Flight)
3	τ_{30°	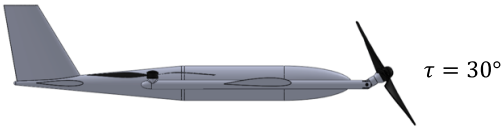	Tiltrotor (Transition Flight)
4	τ_{0°	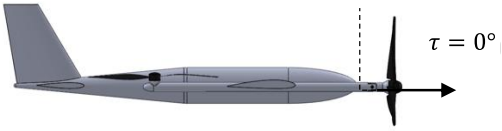	Airplane (Horizontal Flight)

5.2.1 Wing Lift Contribution Ratio

The lift contribution ratio by the wing is illustrated in Figure 5.11 (a). The blue line represents τ_{0°, the orange and yellow lines represent τ_{30° and τ_{60°, and the purple line represents τ_{90°. Up to 70 m/s, the lift ratio increases along a common curve following the lift curve slope governed by (5.13).

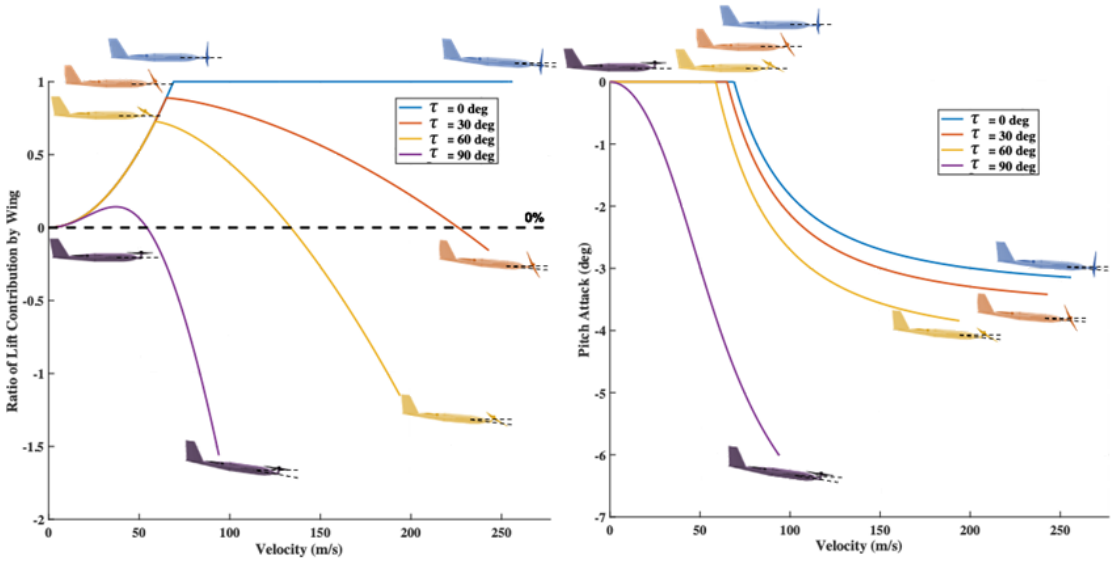

(a) Wing lift contribution ratio against velocity for different shaft angle.

(b) Pitch angle against velocity for different shaft angle.

Figure 5.11: Wing lift contribution and pitch angle against velocity.
Blue represents τ_{0°, orange represents τ_{30°, yellow represents τ_{60° and purple represents τ_{90°.

The pitch angle of the eVTOL aircraft, shown in Figure 5.11 (b) indicates the angle required for horizontal forward velocity, with a positive sign convection indicating a pitch-up motion. These results are used to evaluate the effects of tilt shaft angle and horizontal velocity on the wing lift contribution in an eVTOL aircraft. The following sections details the effect of the shaft angle, τ for each case.

Shaft Tilt Angle at τ_{90°

When the shaft tilt angle is at 90°, the wing lift contribution ratio initially increases with velocity before decreasing into the negative region, as illustrated in Figure 5.11 (a). At this angle, the aircraft operates in a manner similar to a helicopter or multicopter, maintaining a steady hover. In this state, the thrust generated by the front and back rotors must equal the weight of the eVTOL aircraft, as shown in Figure 5.12 (a) and mathematically represented by (5.21). The summation of the vertical thrust forces from all rotors equals the total weight of the eVTOL, keeping the aircraft stationary in hover.

$$\sum T_{z_{\text{rotor}_i}} = W_{\text{eVTOL}} \tag{5.21}$$

(a) Rotor forces in hover flight when $\tau_{90°}$. Four rotors provide vertical lift to balance the aircraft weight.

(b) Gaining horizontal motion as a multicopter, requires a pitching moment that rotates the aircraft to induce a horizontal force.

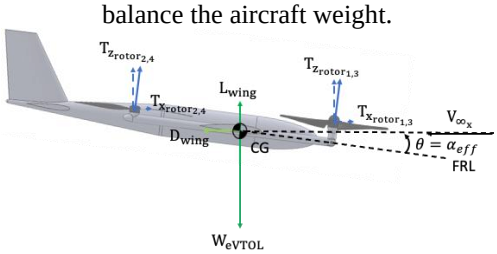

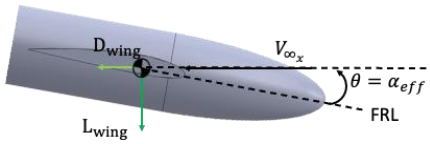

(c) Rotor and wing forces in horizontal motion for $\tau_{0°}$. Rotor forces are tilted forward to generate horizontal motion.

(d) Undesired aerodynamic forces consisting of a negative lift force caused by pitch angle in horizontal flight.

Figure 5.12: Aircraft forces and moments at $\tau_{90°}$ for horizontal motion.

To gain horizontal velocity, a typical helicopter or multicopter pitches forward, generating horizontal force and velocity as shown in Figure 5.12 (b). This forward pitching results in the wing surfaces producing both lift and drag forces during horizontal motion, as illustrated in Figure 5.12 (c). The balance of forces and moments is described as:

$$\sum T_{z_{\text{rotor}_i}} + L_{\text{wing}} = W_{\text{eVTOL}} \tag{5.22}$$

$$\sum T_{x_{\text{rotor}_i}} = D_{\text{wing}} \tag{5.23}$$

$$\sum T_{z_{\text{rotor}_i}} \times x_{\text{cg}_i} = 0 \tag{5.24}$$

Here, (5.22) represents the summation of vertical forces (thrust from rotors and lift from the wing) balancing the aircraft's weight. (5.23) describes the horizontal thrust forces from the rotors equating to the aircraft's drag. (5.24) ensures that the moments about the CG are balanced, allowing for steady level flight.

As the aircraft pitches further forward to increase horizontal velocity, the wing's airfoil encounters a negative angle of attack, as shown in Figure 5.12 (d). Although a positive camber on the airfoil can maintain a positive lift coefficient at lower negative angles of attack, high negative angles lead to a negative lift coefficient, causing the lift contribution to turn negative. This phenomenon results in a negative wing lift contribution ratio, limiting the aircraft's ability to achieve high forward velocity due to thrust limitations in counteracting negative lift. Figure 5.11 (b) shows the aircraft pitch angle increases drastically with greater horizontal velocity. A Lift + Cruise configuration with horizontal propulsors can overcome this limitation by enabling greater forward speeds without significant pitching. Therefore, eVTOL aircraft with

wing surfaces should be designed with an angle of incidence to mitigate large negative angles of attack during horizontal flight.

Shaft Tilt Angle at τ_{60° and τ_{30°

For shaft tilt angles at 60° and 30°, the wing lift contribution ratio initially increases but then decreases into the negative region, as shown in Figure 5.11 (a). At these angles, the aircraft functions similarly to a tiltrotor, achieving horizontal velocity without requiring a forward pitch attitude. This behavior occurs because the front tilting rotors, positioned at non-vertical angles, generate horizontal thrust components that drive forward motion. This forward motion produces aerodynamic loads on the wing, which reduce the vertical thrust demand from the rotors. For steady level forward flight, the forces and moments acting on the aircraft must still satisfy the equilibrium conditions defined by (5.22) to (5.24), ensuring a balanced system about the CG, as illustrated in Figure 5.13 (a) and (b).

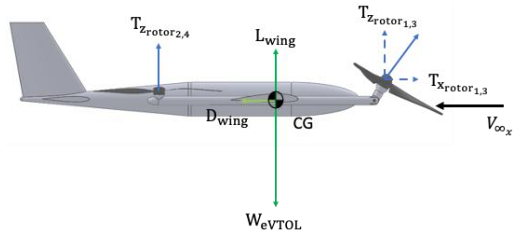

(a) Rotor and wing forces when τ_{60°. Total tiltrotor thrust is broken down into both vertical and horizontal components with greater vertical force to support aircraft weight.

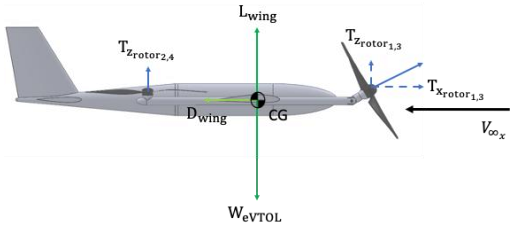

(b) Rotor and wing forces when τ_{30°. Total tiltrotor thrust is broken down into both vertical and horizontal components with greater horizontal force for horizontal motion.

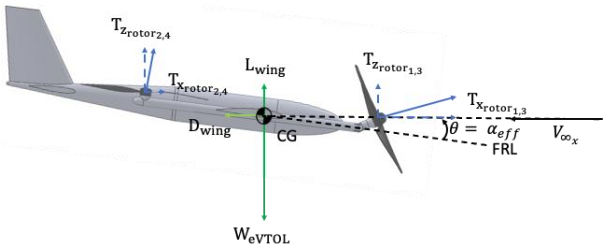

(c) Rotor and wing forces in horizontal motion for τ_{30°. With $\tau > 0°$ and increased aircraft pitch angle, enables the generation of greater horizontal forces and motion, providing greater wing lift contribution.

Figure 5.13: Aircraft forces and moments at τ_{60° and τ_{30° for horizontal motion.

For fixed shaft angles, increasing horizontal velocity still requires pitching forward, similar to τ_{0° as shown in Figure 5.13 (c). The pitch angles for τ_{60° and τ_{30° at higher forward velocities are shown in Figure 5.11 (b). Forward pitching results in the wing

airfoil experiencing a negative angle of attack, eventually generating negative lift at high velocities.

Comparing shaft angles, an aircraft with a 30° shaft angle can achieve higher velocities than one with a 60° shaft angle because the lower angle allows the front rotors to overcome drag more effectively. Consequently, the aircraft with a 30° shaft angle requires less forward pitching at higher speeds, as indicated in Figure 5.11 (b).

Shaft Tilt Angle at τ_{0°

When the shaft tilt angle is 0°, the wing lift contribution ratio increases steadily along the lift curve slope until it reaches unity at the stall velocity, as shown in Figure 5.11 (a) and calculated using (5.25):

$$V_{\text{stall}} = \sqrt{\frac{2}{\rho}\frac{W}{S}\frac{1}{C_{L_{\max}}}} \tag{5.25}$$

At τ_{0°, the aircraft can fly like a conventional airplane, gaining horizontal velocity without forward pitching, as the front rotors align parallel to the flight axis, shown in Figure 5.14. Here, (5.22) becomes (5.26), with vertical forces equating only to wing lift. For steady level flight, the aircraft must pitch slightly forward to avoid climbing due to excess lift, as shown in Figure 5.11 (b).

$$L_{\text{wing}} = W_{\text{eVTOL}} \tag{5.26}$$

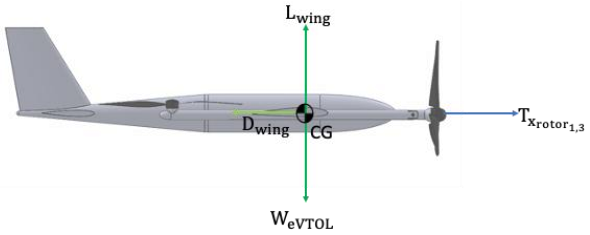

Figure 5.14: Front tiltrotor forces in forward flight when τ_{0°.
Both tiltrotors provide horizontal forces to accelerate the horizontal motion.

5.2.2 Aircraft Power Requirements

The power requirements vary with shaft tilt angles, as shown in Figure 5.15. At τ_{90°, the power required is minimal due to limited forward velocity. At τ_{60° and τ_{30°, the power required increases with higher achievable forward velocities. At τ_{0°, the power requirement decreases significantly as the rear rotors shut off, as shown in Figure 5.16 (b).

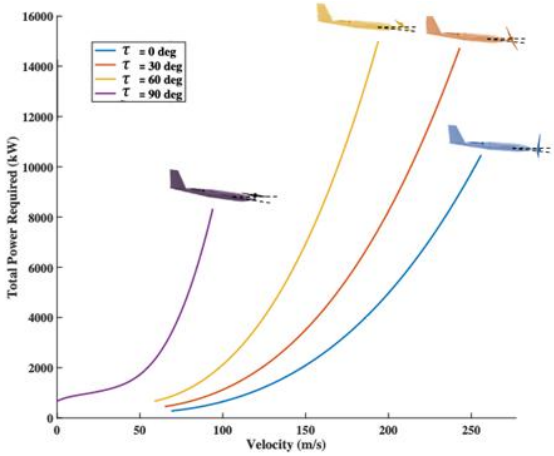

Figure 5.15: Total power against forward velocity for different shaft angle.
Blue represents τ_{0°, orange represents τ_{30°, yellow represents τ_{60° and purple represents τ_{90°.
At τ_{90°, aircraft achieves greater speed at lower power required.

At τ_{90°, the power required for front and back rotors is equal, as they are equally loaded, shown in Figure 5.16 (a) and (b). For other shaft angles, power required decreases with lower shaft angles as wing surfaces support the aircraft weight. At τ_{0°, rear lift-rotor power is minimized with full wing support.

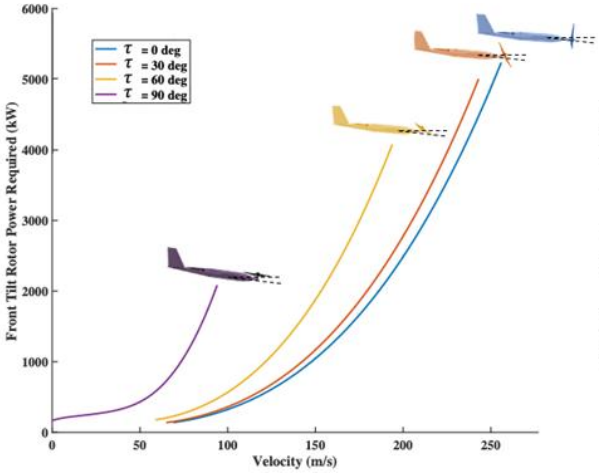

(a) Front tiltrotor power against velocity for different shaft angle.

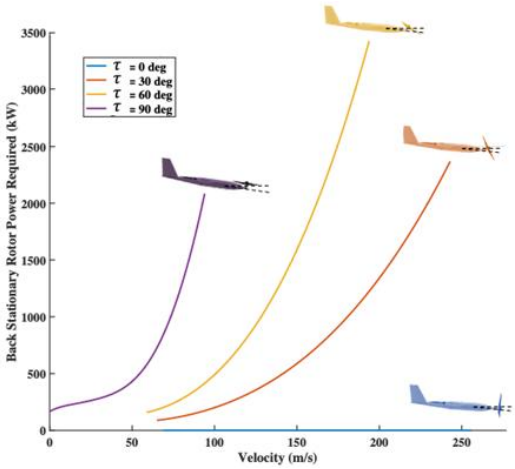

(b) Rear lift-rotor power against velocity for different shaft angle.

Figure 5.16: Breakdown of power required for front tiltrotor and rear lift-rotor.
Blue represents τ_{0°, orange represents τ_{30°, yellow represents τ_{60° and purple represents τ_{90°.

This study highlights the characteristics and benefits of tiltrotor eVTOL aircraft during each stage of transition, focusing on straight and level flight to prevent any loss of altitude. In this approach, any deviation in altitude is compensated by a combination of wing lift and rotor thrust, ensuring the aircraft maintains its desired flight path. The analysis demonstrates how flight velocity and aerodynamic forces dictate the required shaft angle and corresponding power demands. A tiltrotor design enables horizontal velocity gain without relying on increased pitch angles, thereby maintaining positive wing lift across a broader velocity range. This design efficiently transfers vertical support from rotors to wing surfaces, reducing rotor dependency and enabling higher cruise speeds. While the power required for tilting rotors initially increases with shaft angle adjustments during transition, the configuration exhibits superior efficiency at high speeds, leveraging aerodynamic lift for sustained forward flight.

5.3 Transition Climb and Descent Trajectory

The primary objective of this study is to examine the impact of the transition trajectory on the climb and descent segments in terms of flight profile parameters and the power required to execute these maneuvers. This involves defining the transition equations and kinematics representing the transition maneuvers and the forces acting on the aircraft.

5.3.1 Transition Climb Trajectory

Following certification requirement [60–62], the transition climb trajectory follows a vertical take-off approach as shown in Figure 5.3. The transition climb is defined using the trajectory function in Section 5.1.3. During the transition climb, the eVTOL aircraft performs a level climb, maintaining a fuselage reference line aligned with the horizon. Maintaining a fuselage incidence angle of zero degrees during the climb trajectory is a standard assumption aimed at optimizing aerodynamic performance and ensuring structural stability. This condition minimizes aerodynamic drag and interference by keeping the fuselage aligned with the relative airflow, improving energy efficiency during the climb. Additionally, a zero-degree fuselage incidence simplifies control requirements, as it allows the wing and rotor systems to generate the necessary lift and thrust without inducing significant pitching moments. From an operational perspective, adhering to a level fuselage angle aligns with industry practices for passenger comfort and system efficiency, particularly in UAM environments. For instance, this approach

avoids unnecessary structural loads and ensures smooth transitions during climb and cruise phases, which is crucial for meeting certification and safety standards. While specific regulations may vary, maintaining a level fuselage angle is consistent with general guidelines for aircraft stability and performance optimization. The trajectory mimics a vertical take-off trajectory, and the climb angle, measured from the horizon, is depicted in Figure 5.17.

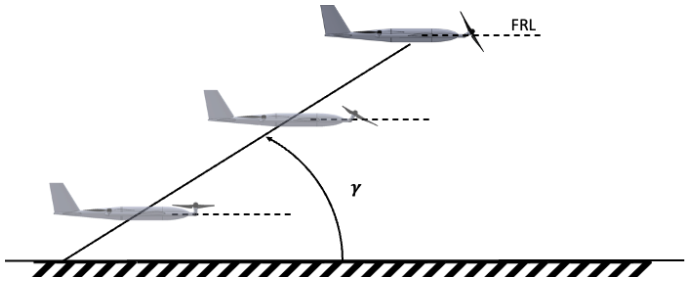

Figure 5.17: Climb angle based on the vertical and horizontal velocities.
Aircraft fuselage reference line is constrained level to the horizon as reference.

Transition Climb Equations

The equations of motion for the transition climb are derived using trimmed force and moment equations. During the transition climb, the eVTOL aircraft may accelerate in both horizontal and vertical directions, implying a dynamic flight state along the x-axis and z-axis. Therefore, acceleration in both directions must be accounted for. The forces must be in equilibrium for both the vertical and horizontal axes, following (5.27) and (5.28). Additionally, the summation of all moments about the CG due to the moment arm of the individual thrust of the rotors must be zero in (5.24), to ensure that the aircraft is not pitching and the fuselage reference line remains parallel to the horizon as shown in Figure 5.17, The lift from the tail is assumed to be negligible.

$$\sum T_{z_{\text{rotor}_i}} + L_{\text{wing}_z} - D_{\text{wing}_z} - W_{\text{eVTOL}} = m_{\text{eVTOL}} \times a_z \tag{5.27}$$

$$\sum T_{x_{\text{rotor}_i}} - L_{\text{wing}_x} - D_{\text{wing}_x} = m_{\text{eVTOL}} \times a_x \tag{5.28}$$

Transition Climb Kinematics

With the trajectory function defined, kinematic variables such as distance, velocity, and acceleration can be determined for both the vertical and horizontal axes, as shown in Figure 5.18 (a) and (b). The climb angle and overall trajectory are illustrated in Figure

5.18 (c). Initially, the eVTOL aircraft ascends vertically before translating horizontally, leading to a decreasing climb angle from a large value during hover to a smaller value during cruise. The lift and drag coefficients are matched against the climb angle of the eVTOL aircraft as shown in Figure 5.18 (d).

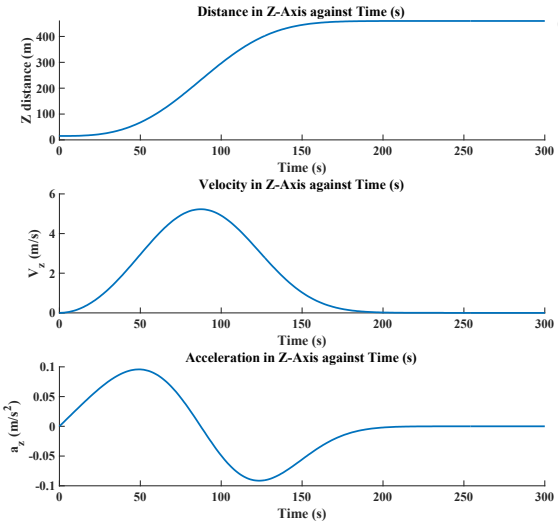

(a) Vertical translation, velocity & acceleration.

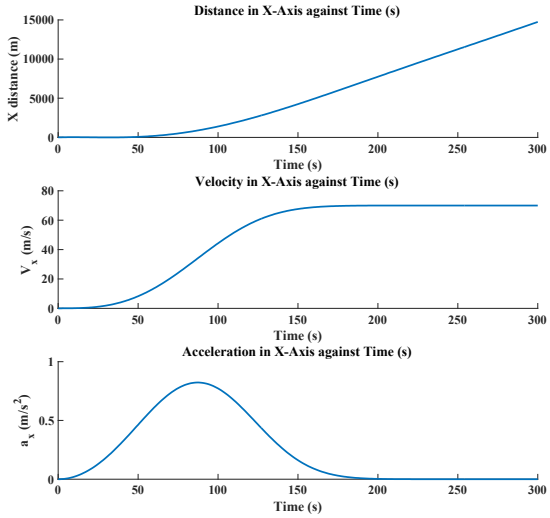

(b) Horizontal translation, velocity & acceleration.

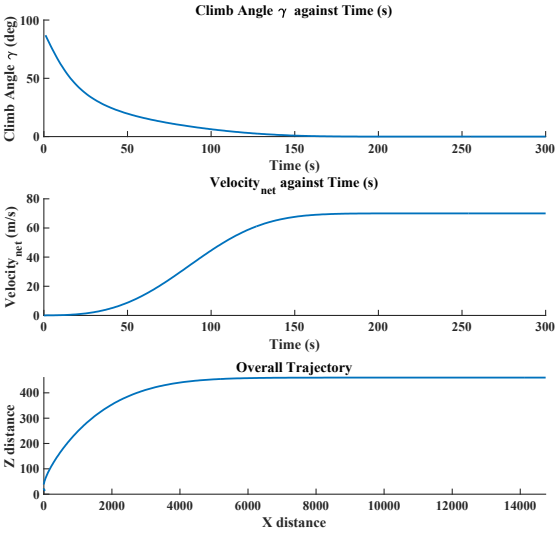

(c) Climb angle, resultant velocity & trajectory.

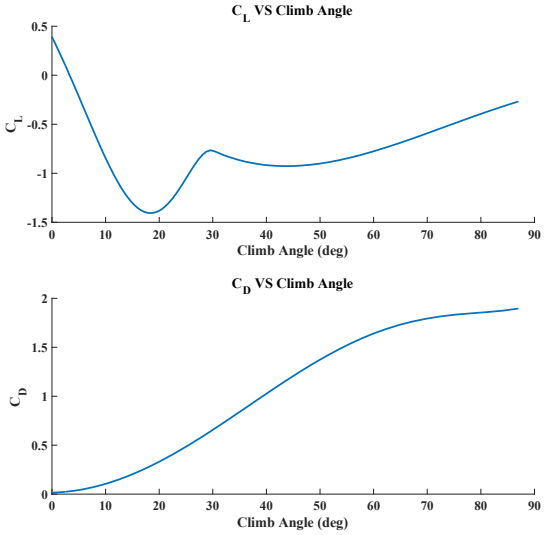

(d) Lift & drag coefficients.

Figure 5.18: Transition climb kinematics results against time.

Transition Climb Forces

The vertical rotor thrust required during the transition climb increases to counteract the rising negative opposing force, which includes lift and drag components in the vertical direction as shown in Figure 5.19 (a). Initially, a large climb angle induces a negative effective angle of attack on the airfoil, resulting in negative lift and consequently higher

thrust requirements. As the climb angle decreases, positive lift helps support the aircraft's weight, reducing the thrust needed from the rotors.

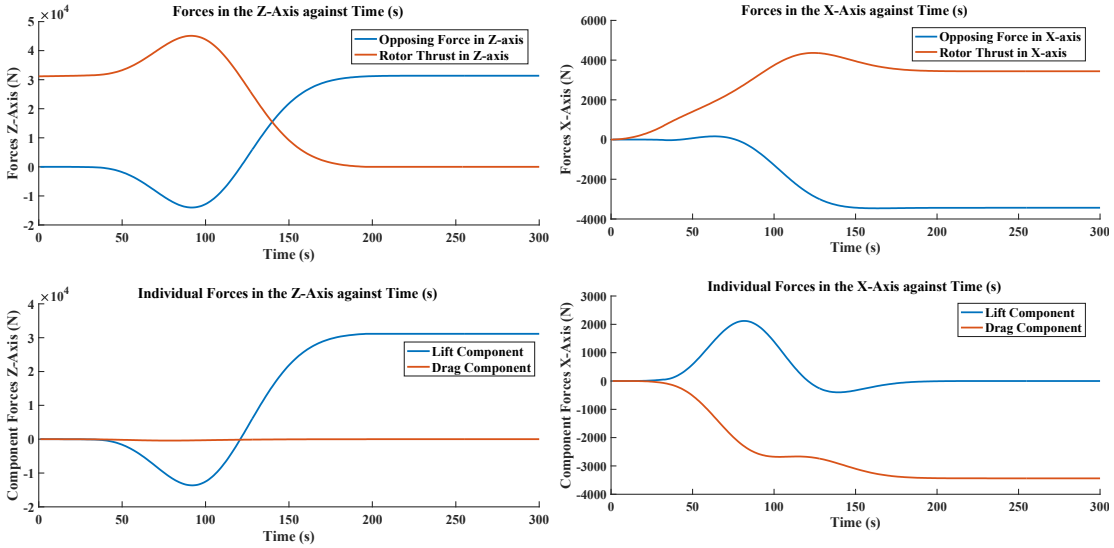

(a) Vertical component forces for rotor thrust, opposing force, lift and drag.

(b) Horizontal component forces for rotor thrust, opposing force, lift and drag.

Figure 5.19: Transition climb horizontal and vertical forces against time.

During the transition climb, when the vertical velocity exceeds the horizontal velocity, a large climb angle is induced along with a resultant velocity as shown in Figure 5.20 (a). This climb angle induces a negative effective angle of attack on the airfoil, generating negative lift in the wind reference frame. This negative lift increases the negative opposing force, thereby burdening the rotors, which must generate additional thrust to support the aircraft as shown in Figure 5.19 (a). Eventually, the climb angle decreases to a smaller value, as depicted in Figure 5.18 (c) for this trajectory.

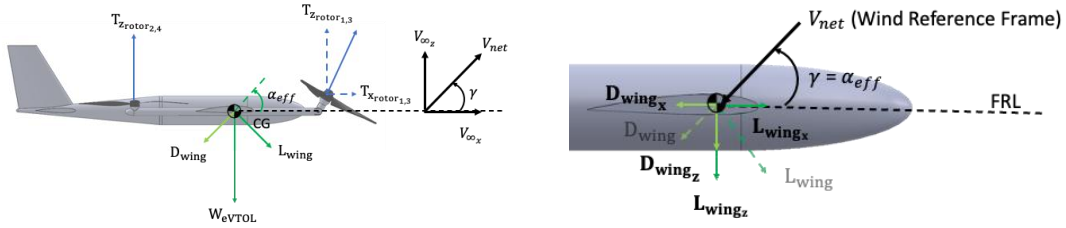

(a) For a large climb angle γ: force and velocity components with lift and drag in wind reference frame.

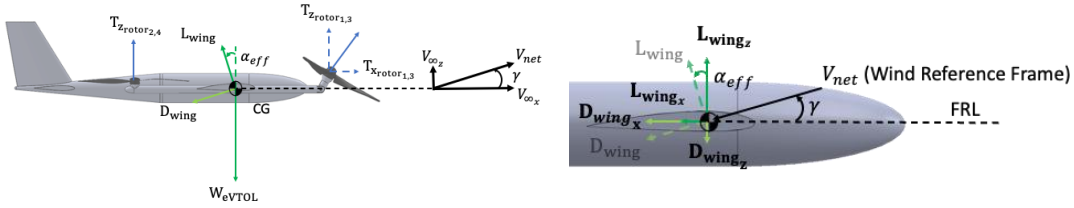

(b) For a small climb angle γ: force and velocity components with lift and drag in wind reference frame.

Figure 5.20: Aircraft force and velocity components during transition climb.

At a small climb angle, the force and velocity components are shown in Figure 5.20 (b). Here, lift and drag are generated due to the resultant velocity on the wing. At this reduced climb angle, the induced negative angle of attack is small. The lift coefficient remains positive at small negative angles of attack, due to the positive camber of the airfoil. Thus, the generation of positive lift from the smaller climb angle supports the weight of the eVTOL aircraft, reducing the thrust required from the rotors.

The thrust required by the rotors in the horizontal direction, as shown in Figure 5.19 (b), exhibits an increasing trend due to the positive acceleration from Figure 5.18 (c). The opposing horizontal forces, which comprise the lift and drag components in Figure 5.19 (b), remain relatively constant initially because of the canceling effect of negative lift and negative drag components. Subsequently, these forces increase negatively to a constant value due to the generation of positive lift.

Transition Climb Power Required

The total power required during the transition climb increases significantly due to the front tilting rotors providing both horizontal and vertical thrust, as shown in Figure 5.21 (a). During this phase, the lift rotors play a critical role in maintaining the aircraft's commanded position and stability as dictated by the predefined trajectory. In a level transition, these lift rotors ensure balance by providing the necessary thrust to counteract destabilizing forces and maintain zero resultant moments about the center of gravity. This balance is achieved through the trimming module, which operates iteratively at each time increment during the transition phase. As the horizontal velocity increases, the wing generates more positive lift, progressively reducing the load on the rotors and, consequently, the overall power requirement.

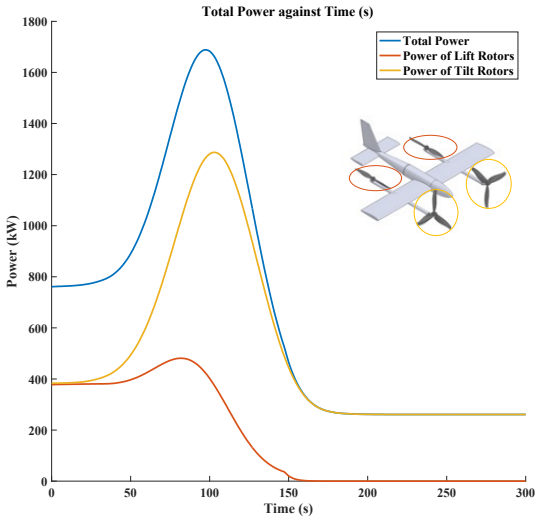

(a) Power breakdown among rotors. Total power in blue, lift rotor power in red and tiltrotor power in yellow.

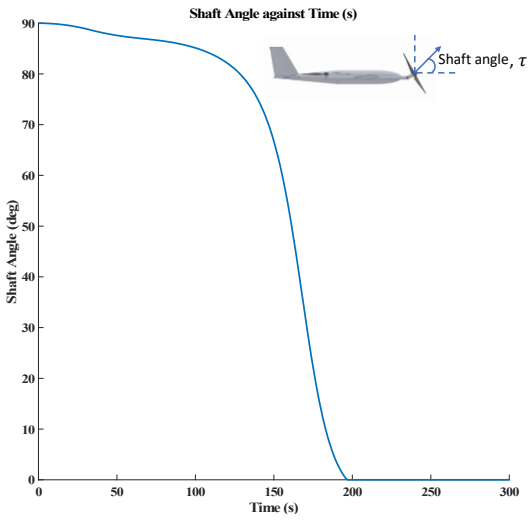

(b) Front tiltrotor shaft angle. Shaft angle is relative constant in early stage, and later follows a quick rotation toward the forward flight.

Figure 5.21: Transition climb results against time for total power and shaft angle.

The power required from the front tilting rotors is a major contributor to the total power increase, as they provide thrust in both horizontal and vertical directions. In contrast, the power required by the rear lift-rotor is solely used to provide vertical thrust to support the eVTOL's weight. As the wing gains horizontal velocity and generates positive lift, the burden on the rotors is reduced, leading to a decrease in the power requirement for both the front tilting rotor and the rear lift-rotor.

Towards the end of the transition climb, the power required by the eVTOL aircraft primarily comes from the front tilting rotor to overcome drag, with the total power curve coinciding with the tiltrotor power curve.

The shaft angle of the front tilting rotor decreases slightly initially to gain horizontal velocity, as shown in Figure 5.21 (b). During this period, the shaft angle is kept almost constant to provide sufficient horizontal and vertical thrust. As the wing generates enough lift to reduce reliance on the tiltrotor, the tiltrotor can transition to a cruise configuration at a faster rate and with a lower power setting. This study provides valuable insights for optimizing transition flight profiles and enhancing performance, ensuring efficient and safe operation during critical transition phases.

5.3.2 Transition Descent Trajectory

For the transition descent, two trajectory approaches for descent can be modeled: (1) a vertical landing, which represents the opposite trajectory of a transition climb, and (2) a non-vertical landing sequence, as illustrated in Figure 5.22 (a) and (b). The vertical landing is defined using the trajectory function in Section 5.1.3. For non-vertical landing, a linear trajectory function is used to model the descent, as some eVTOL configurations lack a mechanism to decelerate using their rotor systems in a leveled attitude due to fixed/non-tilting rotors.

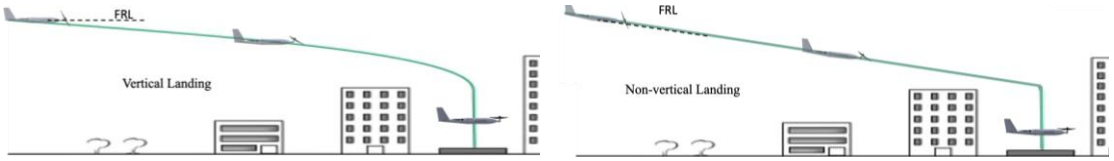

(a) Vertical landing profile with fuselage reference line aligned to the horizon.

(b) Non-vertical landing profile with fuselage reference line aligned with the descent angle.

Figure 5.22: Transition descent profiles for vertical and non-vertical landing.

During a vertical landing, the eVTOL aircraft performs a level descent, maintaining the fuselage reference line parallel to the horizon to ensure a controlled and stable downward motion. To mitigate the risk of entering a vortex ring state (VRS), a phenomenon where the rotor operates in its own recirculated wake, leading to a sudden loss of lift, the descent rate is carefully managed and kept below the critical threshold of the rotor induced velocity where VRS is likely to occur. Additionally, modern eVTOL designs incorporate advanced flight control systems that can detect and adjust flight parameters to avoid conditions conducive to VRS. Some eVTOL configurations also feature distributed propulsion systems, which enhance stability and reduce the likelihood of localized wake recirculation.

In contrast, during a non-vertical landing, the eVTOL aircraft executes a pitched descent. In this scenario, the fuselage reference line is not parallel to the horizon, and the pitch angle varies according to the descent angle, as depicted in Figure 5.23. This type of descent allows for a more gradual and controlled landing approach, which may be beneficial in certain operational contexts.

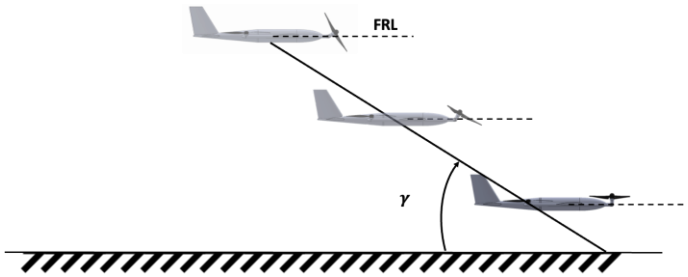

Figure 5.23: Descent angle based on the vertical and horizontal velocities.
Aircraft fuselage reference line is constrained level to the horizon as reference.

Transition Descent Equations

During transition descent, the eVTOL aircraft can decelerate in both horizontal and vertical directions, which is accounted for using trimmed force and moment equations. The forces in the vertical and horizontal axes must be in equilibrium, calculated using (5.29) and (5.30). The summation of all moments acting about the CG, due to the moment arm of the rotor thrust, must be zero in (5.24) to ensure no pitching and to keep the fuselage reference line parallel to the horizon to achieve the vertical landing, while the pitch angle is the equal to the descent angle for a non-vertical landing.

$$\sum T_{z_{\text{rotor}_i}} + L_{\text{wing}_z} + D_{\text{wing}_z} - W_{\text{eVTOL}} = m_{\text{eVTOL}} \times a_z \tag{5.29}$$

$$\sum T_{x_{\text{rotor}_i}} + L_{\text{wing}_x} - D_{\text{wing}_x} = m_{\text{eVTOL}} \times a_x \tag{5.30}$$

Transition Descent Kinematics

To model the transition descent, this study employs a defined trajectory function alongside kinematic variables such as distance, velocity, and acceleration. The results for the vertical and horizontal axes are depicted in Figure 5.24 (a) and (b).

The descent angle and resultant velocity are calculated using (5.10) and (5.12). The overall trajectories for both vertical and non-vertical landings are shown in Figure 5.24 (c). The descent angle starts from zero and increases negatively to a larger descent angle. Using airfoil data from Figure 5.9, the lift and drag coefficients are matched against the descent angle, as illustrated in Figure 5.24 (d).

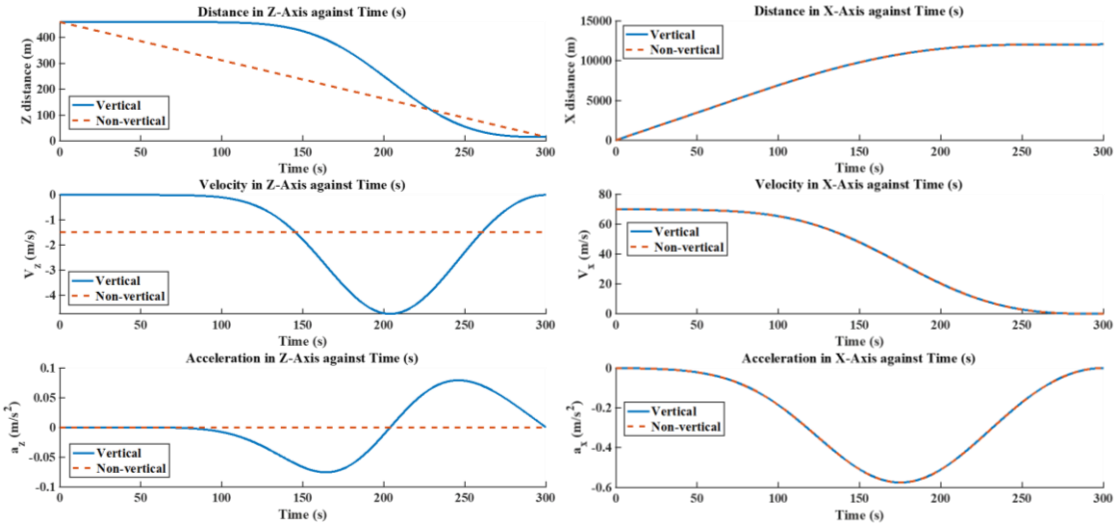

(a) Vertical translation, velocity & acceleration. (b) Horizontal translation, velocity & acceleration.

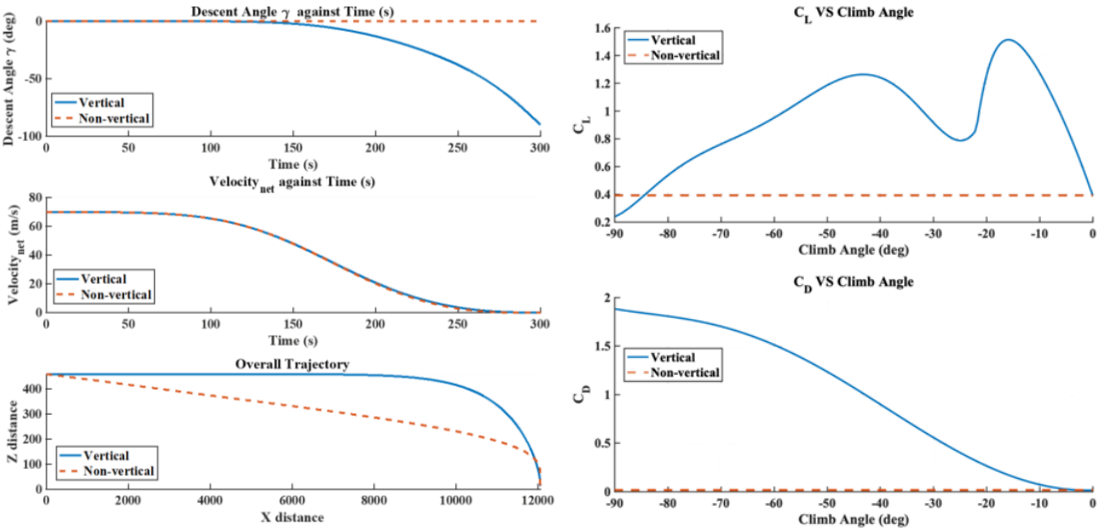

(c) Descent angle, resultant velocity & trajectory. (d) Lift & drag coefficients.

Figure 5.24: Transition descent kinematics results against time.
Solid lines represent vertical landing and dotted lines represent non-vertical landing.

For vertical landing, the trajectory function is essentially a reflection about the y-axis of the transition climb. During vertical landing, the rotor thrust comprises both vertical and horizontal components to support the weight and overcome vertical drag, as shown in Figure 5.25 (a). The descent angle induces a positive angle of attack on the airfoil, which results in a positive lift coefficient. Therefore, only the positive lift coefficient is generated for the vertical landing trajectory, as depicted in Figure 5.24 (d).

In contrast, the non-vertical landing trajectory differs from the vertical descent, as the eVTOL aircraft pitches downward to align with the glide slope, similar to a conventional aircraft, as shown in Figure 5.22. The descent velocity is 1.47 m/s, and descent angle is 1.68°, calculated using (5.31) and (5.32).

$$\text{Descent velocity} = \frac{h_{\text{initial altitude}} - h_{\text{final altitude}}}{t_{\text{descent}}} \tag{5.31}$$

$$\text{Descent angle} = \tan^{-1}\frac{V_{\text{descent}}}{V_{\infty}} \tag{5.32}$$

During the non-vertical landing, the eVTOL aircraft pitches forward slightly for a controlled landing with a small vertical velocity at a descent angle. In this configuration, the fuselage reference line is parallel to the wind reference frame, with the forces and velocity components shown in Figure 5.25 (b).

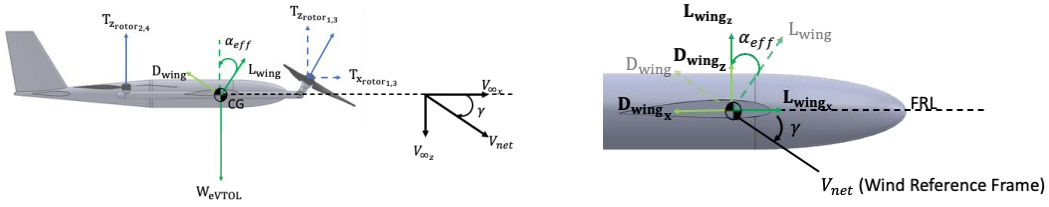

(a) Vertical landing with fuselage reference line parallel to the horizon: force and velocity components with lift and drag in wind reference frame.

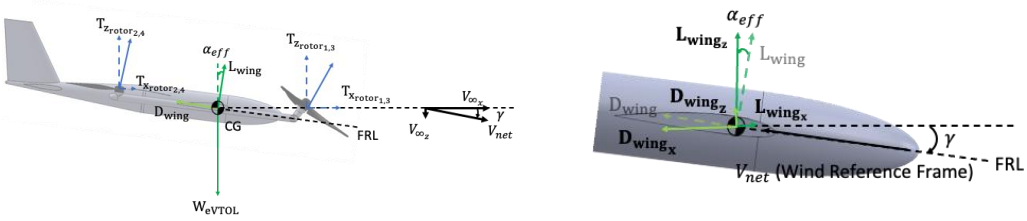

(b) Non-vertical landing with fuselage reference line parallel to the descent angle: force and velocity components with lift and drag in wind reference frame.

Figure 5.25: Aircraft force and velocity components during transition descent.

Transition Descent Forces

At the start of the vertical landing transition descent, the opposing force in the vertical direction, which consists of two components: (1) lift and (2) drag forces as shown in Figure 5.26 (a), remains constant at a high value while the rotors do not provide any thrust. The opposing force decreases around the 75s mark, and the rotors compensate for this decrease by generating the required thrust accordingly. It is evident that the lift component is the major contributor to the overall opposing force due to its larger magnitude. At the beginning of the descent, the wing continues to generate lift to support the eVTOL aircraft's weight. As the eVTOL aircraft decelerates, the net resultant

velocity decreases. Consequently, the lift component generated gradually decreases, necessitating increased thrust from the rotors to maintain the required support.

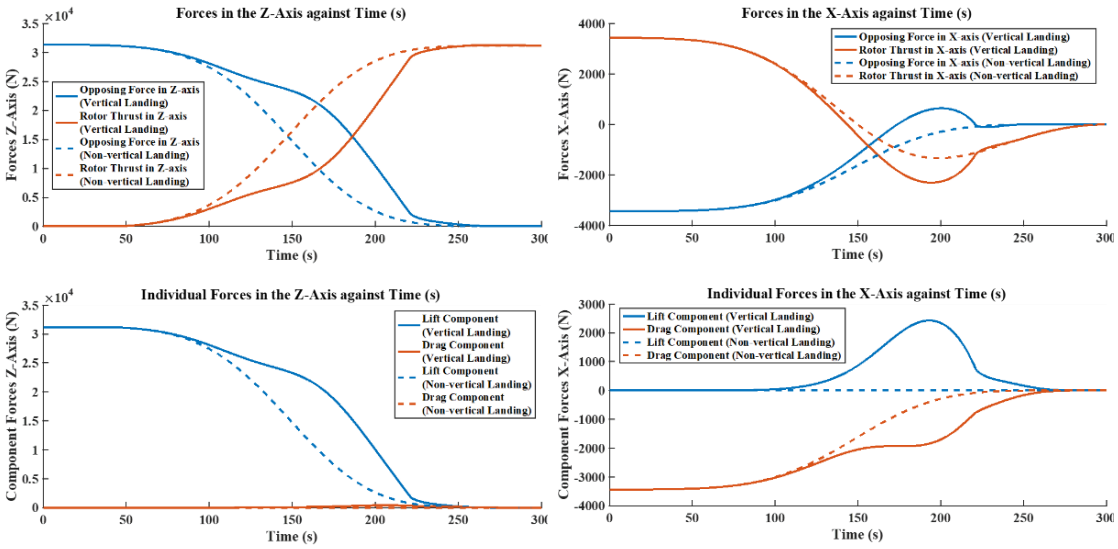

(a) Vertical component forces for rotor thrust, opposing force, lift and drag.

(b) Horizontal component forces for rotor thrust, opposing force, lift and drag.

Figure 5.26: Transition descent horizontal and vertical forces against time.
Solid lines represent vertical landing, and dotted lines represent non-vertical landing.

The thrust generated by the rotors counteracts the opposing force in the horizontal direction, as illustrated in Figure 5.26 (b). This force also consists of lift and drag components. The magnitude of the rotor thrust decreases as the opposing force decreases, and conversely, the thrust increases when the opposing force increases. The rotor thrust enters the negative region to decelerate the eVTOL aircraft during the transition descent in a vertical landing trajectory, as shown in Figure 5.26.

For the non-vertical landing transition descent, the opposing force in the vertical direction is primarily influenced by the lift force, as depicted in Figure 5.26 (a). Due to the small descent angle during the non-vertical landing trajectory, as shown in Figure 5.25, the drag component in the vertical direction is minimal. The changes in lift force are solely due to the decrease in velocity. Therefore, the opposing force and the lift force exhibit a smooth curve, resulting in a gradual increase in the thrust required by the rotors in the vertical direction.

The opposing force in the horizontal direction for the non-vertical landing transition descent is mainly influenced by the drag force, as shown in Figure 5.26 (b). Similarly, the lift component in the horizontal direction is minimal, as indicated in Figure 5.25. The changes in drag force are only due to the decrease in velocity, resulting in a smooth

curve for the drag force and the opposing force. Consequently, there is a smooth increase in the thrust required by the rotors in the horizontal direction.

Transition Descent Power Required

During the transition from cruise to descent, the total power required increases, as illustrated in Figure 5.27 (a). This increase is due to the need for the rotors to provide additional thrust to support the aircraft's weight during the descent phase. For both vertical and non-vertical landings, the lift-rotors remain idle at the start of the transition descent.

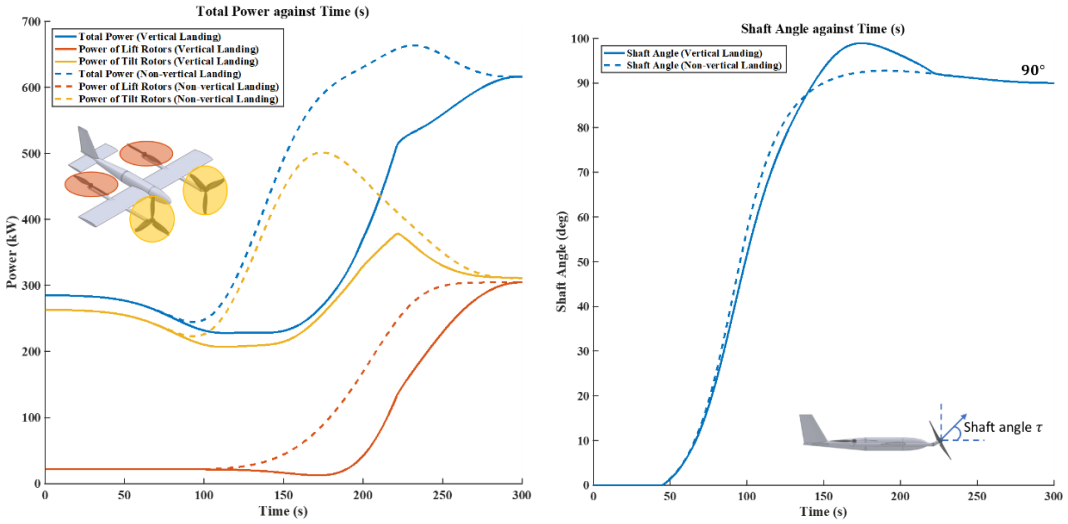

(a) Power breakdown among rotors. (b) Front tiltrotor shaft angle.

Figure 5.27: Transition descent results against time for total power and shaft angle. Solid lines represent vertical landing, and dotted lines represent non-vertical landing.

As the aircraft decelerates, the power required by the lift-rotors increases since the total vertical thrust requirement shifts from the wing to the lift-rotors. Meanwhile, the power required by the tiltrotors decreases due to the reduced need for horizontal thrust to decelerate the aircraft. As the aircraft continues to slow down, the power required by the tiltrotors increases again. This is because the tiltrotors must generate thrust in the vertical direction to support the aircraft's weight and further decelerate the descent. The variations in power requirements for the tiltrotors during the transition descent create a noticeable power fluctuation, often referred to as a "power bucket."

When comparing the power required curves, the non-vertical landing shows a smoother transition than the vertical landing. This smoothness results from the gradual change in thrust required in both vertical and horizontal directions, as seen in Figure 5.26 (a) and (b). The results also indicate that the total power required for transition descent is lower

for vertical landing than for non-vertical landing, leading to reduced power demands on the electric components.

The shaft angle of the tiltrotors increases as they are required to provide additional thrust to support the aircraft weight, as shown in Figure 5.27 (b). A unique feature of tiltrotor configurations is their ability to tilt backward temporarily to decelerate the aircraft during a transition descent in a vertical landing trajectory. The shaft angle trends are similar for both vertical and non-vertical landings, with the main difference being the extent to which the tiltrotor tilts backward for horizontal deceleration.

5.3.3 Combined Power and Energy for a Complete Mission Profile

The overall power required for a general main mission profile of the generic eVTOL aircraft is shown in Figure 5.28. The power requirement is lower for a mission with a vertical landing compared to a non-vertical landing transition descent.

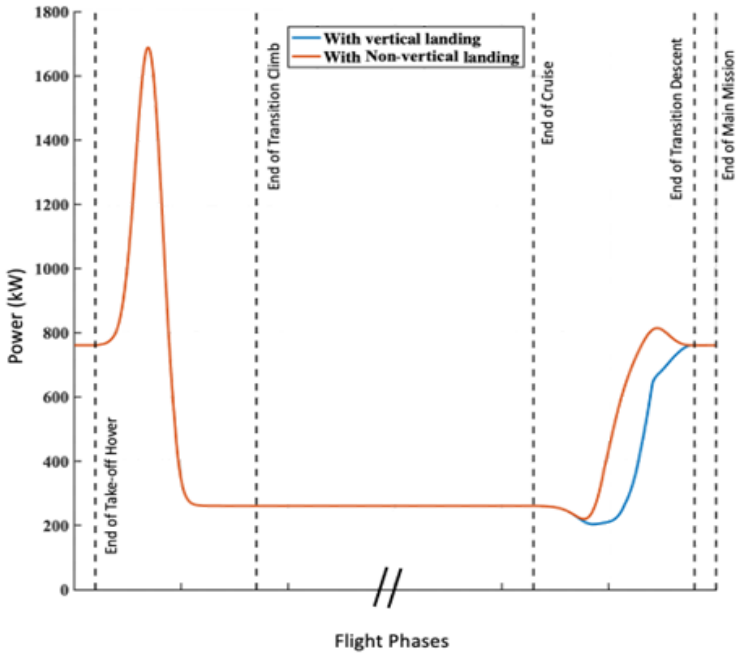

Figure 5.28: Main mission power required for each flight phase.
Generic eVTOL aircraft in both the transition climb and different transition descent trajectories.
Maximum power is required during the transition climb phase.

In a vertical landing, the eVTOL aircraft remains level and parallel to the horizon, allowing the wing to maintain lift for a longer duration due to the positive angle of attack induced by the descent angle, as illustrated in Figure 5.29 (a). In contrast, during a non-

vertical landing, the eVTOL aircraft pitches forward, causing the wing to lose lift more quickly due to its increased sensitivity to changes in velocity, as shown in Figure 5.29 (b). Consequently, the rotor is less burdened in providing thrust to support the weight of the eVTOL aircraft during a vertical landing compared to a non-vertical landing. Thus, the power required for vertical landing is lower than for non-vertical landing.

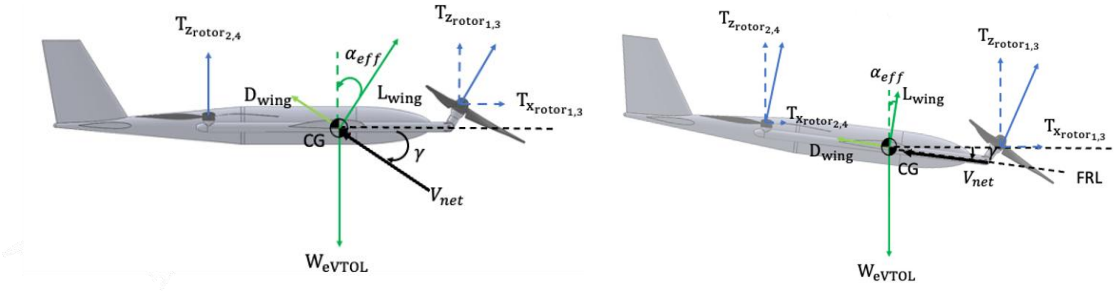

(a) Vertical landing with greater effective angle of angle, increases lift wing generated. Supplementing the thrust required by propulsors.

(b) Non-vertical landing with reduced effective angle of angle, decreases wing lift generated. Requiring greater thrust from propulsors.

Figure 5.29: Rotor and wing forces during vertical and non-vertical landing.

This finding helps estimate the energy usage for the test model of a general main mission profile. The energy usage is divided into two components: (1) the cruise flight phase and (2) the non-cruise flight phase. Based on the energy required for the cruise phase, the range of the test model can be estimated using (5.33). The energy usage for the test model is presented in Table 5.5.

$$\text{Range} = \frac{E_{\text{cruise}}}{P_{\text{cruise}}} \times V_{\text{cruise}} \tag{5.33}$$

From Table 5.5, it is evident that non-vertical landing consumes more energy than vertical landing during the transition descent, resulting in a shorter range for the former. This observation aligns with the power requirement results shown in Figure 5.28.

Table 5.5: Main mission range and energy in cruise and non-cruise segments. Vertical landing consumes less energy in the non-cruise segment, allowing for more energy for the increased cruise segment and total range.

Parameter	Vertical landing	Non-vertical landing
Total Energy Consumption (kWh)	230	230
Cruise Velocity (m/s)	70	70
Total Range (km)	150.4	143.2
Energy in Cruise Segment (%)	68.7	65.4
Energy in Non-cruise Segment (%)	31.3	34.6

From this study, it can be concluded that the power required during the transitional phases of an eVTOL aircraft's descent is highly dynamic and constantly changing over time, as shown in Figure 5.28. This is crucial for sizing the motors of an eVTOL aircraft.

Without considering the impact of the transition on power requirements, an eVTOL aircraft might fail to achieve the desired trajectory during transition, potentially affecting its certification process if it does not meet the regulatory standards set for the transition phase. Hence, this study highlights the importance of understanding trajectory dynamics for the efficient and compliant operation of eVTOL aircraft.

5.4 Analysis of eVTOL Configurations

In this final study, we examine the power requirements and flight performance parameters for a given trajectory across three leading eVTOL aircraft configurations: Tiltrotor, Lift + Cruise, and Lift + Tiltrotor are detailed in Table 4.10. Ideally, each eVTOL configuration has an optimal trajectory to achieve either maximum range or minimum power requirement. However, to comply with regulations, we assume a standard vertical take-off approach for the transition climb trajectory and a standard vertical landing approach for the transition descent trajectory for all eVTOL configurations. For the Lift + Cruise aircraft, which lacks a tiltable rotor for deceleration, a non-vertical landing approach is assumed for its transition descent trajectory, with the rotors fixed in a vertical position.

The basis for performance comparison of the three different eVTOL configurations includes a common mission profile comprising the following phases: (1) hover, (2) transition climb, (3) cruise, (4) transition descent, and (5) landing. The assumptions used for the BEMT in this study include standard values for the correction factor for power calculations, rotor tip speed, and rotor blade drag coefficient. The input parameters for the comparison of the three different configurations are shown in Table 5.6.

Table 5.6: Input parameters for each eVTOL aircraft configuration.

Parameter	eVTOL (A)	eVTOL (B)	eVTOL (C)
Configuration Type	Lift + Cruise	Tiltrotor	Lift + Tiltrotor
Total Mass (kg)	3175	2177	3175
Wingspan (m)	15.2	10.5	15.0
Wing Area (m^2)	19.8	11.6	26.8
Number of Tiltrotors (Primary Rotors)	0	6	4
Number of Pusher Rotors (Primary Rotors)	1	0	0
Number of Lift-rotors (Secondary Rotors)	4	0	4
Primary Rotor Diameter (m)	3.90	3.10	3.10
Number of Rotor Blade for Primary Rotor	3	5	5
Secondary Rotor Diameter (m)	2.15	-	3.30
Number of Rotor Blade for Secondary Rotor	2	-	2
Rotor Blade Drag Coefficient C_{d_0}	0.012	0.012	0.012
Rotor Tip Speed (m/s)	182.88	182.88	182.88
Fuselage Drag Coefficient $C_{d_{fuselage}}$	0.0255	0.022	0.020
Available Energy (kWh)	230	160	230

5.4.1 Transition Climb Power Required

The initial hover power required at $t = 0$ for eVTOL (A) is the highest, followed by eVTOL (C) and eVTOL (B), as illustrated in Figure 5.30. eVTOL (B) has the lowest power requirement, requiring 57.4% and 33.6% less power as compared to eVTOL (A) and (C), due to its lower weight, which results in lower disk loading compared to the other models. The number of rotors used for hover in eVTOL (A) is less than that for eVTOL (C), as shown in Table 5.7. Consequently, the thrust is distributed among more rotors in eVTOL (C), reducing the induced power required.

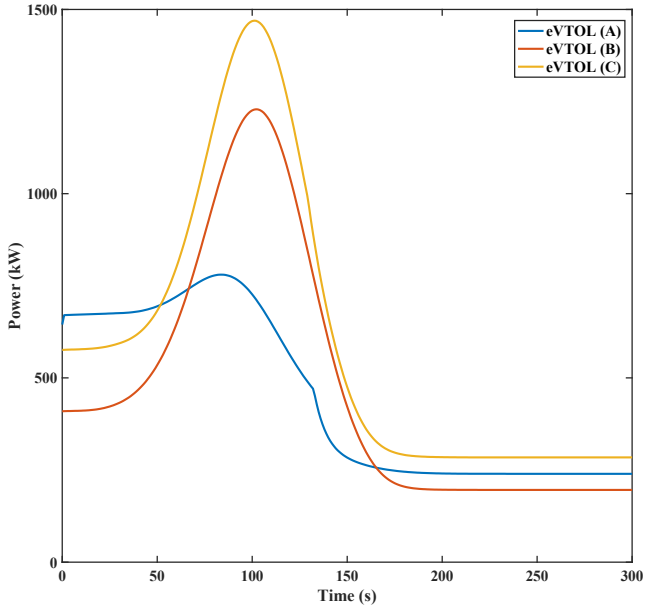

Figure 5.30: Comparison of power requirement for transition climb.

Table 5.7: Comparison of power requirement during hover and cruise.

Parameter	eVTOL (A)	eVTOL (B)	eVTOL (C)
Mass (kg)	3175	2177	3175
Number of Rotors used for Hover	4	6	8
Power to Hover (kW)	644.7	409.7	576.1
Number of Rotors used for Cruise	1	6	4
Power to Cruise (kW)	239.8	196.1	284.2
Peak Transition Power (kW)	781.1	1230.0	1471.0

During the transition climb, the increase to peak power required for eVTOL (A) is less than that for eVTOL (B) and eVTOL (C). This difference is attributable to the number and size of the rotor systems. eVTOL (B) and (C) have increased peak power of 57.5% and 88.3% as compared to eVTOL (A). In eVTOL (B) and eVTOL (C), the tiltrotors are responsible for providing thrust in both the vertical and horizontal directions. In contrast, eVTOL (A) utilizes lift-rotors and pusher rotors to provide vertical and horizontal thrust, respectively. This distribution of rotor system across different axes reduces the burden

on each rotor system. As a result, the increase in power required for eVTOL (A) is less than for the other two configurations, highlighting a key advantage of the Lift + Cruise configuration during the transition climb segment.

When comparing the power required for cruise, eVTOL (C) demands the most power, followed by eVTOL (A) and eVTOL (B). The lower weight of eVTOL (B) means that its wing surface does not need to generate as much lift, resulting in lower induced drag from the wing surface. In contrast, eVTOL (C) requires the most power because it uses a higher number of rotors for cruise, four tiltrotors compared to one pusher rotor in eVTOL (A). Additionally, the tiltrotors of eVTOL (C) use five blades each, whereas the pusher rotor of eVTOL (A) uses three blades. This results in higher profile power for eVTOL (C) than for eVTOL (A), leading to a higher cruise power requirement for eVTOL (C).

5.4.2 Transition Descent Power Required

During the transition descent, eVTOL (B) exhibits the largest spike in power required, transitioning from cruise power to peak power, as shown in Figure 5.31. This occurs because all six rotors on eVTOL (B) tilt, resulting in a high-power requirement as each rotor must provide thrust in both the vertical and horizontal directions.

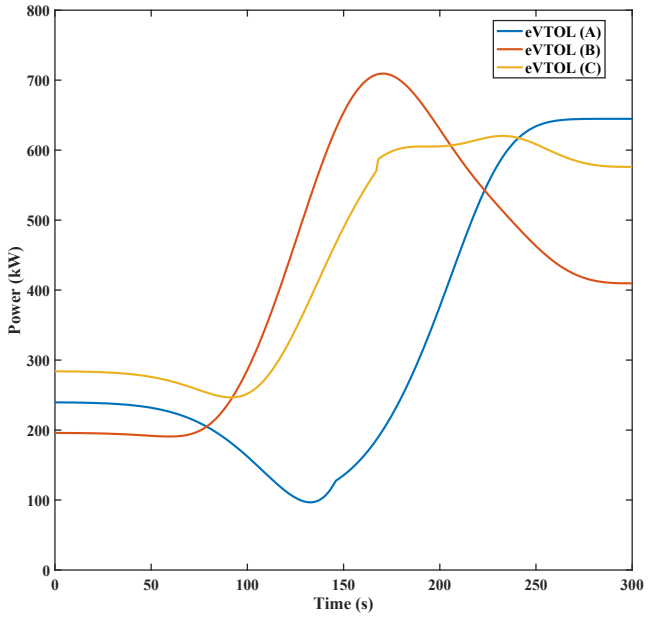

Figure 5.31: Comparison of power requirement for transition descent.

For eVTOL (A), a "power bucket" is observed in Figure 5.31. This phenomenon arises from the decrease in power required for the pusher rotor and an increase in power required from the lift-rotors. During descent, less horizontal thrust is necessary, while more vertical thrust is needed when the wing lift is insufficient to support the aircraft's weight. Consequently, the lift-rotors are engaged to support the aircraft. Similarly, eVTOL (C) experiences a power bucket, as shown in Figure 5.31. This is due to the changes in thrust requirements for the tiltrotors and an increase in thrust needed for the lift-rotor, which is reflected in the overall power requirements for eVTOL (C).

At the end of the transition descent, eVTOL (A) and eVTOL (C) require more power than eVTOL (B), primarily due to the differences in aircraft weight. eVTOL (A) demands more power than eVTOL (C) due to the lower distributed thrust, resulting in higher induced power for eVTOL (A) compared to eVTOL (C) at the end of the transition descent.

5.4.3 Power Required for Complete Mission Profile

The power requirements for a general mission for all three eVTOL configurations are shown in Figure 5.32. The transition climb and descent phases are observed to be highly dynamic compared to other flight phases within the main mission, regardless of the eVTOL aircraft configuration.

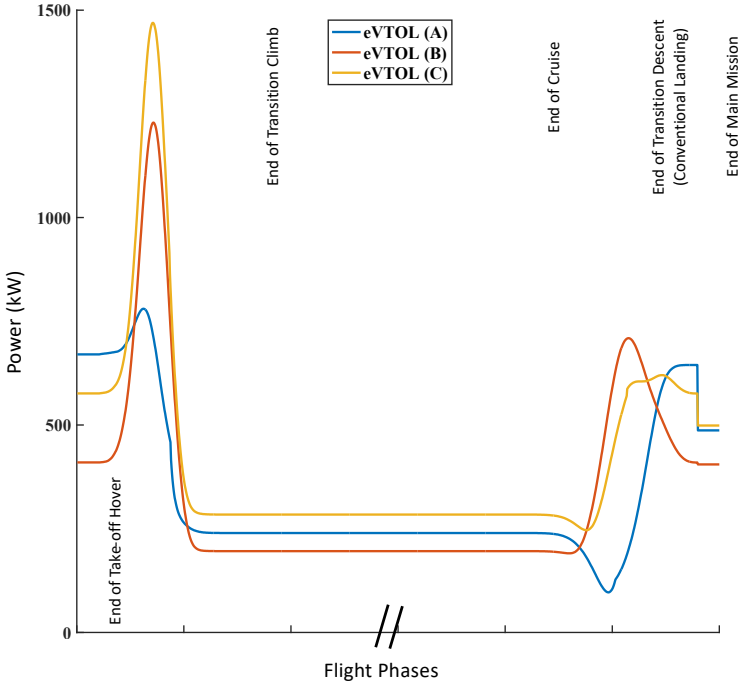

Figure 5.32: Main mission power required for various eVTOL aircraft.

5.4.4 Energy and Range for Complete Mission Profile

The energy distribution for cruise and non-cruise segments for a general main mission for different eVTOL aircraft configurations is shown in Table 5.8. eVTOL (A) has the longest range, as it has the highest available energy for cruise compared to other configurations. This suggests that a Lift + Cruise configuration is more energy efficient during the transitional flight phase. Conversely, the energy available for cruise is slightly higher for eVTOL (C) than eVTOL (B), resulting in eVTOL (C) having a longer range than eVTOL (B) due to its greater total energy.

One major assumption in these calculations is that the rotor tip speed remains constant across all eVTOL aircraft configurations. Each configuration may optimize rotor tip speed differently based on its rotor system and flight phase to enhance power efficiency and energy usage. However, since this study focuses on the performance characteristics of different eVTOL configurations for a main mission profile with transitional phases, a common rotor tip speed is used. The results discussed accordingly demonstrate that a Lift + Cruise configuration has notable performance advantages. A pusher rotor and lift-rotor system alleviate the burden of providing thrust in both horizontal and vertical directions, unlike tiltrotors, which incur higher power requirements. This high-power requirement for tiltable rotors aligns with the findings of the initial study, confirming that tilting the rotors significantly increases power demand.

Table 5.8: Energy distribution in main mission cruise and non-cruise phases.

Parameter	eVTOL (A)	eVTOL (B)	eVTOL (C)
Mass (kg)	3175	2177	3175
Total Energy (kWh)	230	160	230
Cruise Velocity (m/s)	70	70	70
Range (km)	184.3	124.2	139.9
Cruise Energy (%)	77.4	62.2	69.6
Non-cruise Energy (%)	22.6	37.8	30.4

5.5 Summary

Transition modelling is crucial for eVTOL aircraft design and certification, as the transition phase is highly dynamic and significantly different from the hover and cruise phases, which are generally assumed to be in steady-state conditions. Moreover, it is essential to meet regulatory standards and safety guidelines for transition to ensure safe operation and a comfortable trajectory from one flight phase to another. The modelling focuses on three main modules further developed to encapsulate the transition flight phase: (1) power required, (2) trimmed force and moment, and (3) kinematic and trajectory. Together with the improved aerodynamics module, these modules were used to conduct three distinct studies.

In the first study, the effects of tilt angle on the lift contribution of the wing were explored. The study demonstrated that a tilting rotor configuration is beneficial for eVTOL aircraft as it allows the wing to generate positive lift over a large velocity range. This configuration enables the aircraft to achieve a higher maximum velocity, thus offering a wider operating margin. However, it was noted that the tiltrotor configuration incurs higher power consumption during the phase of tilting its rotors forward.

In the second study, different individual transition trajectories were investigated, specifically comparing vertical and non-vertical landings. The findings revealed that the total power required for the transition descent is lower for vertical landings compared to non-vertical landings. This lower power requirement is especially critical when the aircraft's batteries are at a lower state of charge during landing. Additionally, the study highlighted how different trajectories impact performance characteristics, such as power requirements, energy usage, and the shaft tilt angle.

Lastly, a comparison study was carried out between three different configurations of eVTOL aircraft: Tiltrotor, Lift + Cruise, and Lift + Tiltrotor. Although, the Tiltrotor has the lowest power requirement, requiring 57.4% and 33.6% less power as compared to Lift+Cruise and Lift + Tiltrotor. The study showed that the Lift + Cruise configuration is more energy efficient and incurs a lower power limit during the transition phase, as eVTOL (B) and (C) have increased peak power of 57.5% and 88.3% compared to eVTOL (A). This configuration benefits from separating thrust responsibilities between the pusher and lift-rotors, resulting in lower overall power requirements and greater

energy efficiency compared to tiltrotor configurations. The findings also confirmed that higher power is required for tiltrotor configurations during the transition phase, aligning with the results of the first study.

This study indicates that the Lift + Cruise configuration is advantageous in terms of power and energy efficiency, particularly during transitional flight phases. This configuration's separation of thrust responsibilities between pusher and lift-rotors results in lower overall power requirements and greater energy efficiency compared to tiltrotor configurations. This efficiency is crucial for maximizing the range and performance of eVTOL aircraft, which must meet stringent regulatory standards and operational demands.

The conclusions drawn from this analysis, particularly regarding the energy efficiency and power requirements of the transition phase, remain relevant but may require refinement in future studies. Incorporating unsteady aerodynamic models would improve the fidelity of the transition analysis, offering a more accurate representation of real-world operating conditions. Future work should explore these unsteady and rotor wake effects using higher-fidelity computational methods such as vortex wake or free-wake analyses to enhance the accuracy of transition performance predictions, or experimental data to validate the findings and enhance the robustness of the design recommendations.

Chapter 6: Wing Configuration Design and Optimization

This chapter presents an aerodynamic and stability analysis to quantify the benefits of wing surfaces for eVTOL aircraft, following the flow diagram in Figure 6.1. It develops a framework to compare different wing configurations, studies the parametric effects of tandem wings, and demonstrates an optimization method for eVTOL wing design.

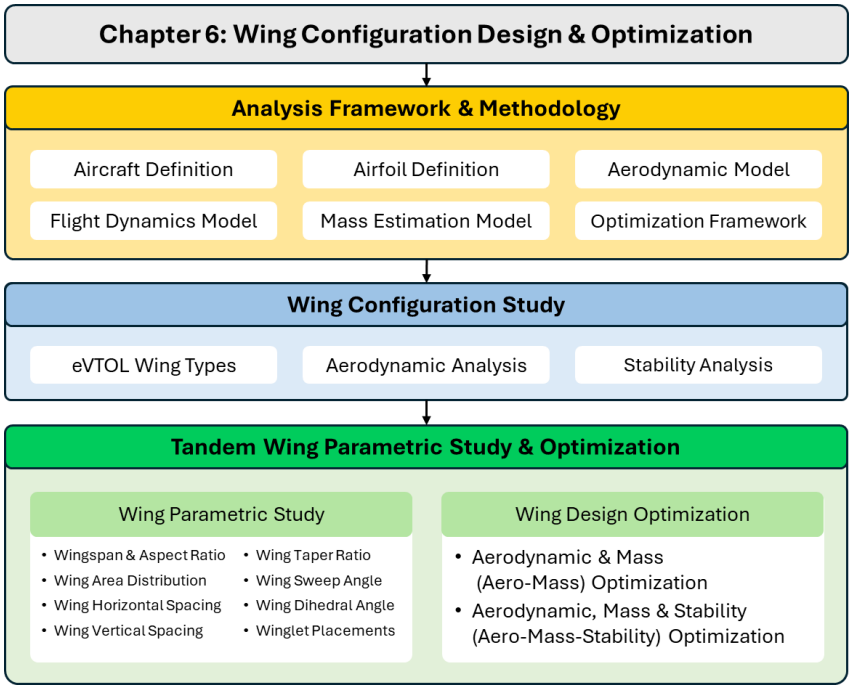

Figure 6.1: Chapter 6 - outline and flow diagram.

6.1 Analysis Framework and Methodology

To investigate various aircraft configurations and parametric variations of tandem wing aircraft, a Python package was developed to automate calculations, significantly reducing computational time. A VLM model was employed using AVL for the parametric and optimization studies. The analysis employed a VLM model using AVL for parametric and optimization studies, while airfoil drag polars accounting for viscous effects were generated using XFOIL in viscous mode [194]. AVL was selected for its reliable computational methods and ease of automation. To enhance efficiency, a Python wrapper for AVL was implemented, enabling streamlined aerodynamic and stability calculations as well as aircraft mass evaluations.

The aerodynamic setup and analysis method were validated against higher-order CFD calculations and deemed accurate and effective for performing parametric studies of various aircraft configurations. The VLM model, being a lower-order model, offers significantly lower computational time compared to CFD models. The structure of the developed framework is illustrated in Figure 6.2.

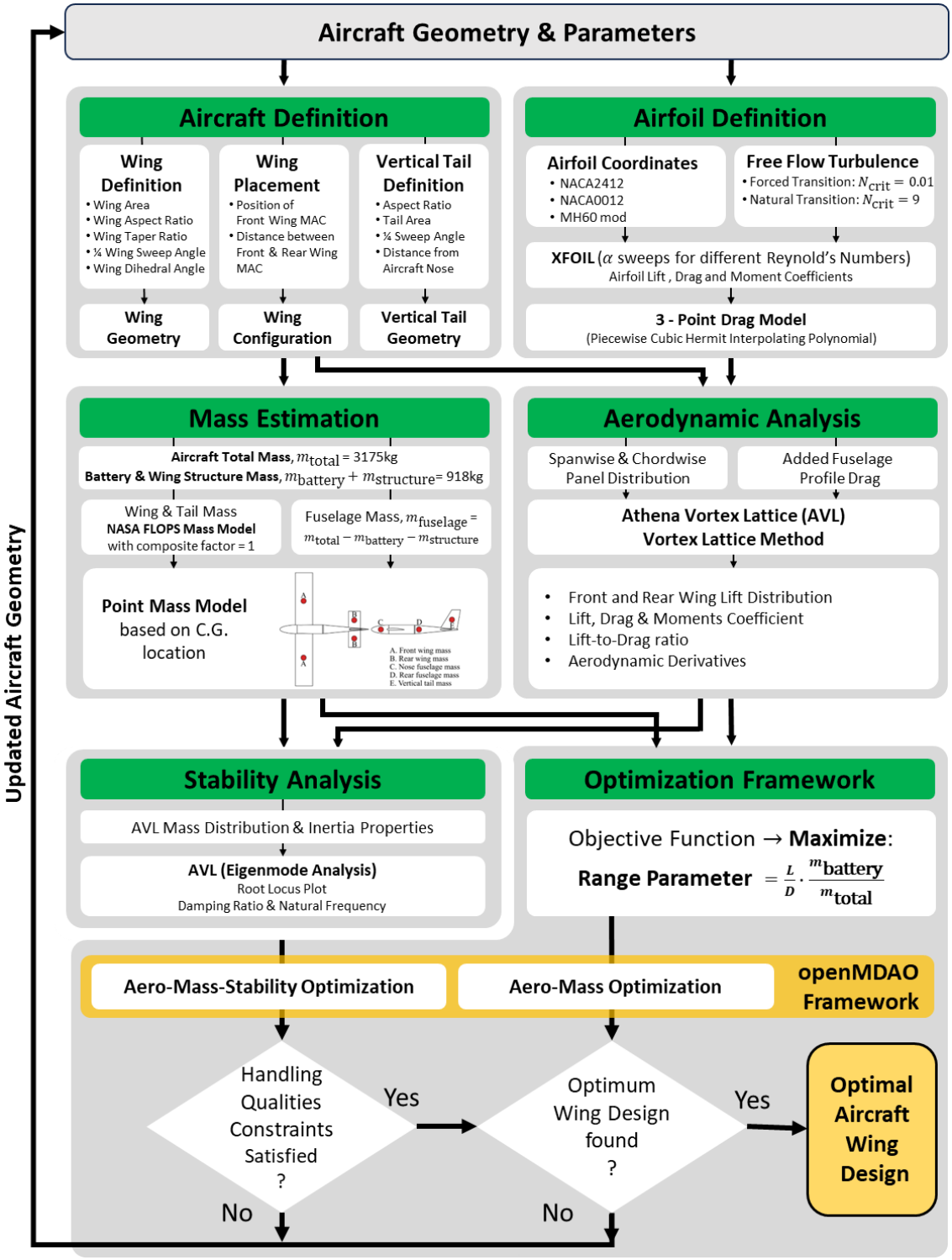

Figure 6.2: Structure of developed framework.

6.1.1 Aircraft and Airfoil Definition

The aircraft geometry focuses solely on the wing geometry, excluding the fuselage, detailed in Figure 6.3, (6.1) and (6.2). Key geometric parameters include wing area, aspect ratio, taper ratio, quarter chord sweep angle, and dihedral angle. These parameters define both the wing and horizontal stabilizer or canard surfaces. The vertical tail geometry is similarly defined. The wing configuration is specified by the distance of the MAC of the front wing from the aircraft nose and the distance between the MACs of the front and rear wings.

$$h_{tip} = \frac{1}{2}(b \tan \Gamma_{¼\ \mathrm{mac}}) \tag{6.1}$$

$$x_{\mathrm{tip}} = \frac{1}{4}(c_{\mathrm{root}} - c_{\mathrm{tip}}) + \frac{1}{2}(b \tan \Lambda_{¼\ \mathrm{mac}}) \tag{6.2}$$

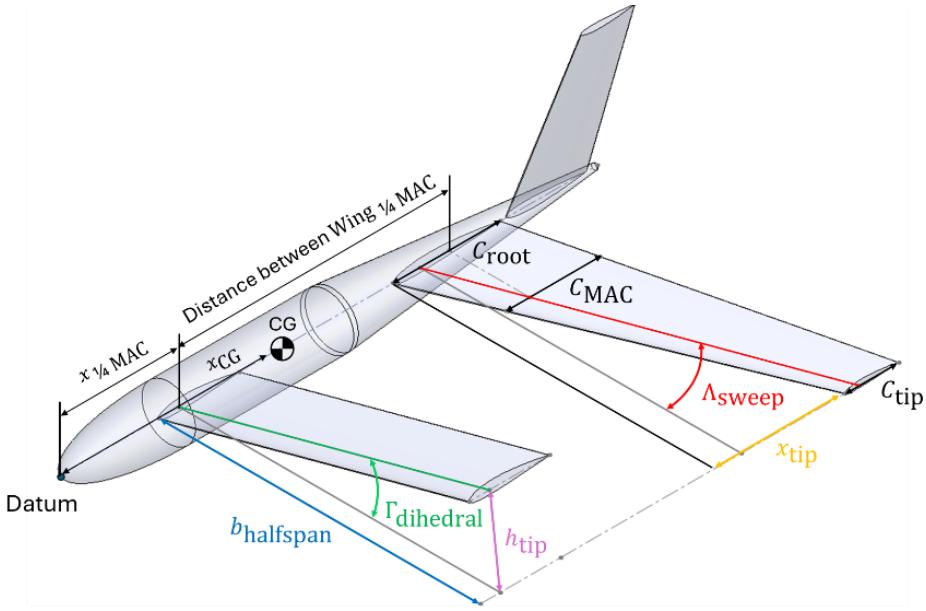

Figure 6.3: Definition of wing geometry and geometric orientations.

The airfoil definition and calculation methods use forced transition calculations to compare with CFD results under fully turbulent conditions. Natural transition conditions are used for other calculations to represent actual flight conditions. A three-point drag model was developed to account for viscous drag in the VLM calculations. This model splits the airfoil drag polar into distinct regions and fits curves to these regions using the least squares method, ensuring smooth transitions at the three points. Figure 6.4 shows the airfoil drag polars with three-point model fits for a Reynolds number of 7.2×10^6.

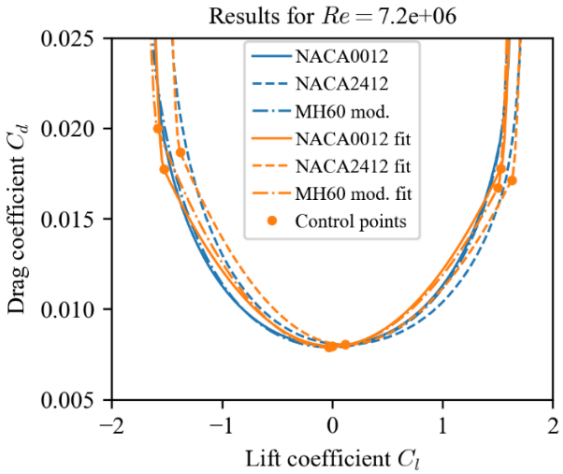

Figure 6.4: Airfoil drag polars with 3-point model fits for AVL analysis.

6.1.2 Aerodynamic Model

The aerodynamic analysis setup aims to accurately calculate wing lift, drag characteristics, and aerodynamic derivatives. Panel distribution was chosen to minimize discretization error and computational time. Panels are distributed equally between the front and rear wings to avoid trailing vortex proximity errors, as shown in Figure 6.5. An intermediate section ensures equal spanwise panel distribution when one wing is longer. A profile drag coefficient of 0.0021, calculated using Gotten et al.'s equations [195], was added to account for fuselage drag and held constant throughout analyses.

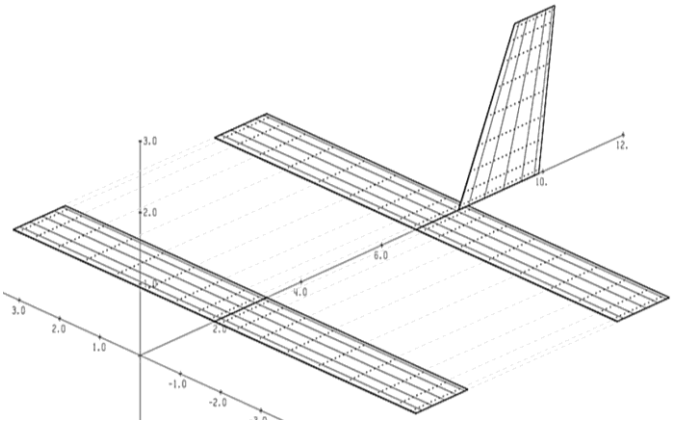

Figure 6.5: Tandem wing surface model with aligned panel distribution.

6.1.3 Mass Estimation and Flight Dynamics Model

Mass estimation and flight dynamics is calculated with the NASA's Flight Optimization System (FLOPS) model [196] and AVL [86]. Other mass estimation methods such as Raymer [172] and Roskam [197] provide various approaches to component weight estimation at the conceptual design stage. While all methods rely on regression equations, they differ in the parameters used, some focus on overall aircraft parameters, such as length, while others emphasize component-specific parameters. The FLOPS weight estimation method, which is similar to the Raymer and Roskam methods, is notable for its relatively smaller number of input parameters, making it easier to apply in early design phases. When applied to existing aircraft, FLOPS provided reasonable accuracy in predicting component weight. However, sensitivity studies revealed that these methods can exhibit significantly different trends when a single variable is altered, primarily due to their reliance on regression equations tailored to subsets of designs [198]. This highlights the need for verification with higher-order methods. Despite being based on real-world data, a common limitation across the methods is the lack of thorough documentation, particularly regarding the data sets and included categories, which complicates comparisons and the designer's understanding of the assumptions.

The mass distribution, defined by calculated point masses, facilitated the flight dynamics calculations using AVL's eigenvalue analysis. The setup involved defining the aircraft mass distribution with specific component masses and coordinates. A composites factor of 1.0 was assumed, reflecting the likely use of advanced composites in new eVTOL designs. The mass distribution was adjusted by varying the fuselage rear weight position to achieve the desired CG position. The wing and tailplane masses were split into two equal parts and positioned at the center of the left- and right-sides of the wings and tailplanes, respectively. The mass of the vertical tailplane was placed roughly at its center. The fuselage mass was divided into two parts, placed at the nose and rear of the fuselage, representing the nose and rear weights. This mass distribution was used by AVL to perform flight dynamics analysis.

To vary the CG position, the rear fuselage weight was made adjustable, allowing it to be shifted to achieve different CG positions. This method of variation simulates rearranging fuselage contents to alter the CG. The CG location could be specified directly or in terms of a Static Margin (SM). If specified as a SM, the required CG

location was calculated using (6.3) with the Neutral Point (NP) position. Once the CG position was known, (6.4) was used to determine the required location of the fuselage rear weight to place the CG at the specified location. After finding the new location of the fuselage rear weight, the mass distribution was updated accordingly.

$$x_{\text{cg}} = x_{\text{np}} - \text{SM} \times c_{\text{ref}} \tag{6.3}$$

$$x_{\text{rear fuselage}} = \frac{m_{\text{total}}\, x_{\text{cg}} - \sum_i x_i m_i}{m_{\text{rear fuselage}}} \tag{6.4}$$

6.1.4 Optimization Approach and Framework

The optimization process was implemented using OpenMDAO, an open-source Python-based framework widely applied in aerospace optimization studies [97–99]. It coupled AVL for aerodynamic analysis and FLOPS for mission performance and mass estimation. By iterating between these models, the framework ensured that the optimized design adhered to handling qualities and stability constraints while maximizing the range parameter. The optimization study of tandem wing aircraft adopts a holistic approach to aircraft design, with the primary objective being the maximization of flight range. The objective function is formulated as follows:

$$\text{Range} = \text{e} \cdot \eta \cdot \frac{L}{D} \cdot \frac{m_{\text{battery}}}{m_{\text{total}}} \cdot \frac{1}{g} \tag{6.5}$$

This equation demonstrates that the flight range of an electric aircraft depends on two key factors: aerodynamic efficiency, represented by L/D, and the battery mass fraction, $\frac{m_{\text{battery}}}{m_{\text{total}}}$. Improving aerodynamic efficiency (L/D) typically increases the structural weight of the wing, which may decrease the battery capacity and thus reduce the overall range. Since the MTGW is constrained to 3175 kg, any increase in wing weight directly reduces the allowable battery mass, highlighting a trade-off between structural and aerodynamic efficiency. The product $\frac{L}{D} \cdot \frac{m_{\text{battery}}}{m_{\text{total}}}$ is referred to as the range parameter and serves as the optimization target.

The optimization framework was developed to capture the interdependence of design variables, crucial in new eVTOL designs where flight range depends on both aerodynamic performance and battery mass allocation. The overall objective was to

maximize the range parameter, striking a balance between enhancing aerodynamic efficiency and minimizing structural weight penalties. The weights for the objective function terms were not arbitrarily assigned; rather, they are implicitly governed by the physics of the system. The objective function inherently balances aerodynamic performance (L/D) and battery mass fraction, as both are equally critical to maximizing range. Since these terms are expressed in multiplicative form, the optimization automatically identifies the trade-offs between them without requiring heuristic weight assignment. However, constraints were applied to ensure that handling qualities and flight stability requirements, standard for commercial passenger aircraft, were met. These constraints implicitly assign importance to aerodynamic stability, ensuring the optimization framework produces feasible and safe designs.

The flight stability constraints were defined according to the MIL-F-8785B standard for a Class II aircraft during Category A and B flight phases, which are pertinent for eVTOL aircraft during cruise, take-off, and landing [199, 200]. An additional constraint on the SM ensured a viable CG position. Table 6.1 summarizes the constraints used in the optimization. The short period constraint is calculated based on the thumbprint plot using (6.6). The phugoid mode damping ratio constraint was relaxed because the analyzed aircraft models are glider-like with fewer drag-producing components, resulting in naturally higher phugoid damping ratios. This relaxation avoids overly restrictive constraints that could hinder aerodynamic optimization.

$$\text{Short Period Thumbprint Plot Constraint} = \frac{\left(\zeta_{spo} - 0.7\right)^2}{0.28^2} + \frac{\left(\omega_{n_{spo}} - 0.5\right)^2}{0.11^2} \qquad (6.6)$$

Table 6.1: Handling qualities constraints for optimization.

Category	Variable	Lower Bound	Upper Bound
Longitudinal Stability (Pitch)	Static Margin	0.10	0.25
	Short Period Thumbprint Plot Constraint	-	1.00
	Phugoid Damping Ratio	0.025	-
Lateral Stability (Roll & Directional)	Roll Constant	0.00	1.40
	Dutch Roll Damping Ratio	0.08	-
	Dutch Roll Damping	0.15	-
	Dutch Roll Natural Frequency (rad/s)	0.40	-
	Spiral Time (s)	20.0	-

The optimizer used the Constrained Optimization by Linear Approximation (COBYLA) scheme, a local optimization algorithm, to find the optimal tandem wing designs [201]. Multiple initial conditions were tested to ensure a reliable local optimum, as COBYLA

does not guarantee a global optimum. Various global optimization algorithms, such as dual annealing and genetic algorithms, were also tested but did not yield satisfactory results due to several challenges. First, the global algorithms required significantly more computational time to converge due to the high-dimensional design space and the complex interdependencies among design variables, often resulting in incomplete convergence within a reasonable timeframe. Second, while global optimizers excel in exploring a broad design space, the solutions they produced lacked the precision necessary for detailed aerodynamic trade-offs, particularly in lift, drag, and stability analysis. Third, the global algorithms' performance was highly sensitive to tuning parameters such as population size and mutation rate, leading to inconsistent outcomes even after extensive parameter adjustments. Finally, the COBYLA approach proved more effective in refining solutions within constrained regions of the design space. By employing multiple starting points, the limitations of COBYLA as a local optimizer were mitigated, resulting in computationally efficient solutions that satisfied the design objectives. These findings highlight the practical and reliable nature of local optimization approaches for this study.

This methodology facilitated a comprehensive study of various tandem wing aircraft configurations, ensuring efficient aerodynamic and flight dynamics calculations, accurate mass estimation, and robust optimization to enhance eVTOL aircraft performance.

6.1.5 Reference Flight Conditions and Quantities

The reference flight conditions and quantities used in the analyses are summarized in Table 6.2. All calculations were conducted at sea level, with atmospheric conditions specified according to ISA [170]. Analyses were performed under steady level flight conditions, with the aircraft's pitching moment trimmed to zero, depending on the type of analysis. The reference values provided in Table 6.2 were employed to calculate all aerodynamic coefficients and aerodynamic stability derivatives.

These reference conditions ensure consistency and comparability across all analyses, providing a reliable basis for calculating aerodynamic properties and stability characteristics.

Table 6.2: Ambient conditions and input reference values.

Parameter	Value	Reference
Air Density (kg/m^3)	1.225	According to ISA standard.
Air Dynamic Viscosity (Pa-s)	1.81×10^{-5}	According to ISA standard.
Air Pressure (Pa)	101.325×10^3	According to ISA standard.
Reference Cruise Speed (km/h)	240	Typical cruise speed for eVTOL aircraft.
Reference MTGW (kg)	3175	Recommended by EASA Special Condition 2020.
Reference Wing Area (m^2)	26.0	According to baseline aircraft dimensions.
Reference Wing Chord (m)	2.0	According to baseline aircraft dimensions.

6.2 Wing Configuration Study

The results for aerodynamics and stability are presented for four baseline aircraft configurations, each defined by specific design parameters. Five test aircraft configurations were defined to isolate the effects of configuration on aerodynamics and stability, modeled after well-known aircraft for conventional, canard, flying wing and tandem wing, as introduced in Section 3.2. These models were resized to typical eVTOL dimensions.

The reference wingspan was limited to 15 m to enable vertical takeoff and landing on helipads, complying with eVTOL regulations. The reference MTGW for each aircraft was set at 3175 kg, following the EASA's Special Condition Guideline for eVTOL aircraft [60–62]. This weight constraint was maintained for all analyses except those varying the MTGW. These constraints keep the reference aircraft within the practical bounds of an eVTOL aircraft design.

A common fuselage and vertical tail were designed for all aircraft configurations, as shown in Figure 6.6. The fuselage is a generic cylindrical design, with dimensions allowing its use across all configurations. The vertical tail was sized based on a trade study of conventional aircraft, with parameters listed in Table 6.3.

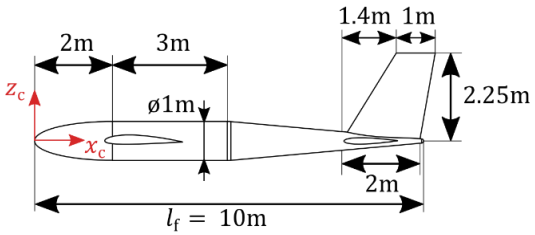

Figure 6.6: Side view with dimensions of fuselage and vertical tail.
A construction reference frame is placed at the nose.

Table 6.3: Sizing parameters for tail and canard surfaces.

Aerodynamic Surface	Tail to Wing Area Ratio	Aspect Ratio
Horizontal Tail/Canard	0.22	3.0 – 5.0
Vertical Tail	0.13	1.5

The vertical tail area was calculated from the wing area, using an aspect ratio of 1.5, within the typical range of 1.2 to 2.2 for conventional aircraft [202]. The NACA 0012 airfoil, depicted in Figure 6.7, was used for the vertical tail. Once sized, the vertical tail was held constant across all configurations to isolate its effects on aerodynamics and stability, ensuring that only the relative placement of the vertical tail with respect to the wing and tail surfaces influences aircraft performance.

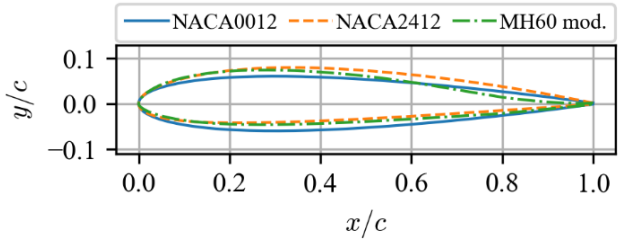

Figure 6.7: Airfoil geometry comparison.

The conventional aircraft configuration features a simple rectangular wing and horizontal stabilizer, designed using NACA 2412 and NACA 0012 airfoils respectively, as shown in Figure 6.8 (a). The wing's size was determined by baseline wing area and aspect ratio, while the horizontal stabilizer size was based on the average ratio of horizontal stabilizer area to wing area from conventional aircraft. A horizontal tail aspect ratio of 3 was chosen. The distance between the ACs of the wing and horizontal stabilizer, d_{ac} of 6 m, was kept constant to ensure stable characteristics.

The canard aircraft configuration closely resembles the conventional design, with identical wing and canard sizes and airfoil cross-sections, except the canard surface uses a NACA 2412 airfoil to serve as a lifting surface, as shown in Figure 6.8 (b).

The flying wing configuration uses a simple rectangular wing with a modified MH 60 airfoil with 12% thickness-to-chord ratio and 2° reflex at 20% trailing edge chord to ensure stability, resembling the NACA 2412 in aerodynamic performance, as shown in Figure 6.8 (c).

The tandem wing configuration includes two rectangular wings with NACA 2412 airfoils. To maintain comparability, the wingspan and aspect ratio were kept constant across configurations, with the total wing area split equally between the two wings. Two tandem wing configurations were defined: TWG-A (equal aspect ratio) and TWG-B (equal wingspan), both with d_{ac} of 5 m between the ACs, as shown in Figure 6.8 (d)

and (e). This dual approach provides a comprehensive comparison of tandem wing aircraft to other configurations, focusing on improving tandem wing performance.

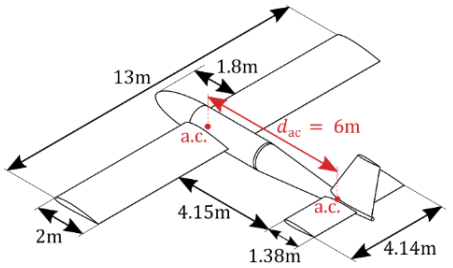

(a) Conventional aircraft (CNV).

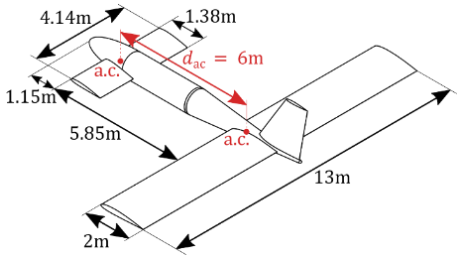

(b) Canard aircraft (CNR).

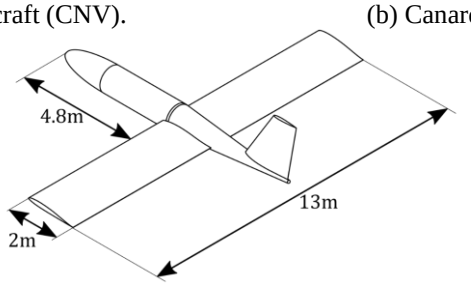

(c) Flying wing aircraft (FWG).

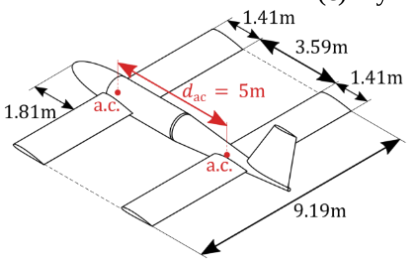

(d) Tandem Wing
Equal aspect ratio (TWG-A).

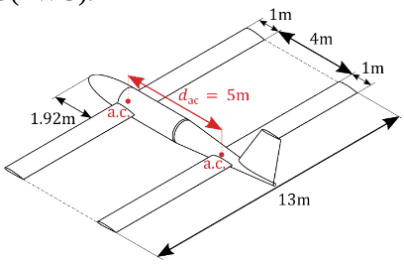

(e) Tandem Wing
Equal wingspan (TWG-B).

Figure 6.8: Isometric view of conventional, canard and flying wing aircraft.

Table 6.4 summarizes the geometrical parameters of each aircraft configuration used in this study. For simplicity, the horizontal stabilizer and canard are referred to as the rear wing and front wing, respectively, in the relevant configurations.

Table 6.4: Input parameters for baseline aircraft.

Surface	Parameter	CNV	CNR	FWG	TWG-A	TWG-B
Front Wing	Wingspan (m)	13.00	4.14	13.00	9.19	13.00
	Aspect Ratio	6.50	3.00	6.50	6.50	13.00
	Wing Area (m^2)	26.00	5.72	26.00	13.00	13.00
	Incidence Angle (°)	0.98	3.74	3.99	3.82	2.01
	Airfoil Profile	NACA2412	NACA2412	MH60mod.[1]	NACA2412	NACA2412
	¼ Chord Position (m)	2.30	1.50	5.30	2.17	2.17
Rear Wing	Wingspan (m)	4.14	13.00	-	9.19	13.00
	Aspect Ratio	3.00	6.50	-	6.50	13.00
	Wing Area (m^2)	5.72	26.00	-	13.00	13.00
	Incidence Angle (°)	-0.37	0.12	-	1.33	-0.10
	Airfoil Profile	NACA0012	NACA2412	-	NACA2412	NACA2412
	¼ Chord Position (m)	8.30	7.50	-	7.17	7.17
	CG Location (m)	2.51	6.26	5.05	3.52	3.77
	Static Margin	0.15	0.15	0.10	0.25	0.25

[1]MH60 mod.: Increased thickness-to-chord ratio of 12%, 2° additional reflex over last 20% of chord, and blunt trailing edge similar as NACA 4 series.

6.2.1 Aerodynamics Performance and Characteristics

The aerodynamic results for the baseline aircraft study include data from both the VLM model and CFD calculations. The CFD model incorporates fuselage lift and drag effects, whereas the VLM model accounts for fuselage drag through an added profile drag coefficient. All baseline aircraft configurations were trimmed at an angle of attack of 2.5° with lift equal to weight and $C_m = 0$, matching the CFD conditions. The aircraft were trimmed for the CG locations listed in Table 6.4 by adjusting the incidence angles or flap deflection angles. The conventional and tandem wing aircraft were trimmed by altering the rear wing incidence angle, the canard aircraft by changing the front wing incidence angle, and the flying wing by adjusting the reflex angle over the final 20% of the chord.

Figure 6.9 (a) shows the variation of the lift coefficient with angle of attack, indicating that all configurations except TWG-A have similar lift curve slopes. TWG-A's lower slope, despite having the same aspect ratio, suggests a lower effective aspect ratio for tandem wing configurations [203]. Both VLM and CFD data show similar trends, with the main deviation in the FWG configuration likely due to differing treatments of the reflex effect.

Figure 6.9 (b) depicts the L/D variation with the lift coefficient, where VLM results align closely with CFD data. The FWG configuration has the highest L/D due to the absence of a drag-producing horizontal tail, while TWG-A has the lowest L/D due to its lower effective aspect ratio. Figure 6.9 (c) illustrates L/D variation with airspeed, mirroring the trends in Figure 6.9 (b). This parameter is crucial for determining optimal cruise speed. The VLM model shows errors at lower airspeeds compared to CFD, likely due to high trim angles of attack beyond the VLM model's applicability. Figure 6.9 (d) shows the change in trim angle of attack with SM for all aircraft configurations. The FWG configuration experiences a large variation in trim angle of attack with changes in SM, likely due to its trimming method using flap deflection. In contrast, the trim angles of attack for the other configurations remain relatively constant across the SM range.

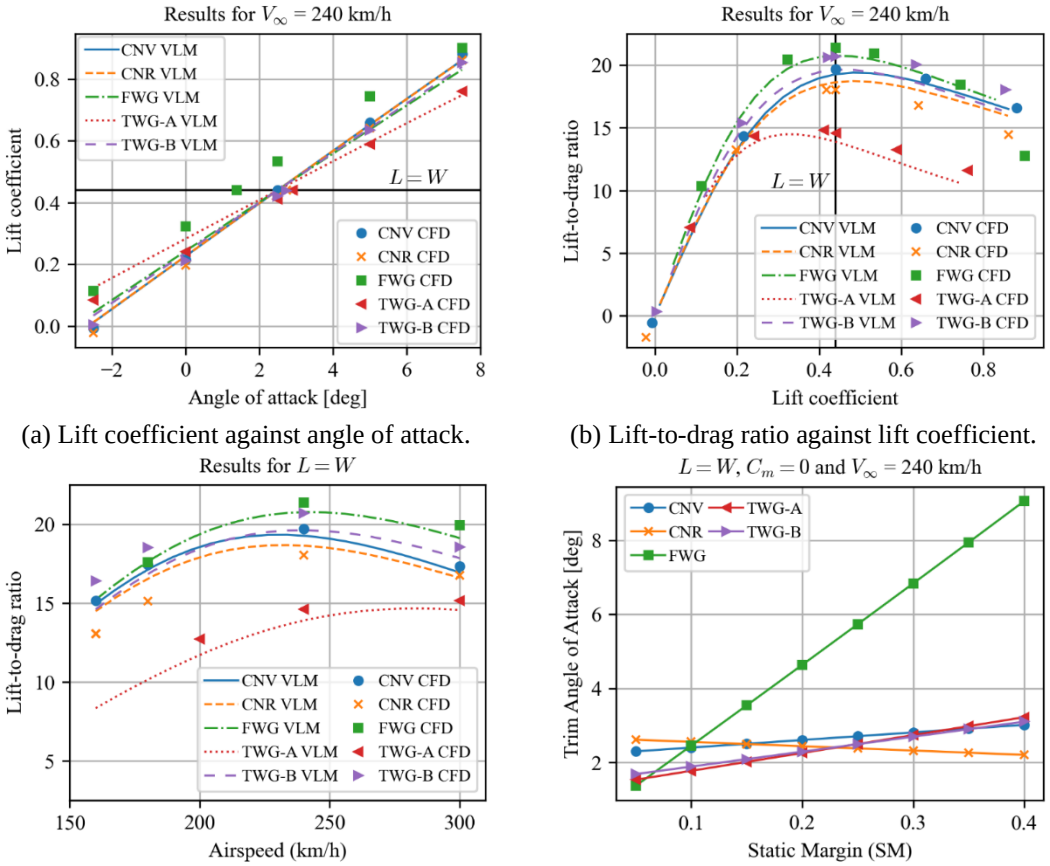

(a) Lift coefficient against angle of attack.

(b) Lift-to-drag ratio against lift coefficient.

(c) Lift-to-drag ratio against airspeed.

(d) Trim angle of attack against static margin.

Figure 6.9: Aerodynamic analysis results for wing configuration study.

The final aspect of aerodynamics analyzed is the spanwise lift distribution over the wings, focusing on the TWG-B configuration. Figure 6.10 (a) and (b) shows the lift distribution of the front and rear wings of TWG-B, respectively. Figure 6.10 (a) indicates that the front wing's lift distribution from the VLM model aligns well with the CFD model, except for fuselage effects and near-stall angles, which are beyond the VLM model's applicability. However, the rear wing lift distribution from the VLM model deviates significantly from the CFD predictions, especially near the tip where the VLM model underpredicts the section lift coefficient. This discrepancy is explained by Figure 6.11 (c), which shows the front wing's tip vortex enhancing suction on the rear wing which increases the lift at the wingtips, an effect not captured by the VLM model. Overall, the VLM model results align reasonably well with CFD data, making it suitable for aircraft conceptual design and for quick parametric and optimization studies of the tandem wing configuration.

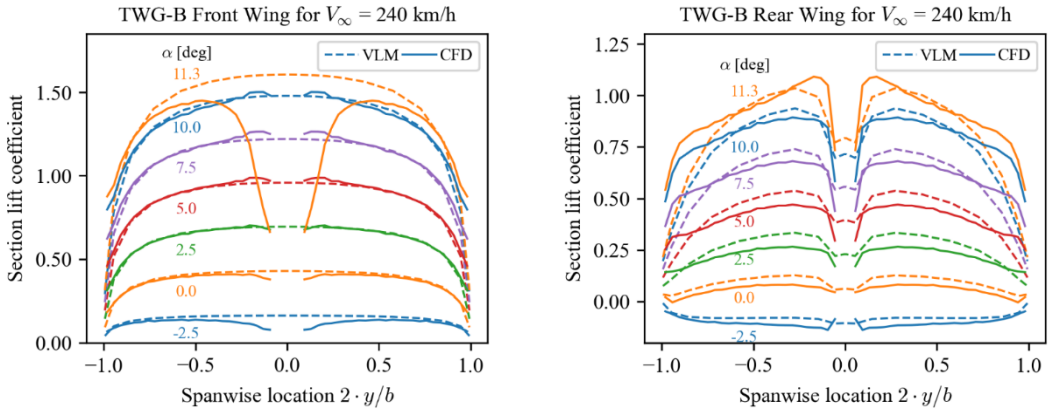

(a) Front wing lift distribution. (b) Rear wing lift distribution

Figure 6.10: Tandem wing spanwise lift distribution at various angle of angle.

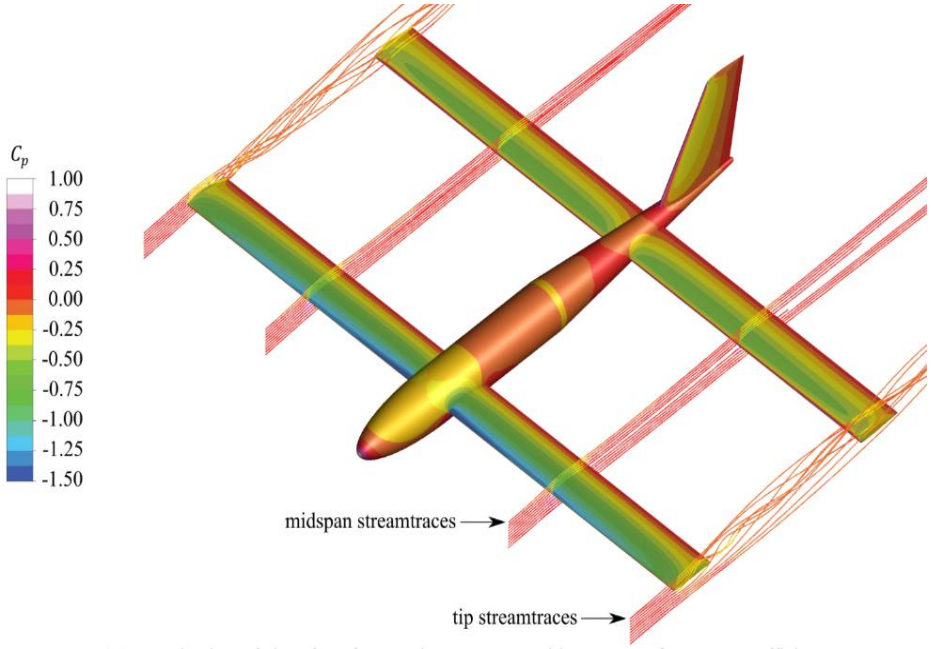

(a) Isometric view of aircraft surfaces and streamtraces with contours of pressure coefficient.

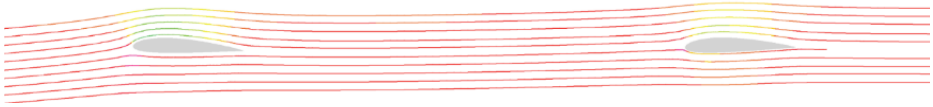

(b) Sideview of midspan streamtraces with contours of pressure coefficient.

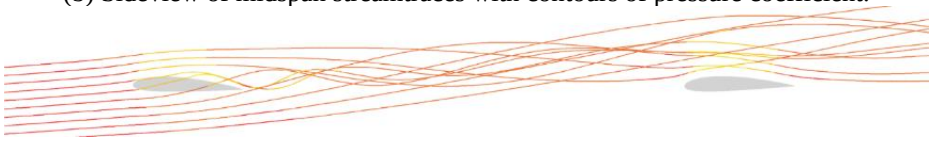

(c) Sideview of tip streamtraces with contours of pressure coefficient.

Figure 6.11: Pressure contours on TWG-B surfaces and stream traces.

6.2.2 Longitudinal Stability and Handling Qualities

To discuss stability and handling qualities, the VLM model's pitching moment data is compared with CFD data. Figure 6.12 (a) shows the variation of the pitching moment coefficient with the angle of attack. Significant differences exist between the VLM and CFD results, likely due to fuselage-wing interactions in the CFD model. However, the average slope of the pitching moment data is similar for both VLM and CFD models, supporting the flight dynamics calculations performed, as the slope gradient is more critical than the coefficient value.

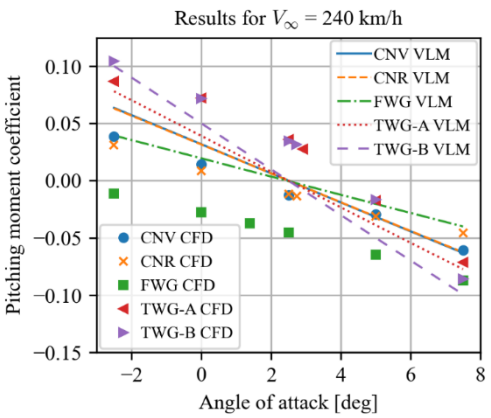

(a) Pitching moment coefficient against angle of attack.

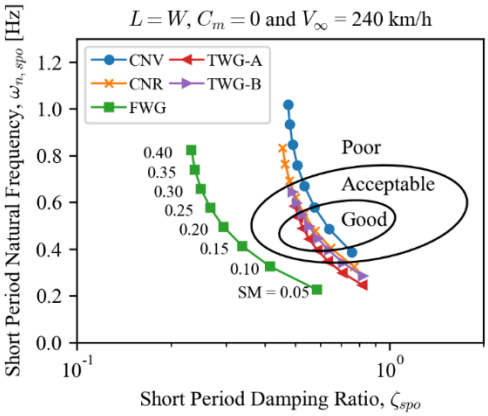

(b) Short period mode handling qualities.

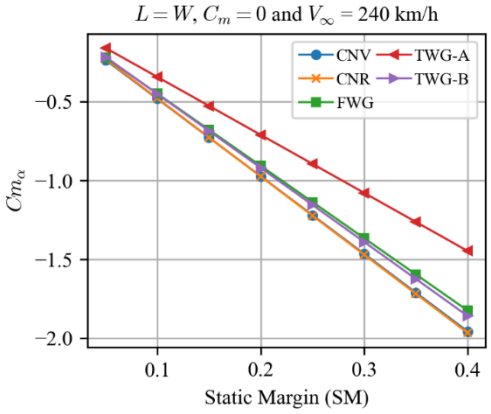

(c) Pitch stiffness against static margin.

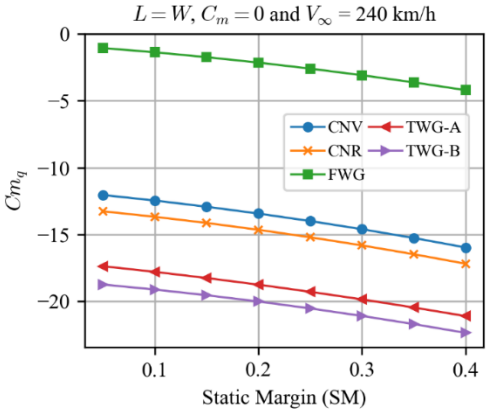

(d) Pitch damping against static margin.

Figure 6.12: Short period handling qualities results.

The comparison of handling qualities starts with the short period mode behavior of each aircraft. Figure 6.12 (b) shows the thumbprint plot of the short period mode for each baseline aircraft. As the SM increases, the short period mode handling qualities of each aircraft, except the flying wing, transition from Poor to Good and back to Poor. This corresponds to the pitch stiffness and damping data shown in Figure 6.12 (c) and (d). The flying wing consistently exhibits poor short period mode handling due to low pitch

damping, resulting from the absence of a horizontal tail and insufficient reflex effect from the MH 60 airfoil. The differences in short period mode handling qualities are directly related to variations in pitch stiffness and damping. Figure 6.12 (b) and Figure 6.12 (d) show these variations with SM for each aircraft. Except for the TWG-A aircraft, pitch stiffness is similar across configurations. Pitch damping trends are more revealing: the flying wing has the lowest pitch damping, the tandem wing the highest, with conventional and canard aircraft in between. The absence of a tail surface in the flying wing reduces pitch damping, while the rear wing of the tandem wing likely enhances it by acting as a large tail surface.

The next stability mode of interest is the phugoid mode, analyzed through the damping ratio. Figure 6.13 (a) shows the variation of phugoid mode damping ratio with SM for each aircraft. The damping ratio generally decreases with a reduction in SM but increases slightly at very low SMs, except for the flying wing aircraft, which continues to decrease. The TWG-B tandem wing has the lowest phugoid mode damping ratio among all aircraft. This is expected as the phugoid mode damping ratio is inversely proportional to the L/D ratio of an aircraft [199]. Hence, TWG-A, with a higher L/D, has a higher damping ratio compared to TWG-B. The flying wing's anomalous behavior is due to its large variation in trim angle of attack with SM. Previous studies indicate that phugoid mode damping increases at large angles of attack [204]. To further explore the dependence of phugoid mode damping on L/D, Figure 6.13 (b) plots the damping ratio against airspeed. Aircraft with higher L/D, like the flying wing, exhibit lower phugoid mode damping ratios. Conversely, the TWG-A, with the lowest L/D, shows the highest damping ratios.

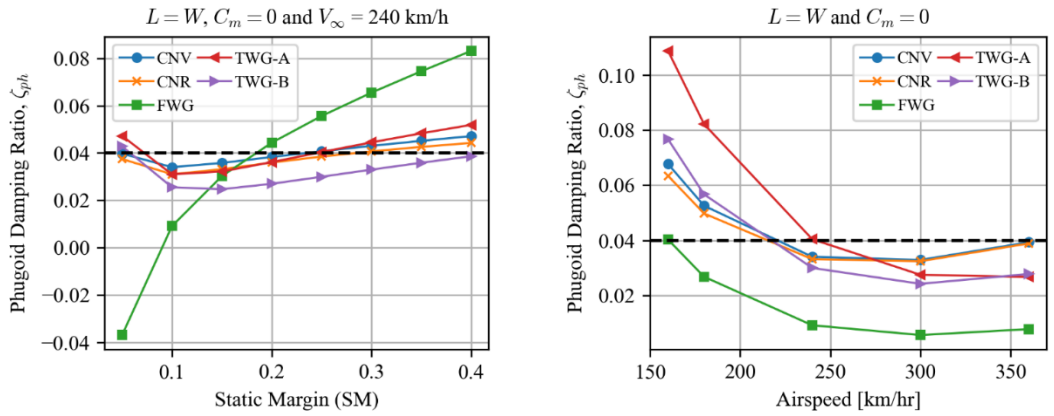

(a) Phugoid damping ratio against static margin. (b) Phugoid damping ratio against airspeed.

Figure 6.13: Phugoid handling qualities results.

6.2.3 Lateral Stability and Handling Qualities

The roll mode, a highly damped lateral stability mode, shows little dependence on SM and is primarily influenced by aircraft design. Figure 6.14 (a) illustrates that roll mode time constants remain constant with varying SMs, with differences attributed to aircraft configuration.

Figure 6.14 (b) shows the Dutch roll characteristics varying with SM. All configurations achieve Level 1 flying qualities for Dutch roll mode, with damping ratio and natural frequency increasing with SM. This improvement in Dutch roll stability correlates with increased directional stability, as seen in Figure 6.14 (c), due to a longer moment arm of the vertical tail at higher SMs. The canard configuration has the lowest directional stability due to its short vertical tail moment arm, resulting from its aft CG position, which may cause Dutch roll stability issues [205].

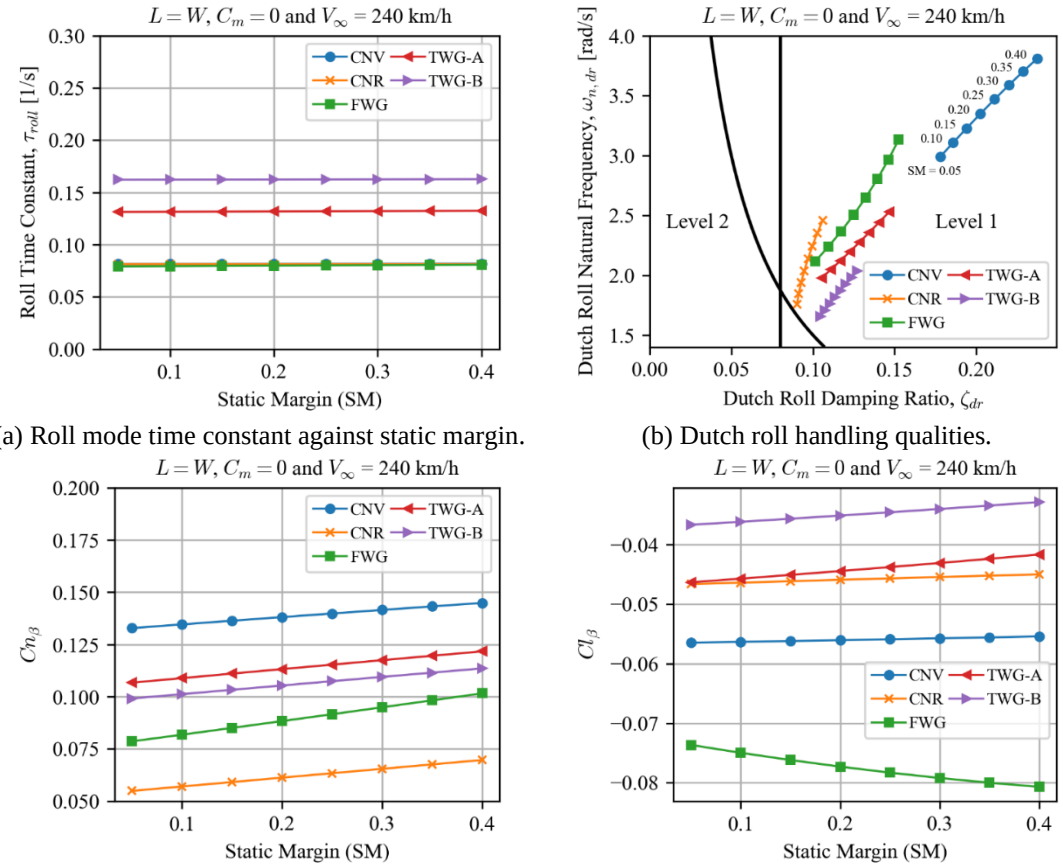

(a) Roll mode time constant against static margin.

(b) Dutch roll handling qualities.

(c) Directional stability against static margin.

(d) Lateral Stability against static margin.

Figure 6.14: Roll and dutch roll handling qualities results.

The Dutch roll behavior trends stem from variations in directional stability and dihedral effect. Figure 6.14 (c) and (d) show that while directional stability improves with increased SM, the dihedral effect remains constant. This enhancement in directional stability, rather than lateral stability, primarily contributes to better Dutch roll handling qualities at higher SMs.

The final stability mode addressed is the Spiral mode. Figure 6.15 (a) shows the variation of the spiral mode eigenvalue with SM. For the flying wing aircraft, the eigenvalue becomes more negative with increasing SM, indicating greater spiral mode stability and a higher time to double amplitude. This is linked to the variation in angle of attack shown in Figure 6.9 (d). As the angle of attack increases, spiral mode stability also increases. Reference suggests that aerodynamic interference between the wing and vertical tail at high angles of attack reduces vertical tail effectiveness, decreasing directional stability and enhancing spiral mode stability [204].

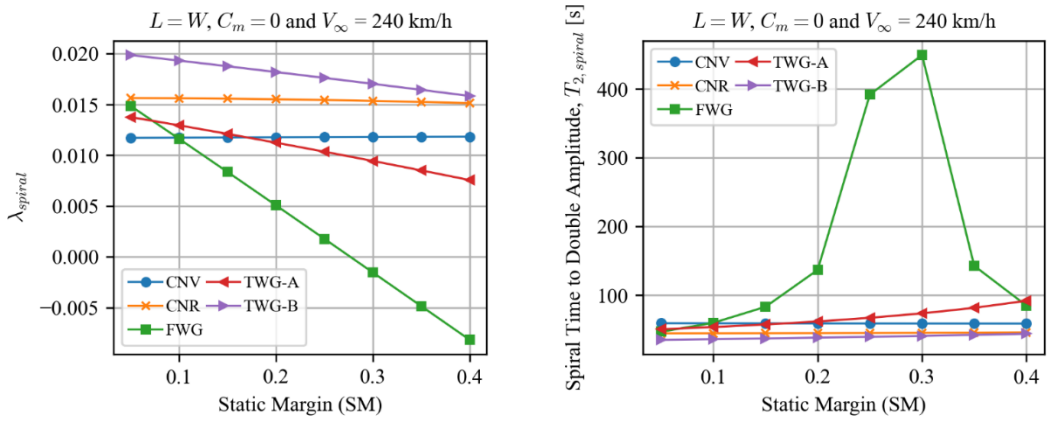

(a) Spiral mode eigenvalue against static margin.

(b) Spiral mode time to double amplitude against static margin.

Figure 6.15: Spiral mode handling qualities results.

Figure 6.15 (b) shows the variation of the time to double amplitude of the spiral mode with SM. The time to double amplitude for conventional and canard aircraft remains fairly constant with changes in SM, while it increases slightly for the tandem wing aircraft. The flying wing aircraft exhibits significant variation in time to double amplitude with SM changes. This anomalous trend in the flying wing aircraft is due to the spiral mode eigenvalue: as the eigenvalue approaches zero, the time to double amplitude first increases and then decreases as the eigenvalue becomes more negative. This inverse relationship to the absolute eigenvalue is also observed in the tandem wing aircraft, explaining the increased time to double amplitude for these configurations.

The stability and handling qualities results are useful for aircraft designers to determine the optimal CG position for different aircraft configurations. Table 6.5 presents the recommended SM range for each configuration. The most constraining factor in determining a good SM is the aircraft's longitudinal stability, particularly the short period mode. Although the phugoid mode damping falls below the required limit for certain SMs, it is important to note that the aircraft models analyzed in this study are glider-like, and full-aircraft models will likely have higher drag and thus higher phugoid mode damping.

Table 6.5: Static margin range for good handling qualities.

Aircraft Wing Configuration	Label	Good Static Margin Range
Conventional Wing	CNV	0.05 – 0.15
Canard Wing	CNR	0.10 – 0.20
Flying Wing	FWG	0.10 – 0.20
Tandem Wing (Equal Aspect Ratio)	TWG-A	0.20 – 0.35
Tandem Wing (Equal Wingspan)	TWG-B	0.15 – 0.30

The average CG range for conventional aircraft configurations has been well studied. For general aviation aircraft, the average CG position is typically between 5% MAC and 30% MAC [206]. The CG positions reported in this study fall between 10% MAC and 20% MAC, aligning with the typical range for General Aviation (GA) aircraft. This confirms that the results are reasonable and consistent with findings from other studies.

6.3 Parametric Study of Tandem Wing

A defined baseline tandem wing aircraft configuration, based on the TWG-A and TWG-B tandem wing configurations, was specified as a reference for the parametric and optimization study. The parametric study is evaluated at the reference conditions in Table 6.2. The geometry includes two rectangular wings and a generic cylindrical fuselage. The wings use a NACA 2412 airfoil profile, while the vertical tail uses a NACA 0012 airfoil, chosen for their generality. The baseline aircraft parameters, listed in Table 6.6, are parameterized to facilitate variations in geometry and performance analysis. These parameters reflect realistic design choices for eVTOL aircraft, based on previous trade studies and aviation regulatory guidelines.

Table 6.6: Parameters of baseline tandem wing aircraft.

Parameter	Front Wing	Rear Wing	Winglet
Wingspan (m)	10.00	10.00	Variable
Root Chord (m)	1.30	1.30	1.30
Airfoil Profile	NACA2412	NACA2412	NACA0012
Aspect Ratio	7.69	7.69	-
Taper Ratio	1.0	1.0	0.5
Surface Area (m^2)	13.00	13.00	Variable
Incidence Angle (°)	3.256	0.8891	-2.0
¼ Chord Position (m)	2.1676	7.1676	-
¼ Sweep Angle (°)	0.0	0.0	40.0
Dihedral / Cant Angle (°)	0.0	0.0	0.0
Twist Angle (°)	0.0	0.0	0.0
CG Location (m)	3.5845		
Reference Static Margin	0.25		

All calculations for this parametric study were performed at sea level and a cruise speed of 240 km/h. Steady level flight conditions were assumed, with the pitching moment trimmed for stability by varying the rear wing incidence angle. The SM was maintained at 0.25. The L/D was used to compare aerodynamic efficiency, while stability derivatives evaluated flight stability.

The aircraft wingspan was chosen to be 10 m for compact dimensions suitable for helipads. The reference MTGW was set at 3175 kg according to EASA guidelines [60–62]. The total wing area was 26 m², reflecting typical eVTOL wing loading. The front and rear wing incidence angles were chosen to trim the aircraft at a 2.5° angle of attack at 240 km/h. The vertical tail was sized based on the comparison of the vertical tail area to wing area ratio in conventional aircraft, with an average ratio of 0.13 used for the design. Additional vertical tail parameters were sourced from statistical data in [202].

A pair of winglets was also implemented in this study. While the design of winglets is complex and typically requires a dedicated study, a simple winglet design was adopted based on [207]. The root chord of the winglet matches the tip chord of the wing, using the NACA 0012 airfoil profile. The winglet area was made a free variable to study its impact on the performance of a tandem wing aircraft.

A comprehensive set of wing design variables was chosen to determine the best design choices for a tandem wing aircraft. These variables and their lower and upper bound ranges are summarized in Table 6.7, which includes illustrations of the AVL models for each variation. Each design parameter was varied independently to isolate its impact on aerodynamics and stability, with other parameters held at baseline values from Table 6.6.

Table 6.7: Design variables for tandem wing parametric study.

Design Parameter	Lower Bound	Upper Bound
Wingspan	9.0 m 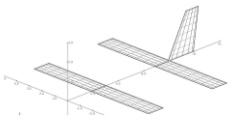	13.0 m 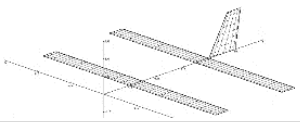
Front Wing Area Fraction (Ratio of front wing area to combined area of both wings)	0.35 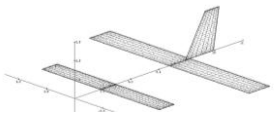	0.65 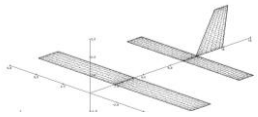
Horizontal Distance Between Wings (Distance between aerodynamic centers of the two wings)	4.0 m 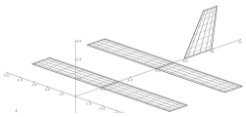	6.0 m 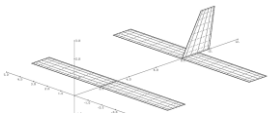
Vertical Distance Between Wings (Front Wing Height)	-0.5 m 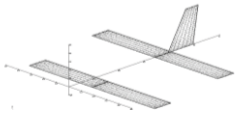	0.5 m 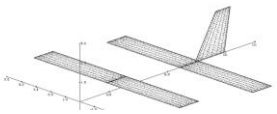
Wing Taper Ratio	0.2 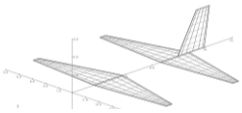	1.0 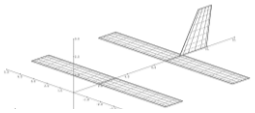
Front Wing Sweep Angle	-10.0 º 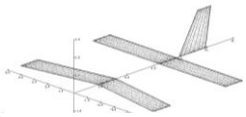	0.0 º 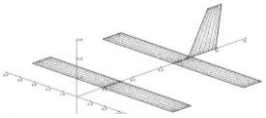
Rear Wing Sweep Angle	0.0 º 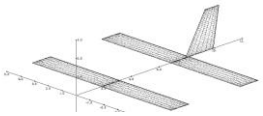	25.0 º 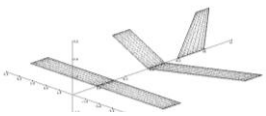
Combined Sweep Angle (Rear Wing: 25.0 º)	Front Wing: -10.0 º 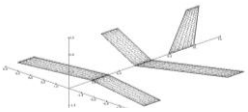	Front Wing: 0.0 º 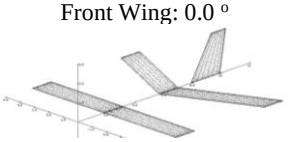
Front Wing Dihedral Angle	-5.0 º 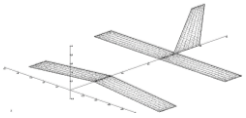	5.0 º 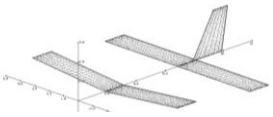
Rear Wing Dihedral Angle	-5.0 º 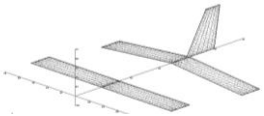	5.0 º 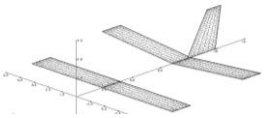
Winglet Position	Front Wing 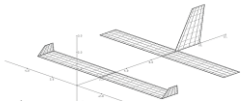	Rear Wing 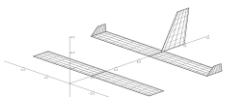

6.3.1 Wingspan and Wing Aspect Ratio

The wingspan and wing aspect ratio are critical design parameters for any aircraft. Figure 6.16 (a) presents a parametric study of tandem wing aircraft span, varying at fixed area, chord, and aspect ratio. Increasing span at a fixed area significantly boosts the L/D due to a rise in aspect ratio, as the downwash is distributed over a wider span, reducing induced drag. However, increasing span at a constant aspect ratio only marginally enhances L/D, as it increases wing area and profile drag. This increase in wingspan is accompanied by an increase in structural weight. Figure 6.16 (b) shows that wing mass significantly increases with span, leading to structural inefficiency and affecting the aircraft's range, which depends on both aerodynamic performance and structural mass.

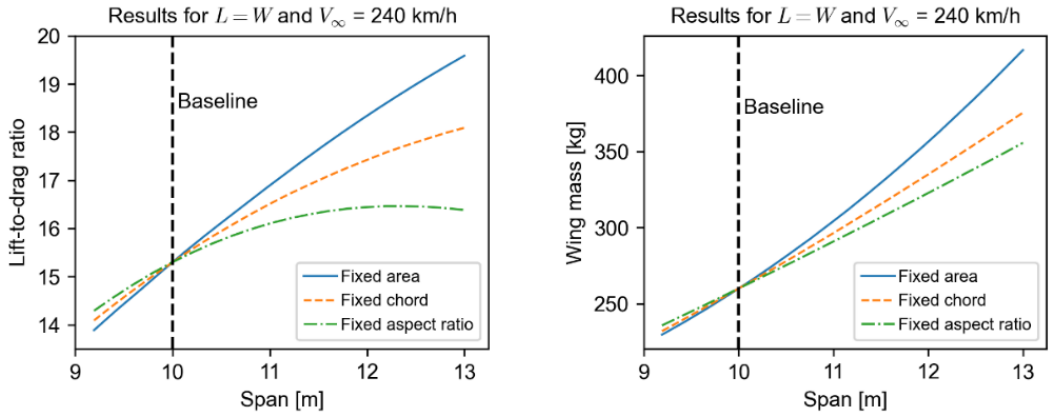

(a) Lift-to-drag ratio against wingspan. (b) Wing mass against wingspan.

Figure 6.16: Parametric results for wingspan and wing mass.

A study on the direct effect of increasing span and aspect ratio on the range parameter is shown in Figure 6.17. This parametric study of the range parameter $\frac{L}{D}.\frac{m_{\text{battery}}}{m_{\text{total}}}$, reveals that as wingspan and aspect ratio increase, the range parameter initially rises, reaches a maximum of 4.7626, and then decreases with further increases.

This indicates an optimal wingspan and aspect ratio for maximum range. The trend occurs because increased wingspan and aspect ratio enhance aerodynamic efficiency but also increase structural weight, reducing the battery mass fraction. The optimal condition balances increased aerodynamic efficiency and reduced battery mass fraction, crucial for achieving the best flight performance.

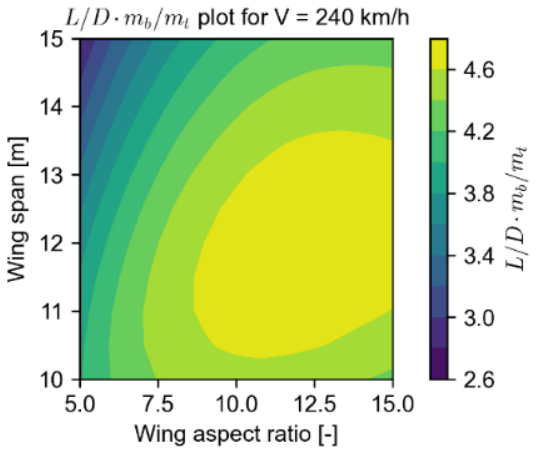

Figure 6.17: Range parameter against wingspan and aspect ratio.

6.3.2 Wing Area Fraction

Figure 6.18 (a) illustrates how L/D and front wing lift fraction vary with front wing area fraction, keeping CG position and wing incidence angles constant. The aircraft is not trimmed to $C_m = 0$, causing the larger wing to generate more lift, as shown in Figure 6.18 (a). The results indicate that unequal wing areas improve aerodynamic efficiency due to the constant aspect ratio of individual wings. Keeping the aspect ratio constant, unequal wing areas increase the overall span, reducing induced drag by spreading downwash over a larger span. Additionally, unequal wing areas minimize aerodynamic interference between the longer and shorter wings, further enhancing aerodynamics.

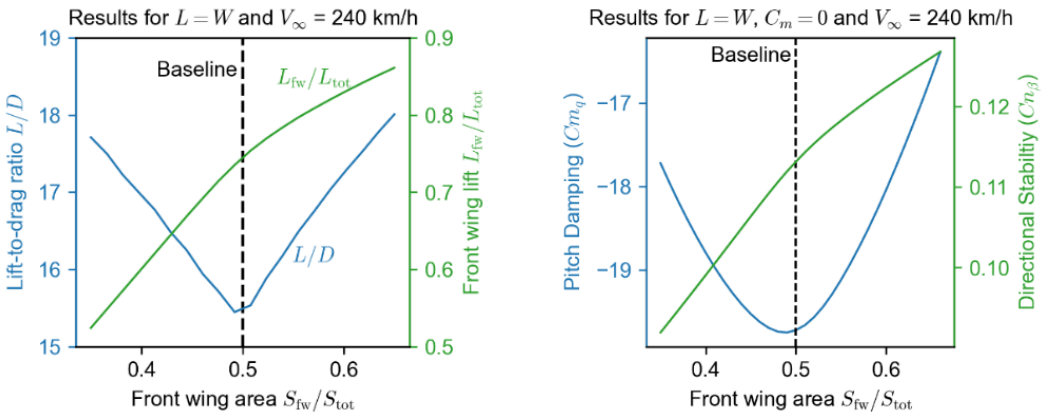

(a) Lift-to-drag ratio against front wing area fraction.

(b) Pitch and directional stability against front wing area fraction.

Figure 6.18: Parametric results for front wing area fraction.

Figure 6.18 (b) shows that equal wing areas provide the best pitch damping, as larger rear wings act as more efficient tail surfaces, and larger front wings serve as more efficient canard surfaces. This setup maximizes pitch damping and enhances directional

stability. With a constant SM, the CG position shifts with the aircraft's NP. Increasing the front wing area shifts the NP forward, allowing a more forward CG position. This forward CG increases the vertical tail's moment arm, improving directional stability. Conversely, reducing the front wing area shifts the NP and CG towards the rear wing, decreasing the vertical tail's moment arm and thus reducing directional stability, which may also negatively impact Dutch roll stability.

A parametric study of CG location was conducted to understand its effect on aerodynamic efficiency, with the constraint of $C_m = 0$ for the design condition causing variations in lift distribution between the aircraft's wings. Figure 6.19 presents the results, with CG location specified relative to the AC of the front wing and normalized by the distance between the front and rear wing ACs.

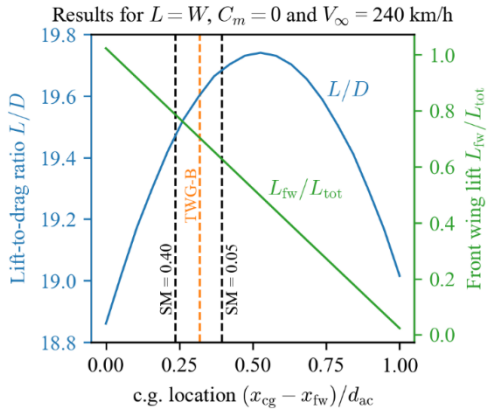

Figure 6.19: Lift-to-drag ratio and front wing lift fraction against CG location.

The results show that CG location significantly affects the aerodynamic efficiency. There is an optimal CG location where the lift is evenly distributed between the front and rear wings, yielding the best aerodynamic performance. However, this optimal CG position results in a negative SM, making the aircraft unstable. This highlights a design trade-off between aerodynamics and stability in tandem wing aircraft, as noted by Andrews and Perez [165]. To balance this trade-off, exploring variations in relative wing sizes is recommended.

6.3.3 Horizontal Wing Distance

Increasing the distance between the wing and tail of an aircraft conventionally improves longitudinal stability. A parametric study was conducted on the effect of varying the horizontal wing distance, d_{ac} in tandem wing aircraft. Figure 6.20 shows that increasing the distance between wing ACs significantly enhances pitch damping. However, as noted in the wing configuration study, there is an optimal pitch damping that provides the best handling qualities. Therefore, d_{ac} should be adjusted to achieve this optimal damping.

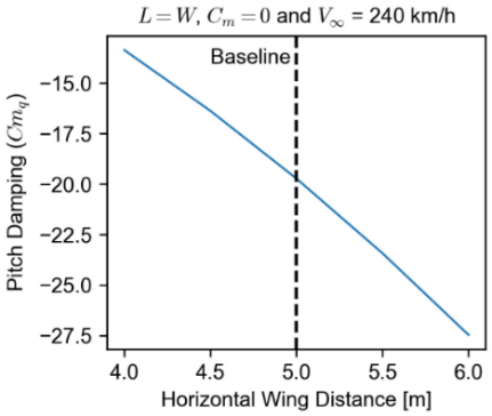

Figure 6.20: Pitch damping against horizontal wing distance.

6.3.4 Vertical Wing Distance

The height difference between the front and rear wings affects aerodynamic interaction in tandem wing aircraft. Figure 6.21 shows that positioning the front wing above or below the rear wing improves aerodynamic efficiency. This creates a non-planar system, reducing induced drag by spreading the front wing's downwash vertically, which lowers the induced angle of attack on the rear wing. This vertical spread of the downwash changes the momentum, influencing a larger air mass with a lower average velocity change which reduces energy expenditure and drag [208]. The effect is similar for both raising and lowering the front wing.

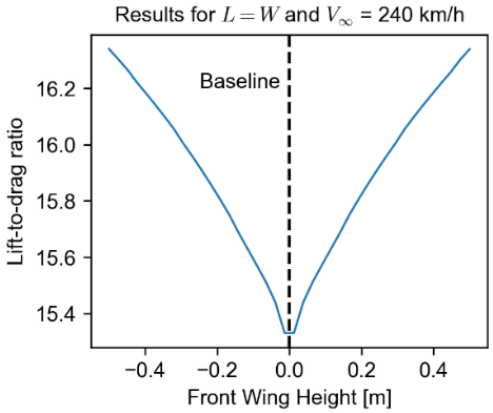

Figure 6.21: Lift-to-drag ratio against front wing height.

6.3.5 Wing Taper Ratio

The taper ratio of a wing affects the spanwise lift distribution and induced drag. A lower taper ratio shifts the lift distribution towards an elliptical shape, reducing induced drag. Historically, an optimal taper ratio is between 0.3 and 0.4, yielding lift distributions closest to elliptical and minimizing induced drag. However, this may differ for tandem wing aircraft. To investigate, a parametric study of wing taper ratio was conducted. Figure 6.22 shows that the L/D varies parabolically with taper ratio, with the optimal ratio at 0.5, higher than the typical range, although the L/D variation is minimal. Thus, for tandem wing configurations, the best aerodynamic efficiency is achieved with a taper ratio of 0.5 on both wings.

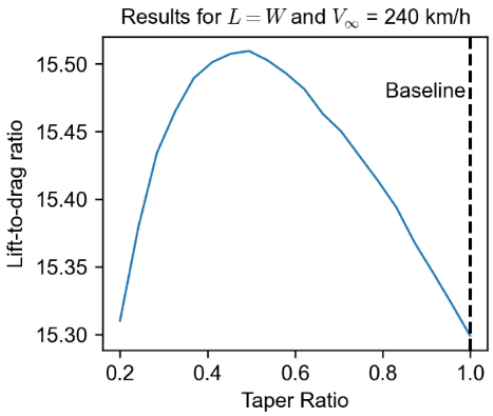

Figure 6.22: Lift-to-drag ratio against taper ratio.

6.3.6 Wing Sweep Angle

Wing sweep minimally affects aerodynamic efficiency, as shown in Table 6.8. Forward sweep on the front wing slightly increases efficiency, while rearward or combined sweeps decrease it. Therefore, sweeping the wings of a tandem wing aircraft should prioritize stability improvements over aerodynamic efficiency.

Table 6.8: Effect of wing sweep on aerodynamic efficiency.

Sweep Angle Parameter (°)	Front Wing	Rear Wing	Lift-to-Drag Ratio
Baseline Aircraft	0.0	0.0	15.300
Non-Baseline Aircraft with Sweep Angles	0.0	25.0	15.162
	-10.0	0.0	15.340
	-10.0	25.0	15.206

The wing sweep angle primarily impacts lateral stability and has a lesser effect on aerodynamic efficiency. It influences directional stability by shifting the aircraft's AC. A forward sweep of the front wing shifts the AC forward, allowing a more forward CG position and increasing the vertical tail moment arm, thus enhancing directional stability, as shown in Figure 6.23 (a). This effect is less pronounced for the rear wing sweep angle due to the AC's bias towards the front wing, resulting in minimal NP and CG position changes with rear wing sweep variations.

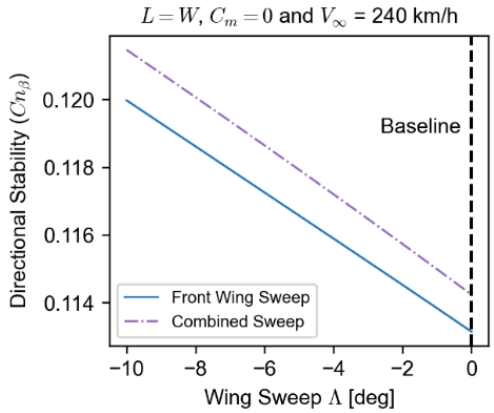

(a) Directional stability against wing sweep angle.

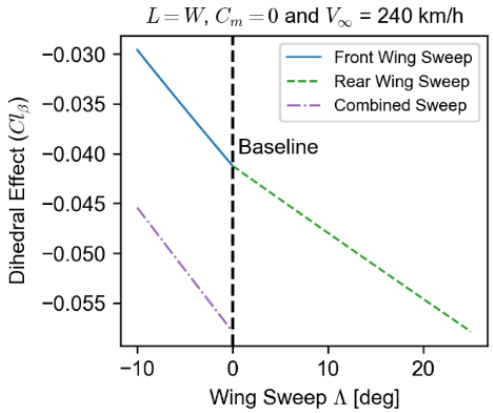

(b) Dihedral effect against wing sweep angle.

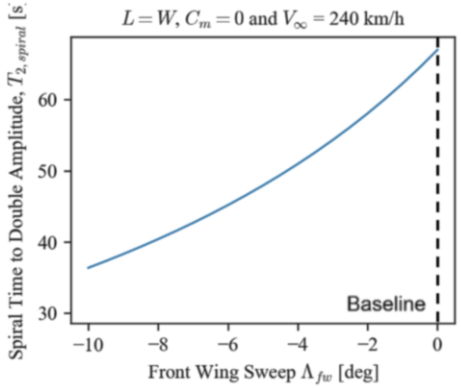

(c) Front wing sweep against $T_{2,\text{spiral}}$.

Figure 6.23: Parametric results for wing sweep angles.

Rearward sweep increases the dihedral effect, mimicking an increased dihedral angle, while forward sweep reduces it. Figure 6.23 (b) shows that increasing forward sweep reduces the dihedral effect. An increased dihedral effect improves spiral mode stability but reduces Dutch roll stability. Conversely, forward sweep decreases dihedral effect and spiral mode stability, complicating pilot control, while rearward sweep increases both dihedral effect and spiral mode stability. Figure 6.23 (c) shows that a forward-swept wing decreases T_2, making spiral recovery harder.

Figure 6.23 (a) and (b) also depicts the directional stability and dihedral effect variation with combined sweep of both wings: a rearward sweep of 25° on the rear wing and varying forward sweep on the front wing. In combined sweep conditions, forward sweep reduces the dihedral effect, but the negative impact is mitigated by the rearward sweep on the rear wing, which balances these effects. The forward-swept front wing allows a forward CG for better directional stability, while the rearward-swept rear wing maintains spiral mode stability. Thus, combined sweep helps balance Dutch roll and spiral mode stability, offering a compromise between these two stability modes.

6.3.7 Wing Dihedral Angle

Figure 6.24 (a) illustrates the variation of dihedral effect with rear wing dihedral or anhedral angles. The wing dihedral angle affects the aerodynamic efficiency of tandem wing aircraft, though less significantly than its impact on stability. Table 6.9 presents data for selected dihedral angle variations. The results show that increasing dihedral or anhedral angles improves aerodynamic efficiency by creating a non-planar wing system, which reduces induced drag.

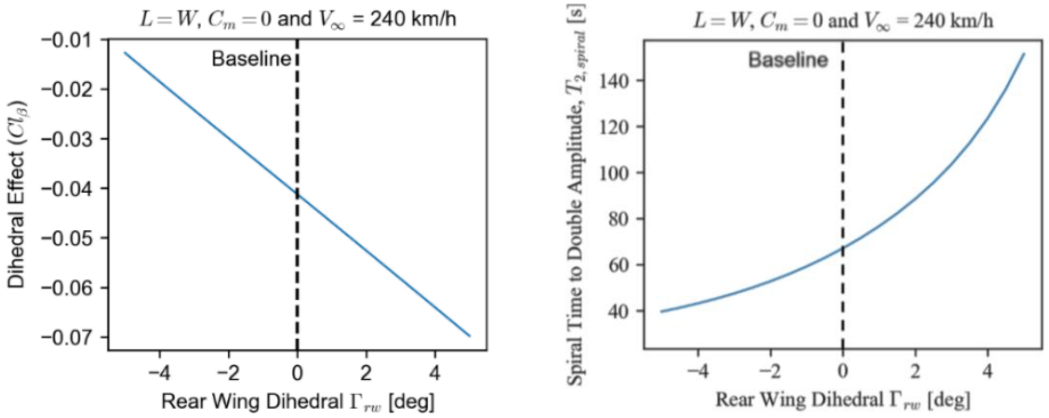

(a) Dihedral effect against dihedral angle.

(b) Rear wing dihedral angle against $T_{2,spiral}$.

Figure 6.24: Parametric results for wing dihedral angle for lateral stability.

Table 6.9: Effect of wing dihedral angle on aerodynamic efficiency.

Dihedral Angle Parameter (°)	Front Wing	Rear Wing	Lift-to-drag ratio
Baseline Aircraft	0.0	0.0	15.300
Non-Baseline Aircraft with Dihedral Angles	-5.0	0.0	16.137
	5.0	0.0	16.201
	0.0	-5.0	16.158
	0.0	5.0	16.169

Changes to the dihedral effect can significantly impact both Dutch roll and spiral mode stability. While the dihedral angle has a mild effect on Dutch roll stability, it greatly improves spiral mode stability. Figure 6.24 (b) shows that increasing the dihedral angle significantly raises the T_2 of the spiral mode, indicating enhanced spiral mode stability. Similar results are observed for variations in front and rear wing dihedral angles. Dihedral angle is more effective than sweep in improving spiral mode stability.

6.3.8 Placement of Winglets

Winglets are crucial for optimizing aerodynamic efficiency in fixed-wing aircraft. The addition of winglets to both the front and rear wings of a tandem wing aircraft was investigated. Figure 6.25 (a) shows the variation of L/D with winglet area for both wings. The results indicate that increasing winglet area improves aerodynamic efficiency by moving wingtip vortices away from the main wing surface, thus reducing downwash and induced drag. The trend is similar for both the front wing and rear wing winglet area. However, beyond a certain winglet size, aerodynamic efficiency may decrease due to increased profile drag.

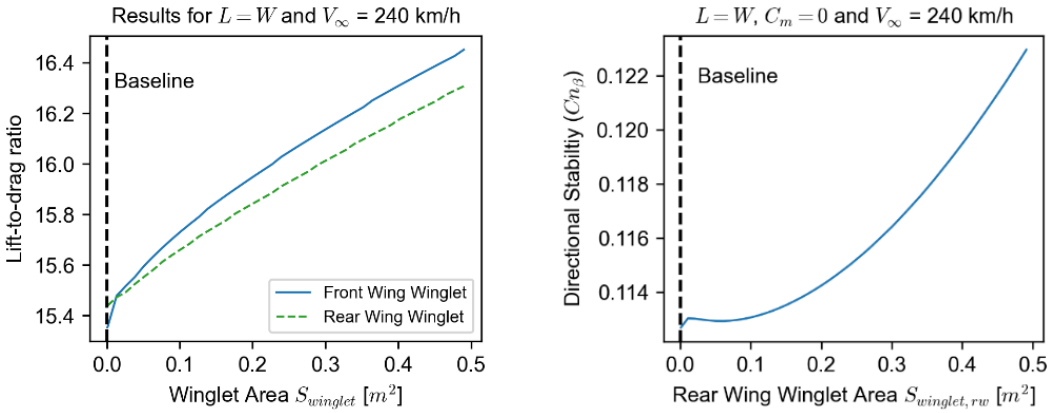

(a) Lift-to-drag ratio against winglet area.

(b) Directional stability against rear wing winglet area.

Figure 6.25: Parametric results for wing dihedral angle.

Figure 6.25 (b) demonstrates that increasing the winglet area on the rear wing enhances the aircraft's directional stability. This is because a winglet acts like an additional vertical tail surface. Placing the winglet on the rear wing is particularly beneficial for maintaining static and dynamic stability, as the aircraft's CG is biased to the front wing. This positioning results in a longer moment arm for the rear winglet, providing greater directional stability.

6.4 Tandem Wing Design Optimization

The previous section's parametric study highlighted the significant impact of wing design on the aerodynamics, weight, and stability of a tandem wing aircraft. However, understanding the interplay between different variables solely from this study is challenging. Therefore, an optimization using various design variables is necessary to identify the best design choices for given reference conditions.

The design variables for the optimization problem, including their respective lower and upper bounds, are listed in Table 6.7. These bounds were selected based on typical ranges observed in similar aircraft designs and engineering feasibility. Additionally, certain parameters were held constant during the optimization process to reduce complexity and focus on the key design variables. These constant parameters include the airfoil profiles, reference flight conditions, and the geometric characteristics of the tail and canard surfaces, as discussed in Section 6.1. To ensure the optimized design meets safety and operational standards, handling qualities constraints were applied, as detailed in Table 6.14. These constraints were based on standard requirements for stability and control in commercial passenger aircraft, ensuring that the optimized design not only maximizes performance but also maintains acceptable flight dynamics and handling characteristics.

Four different initial conditions were used to optimize the baseline tandem wing aircraft design, as summarized in Table 6.10. The initial guess for the optimization problem was chosen based on a combination of industry best practices, typical eVTOL aircraft design data, and insights from preliminary parametric studies, from Sections 3.3 and 6.3. Specifically, initial values for key design variables, such as wingspan, aspect ratio, and taper ratio, were derived from existing eVTOL and conventional aircraft configurations. This approach ensures that the starting point aligns with feasible and aerodynamically

efficient designs, reducing the likelihood of convergence to impractical or suboptimal solutions. Additionally, sensitivity analyses conducted prior to the optimization helped identify ranges for critical variables, ensuring the initial guess falls within these bounds. Given the nonlinear nature of the problem, this method balances computational efficiency with the robustness required to explore the design space effectively. The rationale for these choices lies in their ability to guide the optimization towards realistic and performance-driven solutions while minimizing the risk of stagnation or divergence during the iterative process.

The optimizations focused on wingspan, aspect ratio, and taper ratio, all conducted under the same reference conditions as the parametric study. The optimizations were conducted under different constraint conditions, and the results were studied to elucidate optimized tandem wing geometry with different design considerations. All optimization studies were conducted under steady level flight conditions at 240 km/h at sea level, consistent with the reference conditions used for all other calculations.

Table 6.10: Initial conditions used for the optimization of tandem wings.

Case	Design	Front Wing			Rear Wing			CG Position
		Wingspan (m)	Aspect Ratio	Taper Ratio	Wingspan (m)	Aspect Ratio	Taper Ratio	Measured from Nose (m)
(a)	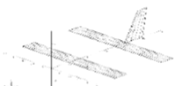	10.0	7.692	1.00	10.0	7.692	1.00	3.5845
(b)	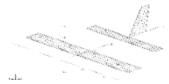	12.0	7.692	1.00	8.0	7.692	1.00	3.5845
(c)	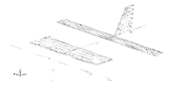	8.0	3.850	1.00	12.0	11.54	1.00	3.5845
(d)	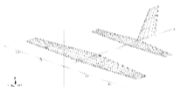	12.0	7.692	0.50	8.0	7.692	0.50	3.5845

The previously defined optimization framework was employed to optimize the baseline tandem wing aircraft under different initial conditions and design variables. The optimization utilized the COBYLA scheme, a gradient-free optimization method. Gradient-based schemes like Sequential Least Squares Programming (SLSQP) were also tested, but they were computationally expensive and yielded unsatisfactory results. Since COBYLA produces local optima, multiple initial conditions were explored to

identify the best possible design. A bound was placed on the CG position to prevent the design from shifting towards a fully conventional or canard configuration.

6.4.1 Aero-Mass Optimization

This section presents the results of aerodynamic and structural weight optimization aimed at maximizing flight range, excluding stability constraints. The optimization, summarized in Table 6.11, identified two primary optimal designs: a conventional wing-tail aircraft and a canard aircraft. Both conventional and canard configurations show a significant improvement in the range parameter with 47.48% and 47.47% respectively, as compared to the baseline tandem wing design.

Table 6.11: Optimization results of aero-mass optimization.

Case	Design	Front Wing			Rear Wing			Range Parameter
		Wingspan (m)	Aspect Ratio	Taper Ratio	Wingspan (m)	Aspect Ratio	Taper Ratio	$\frac{L}{D}\cdot\frac{m_{\text{battery}}}{m_{\text{total}}}$
Base	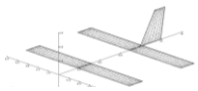	10.0	7.692	1.000	10.0	7.692	1.000	4.4235
(a)	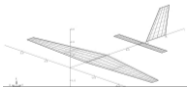	13.0	9.062	0.295	5.0	9.105	0.442	6.5239
(b)	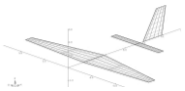	13.0	8.919	0.297	5.0	8.935	1.000	6.5220
(c)		5.0	9.076	0.281	13.0	8.970	0.290	6.4390
(d)		5.0	9.048	0.287	13.0	8.830	0.948	6.5235

These optimal designs, with unequal wing areas and minimal taper ratios, exhibit higher aerodynamic and weight efficiency. This confirms the effectiveness of the optimization setup for specific flight conditions. The parametric study further supports that configurations with longer spans and unequal wing areas have higher aerodynamic efficiencies. However, such designs may not possess adequate handling qualities, and their optimality might change when handling quality constraints are included.

6.4.2 Aero-Mass-Stability Optimization

This section details the optimization results incorporating handling quality constraints as outlined in Table 6.1, with the objective of maximizing flight range while ensuring good flight stability. The results, presented in Table 6.12, indicate that the short period mode constraint is barely satisfied, highlighting its significant limitation on design flexibility. This aligns with earlier findings that the optimal CG position is often governed by short period mode handling qualities.

Table 6.12: Optimization results of aero-mass-stability optimization.

Case	Design	Front Wing			Rear Wing			Range Parameter
		Wingspan (m)	Aspect Ratio	Taper Ratio	Wingspan (m)	Aspect Ratio	Taper Ratio	$\frac{L}{D} \cdot \frac{m_{\text{battery}}}{m_{\text{total}}}$
Base	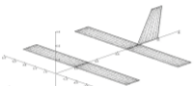	10.0	7.692	1.000	10.0	7.692	1.000	4.4235
(a)	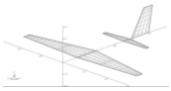	13.0	9.092	0.292	5.0	9.070	0.435	6.5170
(b)	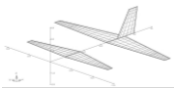	9.55	8.047	0.292	13.0	8.997	0.287	5.5610
(c)	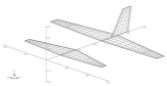	9.36	7.574	0.292	13.0	9.027	0.403	5.5702
(d)	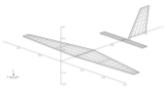	13.0	9.065	0.291	5.0	9.366	0.950	6.5320

The optimized designs under these constraints differ from those in the aero-mass optimization. While conventional wing-tail designs remained optimal with a 47.66% increased range parameter as compared to the canard design with 25.92% from the baseline, some initial conditions resulted in configurations with comparable wing sizes, indicating a preference for such designs when handling qualities are considered. This suggests that a particular tandem wing variant might be optimal for maximizing flight range and improving handling qualities simultaneously. However, other configurations, like canard aircraft, might also achieve good handling qualities under different initial conditions.

The tandem wing configuration demonstrated good pitch damping in the parametric study, making it a preferred choice under strict short period mode constraints. The

increase in the range parameter achieved with stability constraints is lower than that in the aero-mass optimization, with an average increase of 1.6215 compared to 2.0786, highlighting the restrictive impact of handling quality constraints. This indicates that incorporating stability constraints into the optimization framework imposes additional design restrictions, limiting achievable performance improvements. Nonetheless, these constraints lead to more realistic and practical designs for the eVTOL industry.

6.5 Summary

The aerodynamic and stability characteristics of four baseline VTOL aircraft in cruise mode were compared, providing a benchmark for tandem wing aircraft performance. This study included a parametric and optimization analysis focusing on tandem wing configurations, aiming to enhance their performance. A Python-based tool incorporating lower-order aerodynamic, stability, and mass models was developed for calculations, validated against CFD data, showing good agreement in lift coefficient and aerodynamic efficiency. This validated framework is well-suited for initial conceptual aircraft design. The constraints, objectives, and bounds applied in the optimization process were carefully selected to ensure a balance between achieving aerodynamic performance and maintaining stability and handling qualities.

Key findings from the baseline aircraft study from Section 6.2 are summarized in Table 6.13. The conventional configuration demonstrated a balanced performance but showed high sensitivity to CG position. The canard and tandem wing configurations were competitive, although effective tandem wing design requires thorough knowledge of wing aerodynamics. The flying wing configuration, despite having the best aerodynamic efficiency, faces challenges in manufacturing, passenger ingress/egress, and longitudinal stability, though these can be mitigated with design improvements and flight control systems. Its high aerodynamic efficiency makes it ideal for cargo aircraft design.

Table 6.13: Summary of characteristics of aircraft configurations.

Design Aspect	Conventional	Canard	Flying Wing	Tandem Wing
Aerodynamic Efficiency	Good	Good	Best	Sensitive to Wing Design
Stability & Handling Qualities	Good	Good	Sensitive to Aircraft Design	Best
CG Sensitivity	High	Medium	High	Low
Design Freedom	High	High	Low	High
Past Success	High	High	High	High
Difficulties in Manufacturing	Low	Low	High	Low
Difficulties in Aircraft Operations	Low	Low	High	Low

The parametric study from Section 6.3 highlighted the influence of wing design variables on the tandem wing configuration's stability and aerodynamic performance. The various parameters analysed are summarized in Table 6.14. Wingspan significantly affects aerodynamics and structural weight, while wing sweep and dihedral angles impact stability. The parametric study revealed that unequal wing areas typically enhance performance, though they may reduce pitch damping. A taper ratio of approximately 0.5 was found optimal for tandem wing aircraft. Increasing wingspan and distance between wings improved aerodynamic efficiency and pitch damping, respectively. Non-planar wing systems, achieved through varying wing height and differential dihedral angles, also enhanced efficiency. Adding winglets, particularly to the rear wing, improved both aerodynamic efficiency and directional stability.

Table 6.14: Summary of effects of tandem wing design variables.

Wing Design Variables	Aerodynamic Efficiency	Longitudinal Stability	Lateral Stability
Relative Wing Size	✓	✓	✓
Wingspan and Aspect Ratio	✓	-	-
Horizontal Wing Distance	✓	✓	-
Vertical Wing Distance	✓	-	-
Wing Taper Ratio	✓	-	-
Wing Sweep Angle	✓	-	✓
Wing Dihedral Angle	✓	-	✓
Winglets	✓	-	-

The optimization framework effectively demonstrates how specific wing design variables impact the tandem wing configuration’s stability and aerodynamic performance, guiding the identification of optimal designs that balance flight range and handling qualities in accordance with MIL-F-8785B standards. The aero-mass optimization results indicate that configurations with unequal wing areas and reduced taper ratios provide higher aerodynamic efficiency, maximizing range. With both conventional and canard configurations showing a significant increase in the range parameter of 47.48% and 47.47% from the baseline. However, when handling quality constraints were applied, conventional designs remained optimal with a 47.66% increased range parameter as compared to the canard design with 25.92% from the baseline. Designs with similar wing sizes emerged as preferred, while configurations with unequal wing areas still performed competitively, showcasing the framework's ability to accommodate diverse design strategies.

The applied constraints, objectives, and parametric bounds were critical in ensuring that the optimization results are both practical and grounded in realistic design conditions and performance requirements. These constraints helped align the conclusions with industry-standard stability and control requirements, ensuring the designs are not only efficient but also meet operational safety standards. By exploring multiple initial conditions, the framework ensured robust identification of local optima, thereby highlighting viable design solutions under varying constraints. This approach underscores the flexibility of the framework, which can be tailored to meet specific mission profiles and designer preferences, offering a robust tool for advancing eVTOL aircraft design.

This chapter presents a comprehensive approach to eVTOL design, integrating weight estimation, aerodynamic and stability analysis, and optimization. The weight estimation method, based on the NASA FLOPS model, accounts for the use of composite materials in eVTOL aircraft, providing reliable mass estimates in early-stage design by considering key design parameters. While the aerodynamic analysis utilizes CFD and VLM methods, these tools offer valuable insights, although their accuracy could be improved with further validation through experimental data, which is a limitation inherent in early-stage design studies. The study assumes consistent wing technology and simplifies structural optimization for the sake of aerodynamic exploration. While this approach is suitable for conceptual design, future work could incorporate advanced mass models, such as finite element analysis, to capture structural efficiencies and refine wing mass estimates. Additionally, the theoretical curves derived in this study offer clear guidance for design decisions, but the real-world design process will require further refinement to address nonlinear interactions and complex trade-offs. Future research should integrate more detailed simulations and experimental validations to enhance the accuracy and applicability of the design solutions.

Chapter 7: Subscale Experimental Wing Design Validation

To bridge the gap between theoretical design and practical validation, sub-scale testing was conducted to validate findings from Chapter 6: Wing Configuration Design and Optimization for eVTOL aircraft. This chapter focused on determining optimal wing designs by comparing aerodynamic performance, control, stability, and handling qualities across various wing arrangements, as outlined in Figure 7.1. The primary goal was to assess handling qualities during the critical transition phase, characterized by shifts in flight controls and dynamic changes between hover and cruise speeds.

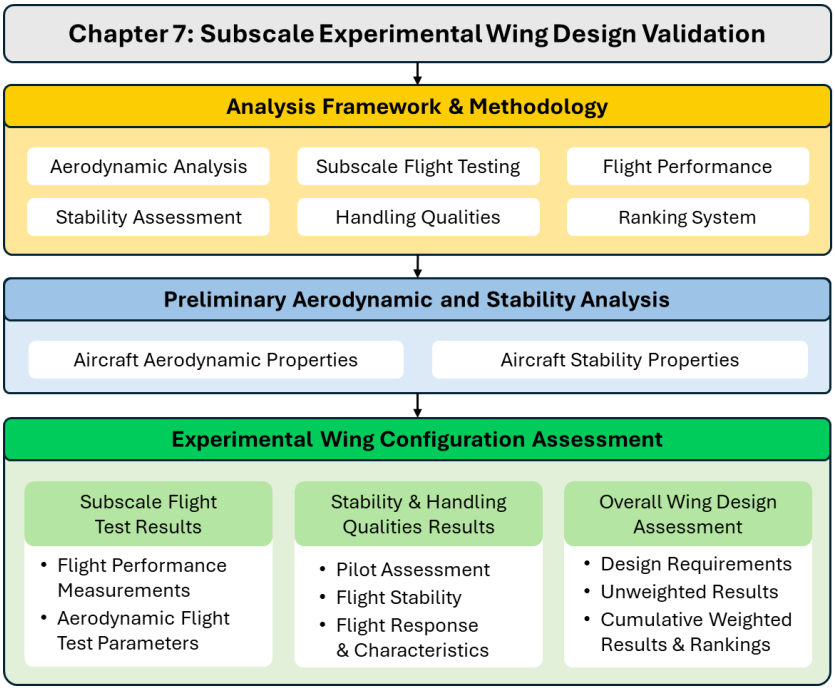

Figure 7.1: Chapter 7 - outline and flow diagram.

A flight test pilot evaluated dynamic stability and handling using the Cooper-Harper Rating (CHR) to identify wing configurations with high aerodynamic efficiency and stability. Low-fidelity simulations provided initial aerodynamic and static stability properties, guiding the design of sub-scale models. These were followed by experimental flight tests to validate dynamic stability. Given resource and space constraints, sub-scale testing offered a cost-effective method to confirm the aerodynamic and stability performance of optimized wing designs.

High-fidelity studies, such as CFD simulations, were beyond the scope of this chapter, focusing instead on practical validation under real-world conditions. Full transition tests were excluded due to the complexity of tuning parameters like PID controllers and transition timing, as well as the lack of precision tracking systems. Despite these limitations, the sub-scale tests yielded valuable insights into wing configuration effects on aerodynamic performance and stability, particularly for urban eVTOL operations. Future work could integrate high-fidelity simulations and transition tests to enhance validation of transition dynamics and refine overall design performance.

7.1 Methodology and Approach

The methodology involves three disciplines: aerodynamics, flight performance, and stability/handling quality. Each discipline affects eVTOL performance and certification requirements, assessed either numerically or experimentally as shown in Figure 7.2. This multidisciplinary approach reveals interactions between disciplines, offering insights not apparent in monolithic studies. The results are used in a weighted assessment to derive suitable wing arrangements for different design requirements.

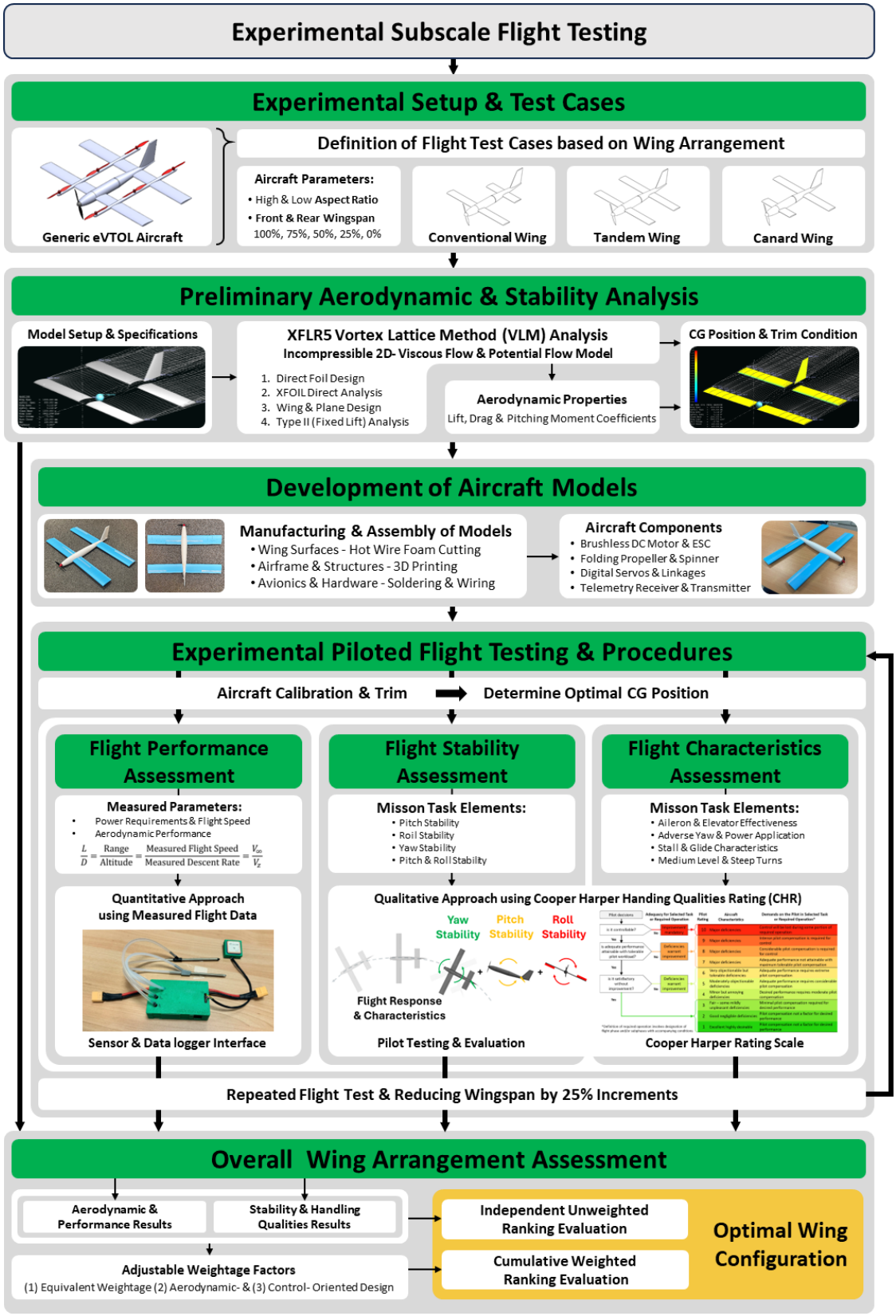

Figure 7.2: Assessment methodology for eVTOL aircraft wing arrangement.

A generic Lift + Cruise tandem wing eVTOL aircraft, featuring equal front and rear wingspans and multiple fixed rotors on a boom structure, serves as the baseline configuration as shown in Figure 7.3.

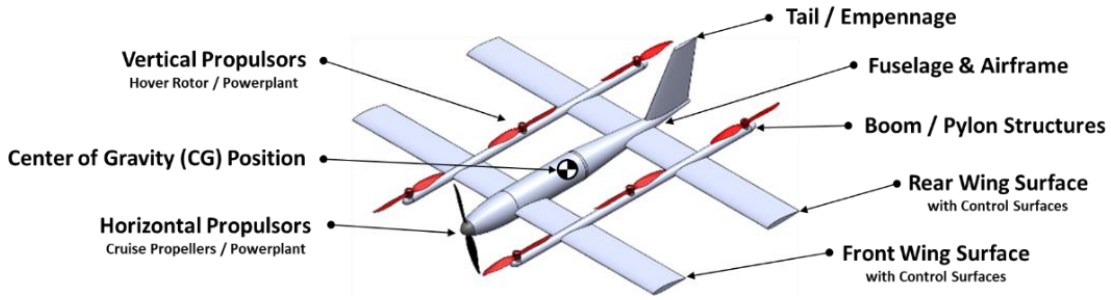

Figure 7.3: Generic baseline tandem eVTOL aircraft.

The baseline aircraft specifications include a maximum takeoff weight of 1 kg, a total wing area of 0.12 m², a 0.25 m inboard halfspan, and a front-to-rear wing spacing of 3.75 × chord (0.45 m). All dimensions are referenced from the front wing root leading edge. The NACA 2412 airfoil is used for both wings, and the NACA 0012 for the vertical tail. The experiment examines the effects of reducing the outboard wingspans of the front and rear wings incrementally by 25%, resulting in five test cases from 100% to 0% outboard wingspan as shown in Table 7.1.

Table 7.1: Wing arrangements with varying outboard wingspan.

Outboard Wingspan %	100%	75%	50%	25%	0%
Canard Configurations (Front Wing Reduction)					
Conventional Configurations (Rear Wing Reduction)					

The research focuses on wing arrangements for forward flight, omitting horizontal hovering propellers and booms. Two baseline tandem wing aircraft, Low Aspect Ratio (LAR) and High Aspect Ratio (HAR), serve as starting points as shown in Figure 7.4. Both LAR and HAR designs have the same wing area but differ in aspect ratios: 8.33 for LAR and 12.00 for HAR. The design ensures that control surfaces remain unaltered when outboard wing sections are shortened for canard and conventional wing arrangements. In this context, "conventional" wing arrangements feature a lifting rear wing, unlike typical conventional aircraft where the horizontal stabilizers generate downward lift for pitch stability.

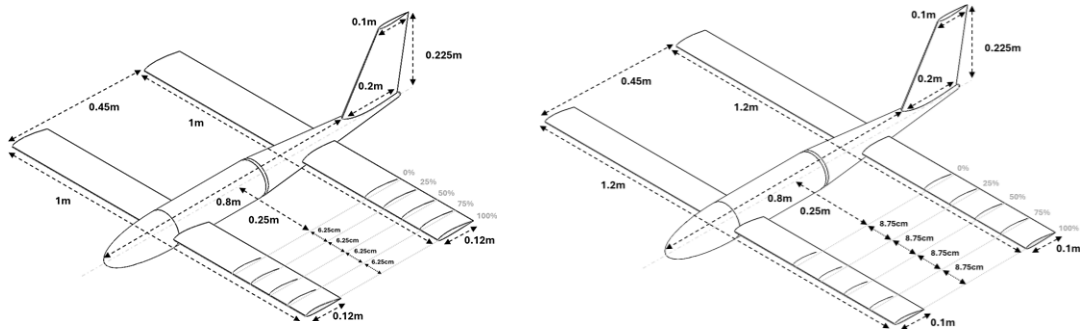

(a) Low aspect ratio aircraft. (b) High aspect ratio aircraft.

Figure 7.4: Specifications and dimensions for various wing arrangements.

7.1.1 Aerodynamic Analysis

Analytical aerodynamic comparisons were performed using the XFLR5 program to determine the aerodynamic properties, CG, and static stability characteristics. This analysis assessed the effects of various wing arrangements and verified and trimmed the baseline tandem wing design. XFLR5 employs both XFOIL and VLM solvers to model surface elements, a method validated in multiple studies [89, 209] and found to compare well with other aerodynamics codes.

Using XFLR5 Type 2 fixed lift analysis, an angle of attack ranges from -5° to 20° was used to determine aerodynamic properties. This approach allowed estimation of the CG position and movement for different wing arrangements and observation of parameter trends across varying flight speeds and aerodynamic coefficients. Special consideration was undertaken to ensure result convergence, with critical lattice panels aligned with wing endpoints to account for generated tip vortices and interactions. The analysis excluded fuselage, booms, and propeller elements, and the non-dimensional aerodynamic coefficients were normalized based on the main lifting surface area. For conventional wing arrangements, the reference was the front surface, while for canard wing arrangements, it was the rear surface.

7.1.2 Flight Testing and Performance Assessment

Experimental flight testing is to evaluate the benefits and trade-offs of different wing arrangements, which can be enhanced or compensated when combined with vertical lift or propulsion elements for optimal and efficient eVTOL aircraft. Four baseline aircraft, consisting of two LAR and two HAR wings, were manufactured. For the flight tests, the front or rear wingspan was shortened for canard and conventional wings test cases, respectively, as shown in Table 7.2.

Table 7.2: Manufactured aircraft models – top and isometric views.

Canard (CANA)	Aircraft Wing Configurations	Conventional (CONV)
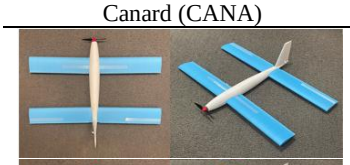	← Outboard Wingspan 100 % →	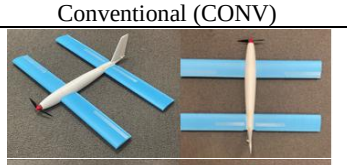
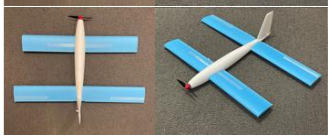	← Outboard Wingspan 75 % →	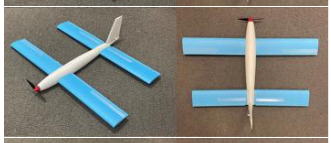
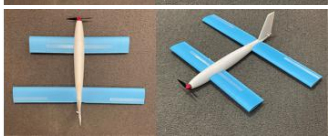	← Outboard Wingspan 50 % →	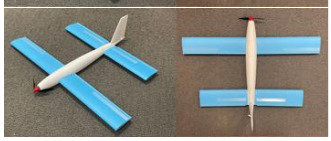
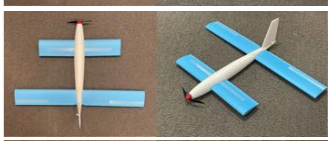	← Outboard Wingspan 25 % →	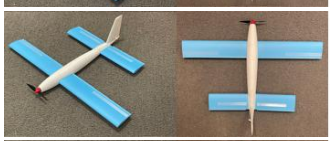
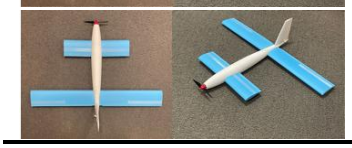	← Outboard Wingspan 0 % →	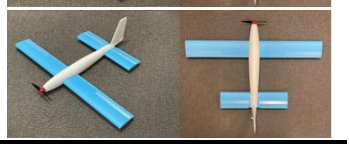

Flight testing was conducted to record in-flight data and pilot evaluations of stability, correlating with aerodynamic analysis to conclude the effects of wing arrangements on eVTOL aircraft. Each time a percentage of the wing section was removed, both analysis and flight tests evaluated the effects to compare properties and characteristics from the previous iteration. All aircraft were flown manually to assess inherent stability and stick-free trim across all airspeeds for forward flight. Repeated flight tests ensured consistency and reliability of results. When the front or rear wing was shortened, the aircraft CG was adjusted to trim the aircraft in horizontal flight. Real-time flight data were recorded using a custom-designed lightweight datalogger (55 g), as shown in Figure 7.5, with various sensors listed in Table 7.3, utilizing the open-source openXsensor (oXs) firmware and program [210].

Table 7.3: Onboard flight test data logging hardware and components.

System	Category	Hardware Component
Aircraft Propulsion & Controls	Brushless Direct Current Motor	SunnySky A2212 - 980kV II
	Electronic Speed Controller	SkyStars Talon Slim 40A BLHeli32
	Propelling Element	GF-Nylon 8060 2-Blade Folding Propeller
	Energy Storage System	CNHL – Black Series 4S 1500mAh 100C
	Servo Actuators	JX PDI - DHV56MG Digital Metal Gear
	Telemetry & Receiver	FrSky R-XSR ACCST D16
	Transmitter & Display	FrSky Tandem X20S 900Mhz & 2.4Ghz
Flight Data Acquisition & Sensor	Microcontroller	Raspberry Pi RP2040 - ZERO
	GPS & Compass	Beitian BN-880 & HMC5883L
	Barometer	Amsys MS5611
	Accelerometer & Gyroscope	InvenSense MPU-6050
	Analog-to-Digital Converter	Texas Instruments ADS1115
	Airspeed Sensor	Sensirion SDP810-500Pa CFSensor XGZP6897D-500Pa

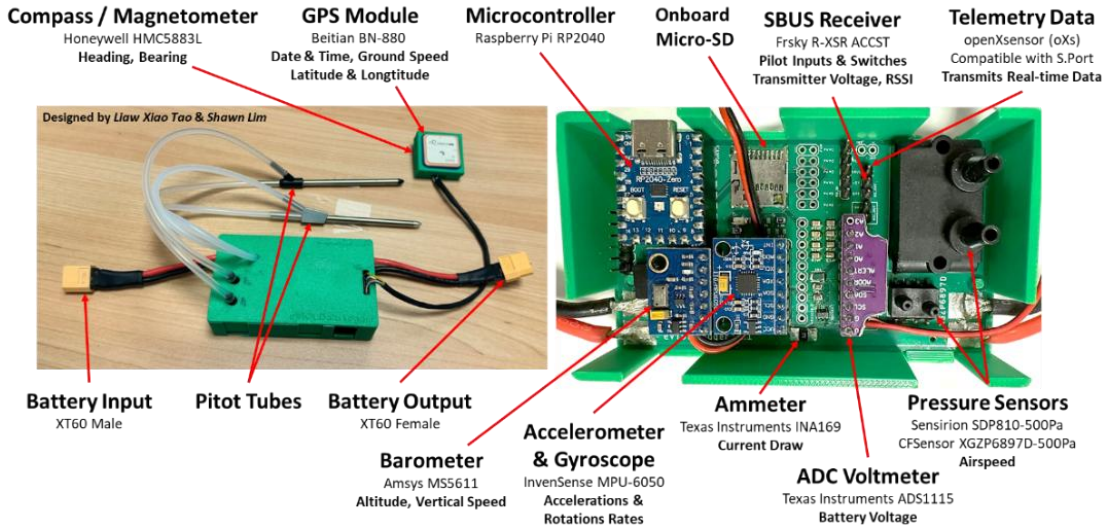

Figure 7.5: Flight data acquisition unit enclosure and sensor layout.

Aircraft performance was assessed by measuring the rate of descent across flight velocity in a zero-throttle setting for different wing arrangements. These recorded parameters provided insights into instantaneous lift and drag performance, determining aerodynamic efficiency in terms of L/D as provided in (7.1). The rate of descent, V_z, was recorded through the barometer sensor, while the flight velocity V_∞, was measured through the airspeed sensor. Although the accelerometer and GPS sensor data could provide altitude, displacements, or velocities to derive lift and drag performance, the recorded data were found to be inconsistent and affected by noise.

$$\frac{L}{D} = \frac{\text{Range}}{\text{Altitude}} \equiv \frac{\text{Measured Flight Speed}}{\text{Measured Descent Rate}} = \frac{V_\infty}{V_z} \tag{7.1}$$

Additionally, power requirements during powered flight were assessed by measuring instantaneous voltage and current values. Powered flight conditions tested included cruise and maximum-thrust flight. Voltage and current values were recorded through a voltmeter and ammeter, respectively, to determine power consumption during different test conditions for various wing arrangements.

7.1.3 Stability and Handling Quality Assessment

The pilot evaluates handling qualities using the Cooper Harper Handling Quality Rating Scale [211] for various Mission Task Elements (MTEs). MTEs are specific tasks performed by test pilots to assess an aircraft's handling qualities, covering aspects such as aircraft control, maneuverability, precision, stability, predictability, control forces, sensitivity, and handling in adverse conditions.

Stability ratings are based on the aircraft's inherent tendency to return to its neutral position after a disturbance without pilot intervention. Handling quality ratings assess the aircraft's response to pilot inputs, noting any abnormal behaviors and its ability to react swiftly in a controllable manner. Stability and handling qualities are influenced by both CG position and wing arrangement, which affect the SM, requiring the pilot's evaluation and description for each MTE. Before data collection, various CG positions are tested to achieve a trimmed condition in forward flight without excessive surface input deflections, and with a slight pitch-up tendency during accelerations, indicating good pitch stability.

The CHR is used for qualitative assessment from the pilot for various MTEs, as shown in Figure 7.6. The ratings range from 1 to 10, where a score of 1 (green) indicates the best performance and 10 (red) the worst. CHR requires the pilot to fly and evaluate the handling and performance characteristics for each assessment parameter. These parameters include low-speed and high-speed characteristics for pitch stability and response with/without turns, roll stability and response, yaw stability and response, stall characteristics, medium-level turns, and steep turns. The following subsection details the assessment parameters, including the pilot tasks and designation of flight phases and/or subphases with their accompanying conditions.

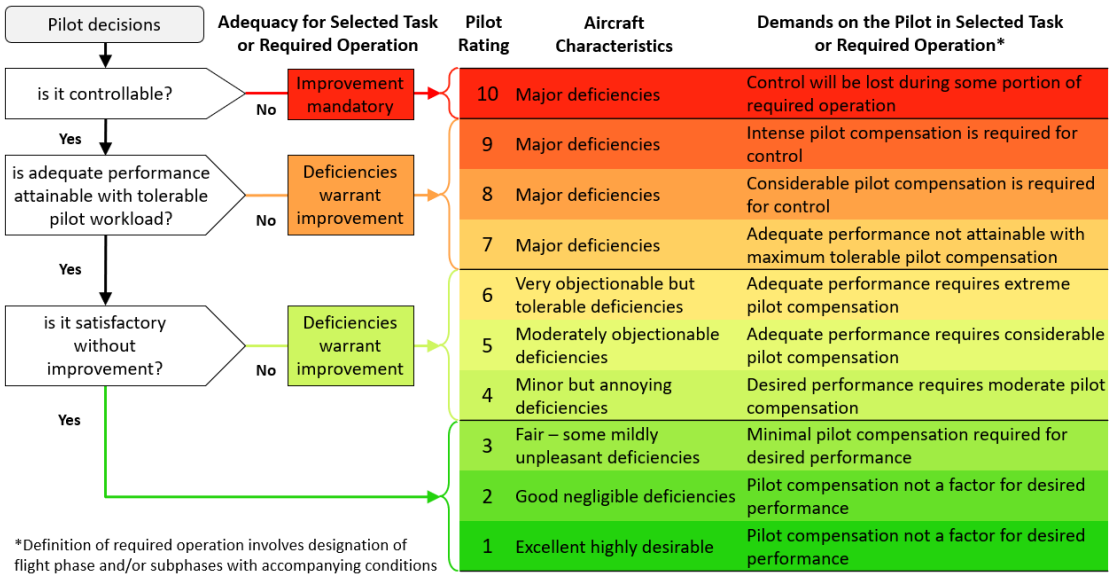

Figure 7.6: Color coded gradient for Cooper Harper handling qualities rating scale.

Aircraft Trim and Center of Gravity

To ensure uniformity across all wing arrangements during testing, the aircraft adopts a CG position that enables Straight and Level (S&L) flight at a comfortable cruise speed. A S&L trimmed flight is characterized by a pitching moment coefficient value of zero $C_m = 0$, where there is no pitching moment, while maintaining constant altitude and zero sideslip angle.

An aft CG causes the aircraft to trim at a high angle of attack, whereas a forward CG leads to a lower angle of attack. An excessively aft CG typically results in undesirable handling qualities. Both situations affect the lift coefficient, preventing optimal operation at the designated cruise speed. The measured cruise speed is defined as the lowest possible speed where the aircraft generates sufficient lift for an angle of attack between 0° and 5°, with adequate aerodynamic damping and control authority based on pilot assessment. Improper CG positions necessitate increased control surface deflection, incurring trim drag and degrading flight performance, thus affecting the accuracy of collected data. Each aircraft therefore adopts a CG position that allows for comfortable cruise speed and controllability based on pilot feedback and workload.

Pitch and Roll Stability

To assess the pitch and roll stability, the aircraft undergo a series of attitude changes in pitch through elevator deflection and in roll through aileron deflection, or a combination of both. Each aircraft is first brought to trimmed flight conditions with constant altitude and heading. For pitch stability assessments, the pilot subjects each aircraft to both a 45° nose-up and nose-down attitude while maintaining level wings with a 0° bank angle, as illustrated in Figure 7.7 (a). For roll stability assessments, the pilot subjects each aircraft to both left and right 45° angle of bank (AOB) while maintaining a 0° pitch attitude, as shown in Figure 7.7 (b). These assessments are conducted at designated cruise speed and at a higher flight speed with a 30% increased throttle setting from cruise speed, which tends to result in greater pitch-up moment and aerodynamic damping, affecting overall inherent stability.

As the aircraft stabilizes to its new attitude and speed, the pilot releases the control stick, allowing the control surfaces to return to their neutral position. This assesses the inherent stability during neutral deflection - stick-fixed conditions. For stable aircraft with positive static stability, a good CHR score is given based on the time and/or height taken to recover to S&L flight. Unstable aircraft that diverge in flight receive a poor CHR score. This MTE allows the pilot to determine inherent stability and stability variation about each axis for each wing arrangement.

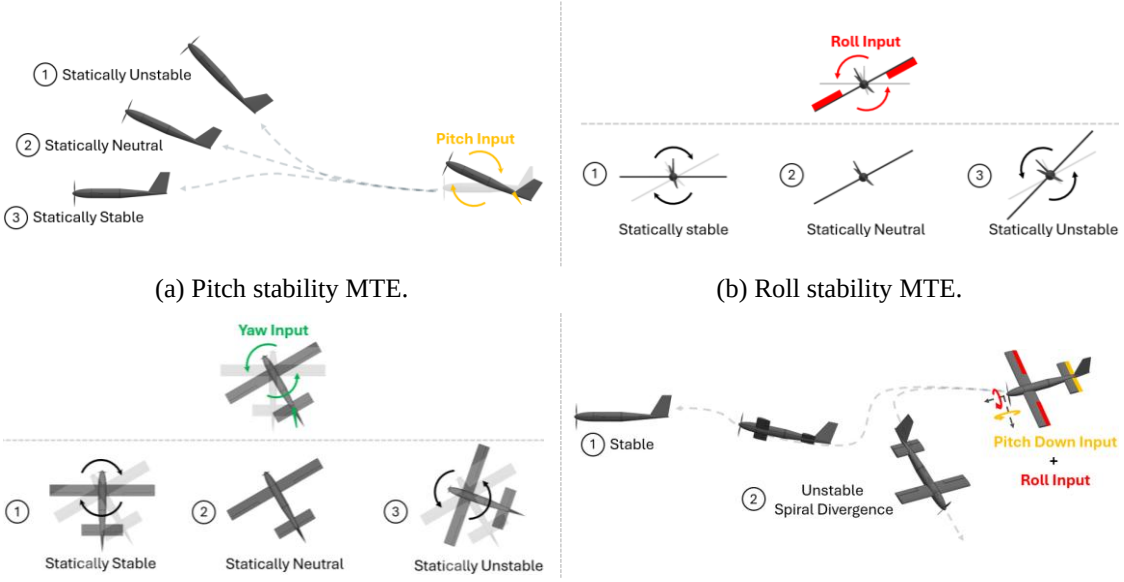

(a) Pitch stability MTE.

(b) Roll stability MTE.

(c) Yaw stability MTE.

(d) Pitch with roll stability MTE.

Figure 7.7: Flight stability mission task elements.

Yaw and Directional Stability

To assess the directional stability, a CHR score is given based on the deviation from the directional axis during S&L flight, observed visually, as shown in Figure 7.7 (c). Each aircraft is first brought to a trimmed level flight condition with a 0° bank angle. This MTE evaluates the effectiveness of the vertical stabilizer and provides insights into potential primary stability issues that could lead to secondary effects such as spiral and adverse yaw tendencies.

Pitch with Roll Stability

To assess pitch with roll stability, the pilot observes the time and height taken for the aircraft to recover from a 45° nose-down attitude combined with a 45° left-roll or right-roll attitude, as shown in Figure 7.7 (d). When the aircraft stabilizes into its commanded attitude, the pilot releases the control inputs, allowing it to enter stick-fixed condition.

This MTE assesses inherent spiral tendencies and recovery characteristics of each wing arrangement. A better CHR score is given to aircraft without spiraling or rapid divergence. These observations evaluate the lateral dynamic stability mode and interactions between roll and yaw effects.

Aileron Effectiveness

To assess aileron effectiveness, the pilot smoothly and swiftly moves the trimmed roll control stick to command maximum deflection on the aileron surfaces, evaluating the roll and turn responses, as illustrated in Figure 7.8 (a). Each aircraft is first brought to a trimmed S&L flight at a designated speed and throttle setting. This MTE is conducted at both cruise and above cruise velocities. A left-roll or right-roll command induces a roll rate, causing the aircraft to deviate to a left or right flight path. A CHR score is subsequently evaluated based on visual observations of the aircraft's turn trajectory and roll response to the given command. This MTE determines if sufficient aileron authority is available to provide desirable rolling moments and evaluates the aircraft controllability in an augmented flight path with a given roll input. Aileron effectiveness varies across different wing arrangements, influencing roll damping and response characteristics.

Elevator Effectiveness

To assess elevator effectiveness, the pilot smoothly and swiftly moves the trimmed pitch control stick to command maximum deflection on the elevator surfaces, evaluating pitch and climb responses, as illustrated in Figure 7.8 (b). Each aircraft is first brought to a trimmed S&L flight at a designated speed and throttle setting. The MTE is conducted at both cruise and above cruise velocities. A pitch command induces a positive or negative pitch rate, resulting in a climb or descent flight path. A CHR score is subsequently given based on visual observations of the aircraft's flight trajectory and pitch response to the command. This MTE determines if sufficient elevator authority is available to provide desirable pitching moments and evaluates the controllability of the aircraft in an augmented flight path with elevator deflection. This assessment is critical during low-speed landings, where sufficient pitch authority is necessary for safe landings.

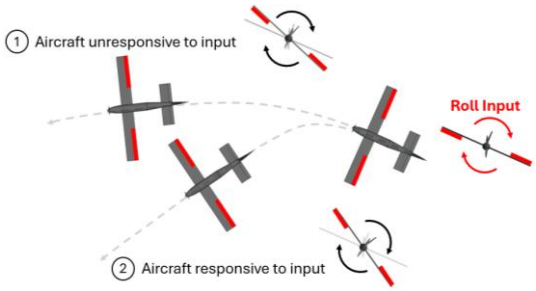

(a) Aileron effectiveness MTE.

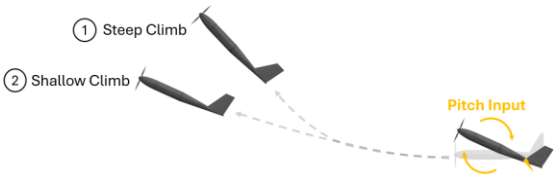

(b) Elevator effectiveness MTE.

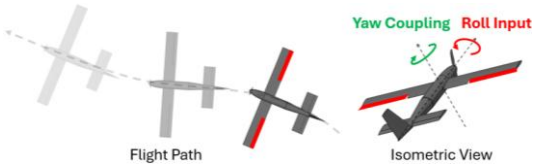

(c) Adverse yaw MTE.

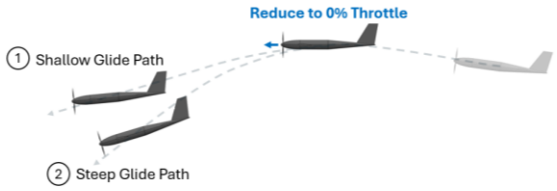

(d) Glide characteristic MTE.

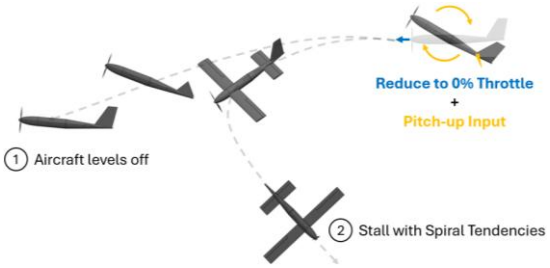

(e) Stall characteristic MTE.

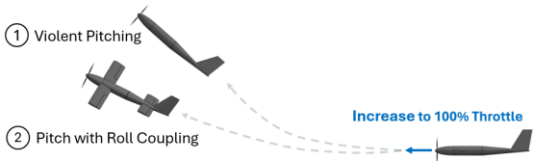

(f) Low-speed power application MTE.

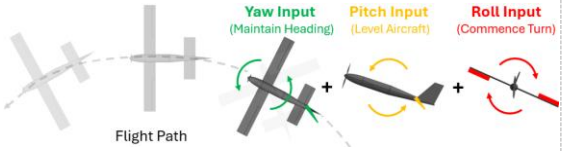

(g) Medium level turn MTE.

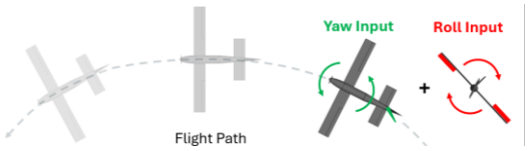

(h) Steep turn MTE.

Figure 7.8: Flight characteristics and response mission task elements.

Adverse Yaw Response

To assess handling qualities during adverse yaw, the pilot executes a turn maneuver with control inputs commanding a roll attitude from S&L flight condition while observing heading deviations due to adverse yaw, as shown in Figure 7.8 (c). A CHR score is given based on visual observations of adverse yaw amplitude and pilot workload related to yaw input corrections when the ailerons are deflected. For instance, during a left-hand banking turn, the right aileron deflects downward to generate a positive rolling moment,

resulting in increased lift and drag, causing undesirable adverse clockwise yaw. Higher pilot workload due to more noticeable adverse yaw results in a poorer CHR score.

Glide Characteristics

To assess glide characteristics during piloted maneuvers, the aircraft is first flown to a higher altitude before reducing the throttle to zero, as shown in Figure 7.8 (d). The aircraft is evaluated based on its non-powered glide characteristics and efficiency in a no-throttle glide flight path. Several glide maneuvers are conducted for each wing arrangement to account for environmental, thermal, and wind factors. Each aircraft is first brought to trimmed flight conditions before having the pilot expeditiously reduce throttle input to zero. The glide path is assessed visually, with the pitch attitude adjusted to maximize glide distance while minimizing vertical descent rate.

As glide characteristics are heavily affected by flight speed, a lower forward airspeed without a significant change in descent rate results in a steeper glide path, indicating suboptimal glide speed. Each aircraft undergoes a series of pitch adjustments to reach optimal glide speed and attitude. Glide maneuvers are conducted at both cruise speed and maximum throttle to determine the effect of airspeed on glide characteristics. Poor CHR scores are given to wing arrangements that are difficult to pilot with increased workloads and achieve unsatisfactory glide paths.

Stall Characteristics

To assess the handling qualities during stall, the pilot commands control inputs to forcefully stall the aircraft, evaluating the effects of divergence and sudden loss of lift for each wing configuration, as shown in Figure 7.8 (e). The stall characteristics of each wing arrangement indicate their suitability for various manned and unmanned full-scale applications. Each aircraft is first brought to trimmed flight conditions, maintaining constant altitude and heading at a higher elevation. The throttle is then instantly reduced to zero while commanding a maximum up elevator input to vigorously pitch the aircraft to its stall angle of attack. The aircraft is allowed to freely deviate from its flight path while maintaining maximum up elevator deflection. Upon completion of the stall characterization, the pilot executes the necessary stick inputs to recover the aircraft.
A CHR score is given based on visual observations of how the aircraft diverges from its flight path and its rate of departure. Aircraft with abrupt and large departure responses,

such as severe wing drop causing the aircraft to turn inverted and spiral or spin, are deemed to have poor stall characteristics and are given poorer CHR scores due to their undesirable responses and loss of controllability.

Low Speed Power Application

To assess the handling qualities during low-speed power application, each aircraft is first brought to trimmed flight conditions with altitude and heading held constant at a higher elevation. A two-stage maneuver is conducted: the pilot initially reduces the throttle setting 10% below cruise setting, then instantly increases to 100% throttle, allowing the aircraft to freely deviate from its flight path, as shown in Figure 7.8 (f). A CHR score is given based on visual observations of the aircraft's flight trajectory, particularly its divergence from the original flight path. Aircraft with undesirable, sudden, or violent pitching responses, or those exhibiting pitching coupled with rolling responses, are considered unsatisfactory and receive a poor CHR score.

Medium Level Turn (MLT)

To assess the handling qualities during a medium level turn, the pilot executes a coordinated level turn maneuver by commanding aileron, elevator, and rudder inputs to maintain a constant AOB, altitude, and yaw rate, as shown in Figure 7.8 (g). The MLT is a common maneuver that requires increased pilot workload depending on controllability and cross-coupling between different control inputs. Cross-coupling effects can manifest as additional rolling moments generated with mixed inputs from ailerons, rudder, and elevators, affecting the overall controllability of the aircraft.

Each aircraft is first brought to trimmed flight conditions with constant altitude and heading. The pilot then increases the throttle by 5% relative to the cruise setting and commands a roll with 30° AOB, while simultaneously compensating pitch input to maintain level altitude. The rudder input is adjusted to provide the required coordination to keep the fuselage aligned with the relative airflow. A CHR score is given based on visual observation of the MLT trajectory, and the overall amount of correction required to complete the maneuver. Aircraft requiring significantly higher pilot workload or unable to perform an MLT satisfactorily receive poor CHR scores.

Steep Turn

To assess the handling qualities during a steep turn, the process follows the MLT procedures but with a higher AOB of 60°, commanded by the pilot to further investigate handling qualities during steep turn maneuvers, as shown in Figure 7.8 (h). The steep turn MTE provides insights into the aircraft's performance under higher load factors and the increased demand for pilot control and coordination.

7.1.4 Optimal Wing Design Analysis Using Weightage Factors

Upon completing the aerodynamic analysis and flight testing for aircraft performance, stability, and handling qualities, weightage factors are introduced for comparing various wing arrangements. These factors are applied to each gathered data point to determine the optimal wing designs by summing the total weighted scores. Weightage factors provide aircraft designers with the flexibility to manipulate the factors towards their desired aircraft design requirements.

Design requirements and constraints are subjective, based on different aircraft applications and missions. For instance, unmanned aircraft are more susceptible to stalling compared to manned aircraft, where pilots can physically experience and react to stall conditions. Additionally, eVTOL aircraft operate across a spectrum of flight velocities from hover to cruise phases. The transition between vertical and forward flight phases is typically the most challenging for eVTOL aircraft, setting them apart from traditional fixed-wing aircraft or rotorcraft. Therefore, acceptable aircraft stability characteristics in all flight phases are paramount for eVTOL aircraft to operate safely and stably, as stability is a function of flight speed.

The gathered results are used along with weighting factors to determine possible optimal designs for three simplified conditions:

- Equivalent Weightage:
  Equal emphasis on aerodynamic and stability parameters.
- Aerodynamic Oriented Designs:
  75% weightage on aerodynamic parameters and 25% on stability parameters.
- Control Oriented Designs:
  25% weightage on aerodynamic parameters and 75% on stability parameters.

These weightage factors are shown in Table 7.4.

Table 7.4: Equivalent, aerodynamic- and stability-oriented weightage factors.

	Assessment Parameter	Equivalent	Aerodynamic-Oriented	Stability-Oriented
Aerodynamic & Performance	Trimmed Lift Coefficient	5%	7.5%	2.5%
	Trimmed Lift-to-Drag	5%	7.5%	2.5%
	Trimmed Total Drag Coefficient	5%	7.5%	2.5%
	Trimmed Cruise Speed	5%	7.5%	2.5%
	Measured L/D ^{LS}	5%	7.5%	2.5%
	Measured L/D ^{HS}	5%	7.5%	2.5%
	Measured Cruise Speed	5%	7.5%	2.5%
	Measured Cruise Power	5%	7.5%	2.5%
	Measured Max Speed	5%	7.5%	2.5%
	Measured Max Power	5%	7.5%	2.5%
	Total Weightage:	50%	75%	25%
Stability & Handling Qualities	Pitch Up Stability ^{LS}	2.63%	1.32%	3.95%
	Pitch Up Stability ^{HS}	2.63%	1.32%	3.95%
	Pitch Down Stability ^{LS}	2.63%	1.32%	3.95%
	Pitch Down Stability ^{HS}	2.63%	1.32%	3.95%
	Elevator Effectiveness ^{LS}	2.63%	1.32%	3.95%
	Pitch Up with Roll Stability	2.63%	1.32%	3.95%
	Pitch Down with Roll Stability*	2.63%	1.32%	3.95%
	Directional Stability	2.63%	1.32%	3.95%
	Roll Stability ^{LS}	2.63%	1.32%	3.95%
	Roll Stability ^{HS}	2.63%	1.32%	3.95%
	Aileron Effectiveness ^{LS}	2.63%	1.32%	3.95%
	Aileron Effectiveness ^{HS}	2.63%	1.32%	3.95%
	Adverse Yaw	2.63%	1.32%	3.95%
	Glide Characteristics ^{LS}	2.63%	1.32%	3.95%
	Glide Characteristics ^{HS}	2.63%	1.32%	3.95%
	Stall Characteristics	2.63%	1.32%	3.95%
	Low Speed Power Application	2.63%	1.32%	3.95%
	Medium Level Turns	2.63%	1.32%	3.95%
	Steep Turns	2.63%	1.32%	3.95%
	Total Weightage:	50%	25%	75%

HS: High Speed, LS: Low Speed, *: Spin Recovery

This simplified approach allows for expedited conclusions to derive an optimal wing design based on preferences between aerodynamics and stability. Each assessment parameter in aerodynamics, performance, and stability and handling qualities has variations in their raw magnitudes.

In the CHR scale, lower values indicate better performance. These CHR results need to be inverted when normalizing around unity for comparison with weightage factors. Thus, values above unity represent better performance. Given that the list of tested wing designs is flyable, airworthy, and within an acceptable wing loading, it ensures no significant outliers that might skew the results. Although specific assessment parameters can be individually adjusted, this complicates the study and results in a vast number of possible permutations for the overall optimal design. A significantly more in-depth sensitivity study, which is beyond the scope of this thesis, would be required to conclude an overall optimal design. Therefore, using these three cases, designs that favor different balances between aerodynamic efficiency and stability are identified.

In this section, results gathered from aerodynamic analysis, along with flight test data for flight performance, stability, and CHR assessments, are presented and compared. Subsequently, a weightage factor is applied to the individual normalized results and summed together to highlight characteristics and conclusions from different wing arrangements toward an optimal eVTOL wing design. By applying these weighted factors and comparing the total scores for each wing arrangement, insights into the most favorable designs for different eVTOL applications are gained. This approach provides a balanced perspective on the trade-offs between aerodynamic efficiency and stability, leading to informed decisions on optimal wing designs for specific mission requirements.

7.2 Aerodynamic Analysis

The XFLR5 aerodynamic analysis for different eVTOL wing arrangements provides valuable insights into the performance, stability, and efficiency of each design. The analysis includes variations in lift, total and component drags, L/D, velocity, and pitch moment coefficient against the angle of attack.

7.2.1 Aerodynamic Properties

The results are visualized with different colors representing each wing arrangement, and round and cross markers indicating the baseline aircraft and configurations with complete removal of the outboard wing section, respectively.

The lift coefficient is a critical parameter for eVTOL aircraft as it affects conventional takeoff and landing requirements and the transition towards wing-borne flight. The analysis in Figure 7.9 (a) indicates that the baseline 100% wings have the highest lift coefficients for every positive angle of attack, highlighting their superior lift performance. When the wingspan is reduced, both conventional and canard wings exhibit decreased lift coefficients, likely due to increased cruise velocity compensating for the reduced wingspan to maintain steady level flight, as shown in Figure 7.9 (f). Comparatively, conventional wings have a higher lift coefficient than canard wings, likely due to the downwash effect from wingtip vortices of the front wing on the rear wing. Among the configurations, HAR 100% baseline wings demonstrate the highest lift coefficients due to more effective lift distribution and reduced trailing tip vortices.

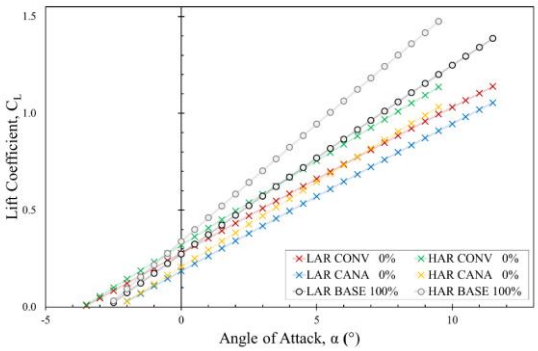

(a) Lift coefficient against angle of attack.

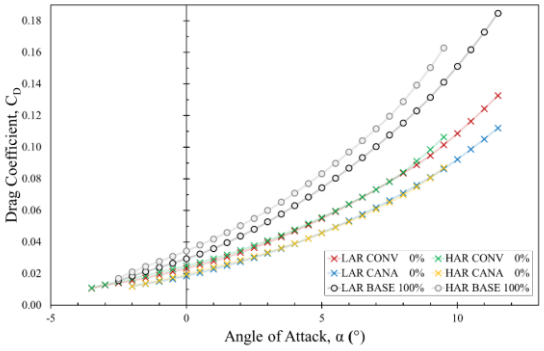

(b) Drag coefficient against angle of attack.

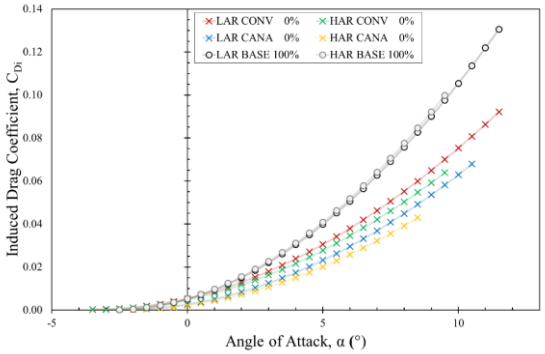

(c) Induced drag coefficient against angle of attack.

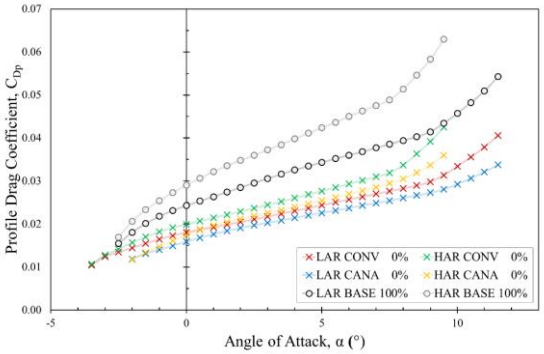

(d) Profile drag coefficient against angle of attack.

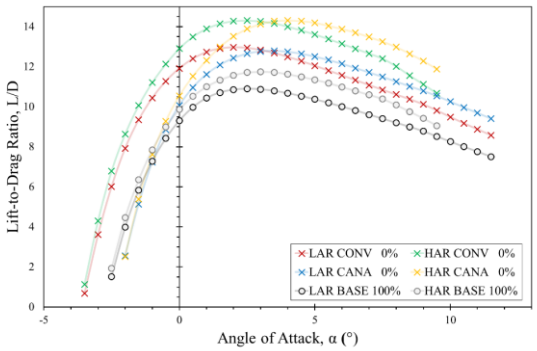

(e) Lift-to-drag ratio against angle of attack.

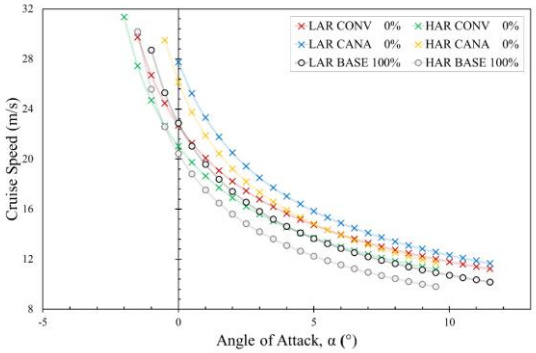

(f) Cruise speed against angle of attack.

Figure 7.9: Aerodynamic results for various wing arrangements.

The total drag coefficient, as shown in Figure 7.9 (b), is higher for baseline wings compared to configurations with reduced wingspans. Conventional wings experience higher drag coefficients than canard wings. The decomposition of total drag into profile and induced drag components provides further insights, as shown in Figure 7.9 (c) and (d). The baseline configurations exhibit the highest profile and induced drag coefficients due to their large wing wetted areas, frontal areas, and high lift coefficients. Canard wings have lower induced drag coefficients compared to conventional wings, as indicated in Figure 7.9 (c), due to their lower lift coefficients. HAR wings show similar induced drag coefficients to LAR wings at lower angle of attack, suggesting that the

increase in lift coefficient is compensated by the increase in aspect ratio for HAR wings. Profile drag, illustrated in Figure 7.9 (d), is higher for HAR wings than LAR wings due to the longer wingspan of HAR configurations, which translates to a larger frontal area and increased form drag.

The aerodynamic efficiency, represented by the L/D in Figure 7.9 (e), increases as either the front or rear wingspan is reduced from the baseline 100% wing configuration. This improvement is due to significant reductions in form and skin friction drag, which outweigh the reduction in lift. The peak aerodynamic efficiency of conventional and canard wings is similar in magnitude, with conventional wings having a slight edge. However, the peak efficiency for conventional wings occurs at a lower angle of attack, which is preferred to avoid operating near stall conditions while maintaining high aerodynamic efficiency. HAR wings exhibit higher aerodynamic efficiency than LAR wings due to better lift distribution and lower induced drag, despite a slight increase in profile drag.

Baseline 100% wings offer the highest lift with lower cruise speeds, making them optimal for scenarios requiring maximum lift. Configurations with reduced wingspans in both conventional and canard designs decrease lift and drag coefficients, potentially increasing aerodynamic efficiency but necessitating higher cruise velocities. Conventional wings provide higher lift coefficients and peak aerodynamic efficiency at lower angle of attack, whereas canard wings have lower induced drag. HAR wings are preferred for maximizing range due to their higher aerodynamic efficiency, provided they are structurally feasible.

7.2.2 Longitudinal Stability Properties

In addition to aerodynamic characteristics, aircraft stability is critical for ensuring ease of handling and pilotability. The stability analysis focuses on the longitudinal axis of the aircraft, examining the NP and CG positions, and pitch moment coefficient C_m under different wingspan configurations.

The NP of an aircraft is the CG location at which the aircraft is neutrally statically pitch stable, with a constant C_m. If the CG is behind the NP, the aircraft will diverge when a pitch disturbance occurs. Figure 7.10 (a) shows that as the rear wingspan decreases for

conventional wings, the NP shifts forward. Conversely, for canard wings, the NP shifts backward as the front wingspan reduces. This shift is due to the reduced lift from the front or rear wings, respectively, which affects the aircraft's pitching moment and NP. The change in the NP is slightly greater for HAR wings compared to LAR wings as the wingspan reduces.

Figure 7.10 (b) illustrates the CG position for HAR and LAR wings as the front or rear wingspan reduces, maintaining a trim and SM of 20%. The trim condition, where $C_m = 0$ at 0° angle of attack, is shown in Figure 7.10 (c). SM, defined by (7.2), is the difference between the NP and CG, divided by the MAC. Most fixed-wing aircraft operate at an SM of around 20%.

$$\mathrm{SM} = \frac{\mathrm{NP}_{\text{ref, le wing}} - \mathrm{CG}_{\text{ref, le wing}}}{\mathrm{MAC}_{\text{wing}}} \tag{7.2}$$

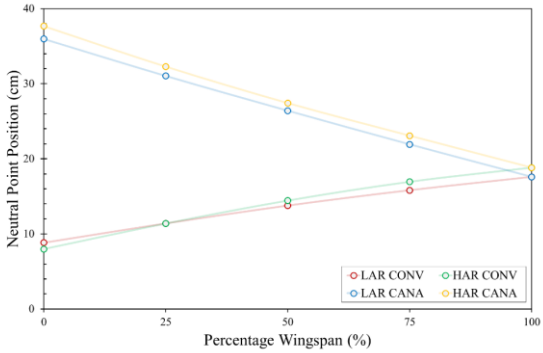

(a) Neutral point against percentage wingspan.

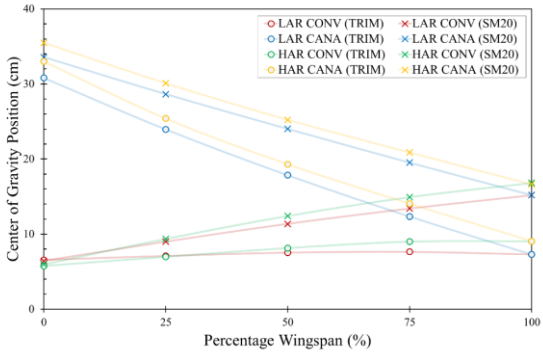

(b) CG location against percentage wingspan.

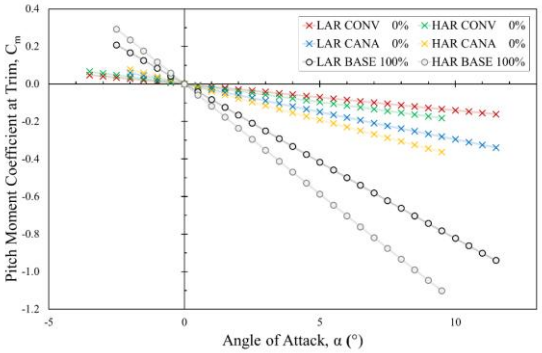

(c) Pitch moment coefficient at trim against angle of attack.

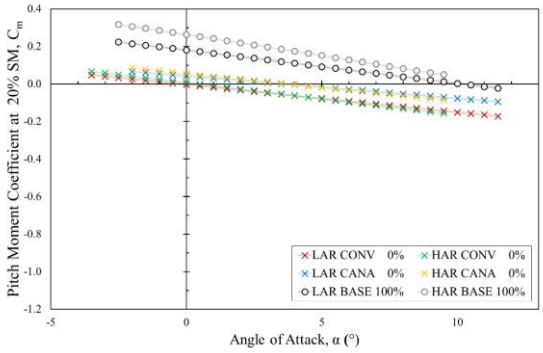

(d) Pitch moment coefficient at 20% static margin against angle of attack.

Figure 7.10: Longitudinal stability results for various wing arrangements.

The gradient of the pitch moment coefficient versus angle of attack in Figure 7.10 (c), indicates the degree of static longitudinal stability. A steeper gradient suggests higher pitch stability, which can result in an overshoot response and prolonged oscillations after

a pitch disturbance. Conversely, low static stability leads to a sluggish response. The degree of pitch stability decreases as the wingspan is reduced, due to smaller changes in CG compared to the changes in the NP. The CG position moves closer to the NP, resulting in lower pitch stability. The canard wings exhibit a higher degree of pitch damping than conventional wings, as indicated by a steeper gradient in Figure 7.10 (b). HAR wings generally show a higher degree of pitch stability than LAR wings, likely due to better lift generation, which translates to greater pitching moments. Figure 7.10 (d) indicates that the CG of all wing cases is positioned at a 20% SM, with similar gradients across different configurations. The HAR baseline wing is not trimmable, as its line does not intercept the x-axis before reaching the stall condition, suggesting an infeasible CG location for a 20% SM. The trim angle of attack decreases as the front or rear wingspan is reduced. Conventional wings have a lower trim angle of attack compared to canard wings, and there is no significant difference in trim angle of attack between LAR and HAR wings.

7.3 Flight Test Performance

The flight tests were conducted to gather performance data for four different wing arrangements using a data logger and sensors listed in Table 7.3. The performance data included measurements for cruise and high-speed flight, as well as no power/throttle glide tests to assess aerodynamic efficiency. Fluctuations in results are likely due to aerodynamic interactions between the front-mounted propeller and the wing surfaces.

7.3.1 Flight Performance Parameters

Figure 7.11 (a) and (b) display the CG positions for various wing configurations. As the front wing is shortened, resembling a canard wing, the NP moves rearward due to changes in lift distribution across the lifting surfaces, necessitating a rearward shift of the CG. For the 0% HAR and LAR canard wings, achieving the required CG position for stability and control was physically impossible, rendering their performance and stability data unusable due to excessive instability and uncontrollability.

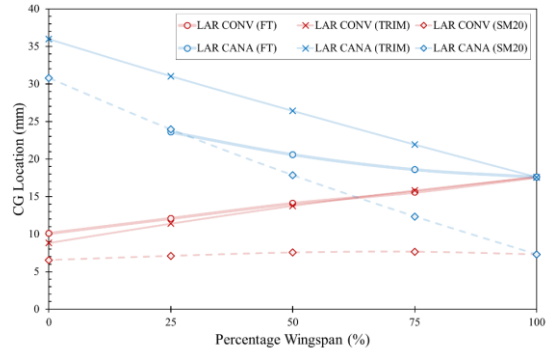

(a) Measured & XFLR5 CG location for LAR against percentage wingspan.

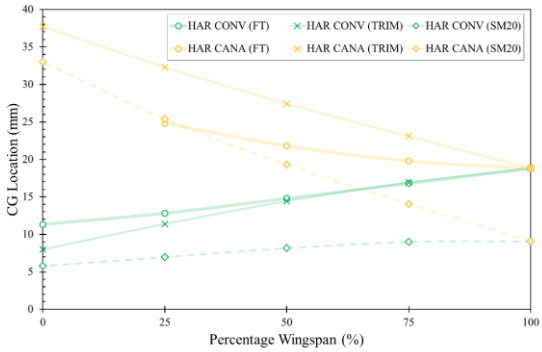

(b) Measured & XFLR5 CG location for HAR against percentage wingspan.

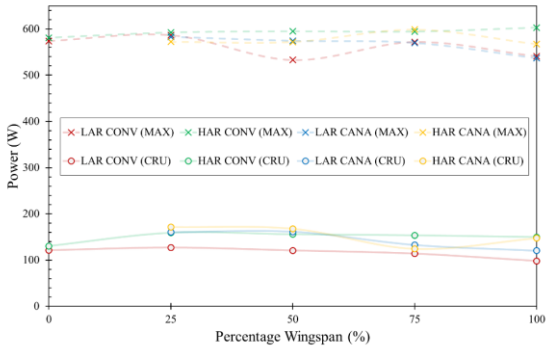

(c) Measured power required against percentage wingspan.

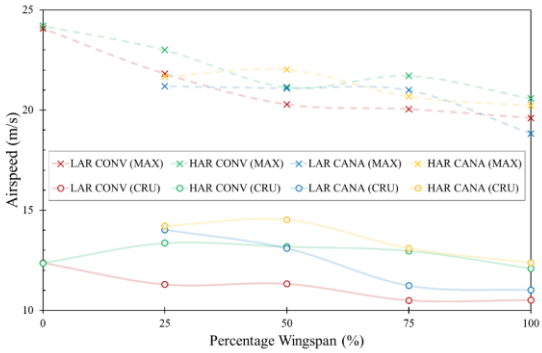

(d) Measured flight airspeed against percentage wingspan.

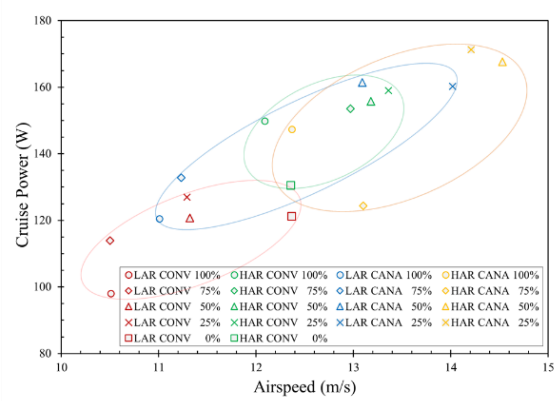

(e) Measured cruise power against airspeed.

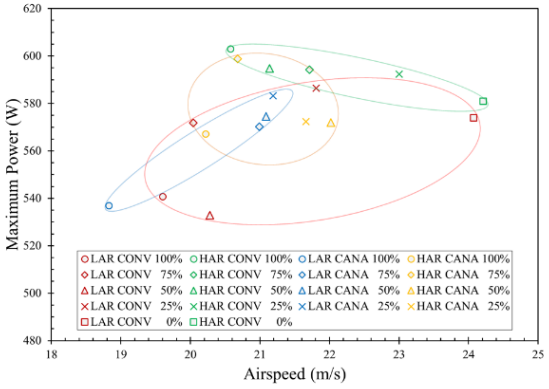

(f) Measured maximum power against airspeed.

Figure 7.11: Recorded flight test parameters for various wing arrangements.

Figure 7.11 (c) presents the power required for forward flight under both cruise and maximum speed conditions. Due to environmental variations, exact replication of flight conditions for each test was not possible. The data show an initial increase in power required as the wingspan is reduced to 50%, followed by a decrease in power required with further wingspan reduction. This trend results from changes in flight velocity and aerodynamic drag. Shortening the wingspan reduces the lift coefficient, necessitating higher speeds to generate sufficient lift. Simultaneously, reduced wing surface area

decreases drag, thereby lowering the power required at higher velocities. There is a notable tradeoff between speed and power: higher speeds demand more power.

Figure 7.11 (d) shows flight speed measurements against wingspan for both cruise and maximum speed conditions. Data from the pitot tube indicates that aircraft with 100% wingspan fly at lower speeds compared to those with shortened wingspan. Shortened wingspan configurations achieve higher speeds but at the cost of increased power requirements. However, the power required does not increase significantly, suggesting that reduced wingspan lowers total drag compared to baseline wings.

Figure 7.11 (e) and (f) show the power required versus airspeed for cruise and maximum speed conditions. The results indicate that LAR conventional wings require the least power across various wingspans during cruise due to lower speeds needed to maintain level flight. At maximum speeds, LAR conventional wings achieve higher velocities with minimal changes in power requirement compared to canard wings. This demonstrates that conventional wings offer greater efficiency in terms of speed and power for both cruise and maximum speed conditions, as power consumption remains relatively stable while speed increases with reduced wingspan.

7.3.2 Flight Test Aerodynamic Parameters

Figure 7.12 (a) presents the measured low and high glide speeds for various wing arrangements under no thrust conditions. The results indicate that canard wings generally exhibit higher glide speeds than conventional wings, aligning with the aerodynamic results shown in Figure 7.10. Specifically, LAR conventional wings have the lowest glide speeds. Additionally, both HAR conventional and canard wings glide at higher speeds compared to their LAR counterparts, likely due to a reduction in induced drag which facilitates greater forward speed for a given horizontal momentum. Among all configurations, the HAR canard 50% wing achieves the highest glide speed, suggesting it experiences the least drag.

Figure 7.12 (b) shows the calculated L/D for both low and high-speed glide conditions, derived using (7.1). The results reveal a diverse range of L/Ds among different wing arrangements. The HAR 50% canard wings attain the highest L/D of 4.03 during high-

speed glide. To better visualize the trends, each corresponding result is normalized to its initial L/D value at the baseline condition, as depicted in Figure 7.12 (c). The normalized results show that conventional wings generally exhibit an increased L/D compared to canard wings. This could be due to the canard wings incurring higher trim drag from additional control surface deflection required at higher airspeeds.

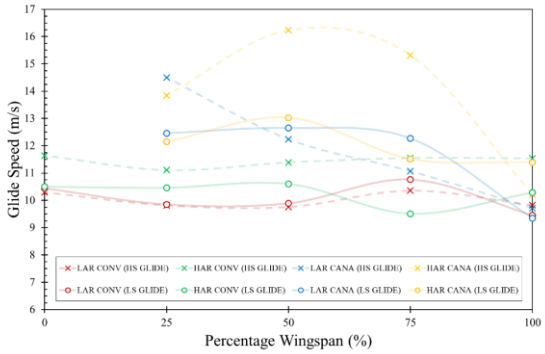

(a) Glide speed against percentage wingspan.

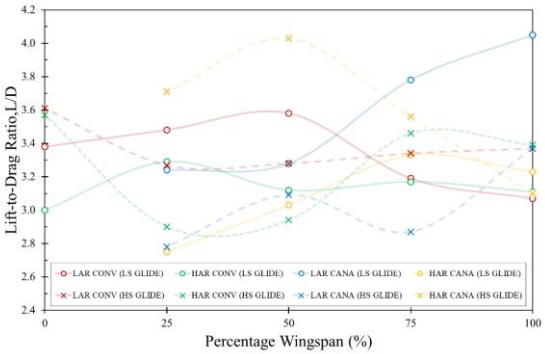

(b) Lift-to-drag ratio against percentage wingspan.

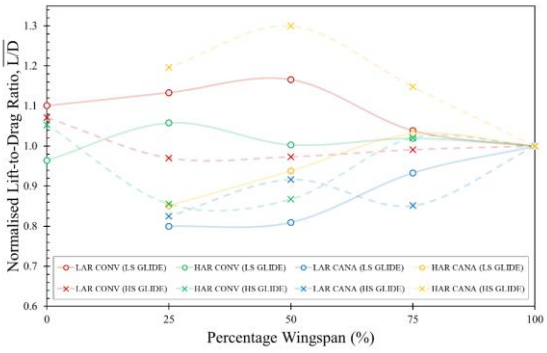

(c) Normalized lift-to-drag ratio against percentage wingspan.

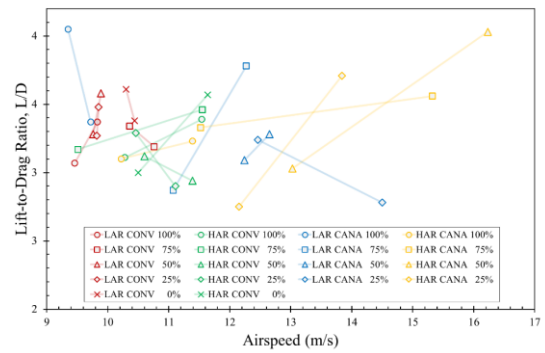

(d) Lift-to-drag ratio against airspeed.

Figure 7.12: Aerodynamic flight test parameters for various wing arrangements.

Figure 7.12 (d) illustrates the calculated L/D against airspeed. The data points, connected by lines for clarity, represent the low and high glide speeds for each wing configuration. Different markers denote various wingspan percentages: circular for 100%, square for 75%, triangular for 50%, diamond for 25%, and cross for 0%. The spread of the data is observed to be wider for canard wings compared to conventional wings. Conventional wings tend to glide at lower speeds but provide an L/D ranging from 2.94 to 3.61, whereas canard wings range from 2.87 to 4.03. This suggests that while canard wings can glide faster and achieve better peak L/Ds at higher speeds, conventional wings are more efficient at lower flight speeds.

7.4 Stability and Handling Qualities

In this study, the Cooper-Harper Rating (CHR) Scale was adapted to evaluate the handling qualities and provides a qualitative assessment of the stability of various wing arrangements, which is controlled wirelessly by a pilot using a transmitter. Although traditionally applied to manned aircraft with onboard pilots, the scale's application here is justified by the direct involvement of a human pilot who provides real-time feedback on the aircraft's control response and behaviour during flight.

The pilot assesses the handling qualities based on two key aspects: (1) Control response through the transmitter: the pilot evaluates the sensitivity, responsiveness, and predictability of the aircraft's control inputs as experienced through the transmitter. This reflects the ease or difficulty of performing specific manoeuvres. (2) Visual observation of aircraft behaviour: the pilot simultaneously observes the aircraft's flight path, stability, and dynamic responses from a ground-based perspective. This provides insights into how well the aircraft maintains its desired trajectory or recovers from disturbances, capturing essential elements of handling qualities in real-world conditions.

Additionally, the Cooper-Harper Scale was applied to various MTEs designed to assess the aircraft's performance under different operational scenarios. These MTEs included manoeuvres that push the aircraft to its operational limits, testing its aerodynamic and control coupling effects, and evaluating its ability to recover from disturbances or unstable conditions. By systematically applying the scale to these tasks, the study ensures a comprehensive assessment of the aircraft's handling qualities across a range of dynamic and potentially challenging conditions. This multi-faceted approach leverages the adaptability of the Cooper-Harper Scale to remote-controlled testing, providing valuable insights into the stability, control effectiveness, and overall manoeuvrability of the aircraft configurations under evaluation.

The CHR results, depicted in Table 7.5 as a colored heatmap and plotted in Figure 7.13 and Figure 7.14, evaluate pitch, roll, and directional stability.

Table 7.5: Cooper Harper rating assessment for various flight tasks and conditions.

Wing Configuration	LAR CANARD					LAR CONVENTIONAL					HAR CANARD					HAR CONVENTIONAL				
Wingspan Percentage	100%	75%	50%	25%	0%	100%	75%	50%	25%	0%	100%	75%	50%	25%	0%	100%	75%	50%	25%	0%
Pitch up Stability ^{HS}	5	5	5			5	7	6	7	4	6	3	2			5	4	5	3	1
Pitch up Stability ^{LS}	2	3	2			1	1	1	4	4	2	1	1			1	1	1	1	1
Pitch down Stability ^{HS}	2	5	3			2	2	2	1	2	2	5	5			1	2	1	5	1
Pitch down Stability ^{LS}	3	5	2			1	4	3	2	2	4	5	5			1	3	2	5	3
Elevator Effectiveness ^{LS}	3	3	1			3	1	2	4	2	2	2	1			2	1	2	3	5
Pitch up with Roll Stability	2	2	2			2	2	2	1	2	3	2	2			1	3	2	3	1
Pitch down with Roll Stability	3	3	4			5	4	3	2	2	3	5	5			1	3	3	4	3
Directional Stability	3	2	2			3	1	1	1	1	1	1	1			1	1	1	1	1
Roll Stability ^{HS}	4	2	4			5	4	4	4	6	4	3	3			3	6	4	5	3
Roll Stability ^{LS}	3	3	3			3	4	4	3	3	3	3	2			3	4	5	4	5
Aileron Effectiveness ^{HS}	1	1	1			2	2	1	1	1	1	1	1			1	1	1	1	1
Aileron Effectiveness ^{HS}	1	1	1			4	2	1	1	1	2	1	1			1	1	1	1	1
Adverse Yaw	3	1	1	6		3	2	1	1	1	2	1	1	3		2	1	1	1	1
Glide Characteristics ^{LS}	1	4	4	6		2	3	3	5	5	3	3	2	6		2	4	4	6	3
Glide Characteristics ^{HS}	2	4	4	7		1	1	1	2	3	2	3	3	4		1	1	2	4	2
Stall Characteristics	1	2	2			1	2	4	5	6	1	1	1			1	2	3	3	3
LSP Application	1	1	2			3	2	1	1	1	2	1	1			1	1	1	2	1
MLT Left	3	2	2			2	1	1	1	1	2	1	2			1	2	1	1	1
MLT Right	2	3	2			2	1	1	1	1	1	1	1			1	1	1	1	1
Steep Turns Left	2	2	1			2	1	2	1	1	2	1	2			2	2	1	1	1
Steep Turns Right	1	1	1			2	1	1	1	1	2	1	1			3	1	1	1	1

Scale	1	2	3	4	5	6	7	8	9	10

HS: High Speed
LS: Low Speed

LSP: Low Speed Power
MLT: Medium Level Turns

To assess pitch stability, the aircraft was subjected to a pilot-induced disturbance in the pitch axis, observing its initial response. A good CHR score indicates that the aircraft quickly returns to S&L flight with minimal altitude loss, whereas a poor CHR score indicates failure to return to S&L flight. The results revealed no significant deviations in the roll or yaw axes, allowing pitch stability to be evaluated in isolation.

7.4.1 Aircraft Flight Stability

Figure 7.13 (a) and (b) show the pitch stability under four conditions: pitch-up stability at high speed, pitch-up stability at low speed, pitch-down stability at high speed, and pitch-down stability at low speed. Notably, the LAR canard, LAR conventional, and HAR conventional wings showed improved pitch-up stability at high speeds as wingspan reduced from 100% to 0%. Increased airspeed and throttle settings can induce a pitch-up tendency, which may be mitigated by applying a downward thrust angle to generate a pitch-down moment about the CG.

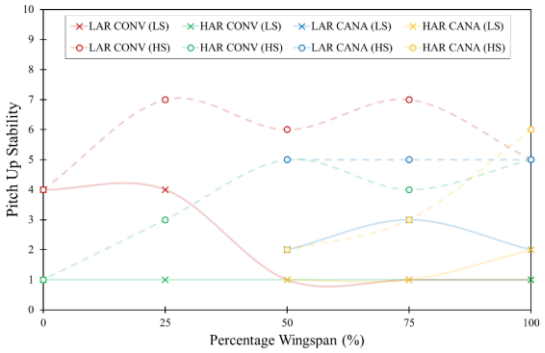

(a) Pitch up stability: low & high speed against percentage wingspan.

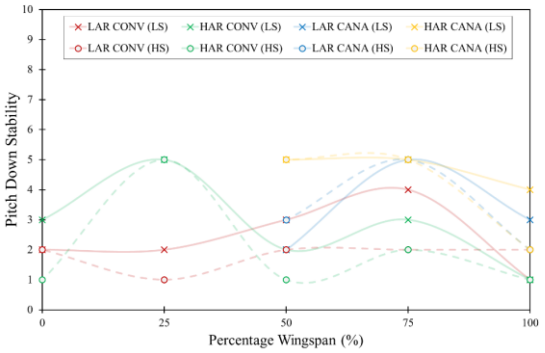

(b) Pitch down stability: low & high speed against percentage wingspan.

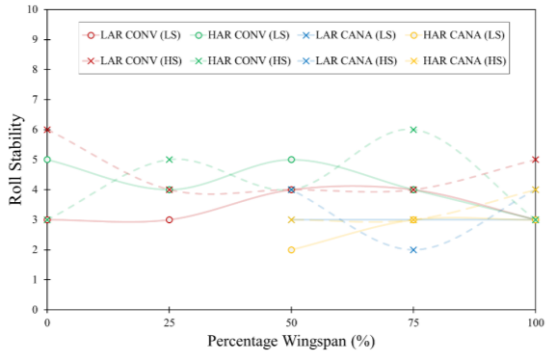

(c) Roll stability: low & high speed against percentage wingspan.

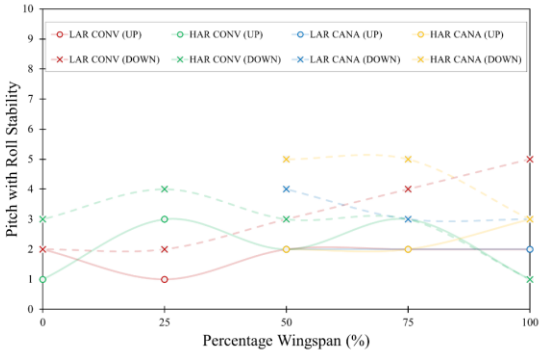

(d) Pitch up & down with roll stability against percentage wingspan.

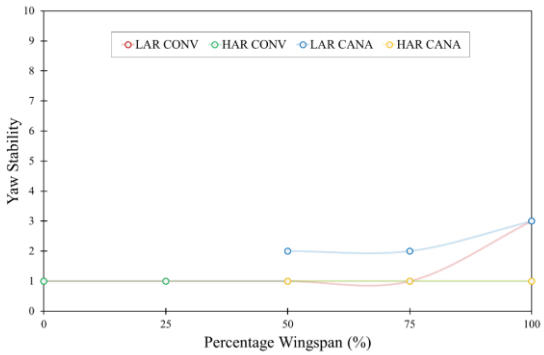

(e) Yaw stability against percentage wingspan.

Figure 7.13: Aircraft flight stability with Cooper Harper rating.

During pitch-up stability assessments, the aircraft flew at a fixed 70% throttle to maintain S&L flight. When pitching up, the fixed thrust eventually becomes insufficient to overcome drag and weight components, leading to deceleration and a natural pitch-down response, which most wing arrangements handled well. Reduced wing area enhances pitch damping, improving the aircraft's pitch rate during recovery.

HAR canard wings showed significant improvements in pitch-up stability at both high and low speeds, likely due to the longer outboard rear wings producing lift needed to generate a pitch-down moment. As the front wingspan decreases, the rear wings become more effective at producing this restoring force. Conversely, canard wings generally exhibited degraded pitch-down stability as front wingspan reduced, potentially because the front wings could not generate sufficient lift to produce a restoring pitch-up moment during a dive.

Figure 7.13 (a) and (b) demonstrate that HAR canard and conventional wings generally exhibit superior pitch-up stability. In LAR wings, pitch stability does not significantly vary with wing arrangement, except for LAR 25% and LAR 0%. Conventional wings are generally more stable and predictable in the pitch axis compared to canard wings, with clearer trends of pitch improvement with wingspan reduction. The HAR conventional wings demonstrate the highest pitch stability, with any shortcomings potentially correctable through piloting.

Figure 7.13 (c) shows the CHR scores for roll stability of HAR and LAR conventional wings, which are inconclusive for reliable correlations. The trend lines vary without strong patterns of increasing or decreasing roll stability as wingspan decreases. In contrast, LAR and HAR canard wings exhibit more significant variations in roll stability with wingspan reduction, as shown in Figure 7.14 (c). HAR conventional wings generally performed worse than LAR conventional wings, possibly due to increased roll damping hindering the aircraft from returning to level flight. Excessive roll stability can also hinder maneuverability, a consideration addressed in subsequent evaluations.

The pitch-down with roll stability assessment, shown in Figure 7.13 (d), evaluates the likelihood of the aircraft initiating a spiral tendency, crucial for dynamic spiral stability. Cross markers with dotted lines represent pitch-down maneuvers with roll stability. All

wing arrangements, except LAR conventional wings, generally degrade in spiral stability as wingspan decreases. LAR conventional wings exhibit the best spiral stability, indicated by their good roll and pitch-down stability CHR scores.

Directional stability assessments, shown in Figure 7.13 (e), reveal that HAR conventional and canard wings generally have superior directional stability, minimally affected by wingspan changes. All HAR wings consistently scored a CHR of 1. For LAR wings, directional stability improves with wingspan reduction. In LAR conventional wings, this is attributed to the forward CG movement with wingspan reduction, increasing the vertical stabilizer's moment arm. For LAR canard wings, the improvement is primarily due to increased flight velocity, enhancing tail effectiveness and restoring forces. Overall, HAR conventional wings exhibit the greatest directional stability among the tested wing arrangements.

7.4.2 Aircraft Flight Characteristics and Response

The aileron effectiveness assessment, shown in Figure 7.14 (a), indicates general improvement across all wings as wingspan is reduced. However, when wingspan is reduced beyond 50%, aircraft display excessive roll authority, becoming overly sensitive to roll inputs. This over-sensitivity, primarily due to reduced roll damping, resulted in all configurations receiving a CHR score of 1, meeting the basic roll authority requirement but making precise control more challenging. Hence, no specific wing configuration was identified as superior in roll authority.

Figure 7.14 (b) shows that low-speed pitch effectiveness generally improved as wingspan decreased, due to reduced pitch damping. However, HAR and LAR conventional wings experienced reduced pitch authority when the rear wingspan was reduced beyond 75%. This reduction caused a delayed aircraft response to pitch inputs, as the aircraft failed to augment its flight path instantaneously, indicating insufficient lift production. The shortened wingspan led to decreased front wing lift relative to angle of attack, necessitating a significant increase in angle of attack to achieve the required lift, thereby nullifying the benefit of reduced pitch damping and reducing pitch responsiveness.

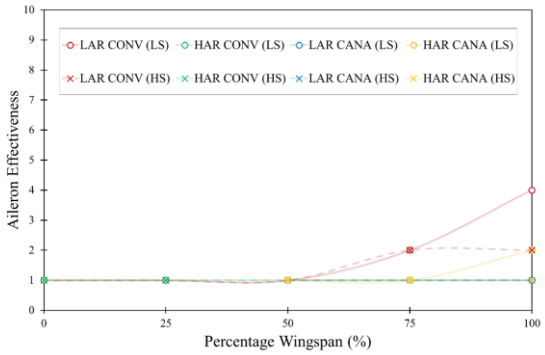

(a) Aileron effectiveness: low & high speed against percentage wingspan.

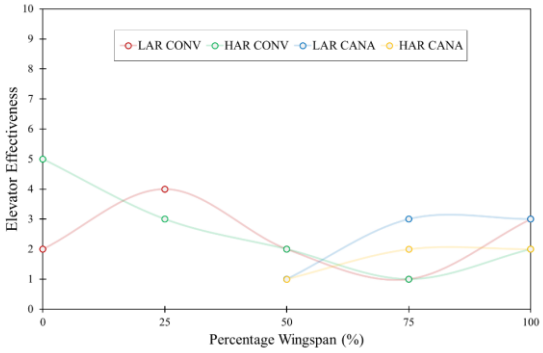

(b) Elevator effectiveness against percentage wingspan.

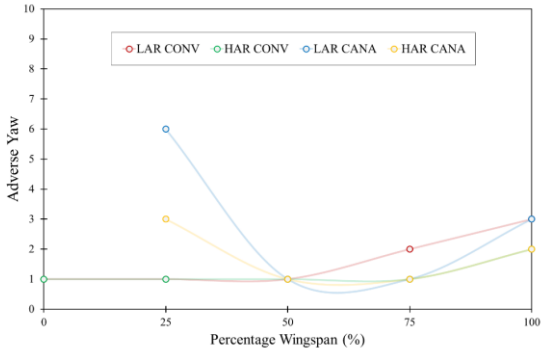

(c) Adverse yaw against percentage wingspan.

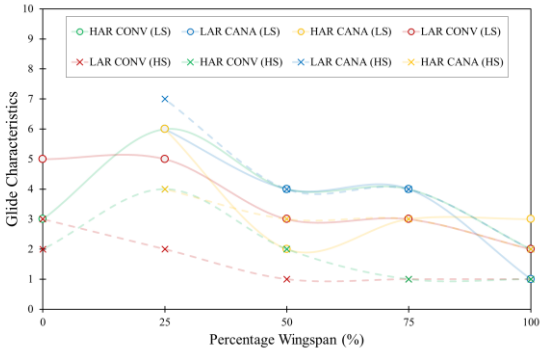

(d) Glide characteristics: low & high speed against percentage wingspan.

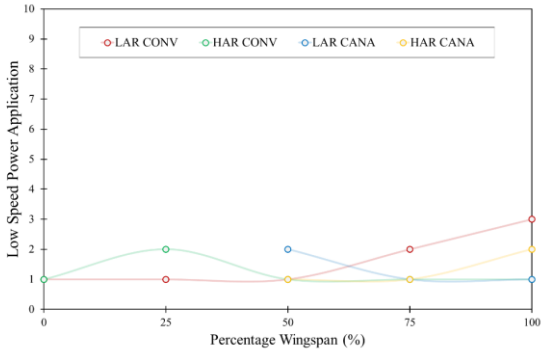

(e) Low speed power application against percentage wingspan.

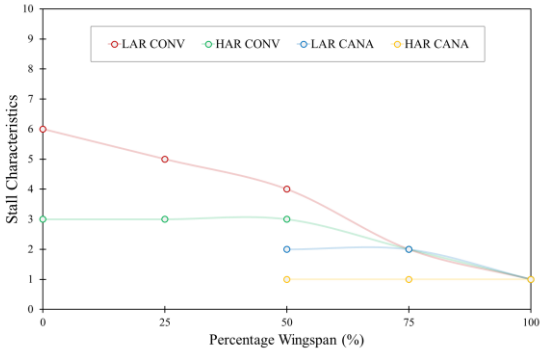

(f) Stall characteristics: no power/throttle against percentage wingspan.

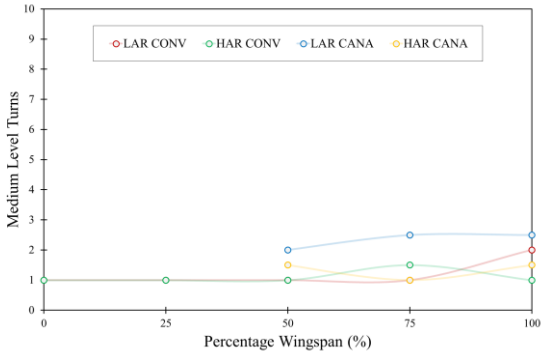

(g) Medium level turns against percentage wingspan.

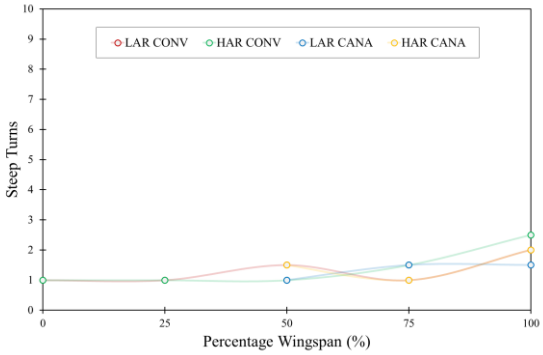

(h) Steep turns against percentage wingspan.

Figure 7.14: Aircraft flight characteristic and response with Cooper Harper rating.

Conversely, HAR and LAR canard wings did not exhibit this delay, likely due to inboard elevators positioned near the front propeller's propwash, which provided positive thrust vectoring effects and reduced pitch damping. This allowed the aircraft to pitch up more quickly, relying on the thrust-generated lift rather than other wing segments. Despite generally degraded pitch response at lower speeds, HAR and LAR canard wings were preferred for their pitch authority and responsiveness. During landings, however, pilots may favor the less sensitive pitch response of HAR and LAR conventional wings. LAR conventional wings are considered superior in low-speed pitch effectiveness due to their consistent performance, with HAR conventional wings showing slightly worse performance, potentially due to a higher susceptibility to stalls.

As shown in Figure 7.14 (c), adverse yaw performance in LAR and HAR canard wings degraded when the front wings were reduced beyond 50%. This degradation was primarily due to the rearward shift of the AC, reducing the moment arm between the CG and vertical stabilizer and causing insufficient directional stability. This instability led to unintentional yaw during aileron inputs, making controlled flight difficult. Therefore, HAR and LAR canard wings with more than 50% front wing reduction would require artificial stabilization systems for safe operation.

HAR and LAR conventional wings showed better performance, with HAR conventional wings experiencing less adverse yaw due to outboard ailerons increasing the roll moment arm, requiring less aileron deflection and reducing adverse yaw effects. Thus, HAR conventional wings are preferred, although adverse yaw effects can be mitigated by asymmetrical aileron deflection.

Figure 7.14 (f) evaluates stall characteristics, which depend on pitch and roll damping. All configurations showed slight reductions in stall stability with reduced wingspan. Canard wings showed no correlation between stall stability and wingspan beyond 75%, while conventional wings continued to deviate, with HAR wings deviating earlier than LAR wings. HAR conventional wings stabilized beyond 50% wingspan, with gradual, predictable turns during stalls. Canard wings, with inboard elevator surfaces stalling early, provided predictable, less abrupt stall recovery.

Conversely, LAR conventional wings experienced severe wing drops and quick departures during stalls, occasionally entering inverted attitudes. HAR conventional wings had more minute wing drops, resulting in slight spiral tendencies but easily recoverable by the pilot.

The MLT assessment in Figure 7.14 (g), HAR and LAR conventional wings showed slight improvements with reduced rear wingspan, due to enhanced directional stability. LAR canard wings performed worse, being temperamental in the yaw axis. HAR canard and conventional wings exhibited slight handling degradation due to longer wingspans and increased secondary rolling effects with yaw input. Overall, LAR conventional wings provided the most consistent handling qualities.

Steep turn assessments indicated slight improvements in handling with reduced wingspan. Compared to MLT, there is a slightly lower correlation between the different wing arrangements, due to the aggressive maneuvering nature of a steep turn. Since the maneuver, requiring high lift to compensate for centripetal force, prioritized pitching and longitudinal stability.

7.5 Comparison of Results and Rankings

To comprehensively evaluate the effect of various wing arrangements on aerodynamics, flight stability, and control performance, results from both analytical and experimental approaches were gathered. Each assessment parameter was normalized and cumulated into an overall score, which was then ranked from best to worst.

7.5.1 Unweighted Results and Rankings

Initially, scores were compared without weighting, as shown in Table 7.6, where each parameter was granted equal influence on the final overall score. This approach provides insights into the individual contributions of each parameter. However, simply summing raw values has its limitations, as minor differences in scores could significantly impact rankings. Despite this limitation, the ranking system aids in data interpretation and classification due to the large number of experimental cases.

In the aerodynamic analysis, the results indicated a general systematic improvement with the shortening of wingspan, with HAR and LAR 0% conventional wings performing the best. Notably, HAR wings generally outperformed their LAR counterparts. Overall, the results demonstrated that conventional wings performed better than canard wings.

Table 7.6: Ranking of aerodynamic analysis, flight testing and stability.

Rank	Aerodynamic Analysis		Flight Testing & Performance		CHR Stability & Response	
1	HAR CONV 0%	1.0869	LAR CONV 0%	1.1264	HAR CONV 100%	1.6632
2	LAR CANA 0%	1.0745	HAR CONV 0%	1.0906	HAR CONV 0%	1.6000
3	HAR CANA 0%	1.0645	LAR CANA 100%	1.0884	[HAR CONV 50%/	1.5684
4	LAR CONV 0%	1.0636	LAR CONV 100%	1.0857	HAR CANA 50%]	1.5684
5	HAR CONV 25%	1.0444	HAR CANA 75%	1.0838	[HAR CONV 75%/	1.5474
6	LAR CONV 25%	1.0284	HAR CANA 50%	1.0823	HAR CANA 75%/	1.5474
7	LAR CANA 25%	1.0261	LAR CONV 50%	1.0806	LAR CONV 50%]	1.5474
8	HAR CANA 25%	1.0156	LAR CONV 25%	1.0641	LAR CANA 100%	1.5263
9	HAR CONV 50%	1.0094	LAR CONV 75%	1.0505	[LAR CONV 75%/	1.5158
10	LAR CONV 50%	0.9971	LAR CANA 75%	1.0463	LAR CANA 50%]	1.5158
11	LAR CANA 50%	0.9899	HAR CONV 75%	1.0441	[LAR CONV 25%/	1.5053
12	HAR CANA 50%	0.9844	HAR CANA 25%	1.0414	HAR CANA 100%]	1.5053
13	HAR CONV 75%	0.9787	HAR CONV 25%	1.0360	LAR CONV 0%	1.4947
14	LAR CONV 75%	0.9682	LAR CANA 50%	1.0244	LAR CONV 100%	1.4737
15	HAR CANA 75%	0.9641	HAR CANA 100%	1.0204	LAR CANA 75%	1.4526
16	LAR CANA 75%	0.9624	LAR CANA 25%	1.0190	HAR CONV 25%	1.4316
17	[HAR CONV 100%/	0.9493	HAR CONV 100%	1.0160	HAR CANA 25%*	1.1789
18	HAR CANA 100%]	0.9493	HAR CONV 50%	1.0105	LAR CANA 25%*	0.1158
19	[LAR CONV 100%/	0.9412	[LAR CANA 0%*/	-	[LAR CANA 0%*/	-
20	LAR CANA 100%]	0.9412	HAR CANA 0%*]	-	HAR CANA 0%*]	-

*Wing arrangement cases that are not successfully tested.

The flight testing and performance assessment showed a similar trend, with HAR and LAR 0% conventional wings emerging as the top performers. However, there was a physical limitation in achieving the required CG location for both HAR and LAR 0% and 25% canard wings, due to the standardized fuselage with a forward-located motor, which restricted the allowable margin of rearward CG locations as the front wingspan was shortened. The test pilot reported that these affected aircraft were unstable and uncontrollable in flight, requiring high pilot workload and corrections, thus preventing the provision of CHR scores for these wing arrangements. Consequently, when neglecting the HAR and LAR 0% canard wings for performance assessment, a general trend emerged that conventional wings performed better than canard wings, which aligned with the aerodynamic analysis.

In the CHR stability and response assessment, canard wings tended to fare worse in control performance compared to conventional wings, as evidenced by their clustering among the lower ranks. It is important to note that certain wing arrangements shared similar ranks due to their comparable cumulative CHR scores, although the makeup of their individual CHR scores for each CHR assessment varied across the different wing arrangements. Notably, the HAR 100% conventional wing was the top performer in terms of control performance. Additionally, 100% to 50% HAR and LAR wings generally ranked higher than the 50% to 0% wings, likely due to the summation of both the stability and response parameters, which are naturally opposing for any given design. However, in contrast to the aerodynamics and flight performance results, the control performance assessment showed a preference for wing arrangements with longer wingspans.

Given that aerodynamics, flight, and control performance are vital parameters for any aircraft design, the importance of each parameter must be evaluated depending on the design requirements, mission intention, and applications. Therefore, in the next section, weightage factors will be introduced to the assessment parameters to determine the sensitivity of each parameter and to showcase a methodology for evaluating optimal wing arrangements for an eVTOL aircraft.

7.5.2 Cumulative Weighted Results and Rankings

In this section, weighted factors were used as shown in Table 7.4, and applied to their corresponding assessment parameters for evaluation, as shown in Table 7.7. Depending on the aircraft requirements and mission intent, various permutations and values of weightage factors can be considered. To limit the test cases, three different sets of general weightage profiles were introduced for further analysis: (1) equivalent weightage, (2) aerodynamic performance-oriented weightage, and (3) control performance-oriented weightage. The aerodynamic and flight performance parameters were combined to determine the overall aerodynamic performance influencing each wing arrangement due to their complementary results.

Table 7.7: Ranking of equivalent, aerodynamic- and stability-oriented designs.

Rank	Equivalent Weightage		Aerodynamic-Oriented Weightage		Control-Oriented Weightage	
1	HAR CONV 0%	1.3445	HAR CONV 0%	1.2168	HAR CONV 100%	1.4948
2	HAR CONV 100%	1.3262	LAR CONV 0%	1.1996	HAR CONV 0%	1.4723
3	HAR CANA 50%	1.3058	HAR CANA 50%	1.1744	HAR CANA 50%	1.4372
4	LAR CONV 0%	1.2980	LAR CONV 50%	1.1722	HAR CONV 50%	1.4289
5	LAR CONV 50%	1.2973	HAR CANA 75%	1.1638	LAR CONV 50%	1.4224
6	HAR CANA 75%	1.2916	LAR CONV 25%	1.1637	HAR CANA 75%	1.4196
7	HAR CONV 50%	1.2892	HAR CONV 100%	1.1578	HAR CONV 75%	1.4151
8	HAR CONV 75%	1.2827	LAR CANA 100%	1.1537	LAR CANA 100%	1.4022
9	LAR CANA 100%	1.2779	HAR CONV 75%	1.1503	LAR CONV 0%	1.3964
10	LAR CONV 25%	1.2775	HAR CONV 50%	1.1496	LAR CONV 25%	1.3915
11	LAR CONV 75%	1.2667	LAR CONV 75%	1.1422	LAR CONV 75%	1.3913
12	LAR CANA 50%	1.2632	LAR CONV 100%	1.1394	LAR CANA 50%	1.3896
13	LAR CONV 100%	1.2508	HAR CONV 25%	1.1374	HAR CANA 100%	1.3770
14	HAR CANA 100%	1.2486	LAR CANA 50%	1.1369	LAR CONV 100%	1.3623
15	HAR CONV 25%	1.2355	LAR CANA 75%	1.1227	LAR CANA 75%	1.3427
16	LAR CANA 75%	1.2327	HAR CANA 100%	1.1203	HAR CONV 25%	1.3336
17	HAR CANA 25%*	0.6050	HAR CANA 25%*	0.8180	HAR CANA 25%*	0.3919
18	LAR CANA 25%*	0.5688	LAR CANA 25%*	0.7953	LAR CANA 25%*	0.3422
19	LAR CANA 0%*	0.2149	LAR CANA 0%*	0.3223	LAR CANA 0%*	0.1074
20	HAR CANA 0%*	0.2129	HAR CANA 0%*	0.3194	HAR CANA 0%*	0.1064

*Wing arrangement cases that are not successfully tested.

In the equivalent weightage profile, with an equal contribution of 50% from both aerodynamic and control performance parameters, the HAR and LAR conventional wings dominate the top 50th percentile, indicating a good balance between aerodynamics and control performance. In contrast, the canard wings are generally ranked lower than their conventional counterparts. This trend differs significantly from the independent evaluation of aerodynamics and flight performance assessment results, where a mixture of conventional and canard wings performed well. Additionally, HAR wings tend to outperform their LAR counterparts, even when assessed in both aerodynamic-oriented and control-oriented aspects. The best-performing wing arrangement is the HAR conventional 0% wing, followed by the HAR conventional 100% wing. This outcome is expected, as the HAR 0% conventional wing topped the ranking in both aerodynamic analysis and was ranked second in terms of control and stability assessment, providing conclusive evidence that conventional wing designs have potential benefits for achieving better aerodynamic and control performance.

Next, the aerodynamic-oriented weightages were applied to derive an optimal aerodynamic-focused design, with less priority on flight stability and control. In this profile, aerodynamic and performance assessment parameters account for 75% of the total weightage, and the remaining 25% are stability and handling qualities assessment parameters. Comparing the pure aerodynamic analysis results with the aerodynamic-oriented weightage case, which considers a portion of control and stability influence,

the canard wings are observed to be susceptible to their control performance results, which pulled down the ranking of most canard wings. Due to poor stability and control results from flight testing, because of physical limitations in CG placement with wing reduction, the HAR and LAR 25% and 0% wings are positioned at the bottom of the rank, despite their above-average performance in the pure aerodynamic assessment. However, the HAR 50% and 75% canard wings rank third and fifth, respectively, diverging from the trend observed in analytical aerodynamic analysis where shorter wingspans beyond 50% reduction are favored. This is likely due to their strong performance in flight tests and CHR results, indicating that canard designs are more efficient when their front and rear wingspans are not the same. Interestingly, the LAR conventional 0% wing increased from fourth to second rank, from the equivalent case to the aerodynamic-oriented weightage case, due to its strong performance in flight testing, resulting in its cumulative weighted score outperforming that of the HAR 100% conventional wing. Thus, the aerodynamic-focused design tends to favor conventional wing arrangements with shortened wingspans.

Lastly, the control-oriented weightages were applied to derive an optimal control-focused design, with less priority on aerodynamic and flight performance. In this profile, stability and handling qualities assessment parameters account for 75% of the total weightage, and the remaining 25% are aerodynamic and performance assessment parameters. Notable observations include the LAR 0% and 50% conventional wings, which performed better in the control performance-oriented weightage analysis when aerodynamic and flight performance results were accounted for. However, most HAR canard and conventional wings now dominate the top 25th percentile, due to their favorable control performance in flight testing and CHR. Thus, the control-focused design tends to favor the HAR wings.

Through various assessments of the three approaches, analyzed with and without weightage factors, a clear trend highlights the HAR conventional 0% wing as the most promising wing arrangement for an eVTOL aircraft. It boasts excellent aerodynamic performance that aligns with its measured flight performance data, along with fantastic stability and response performance. Among the canard wings, the best-performing wing arrangement is the HAR 50% canard wing, which ranked third in all three weightage profiles. However, due to a limitation in CG placement for flight testing, all stability

and response results were voided for HAR and LAR 25% and 0% canard wings. These wings could potentially benefit in control and response performance if configured properly for stable and controllable flight, possibly improving their rankings from the bottom ranks.

7.6 Summary

The aerodynamic analysis showed that reducing the wingspan of either the front or rear wings from the full tandem wing baseline configuration significantly decreases drag more than lift, leading to increased aerodynamic efficiency and longer flight range. Unlike typical conventional aircraft, the rear wings of conventional configurations in this research act as lifting surfaces. This interaction, due to tip vortices between the front and rear wings, results in higher lift coefficients for conventional wings compared to canard wings. However, conventional wings also exhibit higher drag coefficients, resulting in similar peak aerodynamic efficiency. The angle of attack for maximum aerodynamic efficiency is lower for conventional wings, favoring operations away from stall regimes. HAR wings generally perform better than LAR wings, with greater improvements in lift coefficient outweighing the slight increase in profile drag. Thus, the HAR 0% conventional wing emerges as the top performer in aerodynamic performance.

In flight testing and performance assessment, shortening the wingspan generally increased flight speed and power requirements, although the increase in power required was not significant, indicating reduced drag penalties. Aircraft with shorter wingspans demonstrated higher efficiency in terms of flight speed and power requirements. Canard wings showed greater sensitivity to CG location adjustments with wingspan reduction, limiting propulsor design space. Conventional wings provided higher flight speed capabilities, reducing flight time to destination, while canard wings achieved higher glide speeds and L/Ds at higher speeds, suggesting suitability for higher-speed flights. LAR wings were more suited for low-speed flights with lower cruise speed and power requirements compared to HAR wings. The LAR 0% conventional wing performed best in-flight testing, followed by the HAR 0% conventional wing.

For stability, response, and control, HAR wings, both canard and conventional, offered greater stability while maintaining sufficient controllability and maneuverability for commercial applications. Canard wings proved more stable and predictable in roll stability, stalls, and elevator effectiveness but had directional stability issues. Conventional wings, with simpler control layouts and better spiral and pitch-down stability, provided better overall performance. The HAR conventional wings offered the best compromise in stability and control. In the CHR stability and response assessment, longer wingspan arrangements were generally preferred, with the HAR 0% conventional wing ranking second overall.

In the cumulative weighted assessment, with equivalent weightage, HAR and LAR conventional wings dominated, showing a balance between aerodynamics and control performance. In the aerodynamic-oriented profile, canard wings ranked lower due to control performance results, while the HAR 0% conventional wing remained top. In the control-oriented profile, HAR wings dominated, with longer wingspans preferred for stability, and the HAR 100% conventional wing taking the top rank.

Overall, the HAR 0% conventional wing is identified as the most desirable wing arrangement for an eVTOL aircraft, offering excellent aerodynamic performance, greater range capabilities, and high overall power efficiency. This configuration provides a larger design space for rotors due to less sensitivity to CG location, facilitating adequate mounting of vertical thrust motors and propeller elements. The aircraft can cruise at acceptable speeds for safer transition phases and efficiently reach target destinations. Stability analysis confirmed favorable characteristics and maneuverability, with predictable stall patterns requiring manageable pilot corrections.

While the sub-scale tests in this study provide valuable insights into the aerodynamic and stability characteristics of eVTOL designs, careful consideration of scaling processes is crucial when extrapolating results to full-scale implementations. Research indicates that sub-scale and full-scale aircraft exhibit proportional performance in key handling qualities, including time-domain and frequency-domain responses like time delay, rise time, and damping ratios [212]. When appropriately adjusted, control parameters in sub-scale models can accurately reflect the handling qualities of full-scale aircraft, making them effective for preliminary evaluations.

A recent study on Unmanned Aerial Systems (UAS) demonstrated the use of the Froude number for scaling control dynamics, validating UAS-specific maneuvers and performance specifications through flight tests on multirotor and single-rotor configurations [213]. This approach developed a Froude-scaled attitude bandwidth metric based on ADS-33E-PRF standards [214], showing its predictive capability for performance across different UAS types. Extending this framework to full-scale eVTOL aircraft necessitates addressing factors such as Reynolds number effects, structural integrity, inertia properties, and control system dynamics. Reynolds number variations influence aerodynamic behavior, particularly the laminar-turbulent transition, requiring full-scale CFD simulations for accuracy. Structural scaling laws ensure that full-scale components withstand increased loads and material demands. Adjustments to inertia properties, including mass distribution and moments of inertia, are vital for maintaining control dynamics during transitions. Finally, scaling control surfaces and actuators is essential to handle larger aerodynamic forces. This integrated scaling framework ensures that insights from sub-scale tests can be effectively extrapolated, enabling reliable performance predictions for full-scale eVTOL designs across all flight phases.

This chapter emphasizes the importance of sub-scale testing as a practical and cost-effective approach to validate wing configurations for eVTOL applications, focusing on handling qualities during low and high-speed phases. Although high-fidelity studies like CFD offer greater precision, sub-scale tests provided valuable insights into the aerodynamic and stability characteristics critical for urban operations, albeit with limitations in scaling and capturing transition dynamics. The study also highlighted the need for a more comprehensive evaluation framework, advocating for future integration of weighted optimization approaches across hover, transition, and cruise phases to address performance trade-offs. While the analysis concentrated on winged eVTOL configurations to optimize range, the flexibility of the developed framework enables its extension to multi-rotor designs, addressing a broader spectrum of eVTOL architectures. Lastly, the simplified canard configurations ensured consistency and comparability but acknowledged the potential of more advanced designs. Future work should explore refined canard geometries and propulsion setups to maximize their aerodynamic and operational benefits, enhancing the versatility and performance of eVTOL aircraft.

Chapter 8: Conclusion

8.1 Research Outcomes

This thesis presents a comprehensive investigation into the design, performance, and optimization of eVTOL aircraft, addressing key research gaps in Aircraft Design Limitations, Insufficient Methods & Approaches, and Underexplored Subject Areas. The study fulfills the objectives established at the outset, focusing on five critical technical and methodological areas:

1) Incorporating Unique eVTOL Design Factors,
2) Simplifying Early-Stage Design Analysis,
3) Developing Comprehensive Multidisciplinary Frameworks,
4) Characterizing Transition Phases, and
5) Optimizing eVTOL Wing and Rotor Configurations.

The research includes a comparative analysis of various eVTOL configurations, the development of a multidisciplinary performance assessment framework, detailed modeling of transition flight phases, and the evaluation of lifting surface benefits. Each chapter provides valuable insights into these innovative aircraft, contributing to the advancement of eVTOL technologies and laying a strong foundation for future research in this rapidly evolving field.

The first and second objectives focused on conducting a detailed comparative study of eVTOL aircraft design and configurations, selecting 14 eVTOL aircraft based on performance specifications, technological advancements, funding, certifiability, and company reputation. This study identified and analyzed key attributes and configuration types that influence aircraft sizing and performance, offering a range of appropriate design parameters for eVTOL aircraft. The findings highlight how electric propulsion has enabled innovative design concepts distinct from traditional VTOL and commercial aviation. By examining various configurations, the study establishes a foundation for optimal design practices that enhance performance and efficiency. These insights provide a valuable framework for understanding the impact of design choices on overall performance, helping designers make informed trade-offs to achieve balanced and efficient eVTOL designs.

To fulfill the third objective, a comprehensive multidisciplinary eVTOL aircraft model was designed and developed, enabling the assessment of aircraft performance across different flight regimes. This model integrated theoretical formulations and empirical models, providing a robust framework for performance analysis from initial to detailed design phases. The developed performance analysis tool, validated through case studies involving Archer Aviation's Maker and Joby Aviation's S4, proved reliable and accurate. The findings underscore the importance of minimizing aircraft weight to improve hover and cruise performance, as well as energy efficiency. This tool offers valuable insights for optimizing eVTOL designs, emphasizing the critical role of weight reduction. The analysis showing the Tiltrotor requiring 40.8% and 33.6% less hover power as compared to Lift+Cruise and Lift+Tiltrotor respectively. While also requiring 13.3% and 18.1% less cruise power to cruise as compared to Lift+Cruise and Lift+Tiltrotor, while having at the fastest velocity of 63.5 m/s due to its lower weight. These learnings are crucial for eVTOL development as they guide the optimization of design parameters to achieve better efficiency, safety, and performance in real-world applications.

The fourth objective focused on characterizing the transition performance of eVTOL aircraft and its effects during the conversion between vertical and horizontal flight phases. The research implemented a trimming approach and flight trajectory model, incorporating the BEMT method for improved characterization. The analysis highlighted the benefits of the tiltrotor configuration in enabling higher maximum velocities and efficient transition phases without incurring negative lift compared to Lift + Cruise configurations. However, it also noted the higher power consumption associated with tilting rotors. Additionally, the Lift + Cruise configuration was found to be more energy-efficient during transitions, as the Tiltrotor and Lift+Tiltrotor have increased peak power consumption of 57.5% and 88.3% respectively, emphasizing the importance of decoupling hover and cruise thrust requirements for optimal transition performance. Even though, the Tiltrotor has the lowest hover power requirement, requiring 57.4% and 33.6% less power as compared to Lift+Cruise and Lift + Tiltrotor configurations. These findings are crucial for meeting regulatory standards and ensuring safe and efficient operation during the transition phase. For eVTOL aircraft, understanding and optimizing the transition phase is vital for achieving smooth and efficient flight, which is essential for both safety and passenger comfort.

The fifth objective involved quantifying the benefits and design of lifting surfaces for eVTOL aircraft in terms of aerodynamics, stability, and handling qualities. The research developed both analytical and experimental models to assess various wing designs. A parametric and optimization study of tandem wing configurations provided detailed insights into wing design variables, emphasizing their impact on stability and aerodynamic performance. The aero-mass optimization led to the range parameter increase of 47.48% and 47.47% for conventional and canard configurations from the baseline. However, when handling quality constraints were applied in the aero-mass-stability optimizations, conventional designs remained optimal with a 47.66% increased range parameter as compared to the canard design with 25.92% from the baseline. The study concluded that configurations with unequal wing areas generally enhance performance, though they may reduce pitch damping.

Furthermore, experimental subscale flight testing conducted at different flight speed were used to validate the analytical models and identified the HAR 0% conventional wing as the top performer in terms of aerodynamic efficiency, stability, and overall power efficiency. This configuration offers a larger design space for rotors, less sensitivity to CG location, and superior cruise and transition capabilities, making it ideal for eVTOL applications. The optimization and validation of wing configurations directly contribute to the advancement of eVTOL aircraft by improving their aerodynamic performance, stability, and overall efficiency, which are crucial for practical and commercial viability.

In summary, the methodologies and analyses conducted recommend a weight efficient Lift + Cruise configuration with conventional wings for designing a power-efficient passenger carrying eVTOL aircraft under 3175 kg, based on current mission requirements and available energy solutions. Although more complex eVTOL configurations, such as tiltrotors and tandem wing designs, may offer additional capabilities, including increased flight speed and enhanced stability and maneuverability, they are currently less optimal due to complex transition characteristics and increase peak power requirements. These configurations require advanced energy solutions and meticulous design considerations to meet mission requirements effectively.

This thesis has successfully met its objectives by providing a detailed comparative study, developing a comprehensive performance model, characterizing transition phases, and optimizing wing configurations for eVTOL aircraft. The findings contribute significantly to the field of eVTOL design, offering valuable insights and practical tools for future advancements. The research highlights the dynamic nature of eVTOL innovation, emphasizing the importance of multidisciplinary approaches and rigorous validation through analytical and experimental methods. As eVTOL technology continues to evolve, the insights gained from this work will play a crucial role in shaping the next generation of aerial transportation. The practical applications of these learnings ensure that future eVTOL aircraft will be more efficient, safer, and better suited to meet the growing demands of urban and regional air mobility.

8.2 Recommendations and Future Works

This thesis has developed methodologies and models to address various aspects of eVTOL aircraft design and performance. However, several limitations inherent in the proposed approaches highlight opportunities for future research. Below, the key limitations and directions for improvement are outlined for each chapter:

→ Chapter 4: eVTOL Aircraft Design and Performance Analysis

The proposed methodology relies on several assumed parameters, such as motor efficiency, electric system performance, and other efficiency factors, which significantly influence the results. While trade studies and references to prior research provided input values, further investigation through computational or experimental methods is necessary. Sensitivity studies are crucial to quantify the impact of these assumptions and improve the robustness of the analysis. Proper characterization of all eVTOL components is essential, as it directly affects overall performance. Although this thesis outlines a design methodology to identify optimal eVTOL characteristics, further work is needed to validate these models at full scale. This includes applying the methodology to full-scale eVTOL aircraft, conducting extensive flight tests, and using onboard sensors for data collection to support validation and performance comparisons.

Another key limitation is the absence of a rotor wake model, which would allow for better accounting of interactional effects between rotors and the airframe. Similarly,

empirical-based models were used for some components, which could be replaced by physics-based models for greater accuracy. Future work should also include validation studies through high-fidelity simulations or experimental wind tunnel testing to further refine the performance predictions.

→ Chapter 5: Transition Flight Mode Analysis

The trajectory and transition methodologies in this study rely on simplified quasi-steady-state assumptions and conventional methods, such as momentum theory, blade element methods, and analytical or empirical approaches for wing elements. While these methods provide useful insights, they have limitations in capturing complex wake and vortex interactions affecting rotor and wing elements. The Blade Element Momentum Theory (BEMT) used for rotor modeling, though efficient, lacks fidelity. Incorporating high-fidelity models, such as CFD-based simulations, could better capture detailed aerodynamic interactions and improve power estimations. Future research should explore optimal trajectory paths under various constraints, conduct sensitivity analyses to validate assumptions, and include experimental studies for further accuracy.

The study lacks a comprehensive model for unsteady aerodynamic effects and rotor wake dynamics during transition. Future work should incorporate detailed tilt-rotor mechanics, vortex ring state modeling, and control system dynamics, including flight control and RPM control mechanisms. These additions would provide a more realistic representation of transition dynamics. Higher-fidelity computational methods, such as vortex wake or free-wake analyses, along with experimental validation, are essential to improve transition performance predictions and design robustness.

→ Chapter 6: Wing Configuration Design and Optimization

The mass estimation method used in this thesis relies on empirical data, which may not fully capture the structural efficiencies of advanced materials and configurations. Future research should incorporate physics-based models, such as finite element analysis (FEA), to refine mass estimates and explore structural optimization. While this study has analyzed the forces and loads acting on eVTOL aircraft during transitions, it is important to account for structural deformations that may influence aerodynamic properties. Integrating structural models would enable more accurate wing and rotor sizing, significantly impacting aircraft weight and rotor dynamics. Additionally,

acoustic models are crucial due to the stringent noise requirements for eVTOL operations in urban environments.

Additionally, while the study provides theoretical design curves, real-world applications will require addressing nonlinear interactions and complex trade-offs. Incorporating more detailed simulations and experimental validations will enhance the accuracy and practicality of the proposed design solutions.

→ Chapter 7: Subscale Experimental Wing Design Validation

Sub-scale testing was used to validate wing configurations, focusing on aerodynamic and stability characteristics. However, the absence of transition flight experiments limits the validation of the proposed transition models. Future studies should conduct transition flight tests to validate dynamic stability and control during this critical phase.

Scaling control dynamics and handling qualities from sub-scale to full-scale models requires a comprehensive scaling framework. Future research should address factors such as Reynolds number effects, structural integrity, inertia properties, and control system dynamics to ensure accurate extrapolation. Additionally, specific focus on refining canard designs and other wing configurations will further improve the design framework and handling qualities.

→ Summary

The methodologies developed in this thesis provide a foundation for advancing eVTOL aircraft design but require further refinement through higher-fidelity modeling, experimental validation, and comprehensive scaling studies. Even though eVTOL development is still in its design phase, future analysis must include considerations such as lifecycle and cost analysis to ensure the feasibility of future eVTOL operations. This would provide a comprehensive understanding of the economic viability and sustainability of eVTOL aircraft. Addressing these limitations will enhance the robustness, accuracy, and applicability of the proposed solutions, ensuring their relevance in real-world applications.

References

[1] S. A. C. S. Jayasooriya and Y. M. M. S. Bandara, “Measuring the economic costs of traffic congestion,” in *3rd International Moratuwa Engineering Research Conference, MERCon 2017*, Institute of Electrical and Electronics Engineers Inc., Jul. 2017, pp. 141–146. doi: 10.1109/MERCON.2017.7980471.

[2] Uber, J. Holden, and N. Goel, “Fast-forwarding to a future of on-demand urban air transportation,” Oct. 2016. [Online]. Available: https://www.uber.com/elevate.pdf

[3] A. Straubinger, R. Rothfeld, M. Shamiyeh, K. D. Büchter, J. Kaiser, and K. O. Plötner, “An overview of current research and developments in urban air mobility – setting the scene for UAM introduction,” *J Air Transp Manag*, vol. 87, p. 101852, Aug. 2020, doi: 10.1016/J.JAIRTRAMAN.2020.101852.

[4] D. F. Finger, C. Braun, and C. Bil, “The impact of electric propulsion on the performance of VTOL UAVs,” in *Deutscher Luft - und Raumfahrtkongress 2017*, 2017, pp. 1–18.

[5] D. F. Finger, C. Braun, and C. Bil, “Comparative assessment of parallel-hybrid-electric propulsion systems for four different aircraft,” *J Aircr*, vol. 57, no. 5, pp. 843–853, 2020, doi: 10.2514/1.C035897.

[6] A. S. Gohardani, G. Doulgeris, and R. Singh, “Challenges of future aircraft propulsion: a review of distributed propulsion technology and its potential application for the all electric commercial aircraft,” *Progress in Aerospace Sciences*, vol. 47, no. 5, pp. 369–391, 2011, doi: 10.1016/j.paerosci.2010.09.001.

[7] M. J. Duffy, S. Wakayama, R. Hupp, R. Lacy, and M. Stauffer, “A study in reducing the cost of vertical flight with electric propulsion,” *17th AIAA Aviation Technology, Integration, and Operations Conference, 2017*, 2017, doi: 10.2514/6.2017-3442.

[8] O. Cokorilo, “Urban air mobility: safety challenges,” in *Transportation Research Procedia*, Elsevier B.V., 2020, pp. 21–29. doi: 10.1016/j.trpro.2020.02.058.

[9] A. P. Cohen, S. A. Shaheen, and E. M. Farrar, “Urban air mobility: history, ecosystem, market potential, and challenges,” *IEEE Transactions on Intelligent Transportation Systems*, vol. 22, no. 9, pp. 6074–6087, Sep. 2021, doi: 10.1109/TITS.2021.3082767.

[10] S. P. Melo, F. Cerdas, A. Barke, C. Thies, T. S. Spengler, and C. Herrmann, “Life cycle engineering of future aircraft systems: the case of eVTOL vehicles,” in *Procedia CIRP*, Elsevier, Jan. 2020, pp. 297–302. doi: 10.1016/J.PROCIR.2020.01.060.

[11] K. Khavarian and K. M. Kockelman, "Life-cycle analysis of electric vertical take-off and landing vehicles," *Transportation Planning and Technology*, 2023, doi: 10.1080/03081060.2023.2217163.

[12] N. Sirirojvisuth, C. Y. Justin, and S. Briceno, "A life-cycle economic study of eVTOL air taxi service in the U.S. north-east region," *Vertical Flight Society's 76th Annual Forum and Technology Display*, pp. 1–19, 2020, doi: 10.4050/F-0076-2020-16410.

[13] A. Jonas *et al.*, "Morgan Stanley: eVTOL/urban air mobility TAM update: a slow take-off, but sky's the limit," May 2021. [Online]. Available: https://advisor.morganstanley.com/the-busot-group/documents/field/b/bu/busot-group/Electric%20Vehicles.pdf

[14] K. Schunck, K. J. Klasen, L. Dobravsky, and M. Zifaro, "Lufthansa Innovation Hub: Are air taxis ready for prime time?," 2021. [Online]. Available: https://tnmt.com/reports/are-air-taxis-ready-for-prime-time/

[15] A. Brown and W. L. Harris, "A vehicle design and optimization model for on-demand aviation," in *2018 AIAA/ASCE/AHS/ASC Structures, Structural Dynamics, and Materials Conference*, 2018. doi: 10.2514/6.2018-0105.

[16] C. Silva, W. Johnson, K. R. Antcliff, and M. D. Patterson, "VTOL urban air mobility concept vehicles for technology development," in *18th AIAA Aviation Technology, Integration, and Operations Conference*, Atlanta, GA, Jun. 2018. doi: https://doi.org/10.2514/6.2018-3847.

[17] G. Droandi, M. Syal, and G. Bower, "Tiltwing multi-rotor aerodynamic modeling in hover, transition and cruise flight conditions," in *Vertical Flight Society's 74th Annual Forum and Technology Display*, Aug. 2018, pp. 1–16.

[18] G. A. Wilke, "Aerodynamic performance of two eVTOL concepts," in *New Results in Numerical and Experimental Fluid Mechanics XII*, Springer Verlag, 2019, pp. 392–402. doi: 10.1007/978-3-030-25253-3_38.

[19] J. M. Bustamante, C. A. Herrera, E. S. Espinoza, C. A. Escalante, S. Salazar, and R. Lozano, "Design and construction of a UAV VTOL in ducted-fan and tilt-rotor configuration," *2019 16th International Conference on Electrical Engineering, Computing Science and Automatic Control, CCE 2019*, Sep. 2019, doi: 10.1109/ICEEE.2019.8884533.

[20] M. A. Gallani, L. C. S. Góes, and L. A. R. Nerosky, "Effects of distributed electric propulsion on the performance of a general aviation aircraft," *AIAA Propulsion and Energy 2020 Forum*, pp. 1–16, 2020, doi: 10.2514/6.2020-3594.

[21] P. Nathen, P. Bardenhagen, A. Strohmayer, R. Miller, S. Grimshaw, and J. Taylor, "Architectural performance assessment of an electric vertical take-off and

landing (e-VTOL) aircraft based on a ducted vectored thrust concept," in *Lilium*, 2021, pp. 1–35. [Online]. Available: https://investors.lilium.com/static-files/c355ba0f-662c-466c-aa6a-43072b3d34c3

[22] A. M. Stoll, J. Ben Bevirt, M. D. Moore, W. J. Fredericks, and N. K. Borer, "Drag reduction through distributed electric propulsion," in *14th AIAA Aviation Technology, Integration, and Operations Conference*, American Institute of Aeronautics and Astronautics Inc., 2014. doi: 10.2514/6.2014-2851.

[23] Singapore EDB, "Global trade and transport connections." [Online]. Available: https://www.edb.gov.sg/en/why-singapore/global-connectivity.html

[24] C. Tan, "The Straits Times: SMRT fined record $5.4 million for July 7 breakdown." [Online]. Available: https://www.straitstimes.com/singapore/transport/smrt-fined-record-54-million-for-july-7-breakdown

[25] C. Tan, "The Straits Times: Bus, train ridership in s'pore rises but numbers still far from pre-covid-19 levels." [Online]. Available: https://www.straitstimes.com/singapore/transport/bus-train-rides-rise-but-numbers-still-far-from-pre-covid-19-levels

[26] INRIX, "Global Traffic Scorecard | INRIX Global Traffic Rankings." [Online]. Available: https://inrix.com/scorecard/

[27] A. M. Stoll, J. Ben Bevirt, P. P. Pei, and E. V. Stilson, "Conceptual design of the Joby S2 electric VTOL PAV," in *14th AIAA Aviation Technology, Integration, and Operations Conference*, American Institute of Aeronautics and Astronautics Inc., 2014, pp. 16–20. doi: 10.2514/6.2014-2407.

[28] L. Tišljarić, T. Carić, B. Abramović, and T. Fratrović, "Traffic state estimation and classification on citywide scale using speed transition matrices," *Sustainability 2020, Vol. 12, Page 7278*, vol. 12, no. 18, p. 7278, Aug. 2020, doi: 10.3390/SU12187278.

[29] United Nations, *World Population Prospects 2022 Highlights*, 1st ed. New York: United Nations Publications, 2022. [Online]. Available: https://www.un.org/development/desa/pd/sites/www.un.org.development.desa.pd/files/wpp2022_summary_of_results.pdf

[30] C. Al Haddad, E. Chaniotakis, A. Straubinger, K. Plötner, and C. Antoniou, "Factors affecting the adoption and use of urban air mobility," *Transp Res Part A Policy Pract*, vol. 132, pp. 696–712, Feb. 2020, doi: 10.1016/J.TRA.2019.12.020.

[31] A. Stoll, J. Bevirt, A. Stoll, J. Bevirt, and J. Aviation, "Development of eVTOL aircraft for urban air mobility at Joby Aviation," in *Vertical Flight Society's 78th*

Annual Forum and Technology Display, The Vertical Flight Society, May 2022, pp. 1–11. doi: 10.4050/F-0078-2022-17528.

[32] J. Bain, A. Stoll, and G. V. Mikic, "Aerodynamic and acoustic design of the Joby Aviation eVTOL propeller," in *Vertical Flight Society's 77th Annual Forum and Technology Display*, The Vertical Flight Society, May 2021, pp. 1–10. doi: 10.4050/F-0077-2021-16687.

[33] B. Roget *et al.*, "Multi-fidelity investigation of aerodynamics and acoustics of the Joby Aviation aircraft," in *Vertical Flight Society's 80th Annual Forum and Technology Display*, The Vertical Flight Society, May 2024, pp. 1–16. doi: 10.4050/F-0080-2024-1282.

[34] G. V. Mikic, J. Bain, J. Bevirt, and A. Stoll, "A CFD based method to model aerodynamic interactions in complex eVTOL configurations for realtime and medium fidelity simulation," in *Vertical Flight Society's 77th Annual Forum and Technology Display*, The Vertical Flight Society, May 2021, pp. 1–8. doi: 10.4050/F-0077-2021-16786.

[35] A. Stoll and G. V. Milkic, "Transition performance of tilt propeller aircraft," in *Vertical Flight Society's 78th Annual Forum and Technology Display*, The Vertical Flight Society, May 2022, pp. 1–16. doi: 10.4050/F-0078-2022-17443.

[36] M. Muth, M. Keßler, and E. Krämer, "Aerodynamic and aeroacoustic investigation of installation effects of the Volocopter-2X rod structure," in *Vertical Flight Society's 80th Annual Forum and Technology Display*, The Vertical Flight Society, 2024, pp. 1–17. doi: 10.4050/F-0080-2024-1098.

[37] S. Miesner, M. Keßler, E. Krämer, and U. Schäferlein, "Investigation of near ground effects in hover flight for the multi-rotor aircraft Volocopter-2X," in *Vertical Flight Society's 76th Annual Forum and Technology Display*, The Vertical Flight Society, Oct. 2020, pp. 1–15. doi: 10.4050/F-0076-2020-16409.

[38] S. Miesner, M. Keßler, E. Krämer, and U. Schäferlein, "High-fidelity simulation of the Volocopter-2X in cruise flight," in *Vertical Flight Society's 77th Annual Forum and Technology Display*, The Vertical Flight Society, May 2021, pp. 1–13. doi: 10.4050/F-0077-2021-16724.

[39] L. Riccobene, A. Zanotti, D. Grassi, J. N. Braukmann, M. Kerho, and G. Droandi, "Infrared thermography measurements over an eVTOL full-scale wing section equipped with propellers mounted on a boom," in *Vertical Flight Society's 79th Annual Forum and Technology Display*, The Vertical Flight Society, 2023, pp. 1–6. doi: 10.4050/F-0079-2023-17982.

[40] W. Johnson, "A quiet helicopter for air taxi operations," in *Aeromechanics for Advanced Vertical Flight Technical Meeting 2020, Held at Transformative Vertical Flight 2020*, 2020, pp. 36–47.

[41] K. R. Antcliff, M. D. Moore, and K. H. Goodrich, "Silicon valley as an early adopter for on-demand civil VTOL operations," in *16th AIAA Aviation Technology, Integration, and Operations Conference*, 2016, pp. 1–17. doi: 10.2514/6.2016-3466.

[42] B. H. Law, "Medium: eVTOL is the future of flight, so why hasn't it happened yet?," Wisner Baum. [Online]. Available: https://medium.com/@baumhedlund/evtol-is-the-future-of-flight-so-why-hasnt-it-happened-yet-78fdfc5305ba

[43] H. Treeck, "Volocopter air taxi flies over Singapore's marina bay," Volocopter. [Online]. Available: https://www.volocopter.com/en/newsroom/volocopter-air-taxi-flies-over-singapores-marina-bay

[44] S. B. Anderson, "Historical overview of V/STOL aircraft technology," 1981. [Online]. Available: https://ntrs.nasa.gov/api/citations/19810010574/downloads/19810010574.pdf

[45] Y. Liu, M. Kreimeier, E. Stumpf, Y. Zhou, and H. Liu, "Overview of recent endeavors on personal aerial vehicles: A focus on the US and Europe led research activities," *Progress in Aerospace Sciences*, vol. 91, no. March, pp. 53–66, 2017, doi: 10.1016/j.paerosci.2017.03.001.

[46] Vertical Flight Society, "Vertipedia: Canadair CL-84 Dynavert." [Online]. Available: https://vertipedia.vtol.org/aircraft/getAircraft/aircraftID/56

[47] Vertical Flight Society, "Vertipedia: Bell X-22A." [Online]. Available: https://vertipedia.vtol.org/aircraft/getAircraft?aircraftid=309

[48] Sobchak Security, "XV-5A Vertifan Photo Gallery." [Online]. Available: https://sobchak.wordpress.com/2015/08/13/xv-5a-vertifan-photo-gallery/

[49] Vertical Flight Society, "Vertipedia: Bell Boeing V-22 Osprey." [Online]. Available: https://vertipedia.vtol.org/parentType/getParentType/typeID/45

[50] Vertical Flight Society, "Vertipedia: McDonnell Douglas AV-8B Harrier II." [Online]. Available: https://vertipedia.vtol.org/aircraft/getAircraft/aircraftID/59

[51] D. Esler, "AW609: Bringing tiltrotor technology to civil aviation," Aviation Week Network. [Online]. Available: https://aviationweek.com/business-aviation/aw609-bringing-tiltrotor-technology-civil-aviation

[52] Vertical Flight Society, "Vertipedia: Lockheed Martin F-35B Lightning II." [Online]. Available: https://vertipedia.vtol.org/aircraft/getAircraft/aircraftID/365

[53] Vertical Flight Society, "eVTOL Timeline." [Online]. Available: https://evtol.news/resources/evtol-timeline

[54] H. Jin, M. Yamazaki, J. Wong, and D. Evans, “Reuters: Tesla’s Musk hints of battery capacity jump ahead of industry event,” Technology. [Online]. Available: https://www.reuters.com/article/us-tesla-batteries-idUSKBN25L0MC

[55] L. Goldie-Scot, “BloombergNEF: A behind the scenes take on Lithium-ion battery prices,” Bloomberg. [Online]. Available: https://about.bnef.com/blog/behind-scenes-take-lithium-ion-battery-prices/

[56] X. G. Yang, T. Liu, S. Ge, E. Rountree, and C. Y. Wang, “Challenges and key requirements of batteries for electric vertical takeoff and landing aircraft,” *Joule*, vol. 5, no. 7, pp. 1644–1659, Jul. 2021, doi: 10.1016/j.joule.2021.05.001.

[57] T. P. Barrera *et al.*, “Next-generation aviation Li-ion battery technologies - enabling electrified aircraft,” *Electrochem Soc Interface*, vol. 31, no. 3, 2022, doi: 10.1149/2.F10223IF.

[58] E. Fisler, “Comprehensive study and fundamental understanding of lithium sulfur batteries for eVTOL,” PhD thesis, University of Maryland, College Park, United States, 2022.

[59] J. H. An, D. Y. Kwon, K. S. Jeon, M. Tyan, and J. W. Lee, “Advanced sizing methodology for a multi-mode eVTOL UAV powered by a hydrogen fuel cell and battery,” *Aerospace*, vol. 9, no. 2, Feb. 2022, doi: 10.3390/aerospace9020071.

[60] European Union Aviation Safety Agency, “EASA: Proposed Means of Compliance with the Special condition VTOL– MOC SC-VTOL Issue 1,” Cologne, May 2020. [Online]. Available: https://www.easa.europa.eu/en/downloads/114733/en

[61] European Union Aviation Safety Agency, “EASA: Second Publication of Means of Compliance with the Special Condition VTOL – MOC-2 SC-VTOL Issue 3,” Cologne, Dec. 2022. [Online]. Available: https://www.easa.europa.eu/en/downloads/137443/en

[62] European Union Aviation Safety Agency, “EASA: Third Publication of Means of Compliance with the Special Condition VTOL – MOC-3 SC-VTOL Issue 2,” Cologne, Jun. 2023. [Online]. Available: https://www.easa.europa.eu/en/downloads/136701/en

[63] H. D. Kim, “Distributed propulsion vehicles,” in *27th Congress of the International Council of the Aeronautical Sciences*, 2010, pp. 55–65. [Online]. Available: https://ntrs.nasa.gov/api/citations/20100036222/downloads/20100036222.pdf

[64] L. Gipson and J. Banke, “NASA: X-57 technical papers,” NASA. [Online]. Available: https://www.nasa.gov/aeroresearch/X-57/technical/index.html

[65] H. D. Kim, A. T. Perry, and P. J. Ansell, "A review of distributed electric propulsion concepts for air vehicle technology," in *2018 AIAA/IEEE Electric Aircraft Technologies Symposium*, 2018. doi: 10.2514/6.2018-4998.

[66] D. D. North, R. C. Busan, and G. Howland, "Design and fabrication of the langley aerodrome no. 8 distributed electric propulsion VTOL testbed," in *AIAA Scitech 2021 Forum*, 2021, pp. 1–19. doi: 10.2514/6.2021-1188.

[67] A. M. Stoll and G. V. Mikić, "Design studies of thin-haul commuter aircraft with distributed electric propulsion," in *16th AIAA Aviation Technology, Integration, and Operations Conference*, 2016, pp. 13–17. doi: 10.2514/6.2016-3765.

[68] N. K. Borer *et al.*, "Design and performance of the NASA SCEPTOR distributed electric propulsion flight demonstrator," in *16th AIAA Aviation Technology, Integration, and Operations Conference*, 2016, pp. 1–20. doi: 10.2514/6.2016-3920.

[69] A. Khajehzadeh, "Analysis of an over the wing based distributed propulsion system," Master thesis, Delft University of Technology, Delft, Netherlands, 2018.

[70] X. Shi, K. Kim, S. Rahili, and S. J. Chung, "Nonlinear control of autonomous flying cars with wings and distributed electric propulsion," in *IEEE Conference on Decision and Control*, IEEE, 2019, pp. 5326–5333. doi: 10.1109/CDC.2018.8619578.

[71] Y. Ma, W. Zhang, Y. Zhang, X. Zhang, and Y. Zhong, "Sizing method and sensitivity analysis for distributed electric propulsion aircraft," *J Aircr*, vol. 57, no. 4, pp. 730–741, 2020, doi: 10.2514/1.C035581.

[72] N. Natale, T. Salomone, G. De Stefano, and A. Piccolo, "Computational evaluation of control surfaces aerodynamics for a mid-range commercial aircraft," *Aerospace*, vol. 7, no. 10, Oct. 2020, doi: 10.3390/AEROSPACE7100139.

[73] T. H. New, Z. W. Teo, S. Li, Z. A. Ong, and B. Nagel, "Flow structures and aerodynamic behavior of a small-scale joined-wing aerial vehicle under subsonic conditions," *Aerospace*, vol. 10, no. 8, Aug. 2023, doi: 10.3390/aerospace10080661.

[74] T. Sibilli, "Modelling the aerodynamics of propulsive system integration at cruise and high-lift conditions," PhD thesis, Cranfield University, Cranfield, England, 2012.

[75] D. Kim, Y. Lee, S. Oh, Y. Park, J. Choi, and D. Park, "Aerodynamic analysis and static stability analysis of manned/unmanned distributed propulsion aircrafts

using actuator methods," *Journal of Wind Engineering and Industrial Aerodynamics*, vol. 214, Jul. 2021, doi: 10.1016/j.jweia.2021.104648.

[76] A. Zanotti, "Experimental study of the aerodynamic interaction between side-by-side propellers in eVTOL airplane mode through stereoscopic particle image velocimetry," *Aerospace*, vol. 8, no. 9, Sep. 2021, doi: 10.3390/aerospace8090239.

[77] A. Zanotti and D. Algarotti, "Aerodynamic interaction between tandem overlapping propellers in eVTOL airplane mode flight condition," *Aerosp Sci Technol*, vol. 124, May 2022, doi: 10.1016/j.ast.2022.107518.

[78] Ansys, "Simulation advances eVTOL development," Ansys Blog. [Online]. Available: https://www.ansys.com/blog/simulation-advances-evtol-development

[79] W. Shi, H. Zhang, and Y. Li, "The aerodynamic interaction effects between the rotor and fuselage on the drag performance of a civil helicopter in forward flight," *Applied Sciences (Switzerland)*, vol. 13, no. 13, Jul. 2023, doi: 10.3390/app13137376.

[80] D. Ciliberti, P. Della Vecchia, F. Nicolosi, and A. De Marco, "Aircraft directional stability and vertical tail design: A review of semi-empirical methods," *Progress in Aerospace Sciences*, vol. 95, pp. 140–172, Nov. 2017, doi: 10.1016/j.paerosci.2017.11.001.

[81] W. Johnson, C. J. Silva, and E. Solis, "Concept vehicles for VTOL air taxi operations," in *Conference on Aeromechanics Design for Transformative Vertical Flight*, San Francisco, CA, Jan. 2018. [Online]. Available: https://ntrs.nasa.gov/api/citations/20180003381/downloads/20180003381.pdf

[82] A. Bacchini and E. Cestino, "Electric VTOL configurations comparison," *Aerospace 2019, Vol. 6, Page 26*, vol. 6, no. 3, p. 26, Feb. 2019, doi: 10.3390/AEROSPACE6030026.

[83] D. F. Finger, C. Braun, and C. Bil, "Impact of electric propulsion technology and mission requirements on the performance of VTOL UAVs," *CEAS Aeronaut J*, vol. 10, no. 3, pp. 827–843, Sep. 2019, doi: 10.1007/s13272-018-0352-x.

[84] R. C. Bolam, Y. Vagapov, and A. Anuchin, "Review of electrically powered propulsion for aircraft," in *Proceedings - 2018 53rd International Universities Power Engineering Conference, UPEC 2018*, 2018, pp. 1–6. doi: 10.1109/UPEC.2018.8541945.

[85] Y. Zhou, H. Zhao, and Y. Liu, "An evaluative review of the VTOL technologies for unmanned and manned aerial vehicles," *Comput Commun*, vol. 149, no. August 2019, pp. 356–369, 2020, doi: 10.1016/j.comcom.2019.10.016.

[86] M. Drela, "Athena Vortex Lattice (AVL)," Apr. 2022, *Massachusetts Institute of Technology*: avl3.40b. [Online]. Available: https://web.mit.edu/drela/Public/web/avl/

[87] J. Anderson, *Fundamentals of Aerodynamics*, 6th ed. McGraw Hill, 2010.

[88] O. D. Dantsker and M. Vahora, "Comparison of aerodynamic characterization methods for design of unmanned aerial vehicles," in *2018 AIAA Aerospace Sciences Meeting*, 2018. doi: 10.2514/6.2018-0272.

[89] B. Peerlings, "A review of aerodynamic flow models, solution methods and solvers-and their applicability to aircraft conceptual design," Master thesis, Delft University of Technology, Delft, Netherlands, 2018.

[90] A. Deperrois, "XFoil Low Reynolds number 5 (XFLR5)," Nov. 04, 2003, *Sourceforge*: 6.61. [Online]. Available: http://www.xflr5.tech/xflr5.htm

[91] W. Johnson, "A history of rotorcraft comprehensive analyses," Apr. 2012. [Online]. Available: https://rotorcraft.arc.nasa.gov/Publications/files/TP-2012-216012_Johnson_final.pdf

[92] Charles III University of Madrid, "ASD: Aeroelastic and structural design lab." [Online]. Available: https://aero.uc3m.es/asd_lab-home/

[93] W. Johnson, "NDARC: NASA design and analysis of rotorcraft theoretical basis and architecture," 2011. [Online]. Available: https://rotorcraft.arc.nasa.gov/ndarc/media/Files/reportsAndPapers/NDARC-theory-long.pdf

[94] J. M. Vegh, E. Botero, M. Clark, J. Smart, and J. J. Alonso, "Current capabilities and challenges of NDARC and SUAVE for eVTOL aircraft design and analysis," in *AIAA Propulsion and Energy Forum and Exposition, 2019*, 2019, pp. 1–19. doi: 10.2514/6.2019-4505.

[95] S. Karpuk, R. Radespiel, and A. Elham, "Assessment of future airframe and propulsion technologies on sustainability of next-generation mid-range aircraft," *Aerospace*, vol. 9, no. 5, Jun. 2022, doi: 10.3390/aerospace9050279.

[96] T. Lukaczyk *et al.*, "SUAVE: An open-source environment for multi-fidelity conceptual vehicle design," in *16th AIAA/ISSMO Multidisciplinary Analysis and Optimization Conference*, 2015. doi: 10.2514/6.2015-3087.

[97] J. S. Gray, J. T. Hwang, J. R. R. A. Martins, K. T. Moore, and B. A. Naylor, "OpenMDAO: An open-source framework for multidisciplinary design, analysis, and optimization," *Structural and Multidisciplinary Optimization*, vol. 59, no. 4, pp. 1075–1104, Apr. 2019, doi: 10.1007/S00158-019-02211-Z/FIGURES/13.

[98] J. P. Jasa, J. T. Hwang, and J. R. R. A. Martins, "Open-source coupled aerostructural optimization using python," *Structural and Multidisciplinary Optimization 2018 57:4*, vol. 57, no. 4, pp. 1815–1827, Feb. 2018, doi: 10.1007/S00158-018-1912-8.

[99] J. S. Gray, G. K. W. Kenway, C. A. Mader, and J. R. R. A. Martins, "Aeropropulsive design optimization of a turboelectric boundary layer ingestion propulsion system," in *2018 Aviation Technology, Integration, and Operations Conference*, 2018. doi: 10.2514/6.2018-3976.

[100] M. Avera and R. Singh, "Scalability of hybrid-electric propulsion for VTOL UAS," in *North Atlantic Treaty Organization (NATO) Science and Technology Organization (STO) Meetings Proceedings Paper*, 2019, pp. 1–14. [Online]. Available: https://www.sto.nato.int/publications/STO%20Meeting%20Proceedings/STO-MP-AVT-323/MP-AVT-323-10.pdf

[101] M. E. Yazici, "Urban air mobility - The quest for the right shape," 2019. [Online]. Available: https://www.linkedin.com/pulse/urban-air-mobility-quest-right-shape-mehmet-emre-yazici/

[102] G. Bower, G. Droandi, and M. Syal, "Vahana design process part ii: preparing for lift-off," Acubed Airbus. [Online]. Available: https://acubed.airbus.com/blog/vahana/vahana-design-process-part-ii-preparing-for-lift-off/

[103] D. Felix, C. Braun, D. F. Finger, and C. Bil, "A review of configuration design for distributed propulsion transitioning VTOL aircraft," 2017, pp. 1–15. [Online]. Available: https://www.researchgate.net/publication/320617037

[104] Vertical Flight Society, "Airbus CityAirbus." [Online]. Available: https://evtol.news/airbus-helicopters/

[105] Vertical Flight Society, "EHang 216." [Online]. Available: https://evtol.news/ehang-216/

[106] J.-H. Boelens, "Volocopter: Pioneering the urban air taxi," Jun. 2019. [Online]. Available: https://press.volocopter.com/images/pdf/Volocopter-WhitePaper-1-0.pdf

[107] Vertical Flight Society, "Wisk Aero Cora (Generation 5)." [Online]. Available: https://evtol.news/kitty-hawk-cora/

[108] Vertical Flight Society, "Supernal (Hyundai Motor Group) S-A1," Jan. 06, 2020. [Online]. Available: https://evtol.news/hyundai-s-a1/

[109] Vertical Flight Society, "Beta Technologies ALIA." [Online]. Available: https://evtol.news/beta-technologies-alia/

[110] Vertical Flight Society, “Joby Aviation S4.” [Online]. Available: https://evtol.news/joby-s4

[111] Vertical Flight Society, “Kitty Hawk Heaviside.” [Online]. Available: https://evtol.news/kitty-hawk-heaviside/

[112] Vertical Flight Society, “Bell Nexus 4EX.” [Online]. Available: https://evtol.news/bell-nexus-4ex/

[113] Vertical Flight Society, “A^3 Vahana.” [Online]. Available: https://evtol.news/a3-by-airbus/

[114] Vertical Flight Society, “Archer Maker,” Jun. 2021. [Online]. Available: https://gallery.vtol.org/image/PyYYI

[115] Vertical Flight Society, “Vertical Aerospace VX4.” [Online]. Available: https://evtol.news/vertical-aerospace-VA-1X

[116] Vertical Flight Society, “Lilium Jet.” [Online]. Available: https://evtol.news/lilium/

[117] Jaunt Air Mobility, “Jaunt Air Mobility.” [Online]. Available: https://jauntairmobility.com/

[118] Vertical Flight Society, “Volocopter VoloRegion.” [Online]. Available: https://evtol.news/volocopter-voloconnect

[119] Vertical Flight Society, “Dufour Aerospace aEro 3.” [Online]. Available: https://evtol.news/dufour-aerospace-aero-3

[120] Vertical Flight Society, “EHang VT-30.” [Online]. Available: https://evtol.news/ehang-vt30

[121] Vertical Flight Society, “Eve Air Mobility Eve V3.” [Online]. Available: https://evtol.news/embraer/

[122] K. Muraoka, N. Okada, and D. Kubo, “Quad tilt wing VTOL UAV: Aerodynamic characteristics and prototype flight test,” *AIAA Infotech at Aerospace Conference and Exhibit and AIAA Unmanned...Unlimited Conference*, no. April, pp. 6–13, 2009, doi: 10.2514/6.2009-1834.

[123] G. M. Hoffmann, H. Huang, S. L. Waslander, and C. J. Tomlin, “Quadrotor helicopter flight dynamics and control: Theory and experiment,” in *AIAA Guidance, Navigation, and Control Conference 2007*, 2007, pp. 1670–1689. doi: 10.2514/6.2007-6461.

[124] B. Saeed and G. B. Gratton, “An evaluation of the historical issues associated with achieving non-helicopter V/STOL capability and the search for the flying

car," *Aeronautical Journal*, vol. 114, no. 1152, pp. 91–102, 2010, doi: 10.1017/S0001924000003560.

[125] P. M. Rothhaar *et al.*, "NASA langley distributed propulsion VTOL tilt-wing aircraft testing, modeling, simulation, control, and flight test development," in *14th AIAA Aviation Technology, Integration, and Operations Conference*, 2014, pp. 1–14. doi: 10.2514/6.2014-2999.

[126] R. C. Busan, P. C. Murphy, D. B. Hatke, and B. M. Simmons, "Wind tunnel testing techniques for a tandem tilt-wing, distributed electric propulsion VTOL aircraft," in *AIAA Scitech 2021 Forum*, 2021, pp. 1–23. doi: 10.2514/6.2021-1189.

[127] C. Rotaru and M. Todorov, "Helicopter Flight Physics," in *Flight Physics - Models, Techniques and Technologies*, IntechOpen, 2017. doi: 10.5772/INTECHOPEN.71516.

[128] J. Muchowski, M. Szumski, and A. Krzysiak, "Aerodynamic concept of the UAV in the gyrodyne configuration," *Transactions on Aerospace Research*, vol. 2018, no. 1, pp. 49–66, 2018, doi: 10.2478/tar-2018-0005.

[129] International Civil Aviation Organization, *ICAO: The future of aviation*. 2020. doi: 10.4271/430062.

[130] Z. Lovering, "Vahana configuration trade study - part i," Acubed Airbus. [Online]. Available: https://acubed.airbus.com/blog/vahana/vahana-configuration-trade-study-part-i/

[131] G. Bower, "Vahana configuration trade study - part ii," Acubed Airbus. [Online]. Available: https://acubed.airbus.com/blog/vahana/vahana-configuration-trade-study-part-ii/

[132] P. Pradeep and P. Wei, "Energy optimal speed profile for arrival of tandem tilt-wing eVTOL aircraft with RTA constraint," in *2018 IEEE CSAA Guidance, Navigation and Control Conference (GNCC)*, 2018. doi: 10.1109/GNCC42960.2018.9018748.

[133] S. S. Chauhan and J. R. R. A. Martins, "Tilt-wing eVTOL takeoff trajectory optimization," *J Aircr*, vol. 57, no. 1, pp. 93–112, 2020, doi: 10.2514/1.C035476.

[134] E. Senkans, M. Skuhersky, M. Wilde, and B. Kish, "A first-principle power and energy model for eVTOL vehicles," in *AIAA Aviation and Aeronautics Forum and Exposition, AIAA AVIATION Forum 2021*, 2021. doi: 10.2514/6.2021-3169.

[135] D. Escobar and H. Yeo, "Performance and loads of a wing-offset compound helicopter," in *AIAA Science and Technology Forum and Exposition, AIAA SciTech Forum 2022*, 2022. doi: 10.2514/6.2022-0929.

[136] S. Su, Y. Mei, Y. Zhou, X. Shan, P. Yu, and H. Wang, "Flight performance characteristics of a modified quadcopter with and without a wing based on flight test," in *AIAA SCITECH 2023 Forum*, Jan. 2023. doi: 10.2514/6.2023-2103.

[137] D. G. Mitchell, "Fifty years of the Cooper-Harper scale," in *AIAA Scitech 2019 Forum*, 2019. doi: 10.2514/6.2019-0563.

[138] R. P. Harper and G. E. Cooper, "Handling qualities and pilot evaluation," *Journal of Guidance, Control, and Dynamics*, vol. 9, no. 5, pp. 515–529, 1986, doi: 10.2514/3.20142.

[139] B. Donmez, M. L. Cummings, A. S. Brzezinski, and H. D. Graham, "Modified Cooper Harper scales for assessing unmanned vehicle displays," in *10th Performance Metrics for Intelligent Systems*, ACM, 2010, p. 386. doi: 10.1145/2377576.2377620.

[140] M. C. Cotting, "UAV performance rating scale based on the Cooper-Harper piloted rating scale," in *49th AIAA Aerospace Sciences Meeting*, 2011. doi: 10.2514/6.2011-923.

[141] G. D. García, D. Seiferth, V. Meidinger, D. Dollinger, P. Nagarajan, and F. Holzapfel, "Conduction of mission task elements within simulator flight tests for handling quality evaluation of an eVTOL aircraft," in *AIAA Scitech 2021 Forum*, 2021, pp. 1–16. doi: 10.2514/6.2021-1897.

[142] D. H. Klyde, P. C. Schulze, D. G. Mitchell, D. Sizoo, R. Schaller, and R. McGuire, "Mission task element development process: An approach to FAA handling qualities certification," in *AIAA AVIATION 2020 Forum*, 2020. doi: 10.2514/6.2020-3285.

[143] D. H. Klyde, P. C. Schulze, D. G. Mitchell, D. Sizoo, R. Schaller, and R. McGuire, "Developing means of compliance for eVTOL vehicles: phase 1 final report," 2020. [Online]. Available: https://rosap.ntl.bts.gov/view/dot/60631/dot_60631_DS1.pdf

[144] Horten Aircraft, "Horten HX-2," Horten Lift Air. [Online]. Available: https://www.horten-aircraft.com/en/

[145] B. Davisson, "Rutan Long-Ez," Air Progress. [Online]. Available: http://www.airbum.com/pireps/PirepLongEZ.html

[146] Textron Aviation, "Cessna 172," Cessna Skyhawk. [Online]. Available: https://cessna.txtav.com/en/piston/cessna-skyhawk

[147] National Air and Space Museum, "Rutan Quickie," Smithsonian. [Online]. Available: https://airandspace.si.edu/collection-objects/rutan-quickie/nasm_A19830337000

[148] J. Staszek, “Comparison of the aerodynamic properties of aircraft with a canard and a conventional arrangement,” Jun. 1979. [Online]. Available: https://apps.dtic.mil/sti/pdfs/ADA079929.pdf

[149] J. Staszek, “Comparison of aerodynamic properties of a canard aircraft with conventional aircraft,” Nov. 1979. [Online]. Available: https://apps.dtic.mil/sti/tr/pdf/ADA087866.pdf

[150] T. Mc Geer and I. Kroo, “A fundamental comparison of canard and conventional configurations,” *J Aircr*, vol. 20, no. 11, pp. 983–992, Nov. 1983, doi: 10.2514/3.48202.

[151] M. W. Keith and B. P. Selberg, “Aerodynamic optimization, comparison, and trim design of canard and conventional high performance general aviation configurations,” in *21st Aerospace Sciences Meeting*, AIAA, 1983. doi: 10.2514/6.1983-58.

[152] B. P. Selberg and K. Rokhsaz, “Aerodynamic tradeoff study of conventional, canard, and trisurface aircraft systems,” *J Aircr*, vol. 23, no. 10, pp. 768–774, 1986, doi: 10.2514/3.45379.

[153] B. P. Selberg and D. L. Cronin, “Aerodynamic-structural study of canard wing, dual wing, and conventional wing systems for general aviation applications,” Feb. 1985. [Online]. Available: https://ntrs.nasa.gov/api/citations/19850008520/downloads/19850008520.pdf

[154] Vertical Flight Society, “teTra Aviation Mk-5,” Sep. 04, 2021. [Online]. Available: https://evtol.news/tetra-aviation-mk-5

[155] Vertical Flight Society, “Pipistrel Vertical Solutions Nuuva V300,” 2019. [Online]. Available: https://evtol.news/pipistrel-cargo-drone/

[156] Vertical Flight Society, “Opener BlackFly,” 2020. [Online]. Available: https://evtol.news/opener-blackfly/

[157] Vertical Flight Society, “ACS Aviation Z-300.” [Online]. Available: https://evtol.news/acs-aviation-z-300/

[158] Vertical Flight Society, “Ascendance Flight Technologies ATEA.” [Online]. Available: https://evtol.news/ascendance-flight-technologies-atea

[159] J. J. Schoser, M. Cuadrat-Grzybowski, and S. G. P. Castro, “Preliminary control and stability analysis of a long-range eVTOL aircraft,” in *AIAA Science and Technology Forum and Exposition, AIAA SciTech Forum 2022*, 2022. doi: 10.2514/6.2022-1029.

[160] Vertical Flight Society, “Honda eVTOL,” Sep. 30, 2021. [Online]. Available: https://evtol.news/honda-evtol

[161] A. Minardo, “The tandem wing: Theory, experiments, and practical realisations,” Master thesis, Politecnico di Milano, Milan, Italy, 2014.

[162] I. Kryvokhatko, *Aerodynamics of Tandem Wing Aircraft*, 1st ed. Springer Nature, 2023. doi: 10.1007/978-3-031-23777-5/COVER.

[163] R. Jones, D. J. Cleaver, and I. Gursul, “Aerodynamics of biplane and tandem wings at low Reynolds numbers,” *Exp Fluids*, vol. 56, no. 6, Jun. 2015, doi: 10.1007/s00348-015-1998-3.

[164] T. M. Broering and Y. Lian, “The effect of wing spacing on tandem wing aerodynamics,” in *28th AIAA Applied Aerodynamics Conference*, 2010. doi: 10.2514/6.2010-4385.

[165] S. A. Andrews and R. E. Perez, “Analytic study of the conditions required for longitudinal stability of dual-wing aircraft,” *J Aerosp Eng*, vol. 232, no. 5, pp. 958–972, May 2017, doi: 10.1177/0954410017704215.

[166] J. Boling and G. C. Zha, “Numerical investigation of longitudinal static stability of a high-speed tandem-wing VTOL vehicle using coflow jet airfoil,” in *AIAA Scitech 2021 Forum*, 2021, pp. 1–22. doi: 10.2514/6.2021-1732.

[167] T. Goetzendorf-Grabowski and M. Figat, “Aerodynamic and stability analysis of personal vehicle in tandem-wing configuration,” *J Aerosp Eng*, vol. 231, no. 11, pp. 2146–2162, Sep. 2017, doi: 10.1177/0954410016662077.

[168] T. Kaya and S. Özgen, “Aerodynamic design and control of tandem wing UAV,” in *AIAA Aviation 2019 Forum*, 2019, pp. 1–20. doi: 10.2514/6.2019-3139.

[169] Uber Elevate, “UberAir vehicle requirements and missions,” 2018. [Online]. Available: https://s3.amazonaws.com/uber-static/elevate/Summary+Mission+and+Requirements.pdf

[170] International Organization for Standardization, “ISO 2533:1975 - standard atmosphere,” 1975. [Online]. Available: https://www.iso.org/standard/7472.html

[171] Joby Aviation, *The complete flight profile of Joby’s eVTOL aircraft*, (Jul. 24, 2021). [Online Video]. Available: https://www.youtube.com/watch?v=cuJEf4v05Z0

[172] D. P. Raymer, *Aircraft Design: A Conceptual Approach*, 6th Edition. 2018. doi: 10.2514/4.104909.

[173] M. Niţă and D. Scholz, “Estimating the Oswald factor from basic aircraft geometrical parameters,” *DGLR Lilienthal-Oberth e.V., 2012*, 2012, [Online]. Available: https://www.fzt.haw-hamburg.de/pers/Scholz/OPerA/OPerA_PUB_DLRK_12-09-10.pdf

[174] R. McDonald and B. German, "eVTOL stored energy overview," in *Uber Elevate Summit*, San Francisco, CA, USA, 2017. [Online]. Available: https://www.uber.com/us/en/elevate/summit/2017/

[175] E. Villanueva *et al.*, "Thermal management system of battery for electric vehicle," US10960785B2, Mar. 30, 2021 [Online]. Available: https://patents.google.com/patent/US10960785B2/en

[176] J. Bogaisky, "Has Joby cracked the power problem to make electric air taxis work?," *Forbes - Aerospace & Defense*, Nov. 23, 2020. [Online]. Available: https://www.forbes.com/sites/jeremybogaisky/2020/11/23/joby-batteries-electric-aviation/?sh=748c64e276a7

[177] S. Sripad and V. Viswanathan, "The promise of energy-efficient battery-powered urban aircraft," in *National Academy of Sciences of the United States of America*, National Academy of Sciences, Nov. 2021. doi: 10.1073/PNAS.2111164118/SUPPL_FILE/PNAS.2111164118.SAPP.PDF.

[178] B. English and J. Bevirt, "Aircraft control system and method," US20200333805A1, Oct. 22, 2020 [Online]. Available: https://patents.google.com/patent/US20200333805

[179] F. D. Harris, "Hover performance of isolated proprotors and propellers," Jan. 2017. [Online]. Available: https://rotorcraft.arc.nasa.gov/Publications/files/NASA_CR-2017_219486_FINAL.pdf

[180] W. Johnson, *Helicopter Theory*, 2nd ed. Dover Publications, 1994.

[181] Alfred. Gessow and G. C. Myers, *Aerodynamics of the Helicopter*, 8th ed. New York: Frederick Ungar Publishing Co., 1985.

[182] Joby Aviation, *Joby Aviation analyst day video*, (Jun. 03, 2021). [Online Video]. Available: https://ir.jobyaviation.com/about-us/presentations/detail/9754/joby-aviation-analyst-day-video

[183] E. Torenbeek, *Advanced Aircraft Design: Conceptual Design, Analysis and Optimization of Subsonic Civil Airplanes*, 1st ed. John Wiley & Sons, 2013.

[184] S. F. Hoerner, *Fluid-Dynamic Drag*, 1st ed. Sighard F. Hoerner, 1965.

[185] Mathworks, "MATLAB: Optimization toolbox," 2024, *Mathworks*: R2024a. [Online]. Available: https://www.mathworks.com/products/optimization.html

[186] W. L. Fredericks, S. Sripad, G. C. Bower, and V. Viswanathan, "Performance metrics required of next-generation batteries to electrify vertical takeoff and landing (VTOL) aircraft," *ACS Energy Lett*, vol. 3, no. 12, pp. 2989–2997, 2018, doi: 10.1021/acsenergylett.8b02195.

[187] Beta Technologies, “Introduction to EVA & Beta Technologies,” 2021, *Beta Technologies*.

[188] Joby Aviation and Reinvent, “Commercializing aerial ridesharing,” 2021, *Joby Aviation*.

[189] Vertical Aerospace, “Investor Deck 2021,” 2021, *Vertical Aerospace*.

[190] T. F. Tallerico, “NASA reference motor designs for electric vertical takeoff and landing vehicles,” in *2021 AIAA/IEEE Electric Aircraft Technologies Symposium* , Institute of Electrical and Electronics Engineers Inc., 2021, pp. 1–41. doi: 10.23919/EATS52162.2021.9704824.

[191] W. A. Timmer and R. P. J. O. M. Van Rooij, “Some aspects of high angle-of-attack flow on airfoils for wind turbine application,” in *European wind energy conference "wind energy for the new millennium,* 2001. [Online]. Available: https://www.researchgate.net/publication/228650605

[192] T. Patterson, “Joby Aviation claims: fastest flight of an eVTOL aircraft,” Modern Flying. [Online]. Available: https://www.flyingmag.com/joby-aviation-reaches-new-top-speeds/

[193] W. Johnson, “Lilium e-VTOL achieves new top-speed in test flight,” Teslarati. [Online]. Available: https://www.teslarati.com/lilium-achieves-new-top-speed-155-mph-in-newest-test-flight/#google_vignette

[194] M. Drela, “XFOIL: an analysis and design system for low Reynolds number airfoils,” in *Low Reynolds Number Aerodynamics,* 1989. doi: 10.1007/978-3-642-84010-4_1.

[195] F. Götten, M. Havermann, C. Braun, M. Marino, and C. Bil, “Improved form factor for drag estimation of fuselages with various cross sections,” *J Aircr,* vol. 58, no. 3, pp. 549–561, Dec. 2020, doi: 10.2514/1.C036032.

[196] D. P. Wells, B. L. Horvath, and L. A. McCullers, “The flight optimization system weights estimation method,” Jun. 2017. [Online]. Available: https://ntrs.nasa.gov/citations/20170005851

[197] Jan. Roskam, *Airplane Design. Part V: Component Weight Estimation,* 3rd ed., vol. 5. KS: DAR Corporation, 2003. Accessed: Dec. 03, 2024. [Online]. Available: https://books.google.com/books/about/Airplane_Design.html?id=mMU47Ld7yQkC

[198] B. L. Horvath and D. P. Wells, “Comparison of aircraft conceptual design weight estimation methods to the flight optimization system,” in *2018 AIAA Aerospace Sciences Meeting,* American Institute of Aeronautics and Astronautics Inc, AIAA, 2018, pp. 1–19. doi: 10.2514/6.2018-2032.

[199] R. C. Nelson, *Flight Stability and Automatic Control*, 2nd ed. McGraw-Hill Education, 1998. [Online]. Available: http://home.eng.iastate.edu/~shermanp/AERE355/lectures/Flight_Stability_and_Automatic_Control_N.pdf

[200] C. R. Chalk, T. P. Neal, T. M. Harris, F. E. Pritchard, and R. J. Woodcock, "Military specification MIL-F-8785B: Flying qualities of piloted airplanes," Ohio, Aug. 1969. [Online]. Available: https://apps.dtic.mil/sti/tr/pdf/AD0860856.pdf

[201] M. J. D. Powell, "A direct search optimization method that models the objective and constraint functions by linear interpolation," in *Advances in Optimization and Numerical Analysis*, Dordrecht: Springer Netherlands, 1994, pp. 51–67. doi: 10.1007/978-94-015-8330-5_4.

[202] P. Barua, T. Sousa, and D. Scholz, "Empennage statistics and sizing methods for dorsal fins," Apr. 2013. [Online]. Available: http://Reports_at_AERO.ProfScholz.de

[203] I. H. Abbott and A. E. Von Doenhoff, *Theory of Wing Sections Including a Summary of Airfoil Data*, 1st ed. Dover Publications, 1959.

[204] N. K. Sinha and N. Ananthkrishnan, *Advanced Flight Dynamics with Elements of Flight Control*, 1st ed. CRC Press, 2017. doi: 10.1201/9781315151977.

[205] S. B. Anderson, "A look at handling qualities of canard configurations," Sep. 1986. [Online]. Available: https://ntrs.nasa.gov/citations/19870013196

[206] M. Sadraey, "Aircraft configuration optimization through optimal longitudinal center of gravity range," in *9th AIAA Aviation Technology, Integration and Operations (ATIO) Conference*, 2009. doi: 10.2514/6.2009-7024.

[207] B. J. Holmes, C. P. Van Dam, P. W. Brown, and P. L. _ Deal, "Flight evaluation of the effect of winglets on performance and handling qualities of a single-engine general aviation airplane," Dec. 1980. [Online]. Available: https://ntrs.nasa.gov/api/citations/19810003504/downloads/19810003504.pdf

[208] I. Kroo, "Nonplanar wing concept for increased aircraft efficiency," in *VKI lecture: Innovative Configurations and Advanced Concepts for Future Civil Aircraft*, 2005. [Online]. Available: https://lf5422.com/wp-content/uploads/2014/08/vki_nonplanar_kroo-1.pdf

[209] F. Yu, J. Bartasevicius, and M. Hornung, "Comparing potential flow solvers for aerodynamic characteristics estimation of the T-FLEX UAV," in *33rd Congress of the International Council of the Aeronautical Sciences*, 2022. doi: 10.6084/m9.figshare.21656960.

[210] R. Schlosshan and M. Strens, “OpenXsensor,” 2015, *Github*. [Online]. Available: https://github.com/openXsensor

[211] G. E. Cooper and R. P. Harper, “The use of pilot rating in the evaluation of aircraft handling qualities,” Apr. 1969. [Online]. Available: https://apps.dtic.mil/sti/tr/pdf/AD0689722.pdf

[212] United States Army Aviation and Mission Command, “ADS-33E-PRF: Aeronautical Design Standard, Performance Specification, Handling Qualities Requirements for Military Rotorcraft,” Elsevier Masson, Jul. 2000. doi: 10.1016/J.AST.2019.04.032.

[213] C. M. Ivler *et al.*, “Toward a UAS handling qualities specification: Development of UAS-specific MTEs,” in *Vertical Flight Society’s 78th Annual Forum and Technology Display*, The Vertical Flight Society, May 2022, pp. 1–26. doi: 10.4050/F-0078-2022-17542.

[214] “ADS-33E-PRF - Aeronautical Design Standard, Performance Specification, Handling Qualities Requirements for Military Rotorcraft.” Accessed: Dec. 03, 2024. [Online]. Available: https://www.researchgate.net/publication/224989801_ADS-33E-PRF_-_Aeronautical_Design_Standard_Performance_Specification_Handling_Qualities_Requirements_for_Military_Rotorcraft/references

List of Publications and Awards

Publications

- **Lim Kin Yip, Shawn**, Philemon Koh Jun Kai, Satish Suppiah, Eden Lee Yao Rong & James Wang, "Experimental and Analytical Approach Towards Determining an Optimal Wing Arrangement for eVTOL Aircraft based on Aerodynamic Performance and Handling Qualities," Paper 1251. *Vertical Flight Society (VFS) Forum 80*, Montréal, Canada, May 2024. DOI: 10.4050/F-0080-2024-1251.
- **Lim Kin Yip, Shawn**, Boon Zhi Yuan & James Wang, "Trajectory Modelling of Transition Regime Using Blade Element Method for Different eVTOL Configuration," Paper 175. *49th European Rotorcraft Forum (ERF)*, Bückeburg, Germany, September 2023.
- Philemon Koh Jun Kai, **Lim Kin Yip, Shawn**. & James Wang, "Experimental Study on Aerodynamic Drag of Booms and Boom Mounted Stationary Rotors on eVTOL Aircraft," Paper 173. *49th European Rotorcraft Forum (ERF)*, Bückeburg, Germany, September 2023.
- **Lim Kin Yip, Shawn**, Andy Koh Jun Hoong & James Wang, "Simplified Model for Evaluating eVTOL Conceptual Designs and with Example Results for Three Types of eVTOL Aircraft Configurations," Paper 132. *48th European Rotorcraft Forum (ERF)*, Winterthur, Switzerland, September 2022.
- Abhijnan Dikshit, **Lim Kin Yip, Shawn**. & James Wang, "Parametric Study on Wing Design Variables for Tandem Wing Configuration eVTOL Aircraft," Paper 133. *48th European Rotorcraft Forum (ERF)*, Winterthur, Switzerland, September 2022.
- Abhijnan Dikshit, Tom Caton Arnaud Stokkermans, **Lim Kin Yip, Shawn**. & James Wang, "Effect of Lifting Surface and Tail Configuration on the Aerodynamics and Flight Mechanics of VTOL Aircraft," Paper 1237, *Vertical Flight Society (VFS) Forum 78*, Fort Worth, Texas, May 2022. DOI: 10.4050/F-0078-2022-17483.

Awards

- **Lim Kin Yip Shawn**, "Nanyang President's Graduate Scholarship (NPGS)", *Nanyang Technological University*.
- **Lim Kin Yip, Shawn**, "Vertical Flight Foundation (VFF) Scholarship", *Vertical Flight Society*.

Appendix: A

A.1 Flat Plate Analogy

The parasite drag area of a component refers to the area of a hypothetical flat plate which has the same parasite drag as the component and a drag coefficient of 1.0. The flat plate analogy defines the parasite drag area of each component as:

$$F_P = \Phi_f \cdot C_f \cdot S_{\text{wetted}} \tag{A.1}$$

For each component, the respective flat-plate skin friction drag coefficient C_{f_c} is first estimated using the following empirical formula, valid for Reynolds number between 10^6 and 10^8:

$$C_{f_c} = \frac{0.044}{(Re_c)^{\frac{1}{6}}} \quad \text{where} \quad Re_c = \frac{\rho \cdot \vec{V}_{\text{cruise}} \cdot l}{\mu} \tag{A.2}$$

The skin friction drag coefficient is then adjusted upwards using the empirical form factor, Φ_f, to account for pressure drag caused by flow separation. The form factors for the fuselage and the wing can be obtained by substituting their respective frontal to wetted area fraction into the linearised equations obtained from Figure A.1 [183] below:

$$\text{Fuselage:} \quad \Phi_{f,\,\text{fuselage}} = \frac{1.34 - 1}{0.1} \cdot \frac{S_{\text{front}}}{S_{\text{wetted}}} + 1 \tag{A.3}$$

$$\text{Wing:} \quad \Phi_{f,\text{wing}} = \frac{1.5 - 1}{0.1} \cdot \frac{S_{\text{front}}}{S_{\text{wetted}}} + 1 \tag{A.4}$$

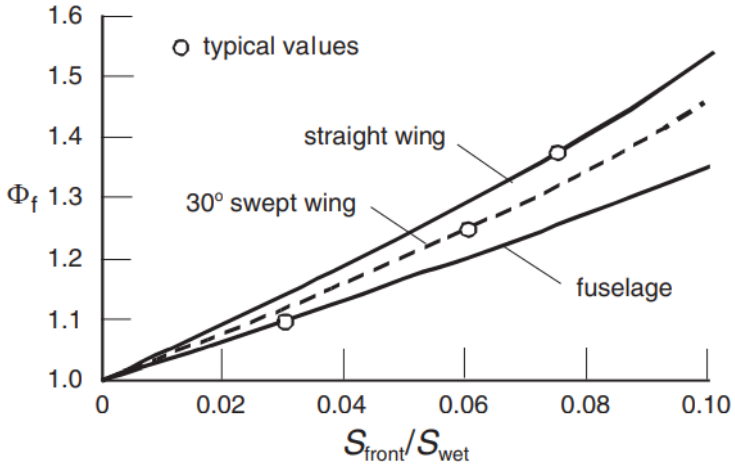

Figure A.1: Form factor chart for fuselage and wing derived from empirical data. Lines represents the form factor values for a straight wing, 30° swept wing and fuselage. Vertical axis represents the form factor, and horizontal axis represents the ratio of frontal wing area to the wetted wing area [183].

A.1.1 Fuselage Parasite Drag Coefficient

The frontal cross-sectional area of the fuselage is approximated by a circle with diameter d_{fuselage}. The wetted surface area of the fuselage is calculated by assuming the fuselage as a cylindrical tube with length l_{fuselage} and diameter d_{fuselage}. l_{fuselage} is adjusted for the tapered nose and tail by $1.3 \times d_{\text{fuselage}}$.

$$S_{\text{front, fuselage}} = \frac{\pi}{4} {d_{\text{fuselage}}}^2 \tag{A.5}$$

$$S_{\text{wetted, fuselage}} = \pi d_{\text{fuselage}} \cdot \left(l_{\text{fuselage}} - 1.3 \cdot d_{\text{fuselage}}\right) \tag{A.6}$$

The determined frontal and wetted areas can be substituted into (A.1) and (A.3) to determine the form factor and the parasite drag area for the fuselage. Normalising this area by the reference area of the wing, the drag coefficient of the fuselage is:

$$\left(C_{D,\text{parasite}}\right)_{\text{fuselage}} = \frac{F_{P,\text{fuselage}}}{S_{\text{wing, ref}}} \tag{A.7}$$

A.1.2 Booms and Pylons Parasite Drag Coefficient

The same methodology is used for booms and pylons. Each boom or pylon is approximated as a cylinder for drag estimation. The boom and pylon differ only in their lengths and diameters.

$$S_{\text{front, boom}} = \frac{\pi \cdot {d_{\text{boom}}}^2}{4} \tag{A.8}$$

$$S_{\text{wetted, boom}} = \frac{\pi \cdot {d_{boom}}^2}{4} + \pi d_{\text{boom}} \cdot l_{\text{boom}} \tag{A.9}$$

As the boom loosely resembles the shape of a fuselage, (A.3) is used for approximating the form factors of the booms and pylons. The drag coefficient of the booms is:

$$\left(C_{D,\text{parasite}}\right)_{\text{boom}} = N_{\text{booms}} \cdot \frac{F_{P,\text{boom}}}{S_{\text{wing,ref}}} \tag{A.10}$$

A.1.3 Wing Parasite Drag Coefficient

The frontal surface area of the wing is estimated to be:

$$S_{\text{front, wing}} = \text{MAC} \times \ (t/c) \times \ b_{\text{wing}} \tag{A.11}$$

The wetted surface area of the wing is given by the equation:

$$S_{\text{wetted, wing}} = \left(2 + 0.5(t/c)_{\text{wing}}\right) \left\{ \frac{Q_{\text{wing}} \sqrt{AR_{\text{wing}}\left(1 + \lambda_{\text{wing}}\right)}}{k_Q (t/c)} \right\}^{\frac{2}{3}} \tag{A.12}$$

The volume factor k_Q is assumed to have a value of 1 for an untapered wing and a value of 0.95 for a tapered wing. The volume Q_w of the wing is given by the equation:

$$Q_{\text{wing}} = \frac{k_Q \left(\frac{t}{c}\right)_{\text{wing}}}{\sqrt{1+\lambda_{\text{wing}}}} S_{\text{wing}} \sqrt{\frac{S_{\text{wing}}}{AR_{\text{wing}}}} \tag{A.13}$$

(A.2) and (A.4) are used to determine the parasite drag area of the wing. The characteristic length used for the wing is taken as its MAC. The drag coefficient of the wing is:

$$\left(C_{D,\text{parasite}}\right)_{\text{wing}} = \frac{F_{P,\text{wing}}}{S_{\text{wing,ref}}} \tag{A.14}$$

For tandem wing configuration, the same formulas are applied for both wings.

A.1.4 Form Factors for Canard and Empennage

The empirical form factor chart in Figure A.1 does not include data points for the empennage and canard. It is assumed that the ratios between the parasite drag area and wetted area of these components are similar to that for the wing. This ratio, defined as $\left(C_{f,\text{eqv}}\right)_{\text{wing}}$, is obtained as:

$$\left(C_{f,\text{eqv}}\right)_{\text{wing}} = \Phi_{f,\text{wing}} \cdot C_{f,\text{wing}} \tag{A.15}$$

A.1.5 Empennage Parasite Drag Coefficient

The total wetted area for the empennage is obtained as an input. The tapered end of the fuselage is assumed to cover a negligible portion for the empennage.

The flat plate parasite drag area of the empennage is given by:

$$F_{p,\text{empennage}} = \left(C_{f,\text{eqv}}\right)_{\text{wing}} \cdot S_{\text{wetted, empennage}} \tag{A.16}$$

The drag coefficient of the empennage is:

$$\left(C_{D,parasite}\right)_{\text{empennage}} = \frac{F_{p,\text{empennage}}}{S_{\text{wing}}} \tag{A.17}$$

A.1.6 Canard Parasite Drag Coefficient

The total wetted area of the canard is:

$$S_{\text{wetted, empennage}} = 2 \cdot \left(c_{\text{root, canard}} + c_{\text{tip, canard}}\right) \cdot \text{Canard Span} \tag{A.18}$$

The fuselage is assumed to cover a negligible portion of the canard.

The flat plate parasite drag area of the canard is given by:

$$F_{P,\text{canard}} = \left(C_{f,eqv}\right)_{\text{wing}} \cdot S_{\text{wetted, canard}} \tag{A.19}$$

The drag coefficient of the canard is:

$$\left(C_{D,\text{parasite}}\right)_{\text{canard}} = \frac{F_{p,\text{canard}}}{S_{\text{wing}}} \tag{A.20}$$

A.1.7 Stationary Propeller Blades Parasite Drag Coefficient

The length of each blade can be estimated by subtracting the spinner radius from the radius of the stationary propeller.

$$l_{\text{blade}} = \frac{d_{\text{stationary propeller}}}{2} - r_{\text{spinner}} \tag{A.21}$$

The total developed blade area is given by:

$$S_{\text{developed, blades}} = N_{\text{stationary propellers}} \cdot N_{\text{blades}} \cdot \ l_{\text{blade}} \cdot c_{\text{blade}} \tag{A.22}$$

The total wetted area is twice the developed blade area.

$$S_{\text{wetted, blades}} = 2 \cdot S_{\text{developed, blades}} \tag{A.23}$$

The blade is assumed to have negligible thickness; hence the frontal area is zero.

Using Figure A.1, the form factor is:

$$\Phi_{f,\text{blades}} = 1.0 \tag{A.24}$$

The parasite drag area and drag coefficient of the stationary propeller blades are:

$$F_{P,\text{blades}} = C_{f,\text{blades}} \cdot S_{\text{wetted, blades}} \tag{A.25}$$

$$\left(C_{D,\text{parasite}}\right)_{\text{blades}} = \frac{F_{P,\text{blades}}}{S_{\text{wing,ref}}} \tag{A.26}$$

A.2 Empirical Estimates of Drag Coefficients

A.2.1 Spinners of Stationary Propellers

For the cylindrical spinner (denoted by *cyl*), the frontal area is assumed to be a rectangle:

$$S_{\text{front,cyl}} = h_{\text{cyl}} \cdot 2\, r_{\text{cyl}} \tag{A.27}$$

The empirical drag coefficient of each cylindrical spinner is found to be 0.3 based on frontal area in Figure A.2 [184].

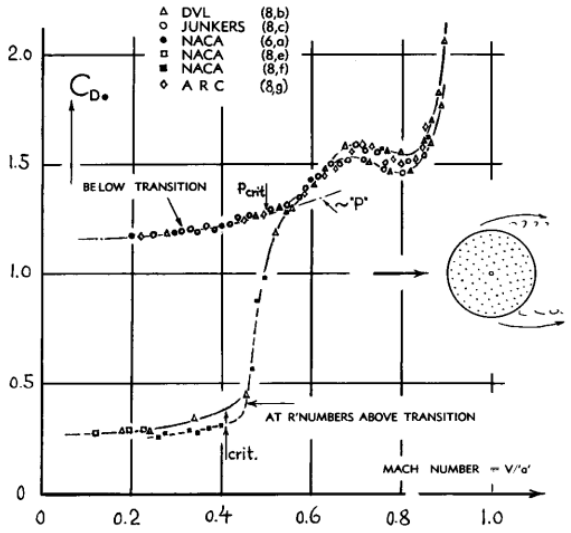

Figure A.2: Empirical drag coefficients of circular cylinders based on frontal area.
Vertical axis representing the C_{D_o} and the horizontal axis representing the Mach number [184].

The combined drag coefficient of the cylindrical spinners of stationary propellers is:

$$\left(C_{D,\text{parasite}}\right)_{\text{cyl}} = N_{\text{stationary propellers}} \cdot 0.3 \cdot \frac{S_{\text{front,cyl}}}{S_{\text{wing, ref}}} \tag{A.28}$$

The frontal area of a hemispherical spinner (denoted by *hemi*) is a semi-circle:

$$S_{\text{front, hemi}} = N_{\text{stationary propellers}} \cdot \frac{\pi r_{\text{hemi}}{}^2}{2} \tag{A.29}$$

The empirical drag coefficient of the sphere at 0.47 is used to model the hemispherical spinner. The drag coefficient of hemispherical spinners of stationary propellers is:

$$\left(C_{D,\text{parasite}}\right)_{\text{hemi}} = N_{\text{stationary propellers}} \cdot 0.47 \cdot \frac{S_{\text{front,cyl}}}{S_{\text{wing, ref}}} \tag{A.30}$$

A.2.2 Landing Gear

As mentioned previously the analysis accounts for two types of landing gear: wheeled non-retractable and retractable. For retractable landing gear, they are hidden during cruise and do not contribute to drag. For wheeled non-retractable landing gear, the landing gear drag coefficient can be selected from Figure A.3 [184].

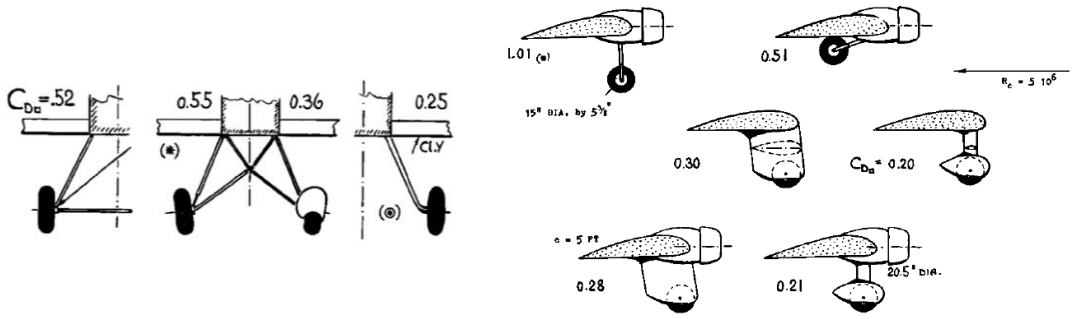

Figure A.3: Empirical drag coefficients for wheeled landing gears.
Based on wheel frontal area for various landing gear designs [184].

A.2.3 Nacelles of Horizontal Propellers

The nacelles are only used to carry horizontal propellers. The frontal area of each nacelle is estimated as the rotor hub frontal area of the horizontal propellers.

$$S_{\text{front, nacelles}} = N_{\text{horizontal prop}} \cdot \pi {r_{\text{spinner}}}^2 \tag{A.31}$$

The drag coefficient of the round nacelle at 0.092 is currently used as it is most representative of current eVTOL designs. Figure A.4 [184] can be used to model other nacelle profile types where necessary.

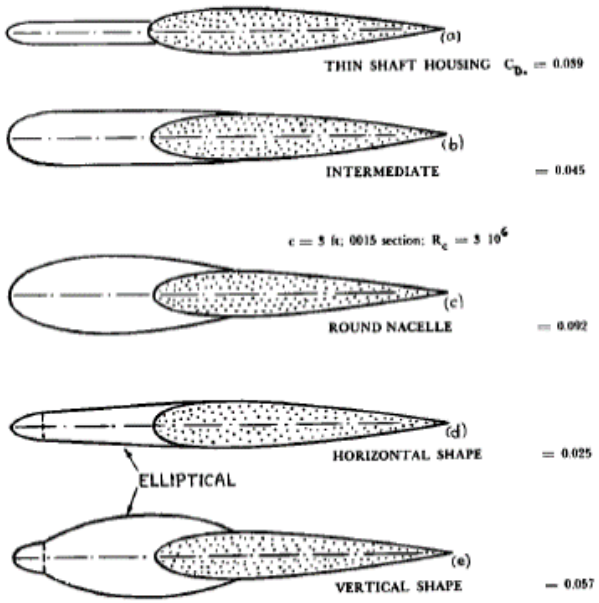

Figure A.4: Empirical drag coefficients for different nacelle types.
Vertical and horizontal frontal area for thin shaft housing, intermediate and round nacelle [184].

A.2.4 Interference Drag between Wing and Fuselage

The interference drag between the wing and fuselage is interpolated from Figure A.5 [184] in the form:

$$C_{D,\,\text{interference}} = \left(0.8\left(\frac{t}{c}\right)^3 - 0.0003\right) \cdot \frac{\text{MAC}^2}{S_{\text{wing}}} \tag{A.32}$$

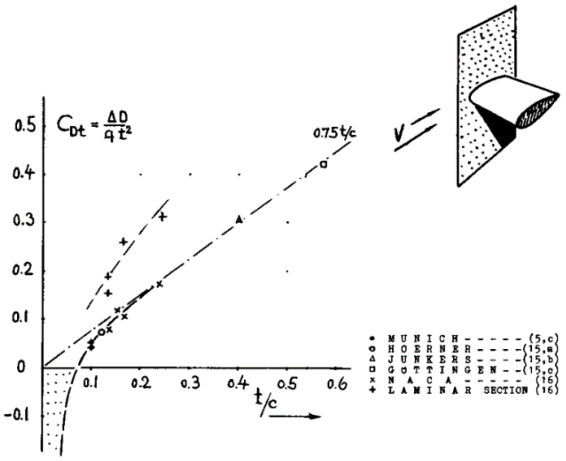

Figure A.5: Interference drag coefficient at junction of wing with a plane wall.
Vertical axis is the normalized drag coefficient and horizontal axis is the thickness to chord ratio [184].

A.3 Oswald Span Efficiency Method for Induced Drag

In steady-state cruise, the lift acting on the aircraft is assumed to be equal to its weight. The lift coefficient for a wing is given by:

$$C_L = \frac{W_{\text{eVTOL}}}{q \cdot S_{\text{wing}}} \quad \text{where} \quad q = \frac{1}{2}\rho \vec{V}^2 \tag{A.33}$$

The induced drag coefficient can be calculated as:

$$C_{Di} = k{C_L}^2 = \frac{{C_L}^2}{\pi \cdot AR \cdot e} \tag{A.34}$$

For tandem wing configuration, the weight of the eVTOL is first divided among the wings using the lift fractions to calculate their separate induced lift coefficients:

$$C_{L,\text{fw}} = \frac{L_{\text{fw}} \cdot W_{\text{eVTOL}}}{q \cdot S_{\text{fw}}} \quad \text{and} \quad C_{L,\text{rw}} = \frac{L_{\text{rw}} \cdot W_{\text{eVTOL}}}{q \cdot S_{\text{rw}}} \tag{A.35}$$

$$C_{Di,\,\text{fw}} = k{C_{L,\text{fw}}}^2 \quad \text{and} \quad C_{Di,\text{rw}} = k{C_{L,\text{rw}}}^2 \tag{A.36}$$

The combined induced lift coefficient for tandem wings is given by:

$$C_{Di,\text{tandem}} = C_{Di,\text{fw}}\left(\frac{S_{\text{fw}}}{S_{\text{total}}}\right) + C_{Di,\text{rw}}\left(\frac{S_{\text{rw}}}{S_{\text{total}}}\right) \tag{A.37}$$

$$\text{where } S_{\text{total}} = S_{\text{fw}} + S_{\text{rw}}$$

A.4 Overall Drag Coefficient

The overall drag coefficient is the sum of parasite drag from each component and the induced drag. The parasite drag coefficient uses the same reference area in the induced drag computation.

$$C_D = C_{D,\text{parasite}} + C_{Di} \tag{A.38}$$